THE UNIVERSITY OF MICHIGAN
DEPARTMENT OF ELECTRICAL ENGINEERING
PLASMA ENGINEERING LABORATORY

ACCELERATION OF PLASMAS BY INDUCTIVELY GENERATED ELECTROMAGNETIC FIELDS

FINAL REPORT

By

David B. Miller

Project 02836

CONTRACT NO. AF 19(604)-4557
UNITED STATES AIR FORCE
AIR FORCE RESEARCH DIVISION
BEDFORD, MASSACHUSETTS

April, 1961

This report has also been submitted as a dissertation in partial fulfillment of the requirements for the degree of Doctor of Philosophy in The University of Michigan, 1961.

ABSTRACT

This dissertation deals with the theory and experimental behavior of an induction electromagnetic accelerator. The induction accelerator, one example of a general class of electrical systems which can be used to accelerate charged particles and ionized gases, employs a time-varying current in a coil to generate the force-producing electric and magnetic fields. The application of the induction accelerator for space propulsion is of particular interest.

Some aspects of the induction accelerator which can be derived theoretically are first brought out. These begin with a study of isolated particle behavior within a cylindrical coil. Charges gain energy from the azimuthally directed electric field; their paths are turned in the radial and axial directions by the magnetic field, and they eventually are ejected out the end of the coil. The exact paths of electrons and helium and argon ions under various field conditions (magnitude and frequency) are calculated by analog computer techniques, and from these calculations are obtained the velocity and angle which the ejected particles ultimately obtain. One important result which comes out of this particle analysis is the quantitative dependence of ejection characteristics on initial position of the particle. Another significant item is the marked difference in behavior when the field period is much less than and much more than the time taken for the particle to be ejected from the accelerator.

Induction acceleration of plasmas is theoretically considered first under the simplifying assumption that the coil is very long. This eliminates radial magnetic field components and thrust in the axial direction, but it realistically treats the radial motion, an important energy-transferring process in the experimental device. The effect of self-fields (electric due to charge separation and magnetic due to the gas current) on the radial motion is extensively studied; this reveals that even at quite low densities the particles are bound to one another by these fields, and it leads to the calculation of the radial motion of such low density plasmas. The radial dependences of magnetic field and current density within the ionized gas are shown to be approximated by Bessel functions. At high densities a skin current is shown to form and to prevent penetration of the magnetic field into the interior of the plasma. For these high densities a "snowplow" analysis is used to calculate the radial motion of the plasma.

The axial motion of plasma within a finite sized coil is next considered. Qualitatively, it is argued that the majority of energy in axial motion arises from energy which is transmitted to the plasma by radial compression and then is converted to axial motion in the diverging magnetic nozzle. Characteristics of the flowing gas which can be obtained from observation of the advancing shock wave are brought out.

Experiments using an induction accelerator are described. The accelerator is a 10 cm long by 10 cm diameter, single turn, cylindrical coil driven by a 37.5 μfd capacitor bank. Capacitor voltages in the 5 to 10 kilovolts range were used. Ionization of the gas within the coil

was accomplished partly by a high frequency preionization circuit and partly by the accelerator field itself.

Data on helium and argon over the general pressure range of 0.010 to 1.00 mm of Hg are reported. Specifically, kinetic characteristics (radial and axial motion, momentum and energy) and internal structure (current and charge) of the accelerating ionized gas were studied. For these purposes, circuit measurements, ballistic pendula, calorimeters, a rotating mirror camera, magnetic probes and electric probes were employed. The separate measurements are discussed and correlated whenever possible with each other and with the theory.

Some experimental results will give an idea of the general characteristics of the induction accelerator. Axial velocity of the gas as it emerges from the coil is typically 0.5 to 10 cm per microsecond. Energy in the amount of approximately 10 to 50 joules is transferred from the circuit to the gas; this represents up to 10 percent of the energy available in the magnetic field of the coil, and about half this transferred energy goes into directed motion of the gas. Ion temperatures, calculated from observations of the radial compression and axial shock, are in the 25,000°K to 100,000°K range; electron temperature, measured for one pressure by an electric probe, is about one-third the concurrent ion temperature.

In the concluding chapter of this report, suggestions are made with regard to continuation of this effort, and characteristics of a propulsion motor using the induction principle are estimated, based on the results of this study.

ACKNOWLEDGMENTS

To the members of my doctoral committee, W. G. Dow, C. L. Dolph, H. C. Early, G. Hok, J. E. Rowe and M. L. Wiedenbeck, should go special thanks for their continued encouragement and aid. Professor Dow, chairman of this committee, has in particular strengthened this work by his frequent advice and counsel.

The majority of the work reported here was carried out in the Plasma Engineering Laboratory, whose director, Mr. H. C. Early, contributed many valuable suggestions during the course of this program. Messrs. F. J. Martin and R. J. Salmer were instrumental in developing the experimental gear, and Miss C. K. Kamii lent valuable editorial assistance.

The technical and editorial staffs of the Electron Physics Laboratory, under the directorship of Dr. J. E. Rowe, also contributed significantly to this effort. It should especially be noted that Mr. R. J. Martin was largely responsible for developing the particular analog system used for the Chapter II trajectory calculations and that Mr. A. J. Pajas carried out the programming for digital computation of Eq. 4.43.

I should also like to thank Dr. Morton A. Levine of the Air Force Cambridge Research Center for his continued support and encouragement and Dr. E. A. Martin for frequent helpful discussions.

TABLE OF CONTENTS

LIST OF TABLES

LIST OF ILLUSTRATIONS

CHAPTER I. INTRODUCTION

1.1 Possibilities of Electrical Propulsion

1.1.1 Introduction. Vehicles traveling outside an atmospheric environment (i.e., in space) must carry along both the mass and energy which are to be used for propulsion*. With the advent of nuclear sources, the energy problem may not be critical, but mass must be considered carefully, since it represents weight which must be lifted through the earth's gravitational field. Propulsion thrust depends on the momentum flow out of the vehicle; thus, mass can be economized by using increased velocity with which the propellant mass is expelled from the vehicle. Let us consider space propulsion, then, from this viewpoint.

In order to compare the various devices, we will want to compare the exhaust velocities V_{ex} achievable by each. For purposes of conformity with standard practice, we will use the specific impulse[1],

$$I_{sp} \triangleq \frac{V_{ex}}{g} \qquad \text{(seconds)} ,$$

rather than V_{ex} itself; in this expression, g is the acceleration due to gravity. This quantity, I_{sp}, as its name implies, measures the impulse (force x time) given to a vehicle per unit weight of propellant, under the condition that the exhaust velocity is much higher than the vehicle velocity.

---

* This statement is in general true but must be qualified by the possibilities of using for propulsion purposes solar energy and "cosmic dust" collected along the way on a space mission.

To date, our space probings have utilized the chemical rocket technique, whereby chemical energy is used to heat the propellant, and the heated gas is converted to a directed stream by means of an exit nozzle. In any thermally operated motor, the exhaust velocity and specific impulse are direct functions of the temperature of the propellant. Thus, the exhaust velocity of a chemical rocket is determined by the temperature of the chemical reaction. For the typical reactions employed in today's rockets, the specific impulses are on the order of 300 seconds[2]. Higher energy fuels, for instance employing free radical reactions, apparently cannot do any better than double this figure[3].

Going beyond the chemical rocket, we can seek to increase the exhaust velocity of the propellant stream either by increasing the temperature of the propellant or by using nonthermalizing acceleration methods. If thermal avenues are pursued, the added materials problem of containing the hot gas must be faced.

Electromagnetic fields can be employed in various manners to meet these propulsion problems. It will be the purpose of this first section to survey the possible electrical methods and to note wherein electromagnetic fields can be used to heat, contain and nonthermally accelerate gases. This review will then lead to a specific electrical propulsion system, the induction accelerator, which will be the object of study for the remainder of this paper.

1.1.2 Electrostatic Acceleration—the Ion Rocket. A beam of charged particles, accelerated through an electrostatic field, will constitute a momentum-carrying stream of high velocity. The potentiality of an ion beam as a means of propulsion was recognized many years

ago[4], and as a practical device, the electrostatically accelerated ion rocket has received a great deal of attention[5-9], being in fact probably the nearest to a practical application of any of the electrical propulsion devices.

The electrostatic ion rocket has the desirable features of achieving high propellant exhaust velocity and of keeping the stream away from any material structures by proper focusing techniques. Disadvantages arise from the limited methods available for creating ions efficiently and from the necessity of microscopically neutralizing the ion beam as it leaves the vehicle.

Specific impulses for an electrostatic ion rocket can take on almost any value, but practical designs are generally in the 3,000-20,000 second range[2,3,10,11].

1.1.3 Electromagnetic Acceleration—Magnetohydrodynamic (MHD) or Crossed-Field Plasma Motors. When an ionized gas is caused to flow through a channel between electrodes, and an external d-c power source is connected to the electrodes, a current with a component parallel to the applied electric field will pass through the gas. Now, if the channel is immersed in a d-c magnetic field perpendicular both to the gas flow direction and the direction of current through the gas, then a steady j x B body force is experienced on the gas, causing the flow to accelerate. This form of crossed-field configuration (electric and magnetic fields "crossed", or normal to one another) is being actively investigated at several locations[12,13]. The basic characteristics of this type of accelerator are shown in Fig. 1.1a.

An alternative form of the d-c crossed-field device exists. In this variation, the electric field drives a current through the ionized

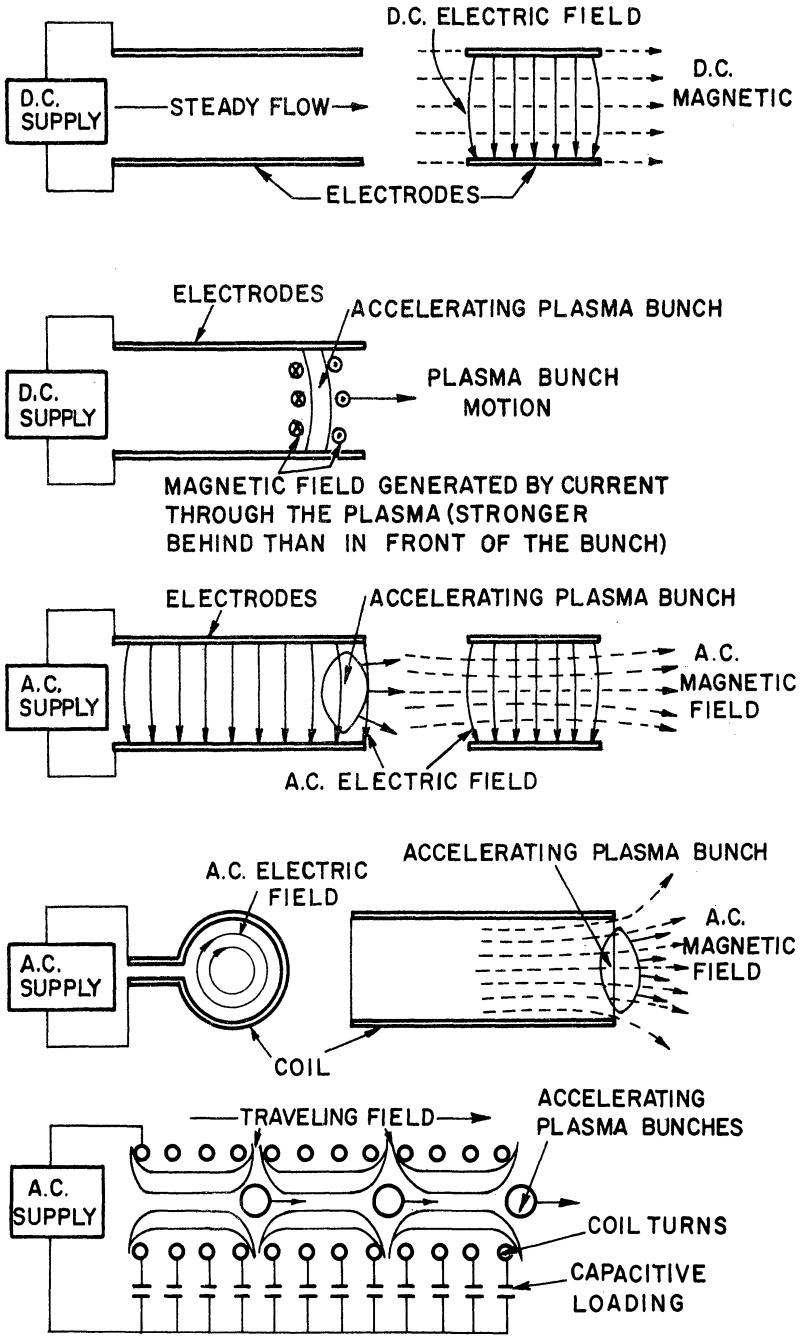

Fig. 1.1. Crossed-Field Accelerators.

(a) D-C Independent Magnetic Field (MHD Channel Flow) Accelerators

(b) D-C Self Magnetic Field (Rail) Accelerator

(c) A-C (Capacitive) Accelerator

(d) A-C (Inductive) Accelerator

(e) Traveling-Wave Accelerator

gas, as before, but the normal magnetic field is generated by this gas current rather than independently[14-20]. In practice, these devices accelerate bunches of plasma down finite-length electrode sections, so they operate on a pulsed basis, but the analysis of their operation does not depend on a time-changing field characteristic. A possible form which can be taken in this case is shown in Fig. 1.1b.

Time-changing forms of the crossed-field accelerator can be conceived. Two specific configurations are shown in Figs. 1.1c and 1.1d. Note that in one (capacitive type), an electric field between electrodes generates a magnetic field normal to itself, while in the other (inductive type), an a-c magnetic field due to current in a coil induces a normal electric field. Thus, the time-varying nature of the fields, by the curl relations,

$$\text{curl } H = \frac{\partial D}{\partial t} \quad ,$$

and

$$\text{curl } E = -\frac{\partial B}{\partial t} \quad ,$$

automatically creates the crossed-field conditions.

One will notice the similarity between the basic configurations of the d-c self magnetic field accelerator (Fig. 1.1b) and the capacitive type of time-changing accelerator (Fig. 1.1c); they differ only in the fact that one type derives its magnetic field from conduction current, while the other depends on displacement current. In any experimental device, both sources of field will undoubtedly be active to some extent. Thus, the accelerators mentioned above[14-20], being driven in fact by an energy storage capacitor, will have some

displacement current effect. No mention of an accelerator designed purposely to operate on the displacement current principle has been found in the literature.

The inductive, a-c geometry (Fig. 1.1d) has received some study[31,33,43], and references will be considered more thoroughly in the next section. The design in Fig. 1.1d might be termed a stationary field device, since the magnetic and electric fields change in time rather than space. Moving field arrangements, where the fields change in position but remain independent of time in a frame moving with the field, can also be realized[40,41]. Such a moving-field, or traveling-wave, accelerator is shown in Fig. 1.1e.

Specific impulses for these crossed-field plasma accelerators are generally considered to be lower than for the electrostatic ion motors[11], but at least one reference cites the range 1000-20,000 seconds as possible[21]. Since more mass is involved in the MHD accelerators than in the electrostatic ion systems, the thrust level is higher.

In the d-c and a-c electrode plasma devices, confinement is of necessity by the materials used to form the electrodes. In the time-changing magnetic field arrangements, on the other hand, no electrodes are needed, since the electric field is induced (giving the popular names of electrodeless or induction motors to these systems), and confinement can be wholly by the magnetic field itself.

1.1.4 Electrothermal Acceleration—Arc Jet Motors. In order to complete our survey of electric thrust devices currently being considered, a third class of devices should be mentioned. In this method, the propellant is heated by an electric arc, and the heated gas is then

expanded through a nozzle to create a propellant stream[11,22,23]. Essentially, this is then quite similar to a chemical or nuclear reaction motor. The temperature attainable in an electric arc is greater than from chemical combustion, leading automatically to higher I_{sp}, so long as the containment problem is solved. Conceivably, temperatures might be reached at which thermal ionization of the gas is great enough to allow magnetic rather than material wall confinement of the propellant; the stability of such a confining system should be considered.

Specific impulses predicted for arc-jet motors range generally from a few hundred to a few thousand seconds[11,22,23].

1.1.5 Classification of Electrical Thrust Systems. All electrically driven reaction motors have the common principle that energy is transferred to the propellant stream by charged particles traveling parallel to an electric field. Within this broad criterion, two characteristics allow division of these devices into several subcategories:

1. One classification is made on the basis of the mean free path within the propellant. If the mean free path is very long, then the motor is basically a particle accelerator, whereas if the mean free path is short, so that the stream energy randomizes rapidly, a plasma forms, thermal effects must be considered, and continuum analytical treatments can be used.
2. The other distinction concerns the field characteristics. The field may be solely a d-c electric field, or there may be both electric and magnetic fields which are normal to one another (crossed fields). Components of magnetic field parallel to the electric field may be useful in confinement

schemes but are not of interest in our propulsion classification.

Two primary features of the crossed-field situation should be mentioned. In the first place, positive and negative charges accelerated in such fields experience Lorentz forces in parallel directions. Thus, the charge neutralization problem of the electrostatic ion engine could be solved by the crossed-field particle device. Secondly, as pointed out above, crossed-field conditions are automatically generated if a time-changing electromagnetic field is used. The field may be generated by capacitive or inductive means.

Table 1.1 summarizes the above thoughts and indicates where in our classification scheme one finds the various electrical propulsion methods discussed previously. In Table 1.1, two examples from outside the propulsion field have been used in the long mean free path, crossed-field situations, since to this author's knowledge experiments in these areas aimed at the propulsion application have not been performed.

1.2 Induction, or Electrodeless, Accelerators

The survey of Section 1.1 indicates that the time-changing inductive type of crossed-field geometry can be used for propulsion purposes. It will be useful to consider this operating mode more thoroughly to indicate where further work might be carried out.

Electrical discharges produced by time-varying currents in coils have long been known and studied[26,60]. Continuously driven, electrodeless discharges ("electrodeless", since the electric field is induced rather than applied through electrodes) using r-f and microwave

Table 1.1. Classification of Electrical Propulsion Systems

FIELD / MEAN FREE PATH	ELECTROSTATIC	CROSSED ELECTRIC AND MAGNETIC	
		D-C	TIME-CHANGING
LONG	Electrostatic ion motor[5-9]	Linear magnetron[24]	Betatron[25]
SHORT	Arc jet motor[22,23]	MHD channel flow[12,13] Rail gun[15] Coaxial accelerator[16]	Electrodeless induction accelerator[31,33,43] Traveling-wave accelerator[40,41]

drivers have been frequently used for generation[27] and study[28] of plasmas. A breakdown criterion similar to the Paschen Law for d-c discharges has been both theoretically[26,29,60] and experimentally[33] demonstrated.

Only recently has the potentiality of plasma acceleration by inductive methods been utilized. Perhaps the earliest reported efforts along this line were experiments described by Thonemann, Cowhig and Davenport[30] in 1952. These investigators were able to show evidence of directed motion of ionized gas within a toroid tube on which was wound an r-f-excited, slow-wave structure.

An early theoretical analysis of a much more simplified geometry was made by Morozov[31], who studied the expulsion of a rigid "plasma" ring from a cylindrical coil in terms of the energies within the system at various times.

Petschek[32] and Blackman[33], have described shock-generating methods using the low density transient discharge induced by single turn circular coils.

Marshall[34], at the 1958 Geneva meeting, discussed his efforts to propel bunches of plasma by a cylindrical traveling-wave structure.

Bostick[35], in 1958, was perhaps the first to discuss in the literature the possibility of applying systems such as used in Marshall's experiments and Morozov's analysis for propulsion. At the time the presently described work was begun[36], mid-1958, the application of pulsed crossed-field acceleration specifically as an electrical propulsion device had, however, received little attention other than in Bostick's report.

Since 1958, the acceleration of plasma by pulsed, induction means has received increasing attention. Among the single coil geometries such as shown in Fig. 1.1c, Scylla, a thermonuclear device which originally developed from plasma acceleration ideas[37], has been studied extensively. The British thermonuclear group has also recently been investigating action of ionized gas within a simple, pulsed, cylindrical coil[38]. The thermonuclear approach of course is to confine the plasma rather than expel it from the coil as propulsion would demand. It turns out, however, that, in both the thermonuclear studies and in the propulsion-oriented investigation which constitutes the body of this report, the important initial activities within the coil, namely ionization and radial compression of the gas within the coil, are the same. Thus, our analysis of this phase of the device has possibly broader interest than strictly for propulsion.

Klein and Brueckner[39], making a more thorough and realistic analysis than did Morozov of plasma acceleration by a circular coil, concluded that efficiency of a device which drives plasma by the magnetic field from a stationary coil is probably too low for propulsion applications.

This lack of efficiency in transferring energy from the circuit to the plasma, as indicated by the Klein-Brueckner study and also by the thermonuclear experiments, has perhaps been a major deterrent to the consideration of a simple inductive system for propulsion. Work which has been reported in the past two years has generally been on traveling-wave systems[40,41,42] where the magnetic field works strongly on the plasma for a considerable length of time and space and so intuitively ought to raise the energy efficiency.

The present work also began along the traveling-wave approach[36], but it was soon felt that perhaps a less complex structure, something which might in effect lie between the Klein-Brueckner, circular coil and the traveling-wave structure, ought also to be considered. Our work then focussed on a cylindrical coil[43], which would enclose and couple with more gas than the "shorter" circular coil while retaining its simple circuit characteristic.

1.3 Preview of Present Work

In reviewing the research on electromagnetic propulsion which has been carried on during the recent past, the previous two sections have indicated that single-coil, inductively driven, plasma accelerators have not been sufficiently analyzed from the propulsion standpoint. It is the purpose of this present study, therefore, to investigate the fundamental processes active in these simple, pulsed, crossed-field systems and to measure some of the basic characteristics which would be of interest in the propulsion application. Thus, this work represents a fundamental study program and does not in itself attempt to develop any economically operable device such as a propulsion motor.

Two approaches could be used in attacking the problem defined in the previous paragraph: Either a completely general treatment could be attempted, from which characteristics of specific systems could be derived by proper reduction, or a specific case could be studied, and if this case were sufficiently typical, general behavior traits could be deduced therefrom.

Since this study is largely oriented around experimental measurements, which of necessity are limited in their scope, the latter method of attack has been chosen. Thus, both theoretical and

experimental results here reported are tied to one specific system. This has the advantage of providing some reasonably reliable numbers which might find eventual use as design criteria while at the same time giving behavioral information on the general class. It behooves us at this point, therefore, to design a specific system which will yield easily to detailed experimental and theoretical scrutiny, but which will exemplify the action of the general class of inductive acceleration devices.

The most important decision which must be reached is the determination of the geometry of the coil through which time-varying current is driven, generating the desired crossed-field conditions. From our earlier discussion (Section 1.2) we have decided to use a coil which is longer than merely a circular wire filament. We must also specify that this be a single-turn coil in order to eliminate "capacitive" fields which are present in many-turn coils. (Note that Josephson[44] has reported briefly on plasma acceleration in a several-turn coil, and it has also been brought to this author's attention that similar unreported experiments have been carried on at General Electric and Litton.)

A cylindrically symmetrical coil will be assumed; its shape must now be decided. A conical design, such as used by Josephson[44], or even a more complicated shaping to optimize the field configuration, might be used. It is felt, however, that operation will differ in <u>degree</u> rather than in <u>kind</u> by coil shaping; so, in the spirit of a fundamental study program rather than a design optimization project, a simple cylindrical coil will be used.

In this cylindrical geometry, the induced electric field will be azimuthal, and current carried by charged particles within the coil will

also be in the θ direction. Since any feasible propulsion device must impart directed momentum to the propellant, we should seek to encourage forces in the z direction on these charged particles, and this means that we must have radial magnetic field components present. The operating region must therefore be in the fringing field emerging from the end of the coil, not in the axial field found in the center of the coil.

In determining the exact length of the coil to be used, we must compromise between a very long coil, which will enclose more propellant at any given instant but which will not present significant radial magnetic field over much of its length, and a very short coil, such as studied by Klein and Brueckner[39], which has strong radial fields but whose influence extends over only a very small volume. A reasonable choice under these circumstances is a coil whose length-to-diameter ratio is unity. In particular, most of the experimental and theoretical work reported in the following chapters considers a 10 cm long by 10 cm diameter coil, shown schematically with its driving circuit in Fig. 1.2. Generalizations from this case will be pointed out when possible.

Qualitative understanding of the principle underlying the operation of the induction acceleration can be obtained by consideration of the forces on a charged particle in the acceleration field. Such a particle is shown in Fig. 1.2, and the forces shown are appropriate during the first quarter of each cycle of the coil current. Note that the coil current is increasing in the clockwise direction (end view) and is thereby generating a magnetic field coming out of the page and inducing a counterclockwise, azimuthal electric field. The electric field causes the particle to begin accelerating in the azimuthal

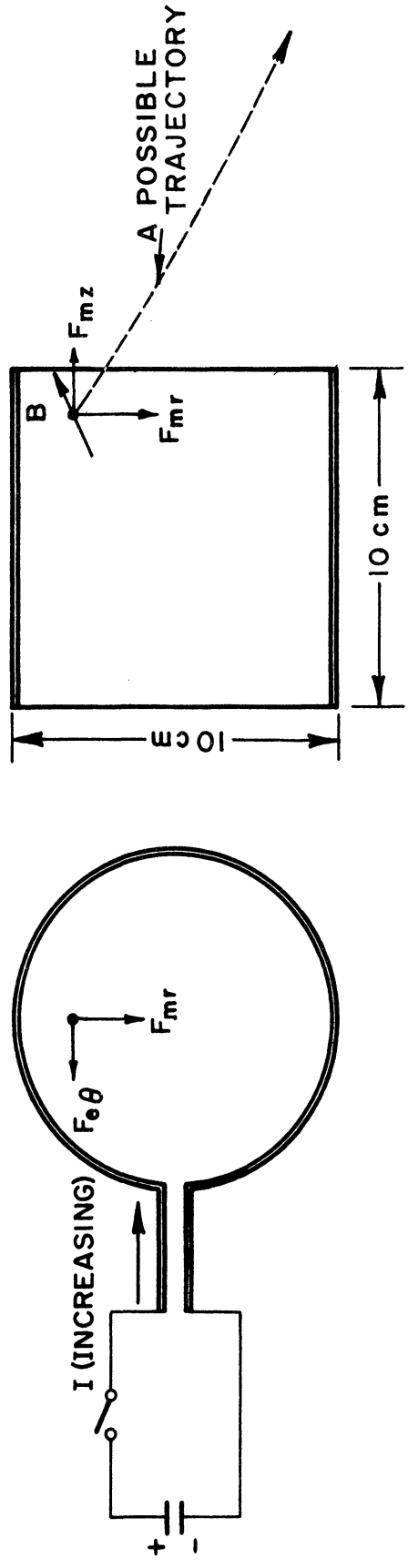

FORCES: $F_{e\theta}$ (AZIMUTHAL ELECTRIC)
F_{mr} (RADIAL MAGNETIC)
F_{mz} (AXIAL MAGNETIC)

Fig. 1.2. Inductive Accelerator Showing Driving Circuit and Forces Existing on a Moving Charged Particle.

direction. As the particle moves in the azimuthal direction through the magnetic field it experiences Lorentz forces in the radial and axial directions, as shown in Fig. 1.2, causing the particle to accelerate at some angle out of the coil. The centrifugal reaction, not shown in Fig. 1.2, tends to balance out the radial force, but, as will be shown in Chapter 2, complete balance is obtained only under very restricting conditions.

In the second quarter-cycle, the electric field reverses; this reverses all the forces and tends to draw the particle back into the coil. In the third quarter-cycle, the magnetic field as well as the electric field are reversed from the condition shown in Fig. 1.2, and this results in the forces being the same as shown in Fig. 1.2. Thus, expulsion conditions repeat each half-cycle.

Theoretical treatment of the pulsed crossed-field device will first be carried out in order to indicate the behavior of ionized gas in the accelerator under a wide variety of field and plasma conditions.

The initial theoretical calculation will treat motion of isolated particles under the influence of the forces outlined in connection with Fig. 1.2. This will involve a reasonably straightforward integration of the equations of motion and will result in trajectories under a wide range of field conditions. These individual particle trajectories will of course be exact only under very long mean free path conditions, where the particles in the plasma are completely uninfluenced by one another. They do, however, give exact behavior in the true field configuration of the 10 cm x 10 cm cylindrical coil, and they lead naturally to the next stage in the theoretical treatment, discussed in the following paragraph.

As the particle density of the plasma increases the individual particles become influenced by one another through their Coulomb interactions, and calculations of the motions of particles or of the plasma as a whole must take into account this internal electric field effect. In addition, if the currents in the plasma become of the same order of magnitude as the coil current, the self-magnetic field of the plasma current must be taken into account. It will be the purpose of Chapter III to consider these self fields; the treatment will of necessity require simplification of the field shape and the analysis will therefore be only approximate, but it will deal with a more realistic experimental situation than does the particle trajectory analysis.

In Chapter IV, some of the restrictions of the Chapter III model are removed, and the realistic action of a column of ionized gas within the induction accelerator is studied. The solutions derived here will be applicable approximately for electron mean free paths several times the coil radius down to mean free paths much less than this radius. Comparisons between these results and experimental measurements described later should yield reasonable agreement.

The experimental program, again concerned with a 10 cm long by 10 cm diameter single-turn cylindrical coil, is described in Chapters VI and VII. Kinetic measurements involving such things as momentum, energy, velocity, and efficiency are presented for a range of initial stored energies, gas molecular weights and mean free paths. The detailed structures of the gas current and charge motion are also reported. In these experiments, the initial particle density was

varied over a wide enough range so that effects due to long and short electron mean free paths would be revealed.

An appendix is included after the summarizing chapter, Chapter VIII, discussing the magnetic field of the 10 cm x 10 cm coil and deriving quantities based on these field values necessary for Chapter I.

CHAPTER II. SINGLE PARTICLE TRAJECTORIES

2.1 Introduction

As pointed out in Chapter I, we first consider single particle trajectories in the pulsed crossed field accelerator, not only because of interest in the trajectories themselves, but also as a natural preliminary to the many-particle analyses which follow.

Closed form solutions in terms of well known functions result when studying the motions of charged particles in time- and space-invariant electric and magnetic fields[45,46]. The problem of particle behavior in fields which change both with time and space is, however, much more complex, and simple, exact solutions exist only under extremely limited conditions.

The procedure often used in attacking such a problem is to incorporate certain simplifying assumptions which allow the solutions to be put in terms of familiar functions. This has the advantage of readily indicating approximate behavior under a wide range of field conditions, but any particular solution is of course only an approximation. We should review the approximations which are frequently employed in light of our particular problem.

One procedure is to assume the fields are uniform in space; Linhart[47] in this way derived an exact solution to charge motion in a plane electromagnetic wave. The case of the single-coil accelerator in the present study could be reduced to a uniform field situation by studying motion within a very long solenoid. Although the radial and azimuthal motion might be satisfactorily approximated, this assumption eliminates the

possibility of acceleration parallel to z and is therefore not suitable to our needs.

If the magnetic field is not spatially homogeneous, but the trajectories are known to follow very tight circular motions, then the magnetic field across the orbit may be assumed to be uniform. This, then, leads to the fact that the ratio, $\frac{\text{particle energy normal to the field}}{\text{magnetic field strength}}$, is a constant[48]. As may be seen from the trajectories presented in Section 2.4.2, this assumption is also invalid in our case.

Another assumption which is often made is that the angular momentum (or the magnetic moment) of the particle is constant[49,50], this again leads to the above specified ratio, but is only valid when changes in magnetic field strength during the time of interest are small compared with the average strength of the field over the same time. Thus, this simplification is not applicable in our case, where the field changes magnitude rapidly with time.

Physicists interested in cosmic phenomena have studied particle motion in the dipole field of the earth. This field can be expressed reasonably simply in terms of the distance from the dipole, and much information has been obtained about trajectories in this situation[51]. The magnetic field generated by a cylindrical coil of the shape shown in Fig. 1.2 is unfortunately expressible only by complicated, infinite series formulae[52] and therefore does not lend itself as readily to solution as does the dipole field.

Since, in approaching the problem of particle behavior in the induction accelerator shown in Fig. 1.2, we have found that none of the usual approximations are applicable, the approach has been taken to solve the problem exactly, using analog computer techniques. The computer will be

used to integrate the equations of motion subject to appropriate initial conditions and electromagnetic field geometry. For this analysis, knowledge of the magnetic field of a cylindrical coil is required, and the necessary information is provided in Appendix I.

Penfold[53] has also been interested in the behavior of isolated charged particles in inductively generated electromagnetic fields, and for this reason the present analysis and his derivations parallel one another to some extent. The two analyses differ, however, in specific objectives and results which have been obtained. Penfold has put the motion equations in terms of space derivatives of a single scalar function. This function he terms the "inductive potential", and from it he can surmise general characteristics of the motion, much as one can deduce much useful information about motion in electrostatic fields from knowledge of the electrostatic potential; calculations of single particle motions in particular cases have not been given by Penfold. We are more interested in the complete and exact motions of specific particles under the specific field conditions in the inductive accelerator, and we have therefore only been concerned with putting the equations of motion in forms suitable for analog computation of these particular situations. The approach used here is, however, quite general in its applicability to inductive systems; likewise, Penfold's technique is not an approximation and could be used for exact trajectory calculations.

2.2 Equations of Motion

The equations of motion in cylindrical coordinates describing the acceleration of a particle having charge to mass ratio η under the influence of instantaneous electric field components (e_r, e_θ, e_z) and magnetic field components (b_r, b_θ, b_z) are given in Eqs. 2.1.

$$r) \quad \ddot{r} - r(\dot{\theta})^2 = \eta e_r + \eta b_z r\dot{\theta} - \eta b_\theta \dot{z} \tag{2.1a}$$

$$\theta) \quad \frac{1}{r}\frac{d}{dt}(r^2\dot{\theta}) = \eta e_\theta + \eta b_r \dot{z} - \eta b_z \dot{r} \tag{2.1b}$$

$$z) \quad \ddot{z} = \eta e_z + \eta b_\theta \dot{r} - \eta b_r r\dot{\theta} \ , \tag{2.1c}$$

where the usual dot time derivative notation is employed, a right-handed system of cylindrical coordinates is used, and η carries the sign of the charge.

Equations 2.1 can be reduced when considering a cylindrical coil carrying only azimuthally directed current, as in Fig. 1.2, since in this case the induced electric field is wholly θ-directed, while the magnetic field has only radial and axial components. These reductions result in the following set of equations applying to charged particles in the induction accelerator being considered in this report (see forces shown in Fig. 1.2 and discussed in connection with that illustration).

$$r) \quad \ddot{r} - r(\dot{\theta})^2 = \eta b_z r\dot{\theta} \tag{2.2a}$$

$$\theta) \quad \frac{1}{r}\frac{d}{dt}(r\dot{\theta})^2 = \eta e_\theta + \eta b_r \dot{z} - \eta b_z \dot{r} \tag{2.2b}$$

$$z) \quad \ddot{z} = -\eta b_r r\dot{\theta} \ . \tag{2.2c}$$

2.3 Integration of the Azimuthal Motion Equation

Equation 2.2b, the azimuthal equation of motion, can be immediately integrated by relating the right-hand terms of this equation to φ, the flux linked by the particle*. Considering each term separately, we find the following interpretation holds for the first term:

---

* By "flux 'linked' by the particle" is meant the magnetic flux passing through the circle which is coaxial with the coil and which passes through the particle position.

$$\eta e_\theta \equiv -\frac{\eta}{2\pi r}\frac{\partial \varphi}{\partial t} \qquad \text{(Change of linked magnetic flux due to coil current changing with time)}$$

Turning to the second term, $\eta b_r \dot{z}$, we calculate b_r by dividing the flux $\partial\varphi$ through an incremental ring of radius r and length ∂z, coaxial with the coil and including the particle at (r, z). This results in the following identity:

$$\eta b_r \dot{z} \equiv -\frac{\eta}{2\pi r}\frac{\partial \varphi}{\partial z}\frac{dz}{dt} \qquad \text{(Change of linked magnetic flux due to particle having axial motion)}$$

Similarly, the third term $\eta b_z \dot{r}$ is interpreted as

$$\eta b_z \dot{r} \equiv +\frac{\eta}{2\pi r}\frac{\partial \varphi}{\partial r}\frac{dr}{dt} \qquad \text{(Change of linked magnetic flux due to particle having axial motion)}$$

Thus, the right-hand side of Eq. 2.2b becomes proportional to the total time derivative of the flux linkage φ given by:

$$\frac{d\varphi}{dt} = \frac{\partial \varphi}{\partial r}\frac{dr}{dt} + \frac{\partial \varphi}{\partial z}\frac{dz}{dt} + \frac{\partial \varphi}{\partial t} \quad .$$

Substituting this result into Eq. 2.2b yields,

$$\frac{1}{r}\frac{d}{dt}(r^2\dot{\theta}) = -\frac{\eta}{2\pi r}\frac{d\varphi}{dt} \quad , \qquad (2.3)$$

which is immediately integrable. Integration results in

$$r^2\dot{\theta} - r_o^2\dot{\theta}_o = -\frac{\eta}{2\pi}(\varphi - \varphi_o)$$

or

$$\dot{\theta}(t) - \left(\frac{r_o}{r}\right)^2\dot{\theta}_o = -\frac{\eta}{2\pi r^2}[\varphi(t) - \varphi_o] \quad , \qquad (2.4)$$

where $\varphi(t)$ is the flux linkage at time t, and φ_o is the flux linked initially by the particle when it is launched, with $\dot{\theta}_o$ tangential velocity, at time t_o.

It will be noted by the reader that the above derivation is a generalization to time-changing axially symmetric fields of a principle known as Busch's Theorem, which is widely used in connection with particle motion in d-c axially symmetric magnetic fields[54,55].

In the analysis which follows, both φ_o and $\dot{\theta}_o$ are assumed to be zero. If we consider motion within the first half cycle of the coil current, $\varphi(t)$ and therefore $\dot{\theta}(t)$ will be zero only at the z-axis, and the trajectory must therefore orbit about this axis or pass through it. For motions occurring over times greater than a half cycle, the angular velocity of the particle must go to zero at each current zero as well as at each passage through the axis. If the combination,

$$\frac{\eta}{2\pi r^2}\varphi_o + \left(\frac{r_o}{r}\right)^2 \dot{\theta}_o \quad ,$$

were not zero, then the particle can never pass through the z axis, but must orbit about some off-axis center. Some characteristics of the motion with nonzero initial conditions are brought out in Penfold's analysis[53].

2.4 Trajectories Within the Experimental Coil

2.4.1 Radial (Betatron) Equilibrium. Substitution of Eq. 2.4 into Eq. 2.2a, assuming the initial flux φ_o and initial angular velocity $\dot{\theta}_o$ are zero, eliminates θ explicitly from the radial equation, thus:

$$\ddot{r} = -\frac{\eta^2}{2\pi}\frac{\varphi b_z}{r} + \frac{\eta^2}{4\pi^2}\frac{\varphi^2}{r^3} \quad . \tag{2.5}$$

From Eq. 2.5, we note that the radial force will vanish when the following condition is met:

$$\frac{\eta^2}{2\pi}\frac{\varphi b_z}{r} = \frac{\eta^2}{4\pi^2}\frac{\varphi^2}{r^3} \quad ,$$

that is

$$b_z = \frac{\varphi}{2\pi r^2} \quad ,$$

$$= \frac{1}{2}\bar{b} \quad , \tag{2.6}$$

where

$$\bar{b} \triangleq \frac{\varphi}{\pi r^2} \text{ (average linked field)} .$$

It is seen from Eq. 2.6 that the field requirements for radial equilibrium in the pulsed crossed-field accelerator and in a betatron accelerator are identical; that is, the instantaneous axial field at orbit must always be equal to half the change in the average linked field within the orbit.

In the detailed analysis of trajectories in the accelerator field which follows, it will turn out that the locus of points of betatron radial equilibrium is a three-dimensional surface coaxial with the coil and extending outward from the end of the coil; at the edge of the coil, this surface has a radius approximately the same as the coil, and the critical radius increases slowly with increasing z (see Fig. 2.2 and discussion pertinent to this chart).

It is interesting to note at this point that true betatron equilibrium cannot be obtained deep within a cylindrical coil, and especially on the central plane, since the field actually increases with radius rather than decreases, as would be required. A confined type of orbit does occur, however, in which the particle experiences strong radial forces and frequently passes through the axis of the system but continues to orbit in the e_θ field between axis crossings. It therefore continues to gain

energy as in a betatron; see discussion of trajectory solutions in Section 2.4.3.

2.4.2 Development of Trajectory Equations and Techniques. If one wishes to expel ions from the accelerator with velocities as nearly as possible free from radial motion, the discussion of Section 2.4.1 tells us that one must start the ions off at a radial position very close to but slightly greater than the driving coil radius. That this initial condition also leads to maximization of the axial kinetic energy delivered to the ion does not necessarily follow. It will therefore be in order at this point to consider ion trajectories in the Fig. 1.2 accelerator and to derive the z-directed velocities attainable for various initial conditions.

In deriving the ion trajectories, the problem to be solved is the integration of the motion equations,

$$\ddot{r} = -\frac{\eta^2}{2\pi}\frac{\varphi_b}{r}z + \frac{\eta^2}{4\pi^2}\frac{\varphi^2}{r^3} \quad , \tag{2.5}$$

$$\ddot{z} = +\frac{\eta^2}{2\pi}\frac{\varphi_b}{r}r \quad , \tag{2.7}$$

where Eq. 2.7 has been formed from Eq. 2.2c by substitution of Eq. 2.4.

For purposes of generalization, we will use the dimensionless lengths ρ and ξ, defined as

$$\rho = r/a \tag{2.8}$$

and

$$\xi = z/a \quad , \tag{2.9}$$

where

$$a \equiv \text{coil radius} \quad ,$$

changing the equations of motion to

$$\ddot{\rho} = -\frac{\eta^2}{2\pi}\frac{\varphi b_z}{\rho a^2} + \frac{\eta^2}{4\pi^2}\frac{\varphi^2}{\rho^3 a^4} \tag{2.10a}$$

$$\ddot{\xi} = +\frac{\eta^2}{2\pi}\frac{\varphi b_r}{\rho a^2} \quad . \tag{2.10b}$$

Since φ, b_z, and b_r have ρ, ξ, and time dependences, we rely on analog computer techniques to solve Eqs. 2.10.

Let us first separate time and space dependencies by noting that φ, b_r, and b_z will each depend linearly on the current in the coil. If now the coil current is sinusoidal,

$$I_c = I_o \sin \omega t \text{ (amperes)} \quad , \tag{2.11}$$

then the field parameters may be expressed as

$$\varphi = I_o \psi_\varphi \sin \omega t \tag{2.12}$$

$$b_r = I_o \psi_{b_r} \sin \omega t \tag{2.13}$$

$$b_z = I_o \psi_{b_z} \sin \omega t \quad . \tag{2.14}$$

The ψ functions are now functions of ρ and ξ only, and are interpreted as the field strengths at the point (ρ, ξ) per unit coil current. Values to be used for ψ_{b_r} and ψ_{b_z} have been calculated and tabulated in Appendix I, Table A.1.

If Eqs. 2.12, 2.13, and 2.14 were inserted into the equations of motion, 2.10, the resulting expressions would retain the coil radius a. This may be eliminated by defining a quantity ψ_{φ_o} as follows:

$$\varphi = \int_S b_z dS = 2\pi \int_0^r b_z r dr \quad ,$$

$$\psi_\varphi = 2\pi \int_0^r \psi_{b_z} r dr = 2\pi a^2 \int_0^\rho \rho \psi_{b_z} d\rho \quad ,$$

$$= a^2 \psi_{\varphi_o} \quad , \tag{2.15}$$

where

$$\psi_{\varphi_o} \triangleq 2\pi \int_0^\rho \rho \psi_{b_z} d\rho \quad . \tag{2.16}$$

ψ_{φ_o} is tabulated in Appendix I, Table A.1.

Now, using Eqs. 2.12 through 2.16, the motion equations 2.10 reduce to:

$$\ddot{\rho} = (\eta I_o)^2 A_\rho \sin^2 \omega t \tag{2.17a}$$

$$\ddot{\xi} = (\eta I_o)^2 A_\xi \sin^2 \omega t \tag{2.17b}$$

where

$$A_\rho \triangleq \frac{1}{4\pi^2} \frac{\psi_{\varphi_o}^2}{\rho^3} - \frac{\psi_{\varphi_o} \psi_{b_z}}{2\pi\rho} \quad , \tag{2.18}$$

$$A_\xi \triangleq \frac{\psi_{\varphi_o} \psi_{b_r}}{2\pi\rho} \quad . \tag{2.19}$$

The necessary equations of motion have now been reduced to a form convenient for further computation. The time dependence has been isolated in the $\sin^2$ terms, and the externally adjustable parameters η and I_o are grouped as a constant multiplying factor. Finally, the space dependence has been grouped completely in the A factors. These geometric magnetic

force functions, defined by Eqs. 2.18 and 2.19, are determined for each point in the r-z plane by the magnetic field strength at the point and the instantaneous flux linkage for that point, relative to the coil current; thus, the factors A_ρ and A_ξ are independent of time and are fixed by the coil geometry. These factors are discussed further in Appendix I, where calculation procedures are outlined and values are tabulated in Table A.1.

By use of an analog computer, Eqs. 2.17 may be integrated, employing the component arrangement shown in Fig. 2.1. The operation of this computation system represents standard analog techniques and needs no explanation except for the method in which the space factors A_ρ and A_ξ are handled. Function generating maps for these quantities are constructed by drawing conducting lines of constant A, using silver paint on graphite-surfaced plates. Specifications for these plates are

size: 11" x 17"

resistance: 20,000 Ω per square

tolerance: 2 percent

supplier: Conductive Surfaces Company, Dearborn, Michigan.

Scaled representations of these contours as they actually appeared on the function generating plates are shown in Figs. 2.2 and 2.3. The betatron equilibrium surface, discussed in Section 2.4.1, appears in Fig. 2.2 as the $A_\rho = 0$ curve; at any point on this surface the local strength of the axial magnetic field is just half the average field strength within the point, and charged particles lying on this surface will experience no net radial force.

Voltages were placed on these conducting silver paint A_ρ and A_ξ contours by connecting the ends of each of them through its individual precision potentiometer to a 100-volt reference supply. The voltage on

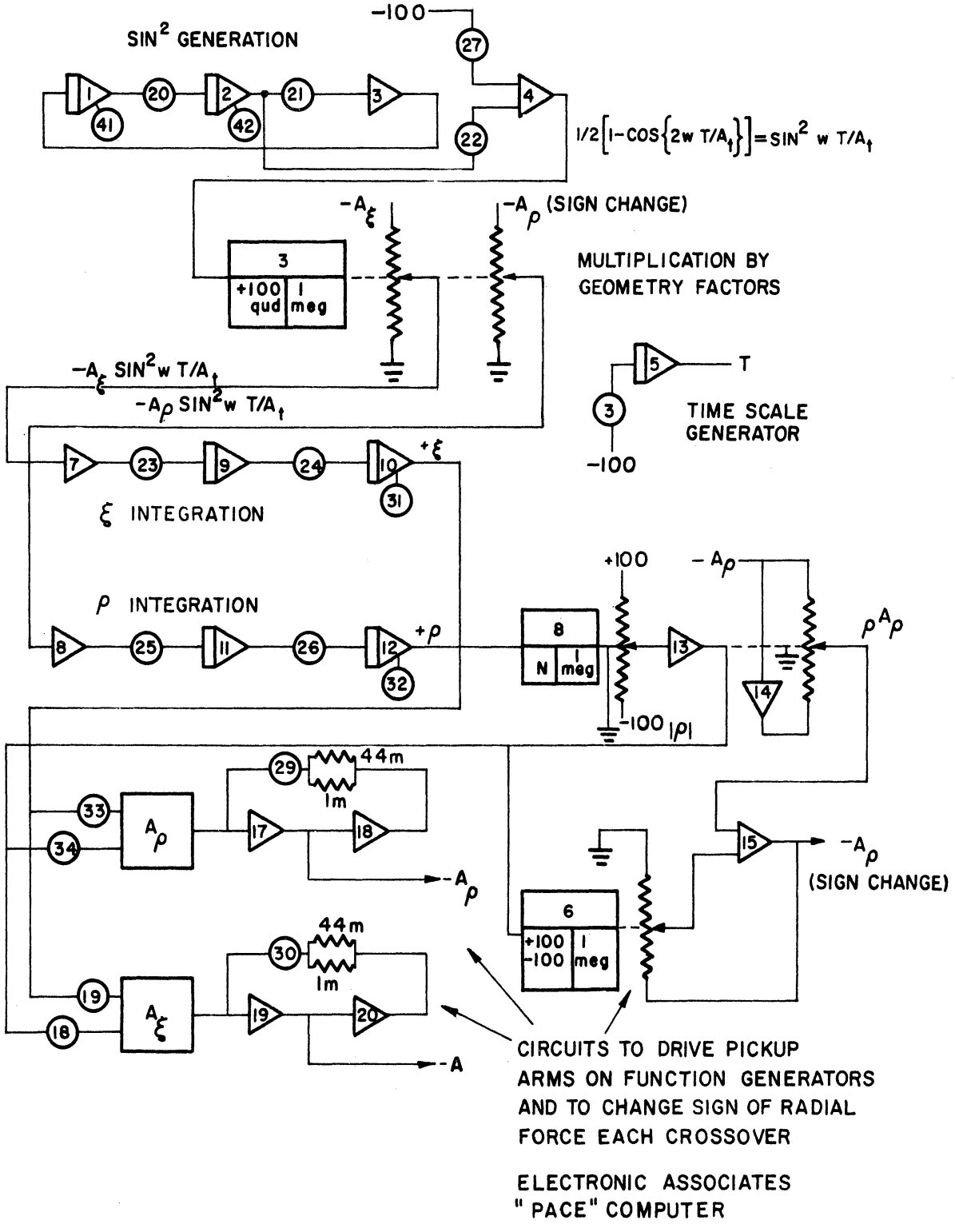

Fig. 2.1. Circuitry for Analog Computations of Single-Particle Trajectories.

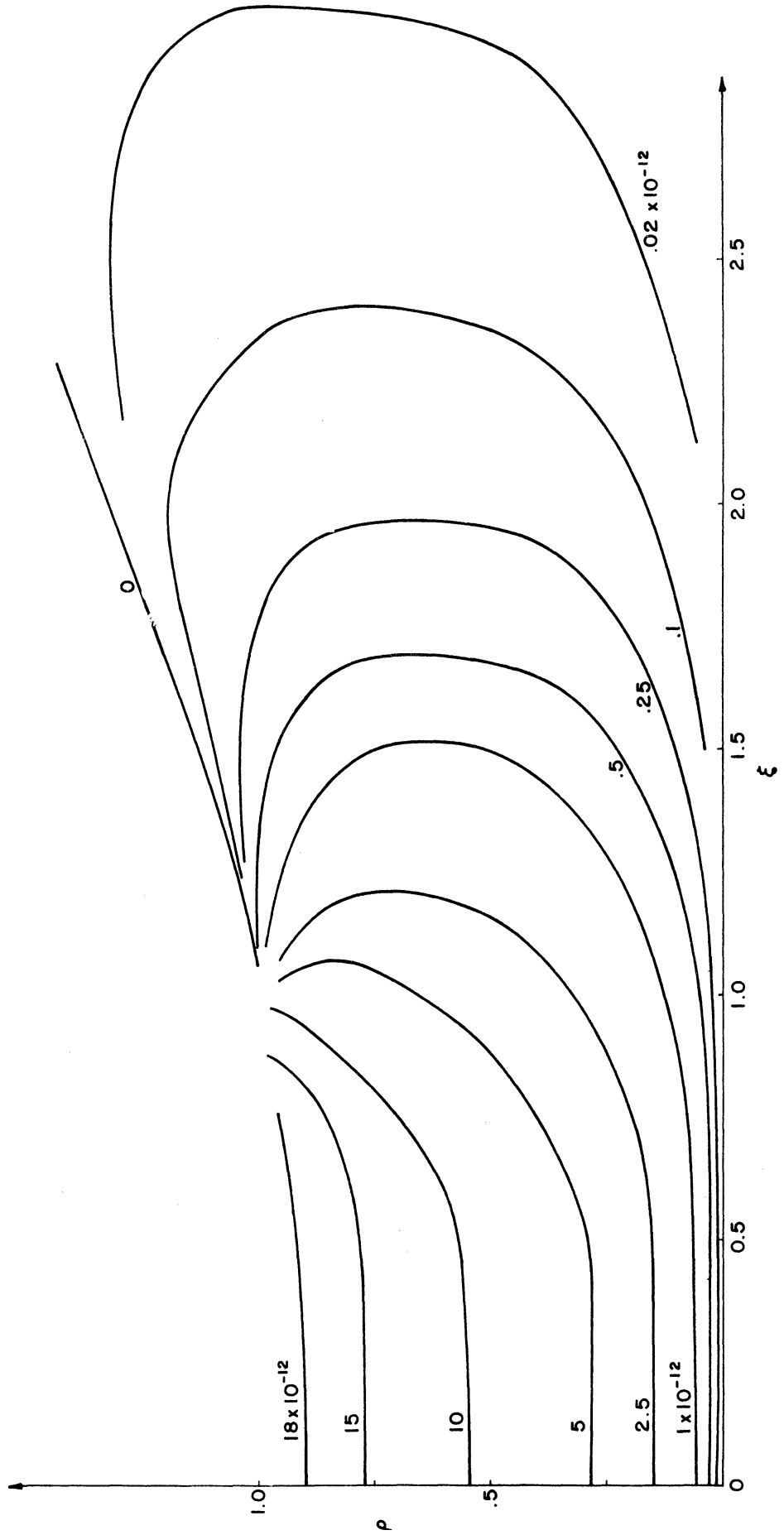

Fig. 2.2. Contours of Constant Radial Magnetic Forcing Function A_ρ. Defining Eq. 2.18.

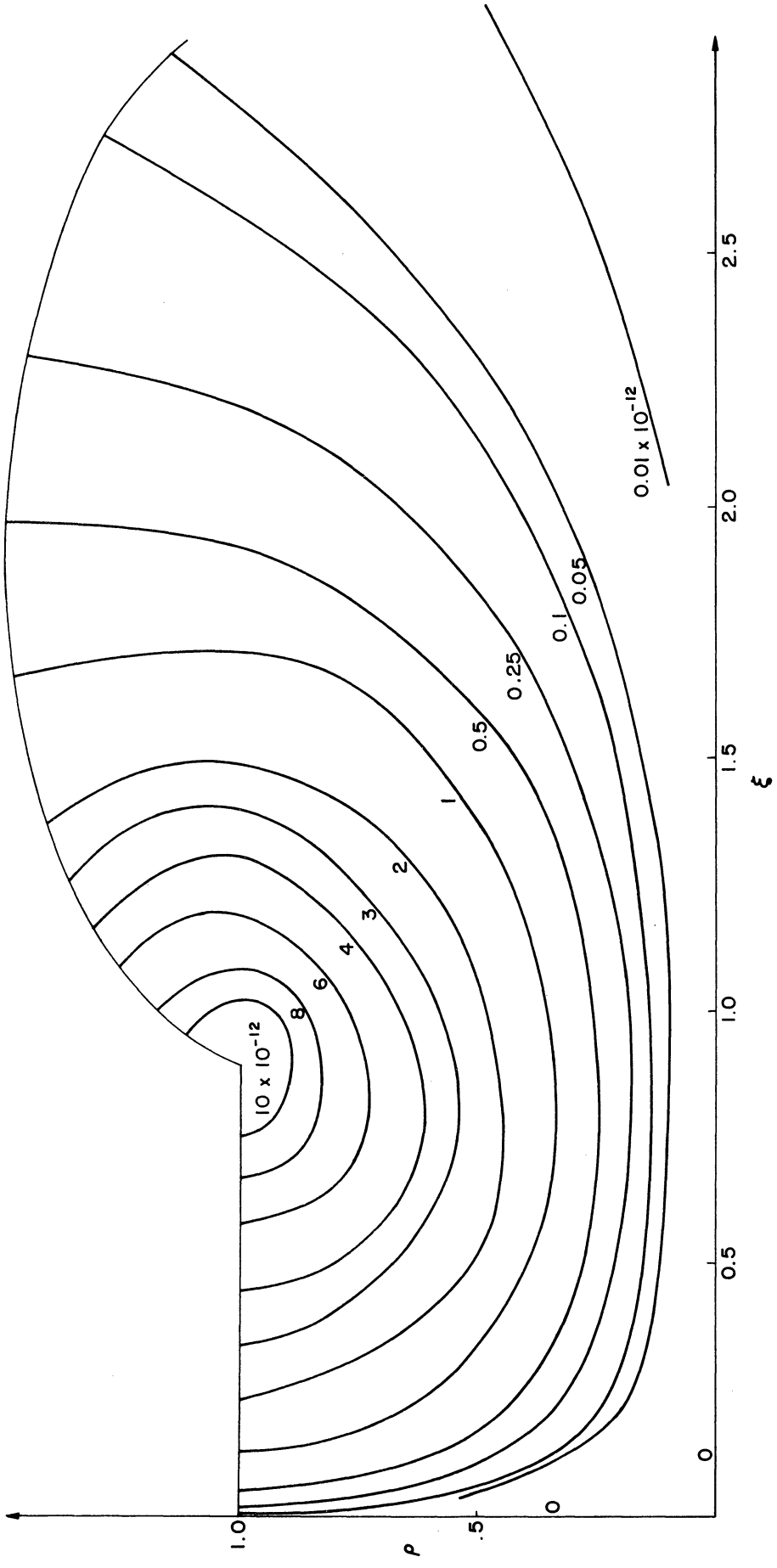

Fig. 2.3. Contours of Constant Axial Magnetic Forcing Function A_ξ. Defining Eq. 2.19.

each line was adjusted to be in proportion to its strength as given in Figs. 2.2 and 2.3, the 10 x 10^{-12} line on Fig. 2.2 for instance being set at 50 volts, while the 4 x 10^{-12} line was adjusted to 20 volts.

Wire probes, motor-driven by two dimensional positioning arms, were used to pick off the A_ρ and A_ξ voltages from the graphite surfaces. The interpolation made by the pickups contacting the graphite plates between constant-value-A contours would be governed by the rectangular Laplace equation. Sufficient of these conducting line contours were used, however, so the discrepancy between this Laplacean interpolation and the interpolation dictated by the true characteristics of the A-functions would be small. These probe pickup voltages were fed into the servo multipliers as indicated by Fig. 2.1, and the probes were positioned with reference to the particle's position.

Note that only a quarter-plane of the coil field is represented by these function generators. This has no effect on z motion, since the particle will always remain on one side of the coil midplane. Symmetry of the A_ρ and A_ξ fields about the axis allows r motion also to be handled using the absolute-value switching circuit incorporated in the Fig. 2.1 system.

In order to determine the behavior of a particle uniquely, several quantities must be specified. If we refer to Eqs. 2.17, the type of particle and the coil current must be known by specifying the value for $(\eta I_o)^2$; the frequency ω of the coil current must also be given. In addition, initial conditions, that is, ρ and ξ position and velocity, must be given at the initial instant. The assumption has already been made in connection with Eq. 2.5 that the initial time is the instant when the magnetic field (and therefore coil current) is zero. Selection of the following values to use in the analysis gives a sufficiently wide range of

conditions to reveal the types of behavior which occur in the pulsed crossed-field device:

a. Initial conditions

$$\dot{\rho}_o = \dot{\xi}_o = 0 \ ,$$

$$0.5 \leq \rho_o \leq 0.9 \ , \text{ and}$$

$$0 \leq \rho_o \leq 2 \ ,$$

b. $(\eta I_o)^2 = 5.808 \times 10^{22} \dfrac{\text{Coulombs}^2 - \text{amperes}^2}{\text{kilogram}^2}$ (He^+, 10^4 amperes, or A^+, 10^5 amperes),

$= 5.808 \times 10^{24}$ (He^+, 10^5 amperes, or A^+, 10^6 amperes), and

$= 3.098 \times 10^{30}$ (e^-, 10^4 amperes).

c. $\omega = 3.142 \times 10^5$ radians/second (50 kc/s), and

$= 6.284 \times 10^6$

Particle action under these conditions is shown in Figs. 2.4 through 2.9 and Tables 2.1 and 2.2, which will now be discussed.

2.4.3 Contrast Between Particle Behaviors in Low and High Frequency Fields—Fast and Slow Particles. The time spent by the particle in the field, in comparison with the duration of a period of the a-c field, has a significant effect on the action of the particle. We will first consider a case where the ion spends less than a quarter-cycle in the accelerator. The behavior of a particle which spends many cycles under the influence of the field will then be investigated. Note that the frequency of the field, the strength of the field, and the specific charge of the particle all enter into determining whether or not a particle moves out of the accelerator during a portion of a field cycle (fast particle) or only after many cycles (slow particle). The terms fast particle and slow particle will appear occasionally during this work to distinguish between

the two types of behavior. Thus, He^+ and A^+ can be either fast or slow ions depending on field characteristics; electrons are fast particles for all practical cases of interest concerning the pulsed, crossed-field accelerator.

In Fig. 2.4 are shown the paths followed by ions when $(\eta I_o)^2 = 5.808 \times 10^{24}$ coulombs^2-amperes^2/kilogram^2 (He^+, 10^5 amperes), and $\omega = 3.142 \times 10^5$ radians/second, for various starting positions. Note that these paths are drawn on a plane surface which is rotating about the axis with angular velocity given by Eq. 2.4 (hereafter called a twisted meridian surface). Two facts are revealed by these curves:

1. The motion has a large radial component, even when the path starts out near the radial equilibrium surface, as for example trajectories 8 and 9.
2. For paths beginning deep within the coil, as for instance trajectories 1, 2, and 3, the particle passes through the axis one or more times coming out each time to a new radial maximum. The particle can therefore orbit for some time in the electric field induced by the changing coil current. It thereby continues to gain energy. This has an important bearing on the ultimate axial velocity with which the particle leaves the accelerator, as shown in Table 2.2 and discussed in the following paragraph.

The times taken for these particles to leave the accelerator, and the manner in which their axial components of velocity are built up are of interest. Both $z(t)$ and $\dot{z}(t)$ are plotted in Fig. 2.5(a) and 2.5(b) for several of the trajectories in Fig. 2.4. These clearly show the gain in energy due to orbiting parallel with the induced electric field.

In contrast with the low-frequency (fast-particle) situation studied above, the high-frequency (slow-particle) case will now be taken up.

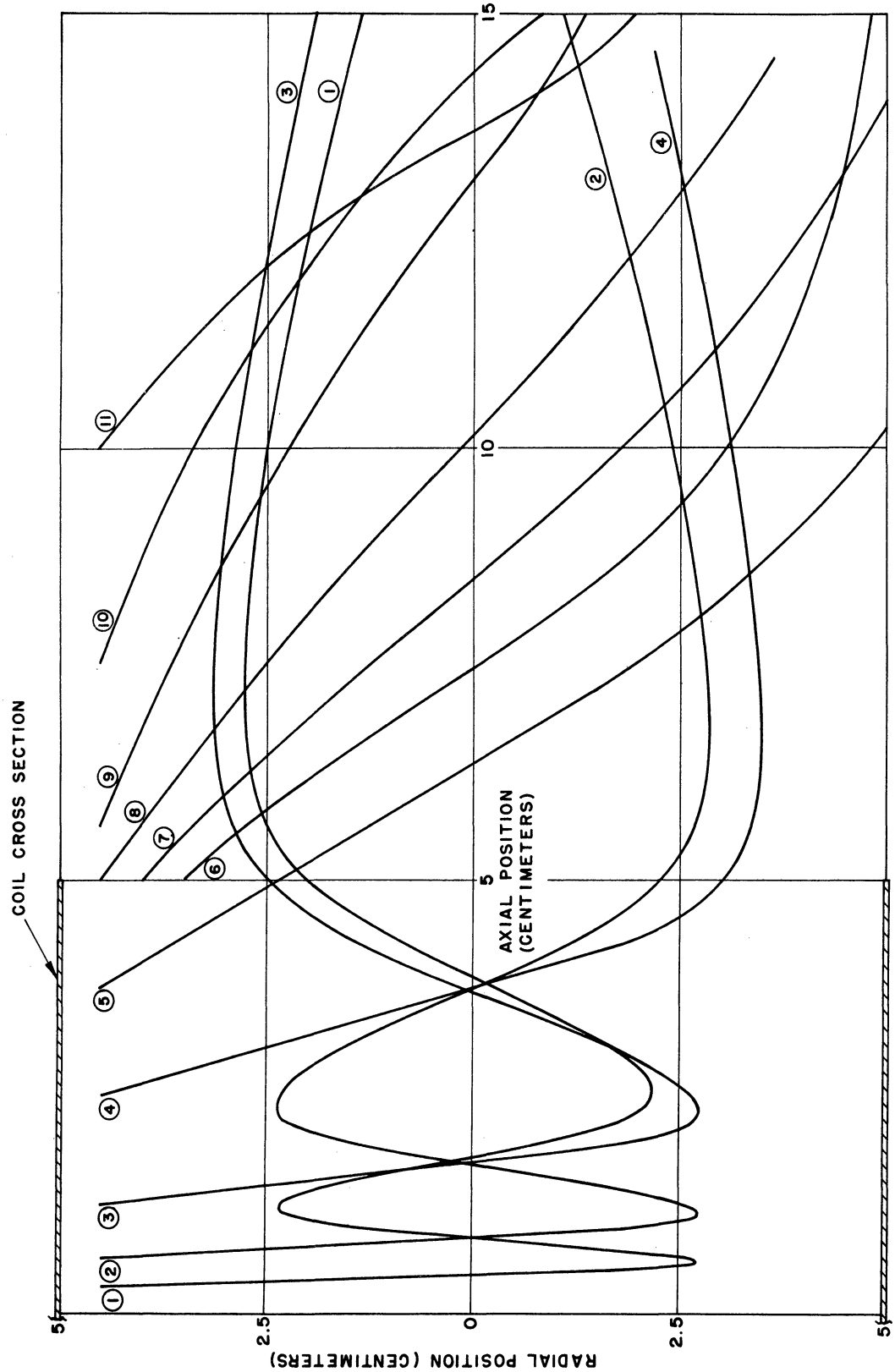

Fig. 2.4. Single Particle Trajectories in the Twisted Meridian Plane—Fast Ion $[\eta I_o)^2 = 5.808 \times 10^{24}$ (e.g., He^+, 10^5 amperes), $\omega = 3.142 \times 10^5$, 10 cm x 10 cm coil].

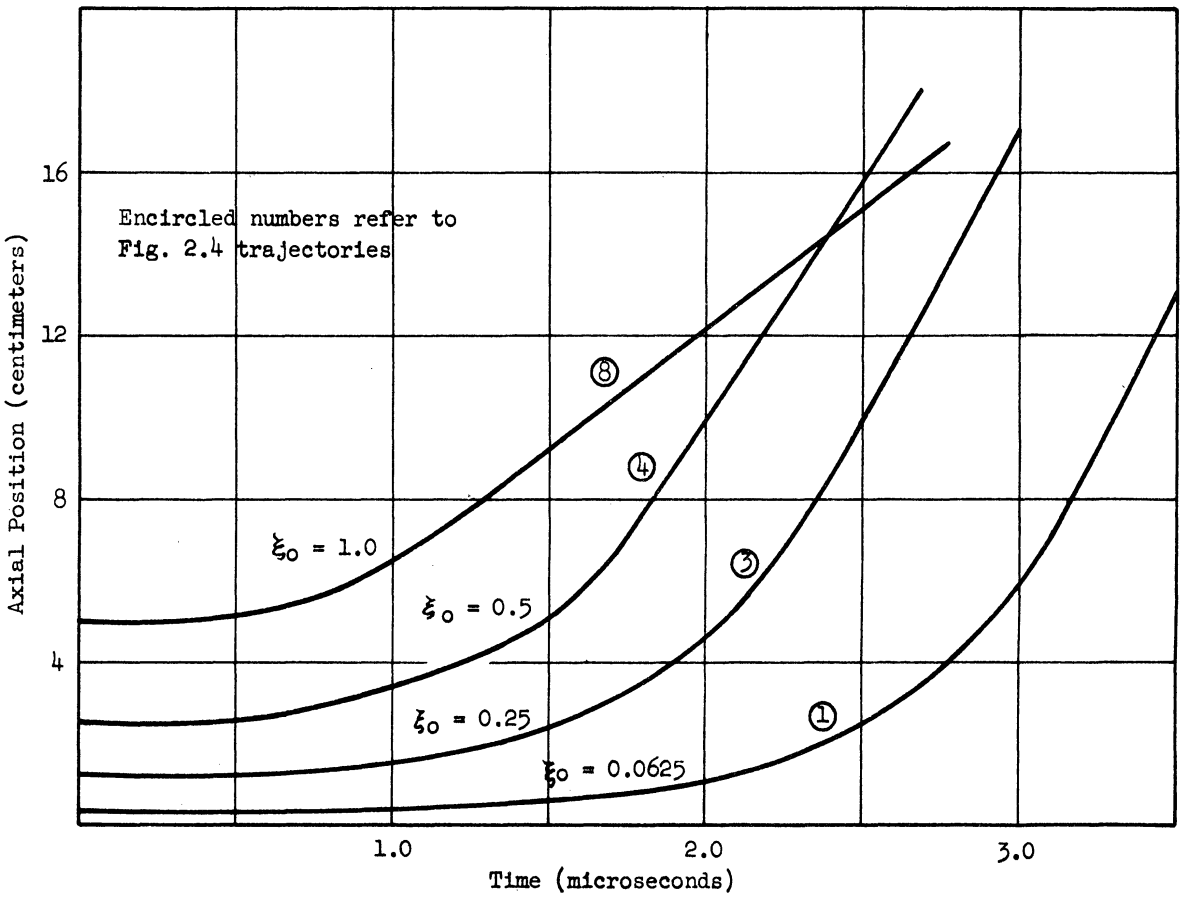

Fig. 2.5(a). Axial Position of Particle as a Function of Time—Fast Ion $[(\eta I_o)^2 = 5.808 \times 10^{24}$ (e.g., He^+, 10^5 amperes), $\omega = 3.142 \times 10^5$, $\rho_o = 0.9$, 10 cm x 10 cm coil].

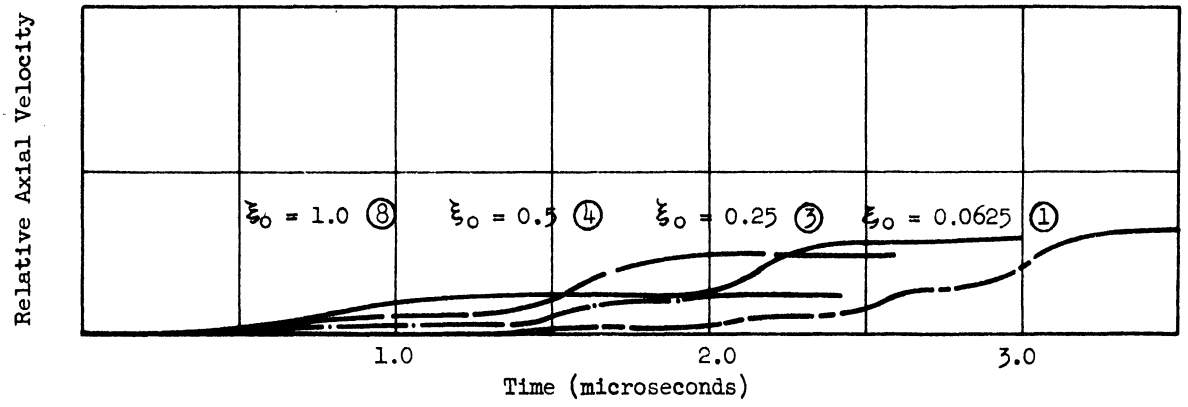

Fig. 2.5(b). Axial Velocity of Particle as a Function of Time—Fast Ion $[(\eta I_o)^2 = 5.808 \times 10^{24}$ (e.g., He^+, 10^5 amperes), $\omega = 3.142 \times 10^5$, $\rho_o = 0.9$, 10 cm x 10 cm coil].

Specifically, let us consider $(\eta I_o)^2 = 5.808 \times 10^{22}$ (e.g., A^+ at 10^5 amperes or He^+ at 10^4 amperes), $\omega = 6.284 \times 10^6$ rad/second. That these are slow-particle conditions is demonstrated by Fig. 2.6 showing that the time to emerge from the accelerator (20 - 30 microseconds) is much longer than the field period (1 microsecond).

Trajectories are shown in Fig. 2.7. On comparing these paths with those of Fig. 2.4, the only obvious difference appearing is that the particles now "bounce" back approximately to their starting radius. This behavior is reasonable, since the influence of the field on the slowly moving particle is now averaged over the complete cycle of the field.

An important difference between the two types of particle behavior studied above is the fact that energy transfer from the field to a fast particle is generally greater than to a slow particle. This may be surmised from a study of Table 2.2 which follows shortly.

The transition range between the fast and slow particle limits has not been thoroughly investigated. Sufficient study was made, however, to indicate that the likelihood of losing a particle radially outward from the system is high. Although this characteristic would be undesirable for the accelerator application, phenomena useful in other respects might be revealed by a more careful study of this transition region. Separation of different ion species might for instance be accomplished by resonance phenomena of this sort.

2.4.4 Electron Behavior Under Low Frequency (Fast Particle) Conditions. Figure 2.8 presents trajectories under the conditions, $(\eta I_o)^2 = 3.098 \times 10^{30}$, $\omega = 6.284 \times 10^6$, which would be appropriate for an electron within a coil carrying 10^4 amperes maximum current. The trajectory paths drawn in Fig. 2.8 are similar in shape to those in Fig. 2.4; the difference

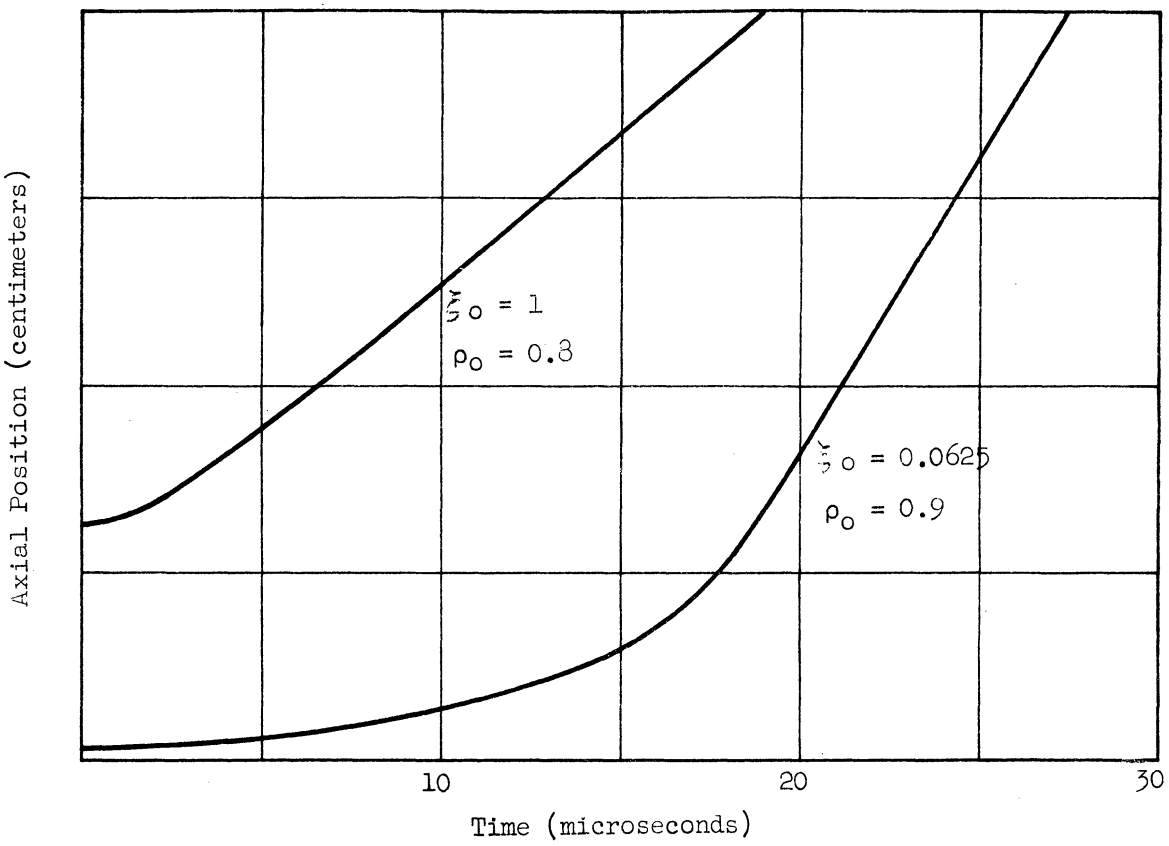

Fig. 2.6. Particle Position as a Function of Time—Slow Ion [$(\eta I_o)^2$ = 5.808 x 10^{22} (e.g., He^+, 10^4 amperes), ω = 6.284 x 10^6, 10 cm x 10 cm coil].

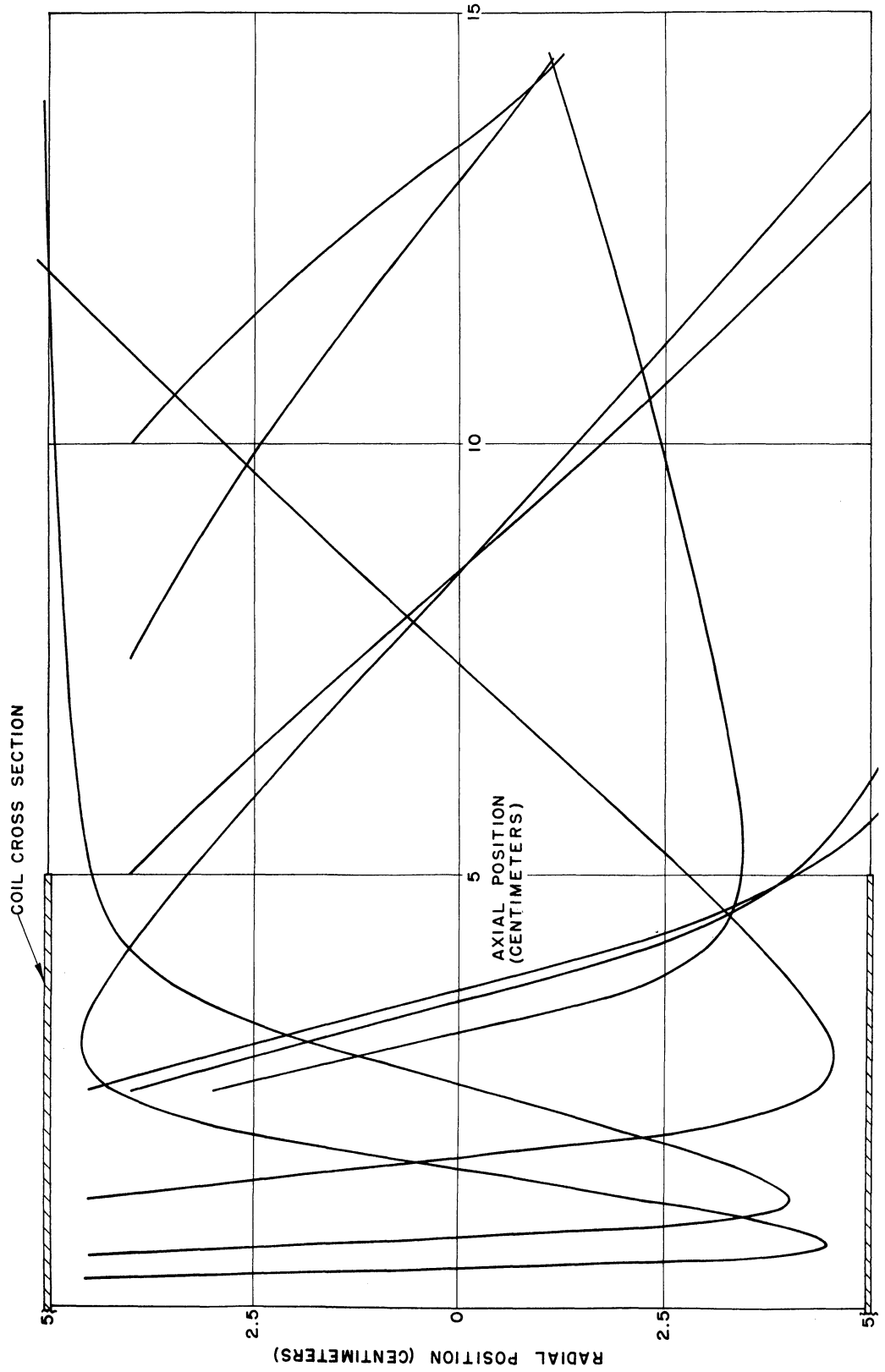

Fig. 2.7. Single Particle Trajectories in the Twisted Meridian Plane — Slow Ion $[(\eta I_o)^2 = 5.808 \times 10^{22}$ (e.g., He^+, 10^4 amperes), $\omega = 6.284 \times 10^6$, 10 cm x 10 cm coil].

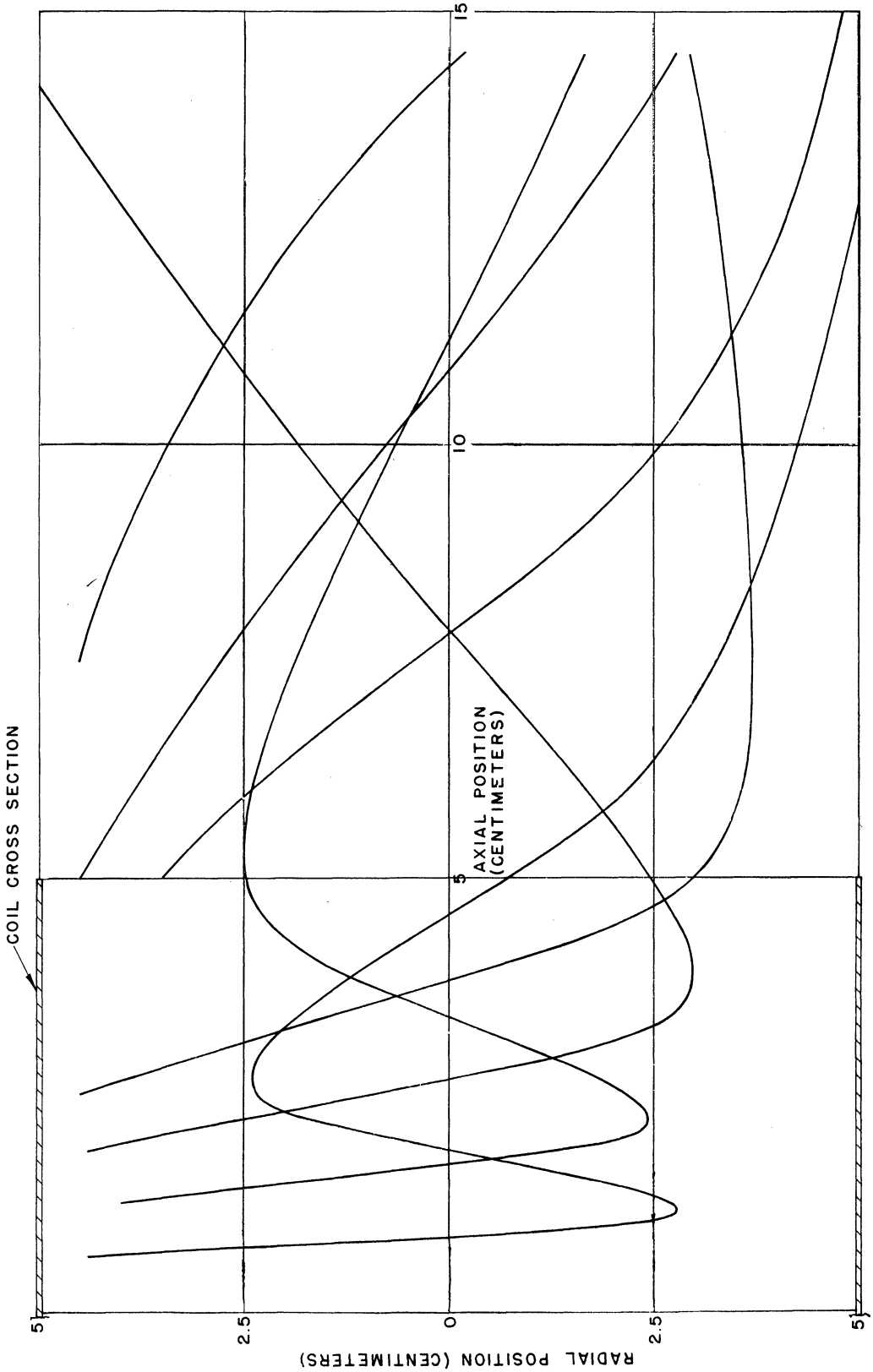

Fig. 2.8. Single Particle Trajectories in the Twisted Meridian Plane—Fast Electron $[(\eta I_o)^2 = 3.098 \times 10^{30}$ (e^-, 10^4 amperes), $\omega = 6.284 \times 10^6$, 10 cm x 10 cm coil].

between the two cases is perhaps most clearly indicated by Table 2.1, which lists the times at which trajectories first cross the axis. Note that the electron is indeed a "fast" particle. It is evident from Table 2.1 that the electrons plunge inward much more rapidly than do the ions; under many-particle conditions, where both ions and electrons are present in large numbers, this tendency for the two species to separate will lead to a positive-ion layer which will carry with it a large electric field.

Table 2.1. Times at Which Various Particles First Cross Axis. (microseconds)

In all cases, $\rho_o = 0.9$

Typical Particle	$(\eta I_o)^2$	ω	ξ_o		
			0.125	0.500	1.000
Electron	3.098×10^{30}	6.284×10^{6}	.0097	.0096	.0142
Ion	5.808×10^{24}	3.142×10^{5}	1.0	1.15	1.69

2.4.5 Behavior in a Long Solenoid: Slow- and Fast-Particle Situations. Motion in the interior of a long solenoidal coil can be approximated by setting ξ_o and A_ξ at zero; trajectories will be confined to the $\xi = 0$ plane, and characteristics are revealed by plotting $\rho(t)$. Such is done in Figs. 2.9(a) and 2.9(b) for He^+ under the two extreme field conditions which have been considered previously. As expected, the particle moving in a "low frequency" field (fast particle) experiences radial excursions dependent on the instantaneous field strength, while in the high-frequency case, the particle always returns to the same radial maximum.

2.4.6 Propulsion Characteristics. For propulsion purposes, we are interested in the z-component of velocity which the particles attain as they leave the region of influence of the coil. This and other

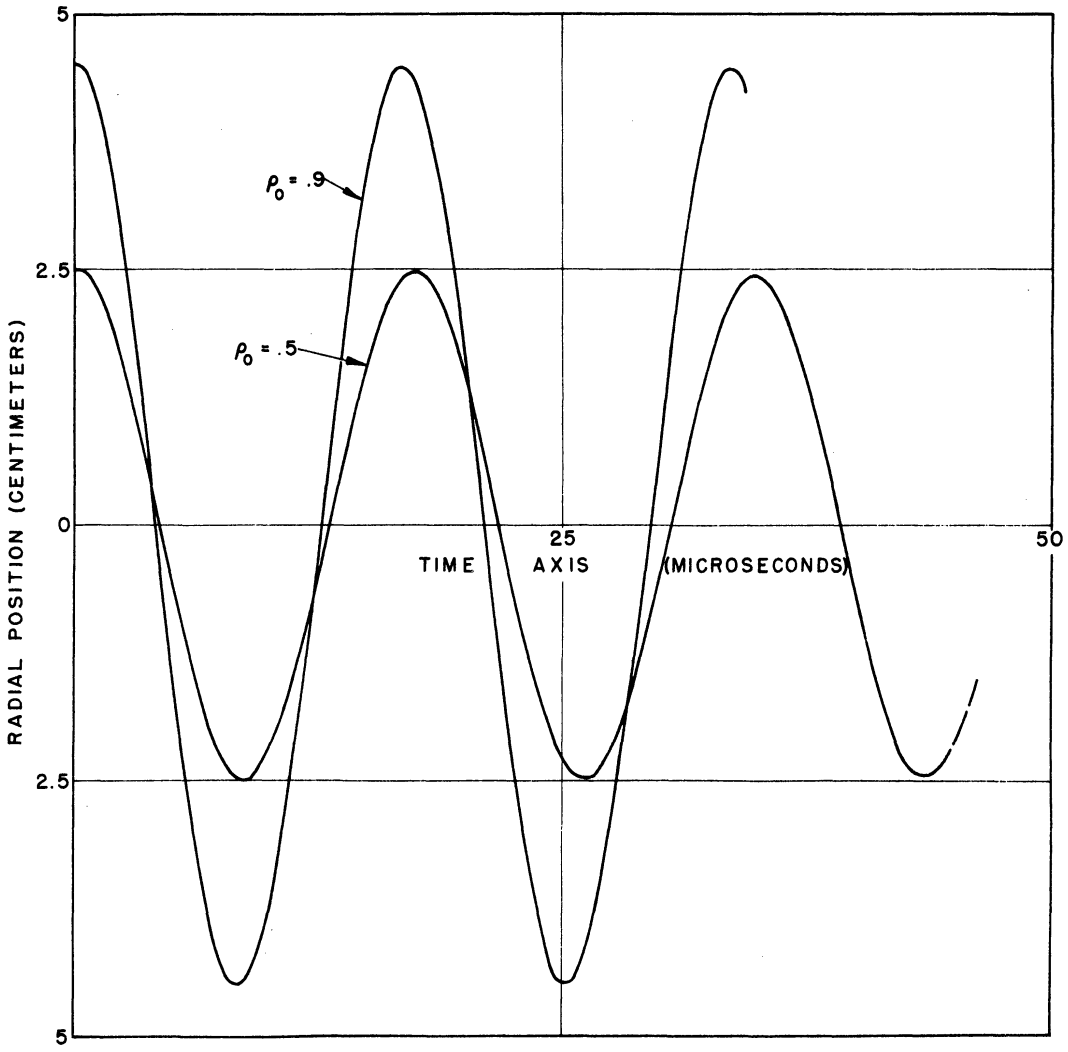

Fig. 2.9(a). Radial Positions of Particle as a Function of Time for the Case of Uniform Field (No Axial Motion)—Slow Ion $[(\eta I_o)^2 = 5.808 \times 10^{22}$ (e.g., He^+, 10^4 amperes), $\omega = 6.284 \times 10^6$, $\xi_o = 0$, $A_\xi = 0$, 10 cm x 10 cm Coil].

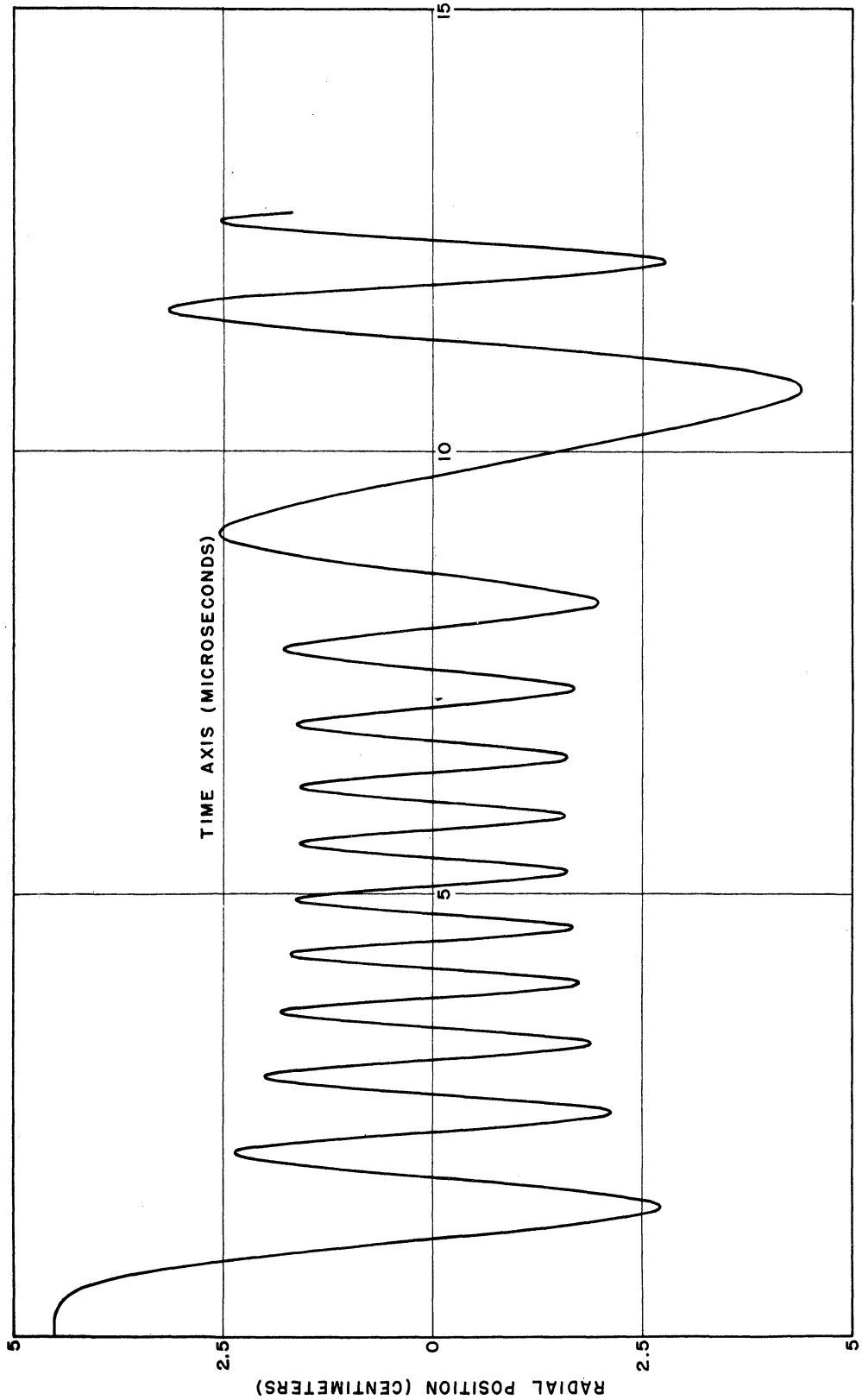

Fig. 2.9(b). Radial Positions of Particle as a Function of Time for the Case of Uniform Field (No Axial Motion)—Fast Ion $[(\eta I_o)^2 = 5.808 \times 10^{22}$ (e.g., He^+, 10^4 amperes), $\omega = 6.284 \times 10^6$, $\xi_o = 0$, $A_\xi = 0$, 10 cm x 10 cm coil].

characteristics for such ejected particles are presented in Table 2.2. Several points of interest are brought out by this table.

1. When the field change is rapid compared with particle motion, the particles spend a relatively long time in the accelerator but do not receive much energy; conversely, if the field frequency is low (fast particle), the energy exchange is greater.
2. Electrons move out with much higher velocities than ions, therefore predicting that charge separation field effects in the z-direction will occur in an induction plasma accelerator.
3. In Section 2.4.1, where betatron equilibrium was discussed, the fact was brought out that, in the induction accelerator, a confined type of orbiting occurs which might lead to energy gain somewhat as in a betatron. Comparing the maximum coil voltage, V_o, with the voltage equivalent of energy of the ejected particles indicates, however, that the energy gained by such orbiting does not in any of the cases studied approach the peak coil voltage. Energy gain equal to or greater than the coil voltage might be obtained for particles launched very near the coil midplane.

Table 2.2. Ejection Characteristics—Induction Particle Accelerator

a. $V_o \triangleq LI_o\omega$; maximum voltage around the coil

b. Assuming He^+ or e^-

c. Electron-volt equivalent of final velocity

d. Angle relative to axis

$(\eta I_o)^2$	Typical Conditions Ion I_o	ω (rad/sec)	V_o [a,b] (volts)	Initial Position ρ_o	Initial Position ξ_o	Time to Reach $\xi = 3.0$ (μsec)	Final Axial Velocity (meters/sec)	Equivalent Voltage [b,c] (volts)	Ejection Angle [d]
5.808×10^{24}	He^+ 10^5 [a] or A^+ 10^6	3.14×10^5	2,200	0.9	0.0625	3.63	15.2×10^4	480	15°
					0.125	3.27	17.4	648	16
					0.25	2.86	14.0	420	12
					0.375	2.79	9.85	201	35.5
					0.500	2.43	11.8	297	12
					0.750	2.65	7.24	108	37
					1.00	2.48	6.18	79.5	34
					1.125	2.44	6.15	78.5	34
					1.50	2.85	4.64	43.1	47
					2.00	3.53	3.00	18.7	52
				0.8	1.00	2.82	5.51	63.1	31.5
				0.7	1.00	3.07	6.09	76.8	9
5.808×10^{22}	He^+ 10^4 or A^+ 10^5	6.28×10^6	4,400	0.9	.0625	27.2	1.24	3.20	44
					.250	19.9	1.07	2.37	47.5
				0.8	.125	24.7	1.43	4.26	2.5
					.375	17.7	1.27	3.34	25
					1.00	17.7	0.63	0.84	46
					1.50	24.7	0.38	0.30	38
					2.00	36.0	0.21	0.09	47
5.808×10^{22}	See above	3.14×10^5	220	0.9	1.00	9.1	1.76	6.44	41

$(\eta I_o)^2$	Typical Conditions Ion I_o	ω (rad/sec)	V_o [a,b] (volts)	Initial Position ρ_o	Initial Position ξ_o	Time to Reach $\xi = 3.0$ (μsec)	Final Axial Velocity (meters/sec)	Equivalent Voltage [b,c] (volts)	Ejection Angle [d]
5.808×10^{24}	See above	6.28×10^6	44,000	0.9	1.00	13.9	$.98 \times 10^{-4}$	1.99	42
3.098×10^{30}	e^- 10^4	6.28×10^6	4,400	0.9	0.125	.0245	20.6×10^6	1210	12
					0.375	.0207	14.9	631	35
					0.500	.0189	16.6	781	9
					1.00	.0187	8.34	197	33
					1.5	.0213	6.25	111	49
				0.8	.25	.0238	15.8	710	25
				0.7	1.0	.0231	7.77	171	12.5

CHAPTER III. SHEET BEAM ANALYSIS (SELF-FIELD EFFECTS)

3.1 Introduction

In studying motion of the propellant gas through the pulsed, crossed-field, induction accelerator, the analysis of Chapter II would apply only to very low particle density conditions, where each individual particle acts completely independently of its neighbors. As the density of particles increases, several effects arise which cause the particles to be influenced by their neighbors. Since in our case the particles are ionized, each will carry with it an electric field. This leads first of all to the necessity of taking space-charge forces into account when determining the behavior of a particle. In addition, as the current flowing in the gas becomes comparable with the current in the coil, the self-magnetic field of the gas current must be considered. Both self-electric and self-magnetic effects will be considered in the following sections.

In order to discover the basic effects which are caused by self-fields, we will assume a simplified model which will allow these effects to be revealed without being encumbered by detailed mathematical procedures. This model will be established with reference to the experience gained both in the single-particle analysis presented in the previous chapter and in the experimental work discussed later in this report.

The single-particle work tells us that the radial component of motion predominates during at least the initial stages of particle travel. We will therefore in the present section limit study to conditions within a long cylindrical coil, where both radial magnetic

field and axial force components are absent, and where consequently a two-dimensional analysis may be carried out.

The experimental measurements indicate that, at least at higher-particle densities, initial ionization occurs in a very thin shell at the outer radius of the cylindrical gas volume, and that the gas current is subsequently carried in a relatively narrow shell which advances with time inwardly toward the axis of the system. This suggests that we limit our attention to a thin shell which initially contains all the charged particles to be considered, and the total system will therefore be as presented in Fig. 3.1. In this model, we will assume that there are n' positive charges (ions) and n' negative charges (electrons) per meter of length, distributed uniformly in both the z and θ directions.

When the coil current i_c' (amperes per meter) changes with time, the charges will be accelerated by the induced electric field, and two things will happen as a result.

1. The electrons will attempt to travel inward much faster than the ions, as we have learned from Chapter II; a radial self-electric field will then develop between the electron shell and the ion shell, and this field will tend to hold the electrons back and drag the ions more rapidly inward.
2. The gas current caused by the tangential motion of the charges will give rise to a magnetic field which must not be ignored when calculating magnetic field effects.

Throughout this analysis, the assumption will be made, and later shown to be valid, that the mean free path for close-range collisions between particles is extremely long. It will further be assumed that all other mechanisms by which the distribution of particle energies can be

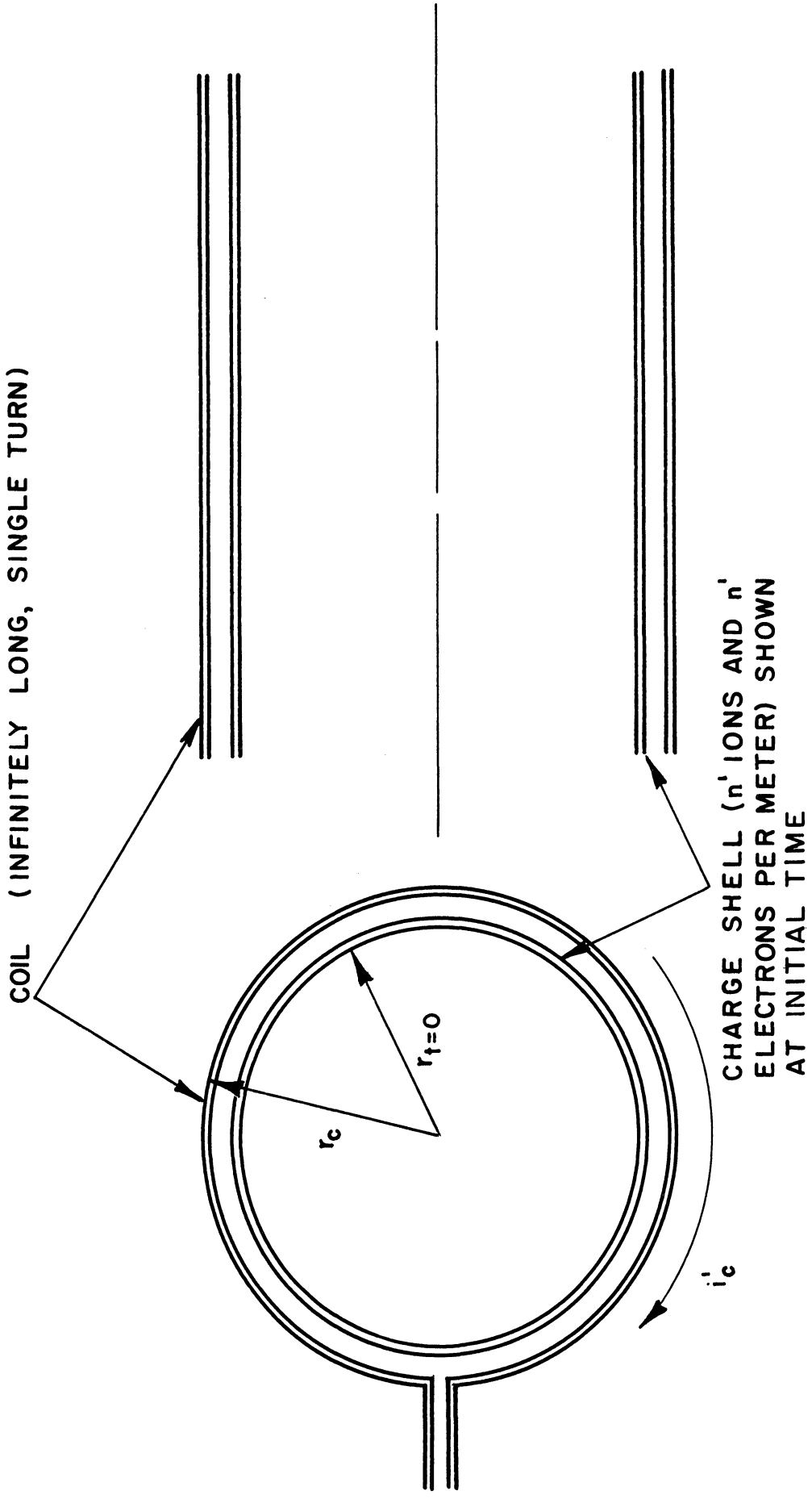

Fig. 3.1. Sheet Beam Model.

randomized are absent, so that the group motion of the charge shells (ion and electron) will be high compared with their random motion. Under these conditions, the term "beam" rather than "plasma" is appropriate. Characteristics will however result which can be carried over to the plasma experiments described later.

It should be mentioned at this point that the concept of the Debye length[56] does not enter into this analysis. This length arises as an intrinsic parameter when considering the energy stored in self-generated electric fields within an ionized gas as compared with the thermal energy content of the gas. We are not, however, interested here in the thermal effects of the gas but rather in the balance between these internal field forces and forces due to externally imposed fields.

3.2 Derivation of Field Components

The electric field between charged coaxial cylinders (e.g., the ion and electron shells) is radially directed, and of magnitude

$$e_r = \frac{q_e n'}{2\pi\epsilon_o r} , \tag{3.1a}$$

the magnitude of the field acting on the charges in each shell is given by:

$$e_r = \frac{q_e n'}{4\pi\epsilon_o r} . \tag{3.1b}$$

In addition, the induced azimuthal electric field will be present and given by the usual formula,

$$e_\theta = - \frac{1}{2\pi r} \frac{\partial \varphi}{\partial t} . \tag{3.2}$$

The magnetic field will have only a z component and will be determined at any radius r by the total current i' (amperes per meter) outside r:

$$b_z = \mu_o i' \quad . \tag{3.3}$$

The current carried by a shell of n' particles per meter, each charged to $\pm q_e$ coulombs and each having $\dot{\theta}$ angular velocity, is

$$i' = \frac{\pm q_e n' \dot{\theta}}{2\pi r} \qquad \text{(amperes/meter)} \quad . \tag{3.4}$$

Now, the azimuthal equation of motion may again be integrated as in Section 2.3, yielding, as before,

$$\dot{\theta} = - \frac{\eta \varphi}{2\pi r^2} \quad . \tag{3.5}$$

Here, η is numerically positive for positive ions and numerically negative for electrons. One must calculate φ, however, as the total flux within the orbit due to both coil and particle currents. For this purpose, let us divide the coil cross section into three coaxial sections, as shown in Fig. 3.2. The flux in each region is given by

$$\varphi_1(r_c > r > r_i) = \mu_o \pi (r_c^2 - r_i^2)\, i_c' \quad , \tag{3.6}$$

$$\varphi_2(r_i > r > r_e) = \mu_o \pi (r_i^2 - r_e^2)\, (i_c' + i_i') \quad , \tag{3.7}$$

$$\varphi_3(r_e > r) = \mu_o \pi\, r_e^2 (i_c' + i_i' + i_e') \quad , \tag{3.8}$$

and therefore the flux values within the ion and electron shells, respectively, are:

$$\varphi_i = \mu_o \pi [r_i^2 (i_c' + i_i') + r_e^2\, i_e'] \quad , \tag{3.9}$$

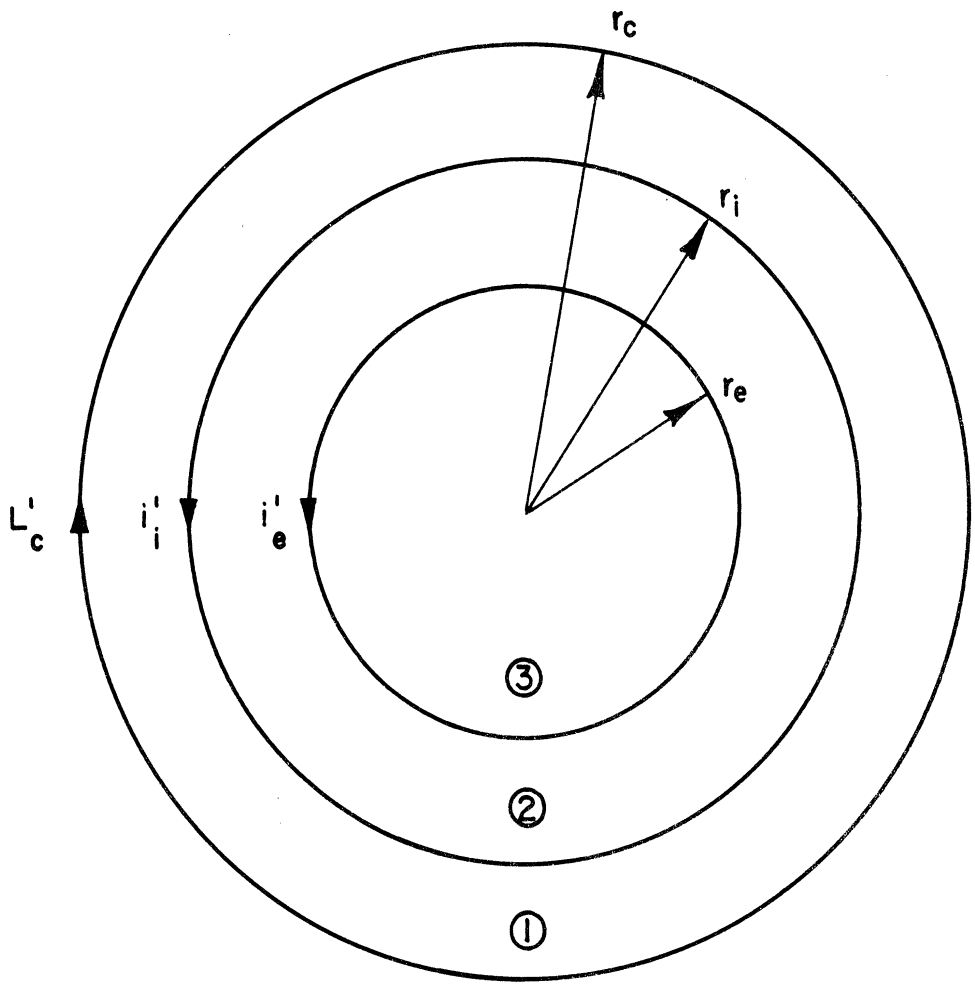

COIL LOCATION: r_c

ION SHELL LOCATION: r_i

ELECTRON SHELL LOCATION: r_e

Fig. 3.2. Positions of Ion and Electron Shells—Sheet Beam Model.

$$\varphi_e = \mu_o \pi r_e^2 (i_c' + i_i' + i_e') \quad . \tag{3.10}$$

Substitution of Eqs. 3.5, 3.9, and 3.10 into Eq. 3.4 then yields the following expressions for current in each shell.

$$i_i' = - \frac{q_e n' \eta_i \mu_o}{4\pi r_i} \left[(i_c' + i_i') + \left(\frac{r_e}{r_i} \right)^2 i_e' \right]$$

$$i_e' = + \frac{q_e n' \eta_e \mu_o}{4\pi r_e} (i_c' + i_i' + i_e') \quad .$$

Combining these gives the following complete expressions for the current in each shell in terms of the instantaneous coil current.

$$i_e' = - \frac{k_e}{1+k_e} i_c' \left\{ 1 - \frac{k_i \left[1 - \left(\frac{r_e}{r_i} \right)^2 \left(\frac{k_e}{1+k_e} \right) \right]}{1 + k_i \left[1 - \left(\frac{r_e}{r_i} \right)^2 \left(\frac{k_e}{1+k_e} \right) \right]} \right\} , \tag{3.11}$$

$$i_i' = - k_i i_c' \left\{ \frac{1 - \left(\frac{r_e}{r_i} \right)^2 \left(\frac{k_e}{1+k_e} \right)}{1 + k_i \left[1 - \left(\frac{r_e}{r_i} \right)^2 \left(\frac{k_e}{1+k_e} \right) \right]} \right\} , \tag{3.12}$$

where

$$k_e \equiv - \frac{q_e n' \eta_e \mu_o}{4\pi r_e} \quad , \tag{3.13}$$

$$k_i \equiv + \frac{q_e n' \eta_i \mu_o}{4\pi r_i} \quad . \tag{3.14}$$

(Note that both k_e and k_i are positive dimensionless numerical quantities).

When both k_e and k_i are small compared with unity, the following approximate forms hold.

$$i_e' \cong - k_e\, i_c' \quad , \tag{3.15a}$$

$$i_i' \cong - k_i\, i_c' \quad . \tag{3.15b}$$

Two further asymptotic forms result when k_e and k_i are not necessarily small, but when either

1. $\left(\frac{r_e}{r_i}\right)^2 \ll 1$;

$$i_e' \cong - \left(\frac{k_e}{1+k_e}\right)\left(\frac{1}{1+k_i}\right) i_c' \quad , \tag{3.16a}$$

$$i_i' \cong - \left(\frac{k_i}{1+k_i}\right) i_c' \quad , \tag{3.16b}$$

or

2. $\left(\frac{r_e}{r_i}\right)^2 \cong 1$ (and therefore $k_e \gg k_i$) ;

$$i_e' \cong - \left(\frac{k_e}{1+k_e}\right) i_c' \quad , \tag{3.17a}$$

$$i_i' \cong - \left(\frac{k_i}{1+k_e}\right) i_c' \quad . \tag{3.17b}$$

From Eqs. 3.15, we can say that so long as n' (and therefore k_e and k_i) is small, the particle current and its field will be small compared with the coil current and field. For higher particle densities, so long as the charge separation distance is small, we can surmise from Eqs. 3.17 that the majority of the particle current will

be carried by the electrons; when r_e becomes very small, however, the current will be carried primarily by the ion species, as indicated by Eqs. 3.16.

3.3 Effects of Self-Fields on Particle Motion

In order to investigate the role which each of the self-fields plays in the motions of charged particles, we will study the appropriate equations of motion with the approximate particle current forms given by Eqs. 3.17; these approximations will be adequate in all cases so long as the electron position r_e does not become a great deal less than the ion location r_i.

Since z-forces have been eliminated in our model, and since the θ equation of motion has been integrated to give Eq. 3.5, only the r equations need be considered; when the appropriate values are inserted from Eqs. 3.1 through 3.17, these take the following forms for the ion and electron shells, respectively.

Ion:

$$\ddot{r}_i - r_i(\dot{\theta}_i)^2 = \eta_i e_r + \eta_i b_z r_i \dot{\theta}_i \quad ,$$

$$\ddot{r}_i = -\frac{\eta_i q_e}{4\pi\epsilon_o}\frac{n'}{r_i} + \frac{\eta_i^2\mu_o^2}{4} r_i (i_c')^2 \left[\left(\frac{r_e}{r_i}\right)^4 \left(\frac{k_e}{1+k_e}\right)^2 - 1\right] . \qquad (3.18)$$

Electron:

$$\ddot{r}_e - r_e(\dot{\theta}_e)^2 = \eta_e e_r + \eta_e b_z r_e \dot{\theta}_e \quad ,$$

$$\ddot{r}_e = -\frac{\eta_e q_e}{4\pi\epsilon_o}\frac{n'}{r_e} - \frac{\eta_e^2\mu_o^2}{4} r_e (i_c')^2 \left(\frac{1}{1+k_e}\right) . \qquad (3.19)$$

In deriving these expressions, the assumption was made that the ion current was always negligible compared with the electron current and coil current (see Eqs. 3.17).

The first term in each of Eqs. 3.18 and 3.19 indicates the effect of the internal electric field due to charge separation. Note that, because the electrons tend to run inward more rapidly than the ions, this force is an inward force on the ions, while it is outwardly directed on the electrons.

The second term on the right of Eqs. 3.18 and 3.19 involves the centrifugal term as well as the external and self-magnetic fields. While these terms differ somewhat in appearance, the behavior of each is the same; both go to zero in the limit of a large charge density n'.

A detailed study of each of these equations will reveal under what conditions and in what manner the internal fields affect the motion of the particle. Each equation is uniquely satisfied by specification of four independent parameters: linear charge density n', coil current i_c, and charge positions r_e and r_i.

Two limiting conditions exist:

When n' is very low, the particle motions will be completely determined by the external field, as calculated in Chapter II, especially as presented in Fig. 2.9b (long solenoid solution).

2. When n' is above a certain range, both equations will be dominated by the electric field term, which physically means that the ion and electron sheets will be bound tightly to one another and will travel radially inward together.

Under the latter condition, a combined motion equation must be used, describing the behavior of the combined ion/electron shell. The

complete form of this equation, derived by adding together Eqs. 3.18 and 3.19 but omitting the internal electric field term, is as follows:

$$(m_i+m_e)\ddot{r} - m_e r(\dot{\theta}_e)^2 - m_i r(\dot{\theta}_i)^2 = q_e b_z r(\dot{\theta}_i-\dot{\theta}_e) \quad . \qquad (3.20)$$

If the large difference in mass of the ion and the electron is taken into account and if Eq. 3.5 is inserted, Eq. 3.20 immediately reduces to:

$$m_i\ddot{r} - \frac{q_e^2 \varphi^2}{4\pi^2 m_e r^3} = -\frac{q_e^2 b_z \varphi}{2\pi r m_e} \quad . \qquad (3.21)$$

Flux and field values, φ and b_z, may be obtained from expressions derived in Section 3.2, again using the current approximations given by Eqs. 3.17. These yield

$$b_z = \mu_o(i_c' + \tfrac{1}{2} i_e')$$

$$= \mu_o i_c' \left[1 - \frac{1}{2}\left(\frac{k_e}{1+k_e}\right)\right] \qquad (3.22)$$

and

$$\varphi = \mu_o \pi r^2 (i_c' + i_e')$$

$$= \mu_o \pi r^2 i_c' \left[1 - \left(\frac{k_e}{1+k_e}\right)\right] \quad . \qquad (3.23)$$

Inserting these back into Eq. 3.21 gives the final form for the radial acceleration.

$$\ddot{r} = \frac{1}{4}\eta_e \eta_i \mu_o^2 r(i_c')^2 \left(\frac{1}{1+k_e}\right) \quad . \qquad (3.24)$$

A comparison of this with the equivalent expression for an isolated particle having specific charge η in a long solenoid (derivable from Eq. 2.5),

$$\ddot{r} = \frac{1}{4}\eta^2\mu_o^2\, r(i_c')^2 \quad , \tag{3.25}$$

indicates clearly the effects of the internal fields.

First of all, the electric field binding causes the ions to move inward with an acceleration which is increased in proportion to the ion/electron mass ratio, while the electrons slow down by the ratio of electron to ion mass. Inasmuch as the electrons are still free to move in the θ direction, they would now be able to pick up considerably more energy from the e_θ field than in the isolated particle case. On the other hand, the increased radial speed of the ions might also lead to increased energy gain by changing them from slow to fast particles (see Section 2.5).

Secondly, the self-magnetic field effect enters as the k_e factor in Eq. 3.24. Since k_e is proportional to n'/r, this internal field will act in all cases to reduce the inward acceleration of the charge sheet. This influence tends to counteract the energy gain potentialities brought out in the previous paragraph, since it reduces the angular velocity of the electrons, allowing them to gain less energy from the e_θ field, and it acts to prevent ions from changing from slow to fast.

We wish now to investigate phenomena which might arise in the transition region between high and low particle densities and to calculate approximate numerical values for conditions under which these self-field effects will take place.

The effect of the self-magnetic field is determined by the value of k_e relative to unity. This effect is therefore independent of i_c', and in fact depends only on n' and r_e. Table 3.1 lists k_e for various typical charge densities and electron positions. The internal magnetic

field may be expected to play an important role whenever operating conditions fall to the right of the diagonal in this table.

Table 3.1. Magnetic Field Factor k_e (Defining Eq. 3.13)

n' (particles/meter)	r_e (meters) = 1	10^{-1}	10^{-2}	10^{-3}
10^{11}	.00028	.0028	.028	.28
10^{12}	.0028	.028	.28	2.8
10^{13}	.028	.28	2.8	28
10^{14}	.28	2.8	28	280

The internal electric field will be significant whenever the first terms on the right-hand side of Eqs. 3.18 and 3.19 become of the same order as the second terms.

The next four paragraphs will describe behavior when the self-magnetic field is negligible ($k_e \ll 1$). In Table 3.2 are presented the values of unique linear particle densities n_i' and n_e' necessary to make the first and second terms equal in Eqs. 3.18 and 3.19 respectively for various coil currents and particle positions. All conditions which contradict $k_e \ll 1$ are enclosed in a box outline.

From Table 3.2, one concludes that as the particle density increases, the ion constituent will be the first to be influenced by the self-electric field, since in all cases $n_i' < n_e'$. The transitions which occur as n' increases through the range from below n_i' to above n_e' are described in Fig. 3.3 and discussed in the following sentences. When $n' \ll n_i'$, as in Fig. 3.3(a), the shells are very tenuously

Table 3.2. Unique Values of Ion and Electron Linear Particle Density n_i' and n_e' to Give Balance of Forces in Eqs. 3.18 and 3.19

i_c' (amp/meter)	Particle Position r (meter)	n_i' (meter^{-1})	n_e' (meter^{-1})
10^3	1	6.38×10^9	4.84×10^{13}
	10^{-1}	6.38×10^7	4.84×10^{11}
	10^{-2}	6.38×10^5	4.84×10^9
	10^{-3}	6.38×10^3	4.84×10^7
10^4	1	6.38×10^{11}	4.84×10^{15}
	10^{-1}	6.38×10^9	4.84×10^{13}
	10^{-2}	6.38×10^7	4.84×10^{11}
	10^{-3}	6.38×10^5	4.84×10^9
10^5	1	6.38×10^{13}	4.84×10^{17}
	10^{-1}	6.38×10^{11}	4.84×10^{15}
	10^{-2}	6.38×10^9	4.84×10^{13}
	10^{-3}	6.38×10^7	4.84×10^{11}
10^6	1	6.38×10^{15}	4.84×10^{19}
	10^{-1}	6.38×10^{13}	4.84×10^{17}
	10^{-2}	6.38×10^{11}	4.84×10^{15}
	10^{-3}	6.38×10^9	4.84×10^{13}

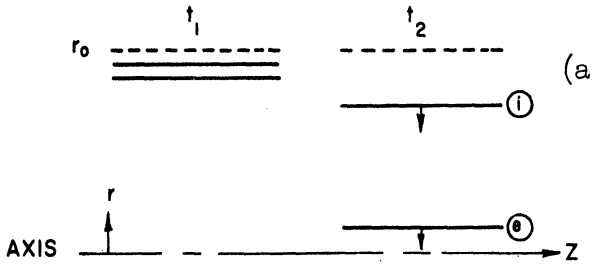

(a) $n' \ll n_i' < n_e'$, Shells Tenuously Populated, Motion Not Influenced by Self-Field Effects

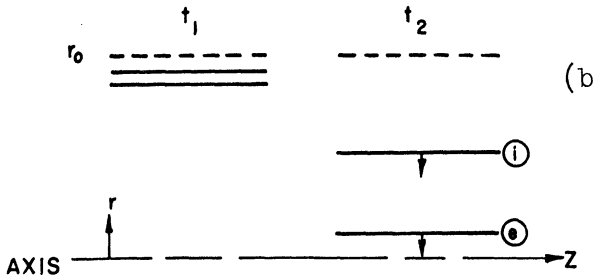

(b) $n_i' < n' < n_e'$, Shell Population Greater Than in (a); Electron Motion Only Slightly Influenced by Self-Field; Ion Motion Largely Influenced by Self-Electric Field Between Shells.

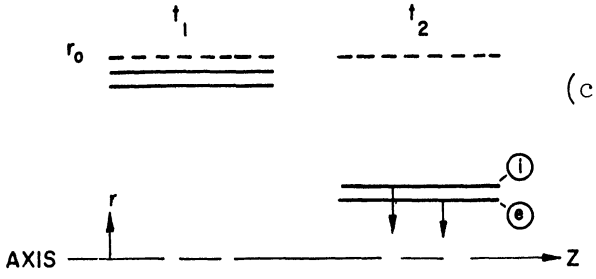

(c) $n_i' < n_e' < n'$, Shell Population Greater Still; Self-Electric Field Causes Strong Binding Between the Two Shells, and They Proceed Radially Inward Together.

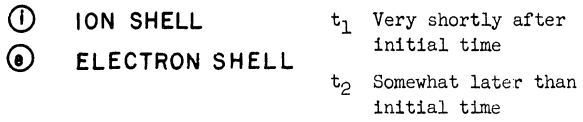

Fig. 3.3. Relative Ion and Electron Shell Motions for Various Particle Densities—Sheet Beam Model.

populated, the forces on the ions and electrons are not influenced by self-fields, and the motions will be as calculated in Section 2.4.5. When n' is between the unique values n_i' and n_e', as in Fig. 3.3(b), the following aspects are noted.

a. The electron radial motion, still uninfluenced by the ions, follows the single-particle behavior.

b. The ion motion will be determined more by the attraction to the electron shell than by the Lorentz force due to the magnetic field.

Finally, when n' is greater than both n_i' and n_e', as in Fig. 3.3(c), the electrons become "bound" to the ions as well as vice versa, and motion of the combined shells is governed by Eq. 3.21 as discussed below that equation. The motion is affected by forces on both kinds of particles.

A condition intermediate between situations (b) and (c) in Fig. 3.3 can under some circumstances exist. This will occur when n' is slightly less than n_e' initially. Initial motion will then be as for the (b) case. Since the cross-over point n_e' is dependent on radius, however, a point in the electron shell motion will be reached at which n' becomes greater than n_e', and the shells will not separate any further.

We have now to investigate the influence of the self-magnetic field on the action due to the self-electric field. Qualitatively from Eqs. 3.18 and 3.19, one can see that as k_e becomes comparable to, or larger than, unity, the second terms will diminish in magnitude. This means that in all cases encircled in Table 3.2, the electric field term will become important at lower n' values than calculated in Table 3.2.

As a specific example to point this out, the case $i_c' = 10^5$ amperes/meter, $r_e = 10^{-1}$ meters, has been solved for $\ddot{r}_e$ as a function of n', and is presented in Fig. 3.4. Curves 1 and 2 on this figure compare the acceleration with and without taking into account the internal magnetic field. The inclusion of this effect reduces the balance point ($\ddot{r}_e = 0$) by approximately a factor of ten. As the current is increased, for instance to 10^6 amperes/meter, the applicable curves in Fig. 3.5 show that the cross-over point is reduced by an even greater factor than is read from the predictions of Table 3.2.

This result of Fig. 3.5 is particularly interesting, since it represents approximately the conditions in the experimental accelerator to be described later. Above a linear particle density of about 10^{16}/meter (which corresponds to a volume density of 3×10^{17} particles/meter^3 in a 10^{-1} meter radius tube), the distance through which the oppositely charged species separate should be extremely small. Experimentally, however, the electric field in this very thin ion sheath has been found to be observable.

The internal electric field due to charge separation has long been known to play an important role in all gas discharge situations. Langmuir[57] took into account the role of the ion sheath in his analysis of the low pressure, d-c glow discharge. Morozov[31] solved the equations of motion applying to a thin, planar, ion-electron layer in orthogonal d-c electric and magnetic fields taking into account the self-electric field due to the electrons running ahead of the ions (but neglecting the magnetic field due to the motion of these charges). Finally, Penfold[58] has recently studied the cylindrical case in terms of ion-electron pairs, considering the electric field between each member but

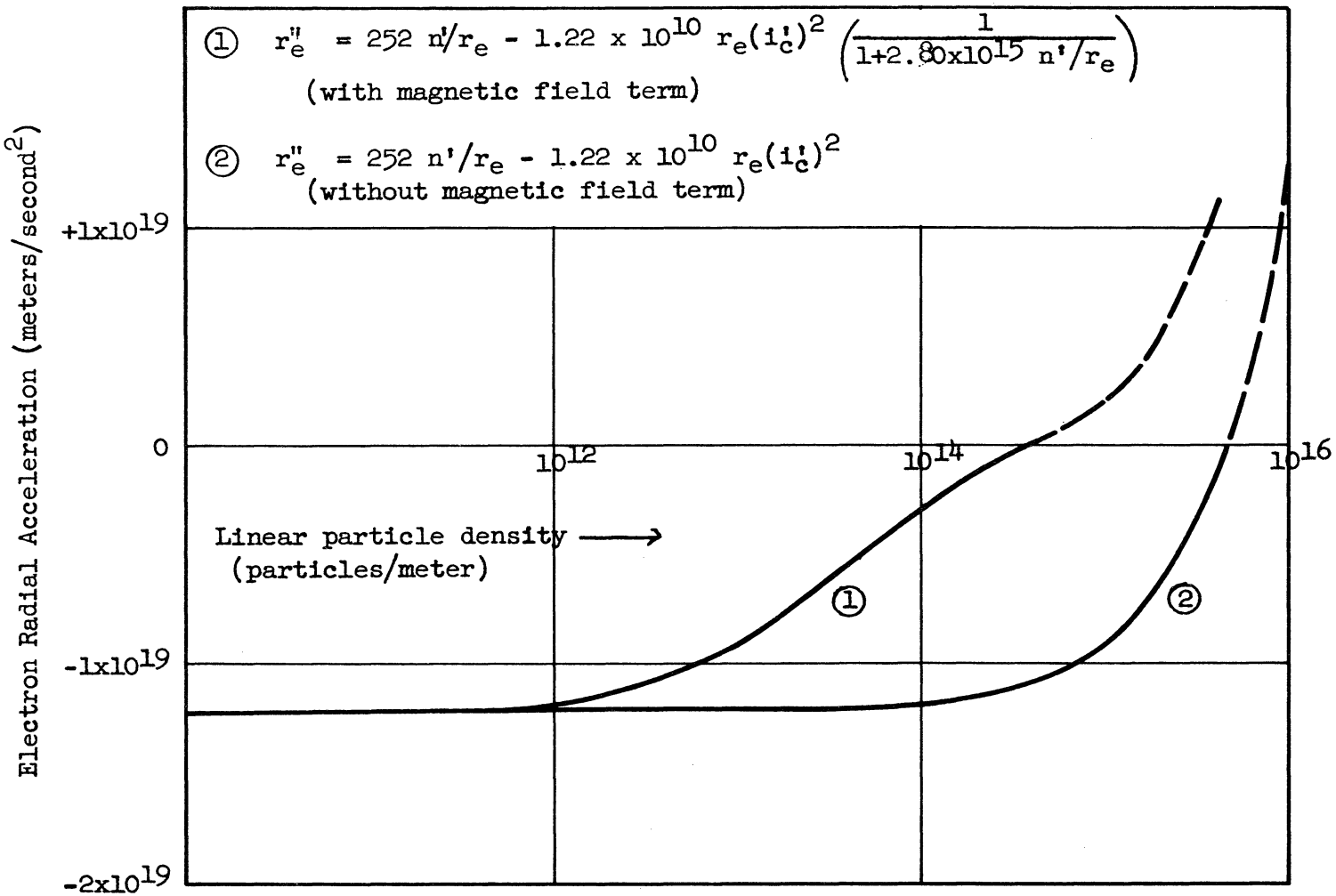

Fig. 3.4. Electron Acceleration With and Without Internal Magnetic Field Term ($i'_c = 10^5$ amperes/meter, $r_e = 10^{-1}$ meters).

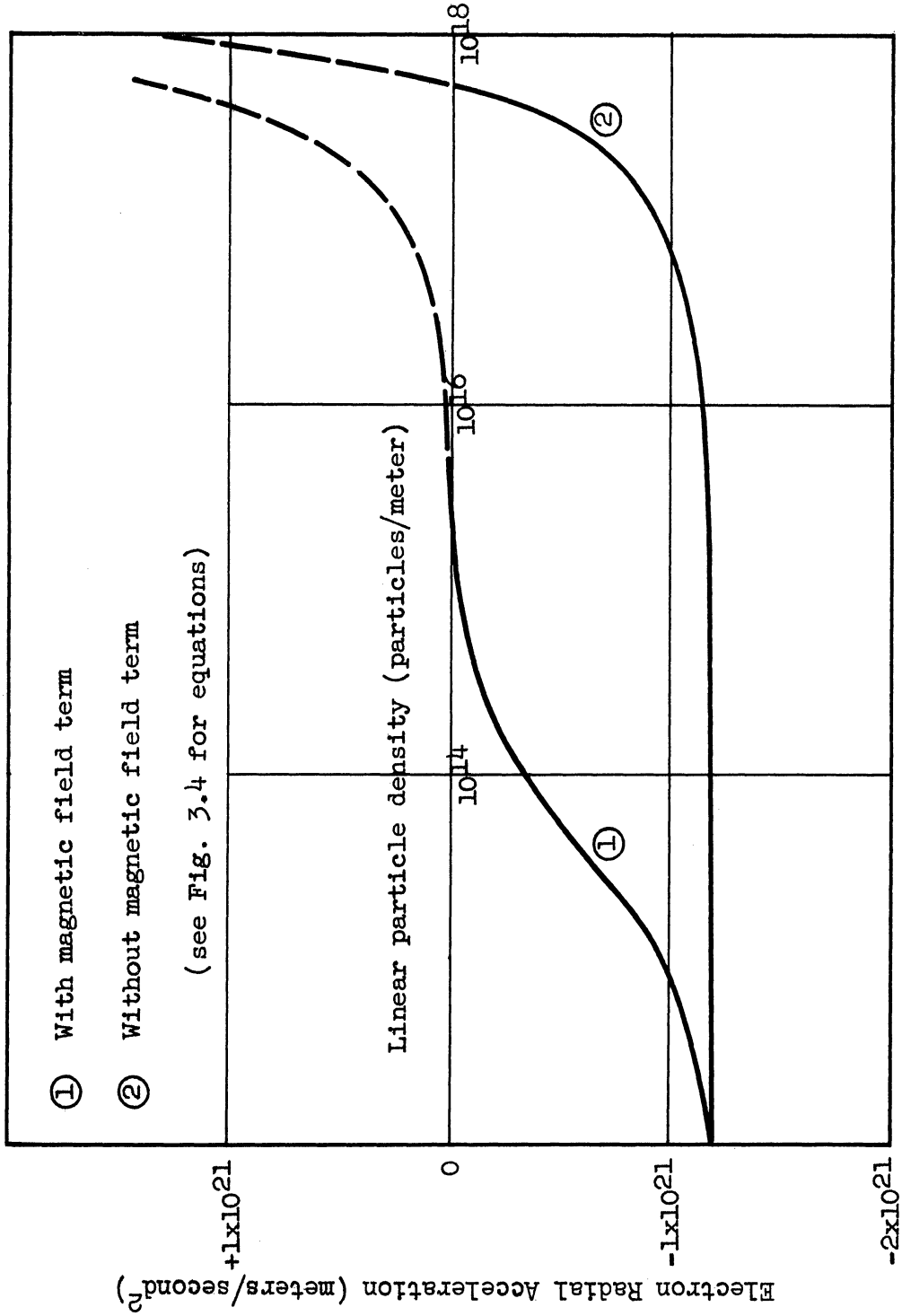

Fig. 3.5. Electron Acceleration With and Without Internal Magnetic Field Term ($i'_c = 10^6$ amperes/meter, $r_e = 10^{-1}$ meters).

again neglecting the magnetic field due to the azimuthal motion of the charges; his resulting radial acceleration expression is of the same form as Eq. 3.24 but does not include the self magnetic field factor (k_e).

The present analysis corroborates results of these earlier efforts. In addition, it has clearly defined the particle density range (limited at one end where the particles may be considered independent of one another and at the other end where very tight ion/electron binding exists) over which the separation of charges will be a primary factor in determining the behavior of experimental devices. A further significant item brought out in this derivation is the considerable influence exerted by the magnetic field arising from charge motion.

CHAPTER IV. CONTINUUM BEAM ANALYSIS

4.1 Description of Model

We now wish to continue the analysis of the cylindrical coil induction accelerator shown in Fig. 1.2 by eliminating some of the restrictions of the sheet beam model. As in Chapter III, z variations will be eliminated by using a model in which the charged particles exist within a long cylindrical coil. Now, however, instead of restricting these charges to thin shells, the total volume will be assumed initially to be uniformly ionized with n ions and n electrons per cubic meter. Current i_c' amperes per meter is assumed to flow in the surrounding coil, and initially the ionized volume is devoid of any magnetic field. This system is shown in Fig. 4.1.

A qualitative description of the plasma behavior will help in further delineating the model to be studied. The motions of isolated particles in a long solenoid derived in Chapter II indicated that the electrons traveled radially inward much more rapidly than the ions when current was introduced into the coil. We would expect the same tendency to exist in the present model. Thus, the originally space-charge-neutral ionized volume would after a short while exhibit an ion layer on its outer boundary due to the electrons' more rapid inward travel.

Two possible particle distributions might exist when such an ion sheath is present. In one configuration, the whole electron cloud has compressed with respect to the ion column, leaving a positively charged sheath and a negatively charged core; the charge and potential distributions

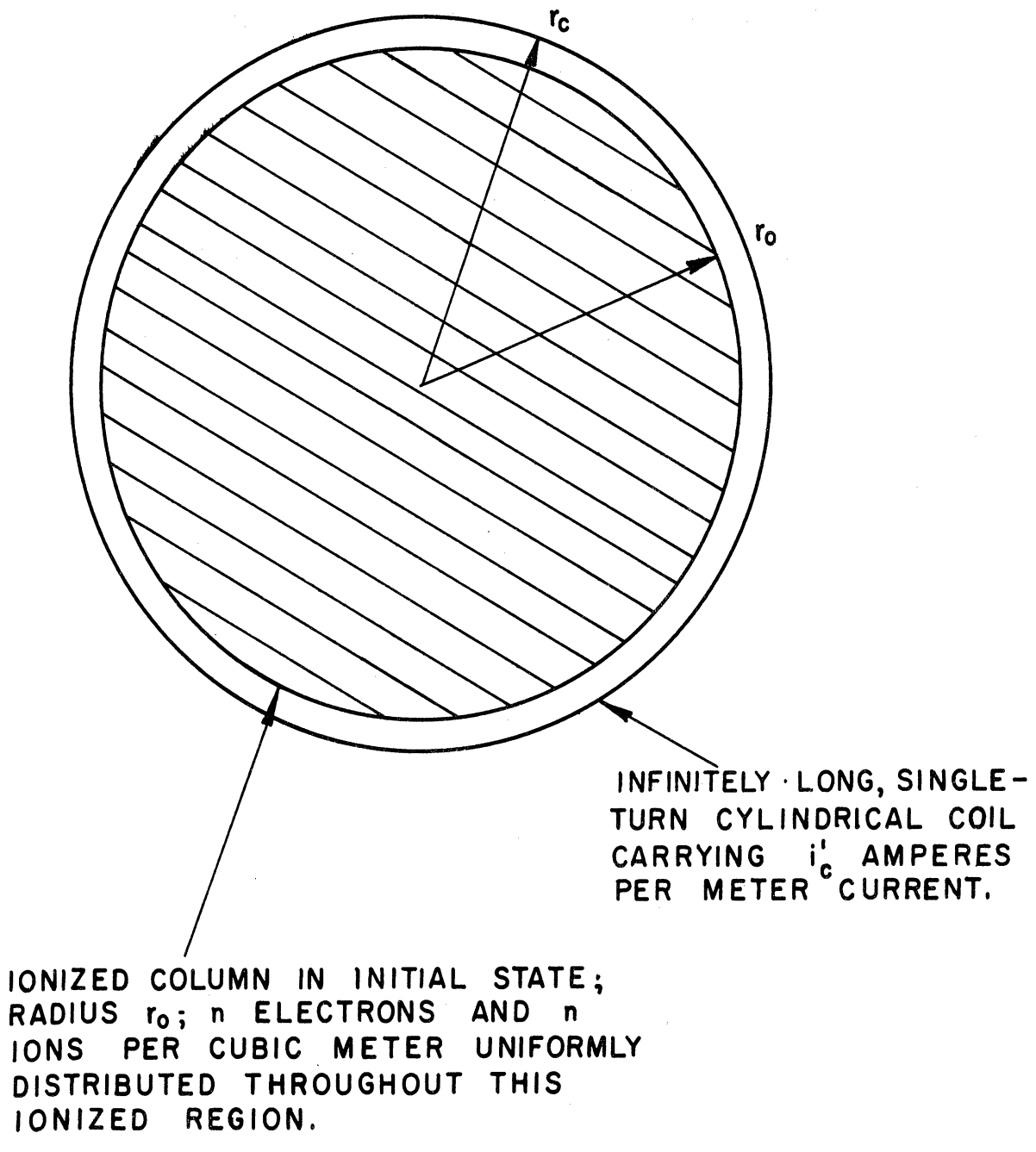

Fig. 4.1. Continuum Beam Model.

in this case are shown in Fig. 4.2(a). In the other possibility, the electrons which have left the positive-ion sheath region all appear as a thin layer separating the sheath from the core; this distribution is indicated in Fig. 4.2(b).

The procedure in this analysis will in some ways follow the sheet-beam study carried out in Chapter III; that is, we will first derive applicable expressions for the current, magnetic field and space-charge electric field and then insert these into the radial equation of motion. Charge separation effects will then be deduced as well as motion of the column under special conditions.

The general approach will be to assume initially that the collection of charged particles contains no random energy component and that randomizing mechanisms are absent; thus, as in Chapter III, the term "beam" still describes the particle collection more accurately than "plasma". This requirement will be re-examined in later sections of this chapter, and, in the case of large n, where such a restriction might be questionable, a random energy component will be included in the analysis.

4.2 Derivation of Magnetic Field and Current Density Expressions

Let us consider the column of ionized gas within a long solenoid coil at some instant after the coil current i_c' has begun to rise. The electrons and ions will have been accelerated inward so that the ions will populate the region $r_{io}(t) \geq r > 0$ with density $n_i(r)$, in general a function of radius, while the electrons will all be located in the range $r_{eo}(t) \geq r > 0$, also with their density being a function of radius. As explained in Section 4.1, r_{eo} will be less than r_{io}, leaving a positively charged layer on the surface of the compressing column.

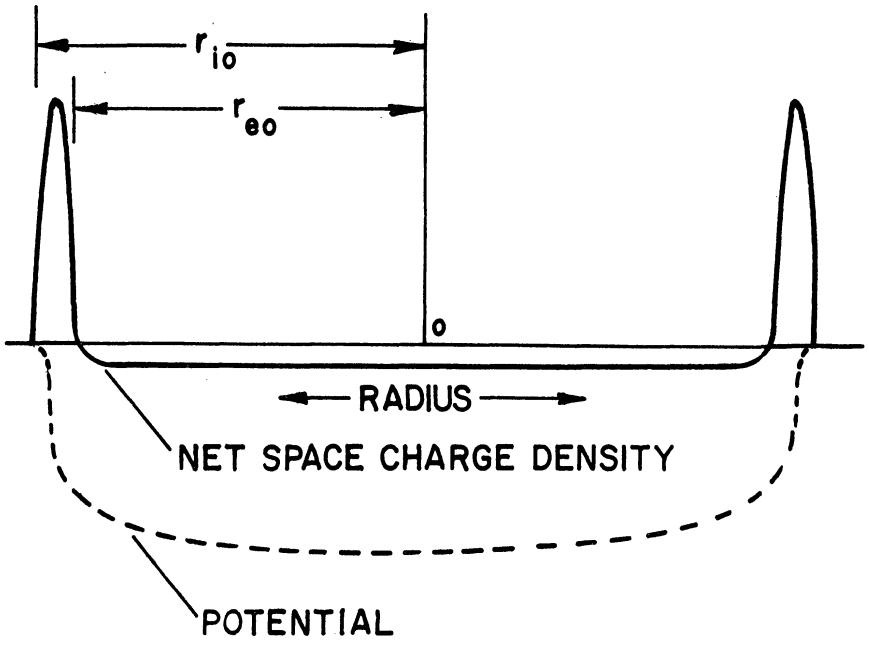

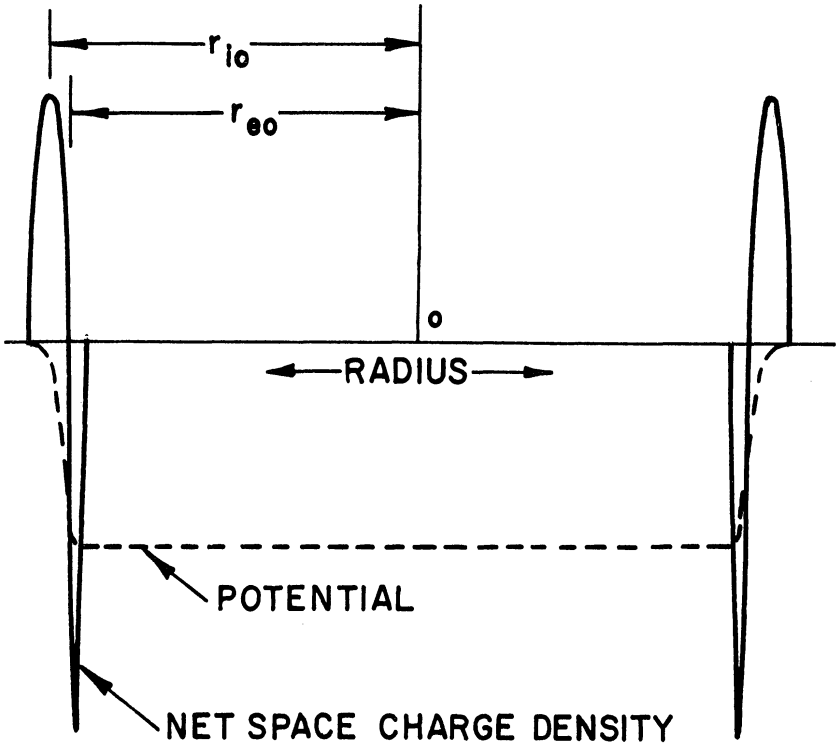

Fig. 4.2. Radial Distribution of Net Space Charge and Potential (Approximate) for Surplus Electrons Distributed in Two Ways.

(a) Surplus Electrons Distributed Uniformly Within r_{eo}.

(b) Surplus Electrons All in a Thin Layer at r_{eo}.

The current density i_θ flowing at any radius within the gas will be given by the continuity equation. Since only azimuthal currents (that is, currents parallel with the coil current) will arise in the gas, this takes the following form:

$$i_\theta = q_e r(n_i\dot{\theta}_i - n_e\dot{\theta}_e) \quad , \tag{4.1}$$

where subscripts i and e refer respectively to ions and electrons, and q_e is a positive number.

The angular velocity may be derived from the θ equation of motion in the manner of Section 2.3, giving

$$\dot{\theta} = -\frac{\eta\varphi}{2\pi r^2} \quad , \tag{4.2}$$

where initial values, $\dot{\theta}_o$ and φ_o, have been assumed zero, r is the radius of the particle being considered, φ is a function of coil current and r, and η is a quantity positive for ions and negative for electrons. Since η_i is so much smaller than η_e, we may ignore $\dot{\theta}_i$. With this simplification, substitution of Eq. 4.2 into Eq. 4.1 yields:

$$i_\theta = \frac{q_e n_e \eta_e \varphi}{2\pi r} = \frac{q_e n_e \eta_e \varphi}{2\pi r_{eo}\rho} \quad , \tag{4.3}$$

where a dimensionless radial coordinate,

$$\rho \triangleq \frac{r}{r_{eo}} \tag{4.4}$$

(being less than unity for electrons), is assumed as in Chapter II, where r_{eo} is the outer radius of the electron cloud (see Fig. 4.2).

The magnetic field is related to the current density and electric field through the differential Maxwell expression:

$$\text{curl } H = i + \frac{\partial D}{\partial t} \quad . \tag{4.5}$$

If only the azimuthal component is considered, this reduces to

$$\frac{1}{r_{eo}} \frac{\partial b_z}{\partial \rho} = - \mu_o i_\theta - \mu_o \epsilon_o \frac{\partial e_\theta}{\partial t} \quad , \tag{4.6}$$

where the magnetic induction field B has been related to the magnetic intensity field H through the vacuum permeability μ_o, and the electric intensity and electric displacement fields are related through the vacuum permittivity ϵ_o. The e_θ field is generated by the changing of the magnetic field due to the coil current.

Use of the Eq. 3.2 expression for the electric field converts Eq. 4.6 to

$$\frac{1}{r_{eo}} \frac{\partial b_z}{\partial \rho} = - \mu_o i_\theta + \frac{\mu_o \epsilon_o}{2\pi r_{eo} \rho} \frac{\partial^2 \varphi}{\partial t^2} \quad . \tag{4.7}$$

Equation 4.7 can be put into second-order form by multiplying through by ρ and differentiating with respect to ρ:

$$\frac{1}{r_{eo}} \frac{\partial}{\partial \rho} \rho \frac{\partial b_z}{\partial \rho} = - \mu_o \frac{\partial}{\partial \rho} \rho i_\theta + \frac{\mu_o \epsilon_o}{2\pi r_{eo}} \frac{\partial}{\partial \rho} \frac{\partial^2 \varphi}{\partial t^2} \quad . \tag{4.8}$$

The flux φ must be calculated as an integral over the magnetic field linked by the particle (see Chapter II):

$$\varphi = 2\pi r_{eo}^2 \int_o^\rho \rho b_z d\rho \quad , \tag{4.9}$$

where the integration is at any given instant. Inserting this relation and Eq. 4.3 into Eq. 4.8 gives finally:

$$\rho \frac{\partial^2 b_z}{\partial \rho^2} + \frac{\partial b_z}{\partial \rho} - \alpha^2 \rho b_z - \gamma^2 \rho \frac{\partial^2 b_z}{\partial t^2} = 0 \quad , \tag{4.10}$$

where

$$\alpha^2 \triangleq - \mu_o q_e \eta_e n_e r_{eo}^2 \quad ,$$

and

$$\gamma^2 \triangleq + \mu_o \epsilon_o r_{eo}^2 \quad .$$

Equation 4.10 is a general expression for the magnetic field as determined both by convection and displacement currents. If we now limit ourselves to the case where the displacement current is much less than the convection current (thereby eliminating the time derivatives in Eqs. 4.5 and 4.10), the descriptive equation becomes

$$\rho \frac{d^2 b_z}{d\rho^2} + \frac{db_z}{d\rho} - \alpha^2 \rho b_z = 0 \quad . \tag{4.11}$$

According to our model, n_e, and therefore α^2, are unknown functions of radius. Since, however, n_e initially was assumed to be independent of ρ, we will temporarily assume α^2 is also independent of ρ; the validity of this assumption will be considered later. This allows us immediately to write the solution of Eq. 4.11, since it is in the form of Bessel's Equation whose solutions are Bessel Functions of imaginary argument[59]:

$$b_z(\rho) = A_1 J_o(j\alpha\rho) + A_2 H_o(j\alpha\rho) \quad . \tag{4.12}$$

The constants in Eq. 4.12 can be evaluated by noting that as ρ goes to zero b_z must remain finite, necessitating that

$$A_2 = 0 \quad ,$$

while at $\rho = 1$, b_z must be equal to the instantaneous exterior field b_o at r_{eo}, giving

$$A_1 = \frac{b_o}{J_o(j\alpha)} \quad . \tag{4.13}$$

We arrive now at the final expression for field distribution,

$$\frac{b_z}{b_o} = \frac{J_o(j\alpha\rho)}{J_o(j\alpha)} \quad . \tag{4.14}$$

The distribution of current density may be evaluated from Eq. 4.3, using Eqs. 4.9 and 4.14, giving

$$\frac{i_\theta}{i'_c} = -\frac{\alpha}{r_{eo} J_o(j\alpha)} [-jJ_1(j\alpha\rho)] \quad . \tag{4.15}$$

For comparison with experimental results described later in this report, the variations of b_z/b_o and i_θ/i'_c with ρ are shown for several particle densities in Figs. 4.3 and 4.4.

It is interesting to note the effect on the field and current distributions as the electron cloud compresses radially inward. If we can assume that the whole electron column shrinks uniformly so that n_e remains independent of ρ, then, in order to conserve particles, $n_e r_{eo}^2$ must remain constant. Thus, in this case, α does not change, and neither does the magnetic field distribution, given by Eq. 4.14. However, the current density in the electron stream (amperes per unit area) does increase in magnitude inversely with r_{eo} as indicated by Eq. 4.15.

The Bessel Function dependence of field on radius also results when a constant scalar conductivity is ascribed to the ionized gas in an electrodeless discharge, as shown by Sir J. J. Thomson[60] in 1927. Since Thomson did not carry out his derivation in detail, it was felt desirable

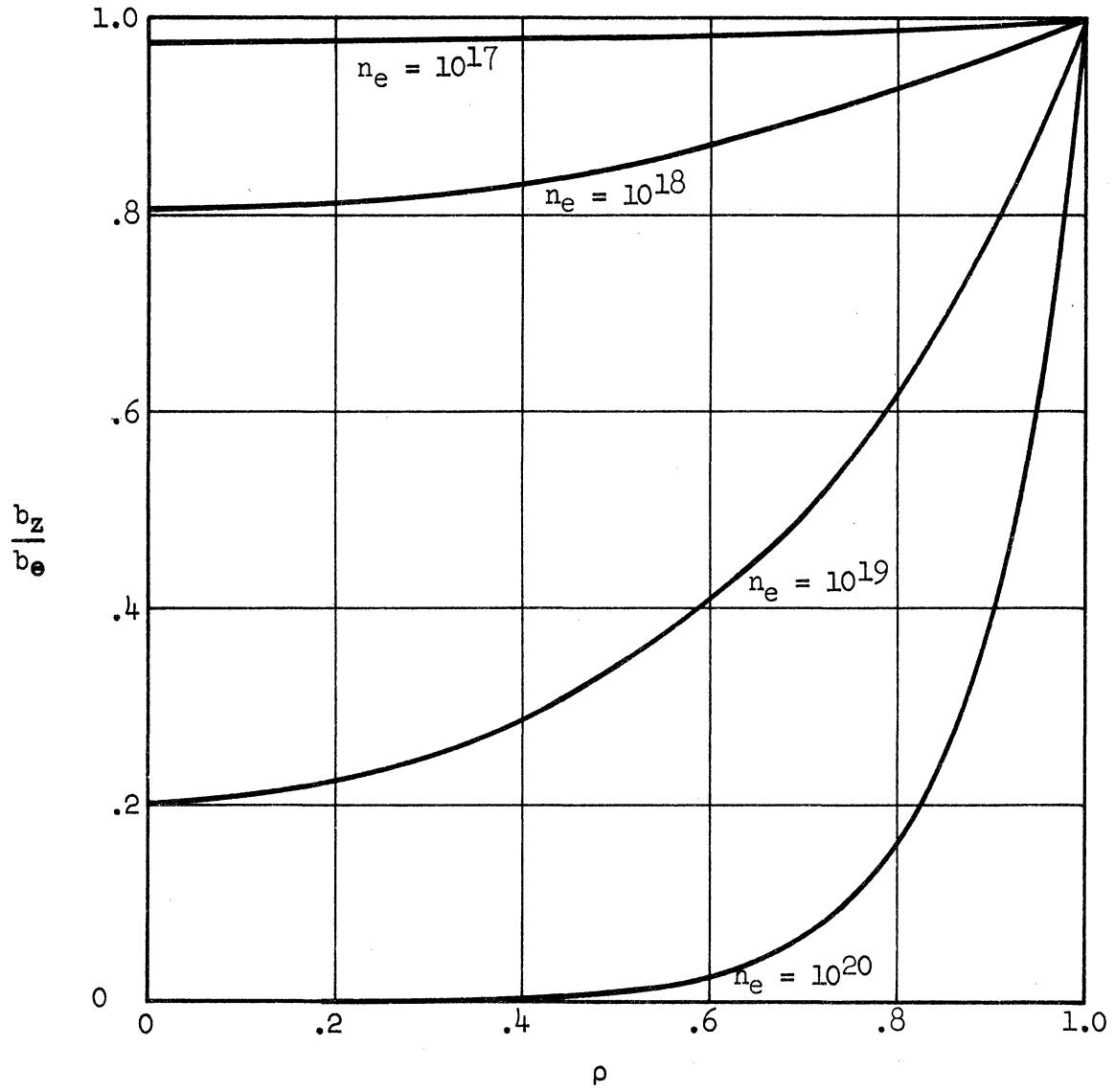

;. 4.3. Theoretical Distribution of Magnetic Field for Several Particle Densities [Reference: Eq. 4.14].

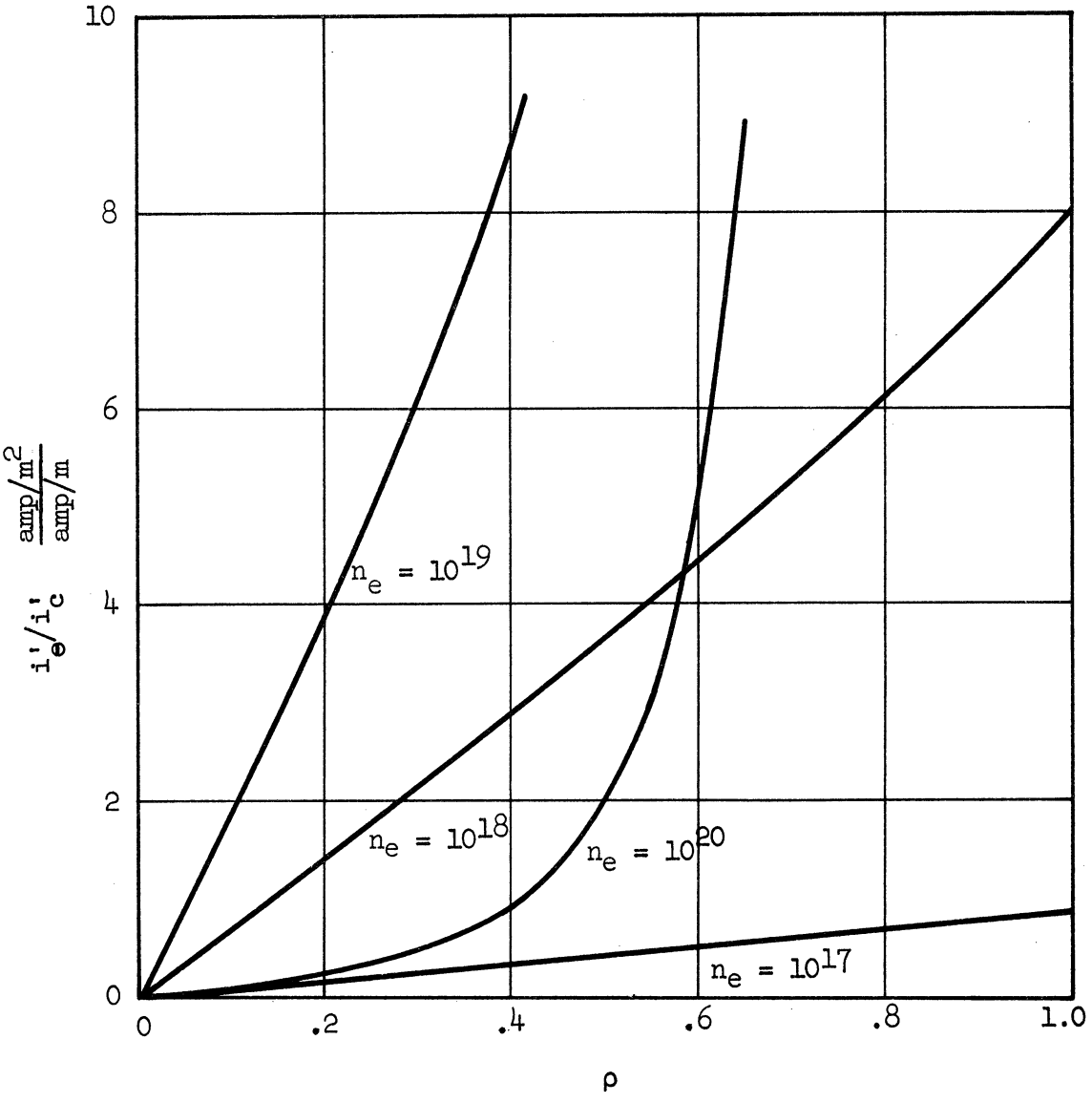

Fig. 4.4(a). Theoretical Distribution of Current Density for Several Particle Densities [Reference: Eq. 4.15].

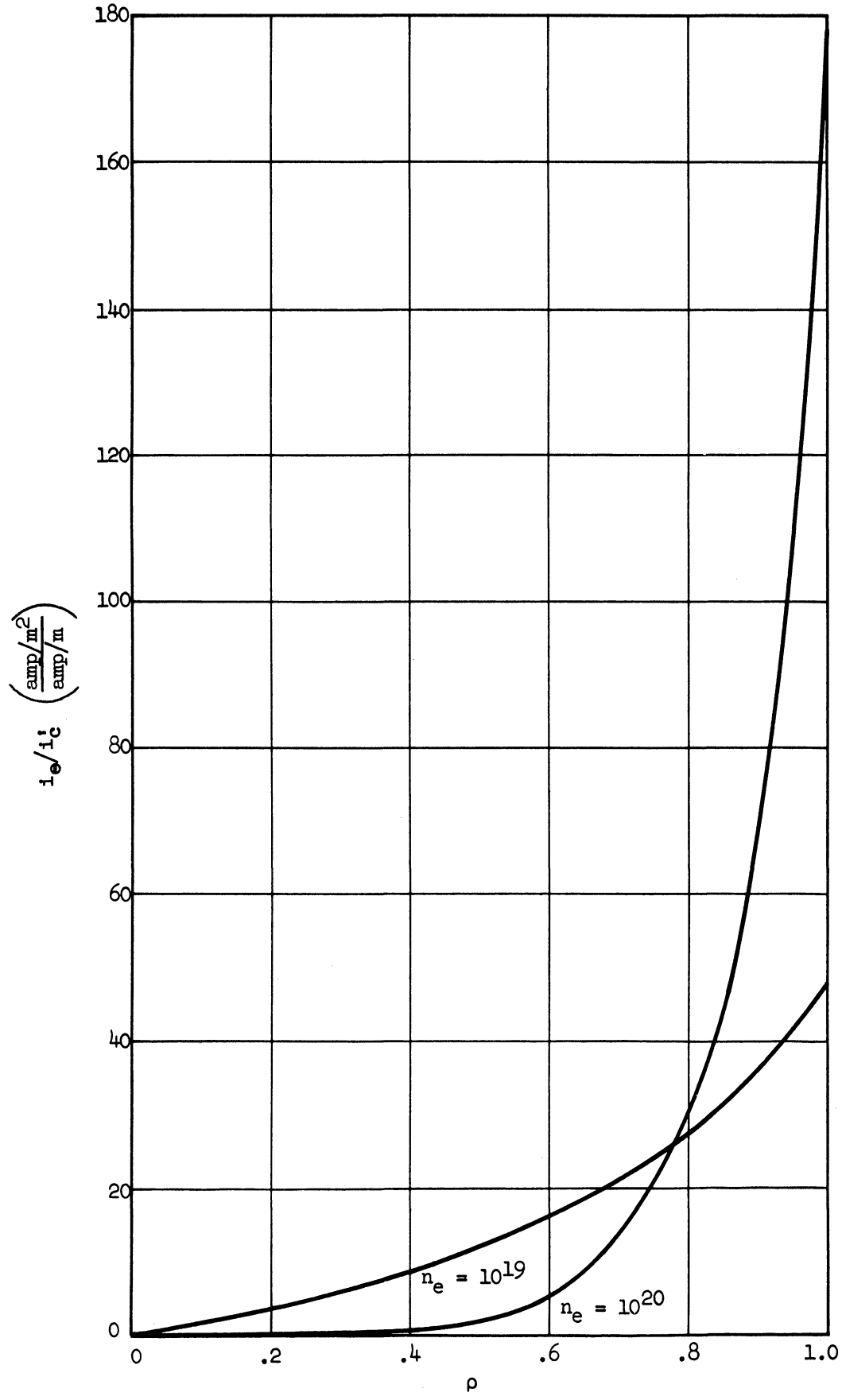

Fig. 4.4(b). Theoretical Distribution of Current Density for Several Particle Densities [Reference: Eq. 4.15].

to include the entire derivation here, based however on particle density rather than conductivity. Eckert[29,61] has carried on Thomson's analysis, considering nonuniform conductivity, ionization rate and diffusion and deriving a breakdown criterion for the inductively driven electrodeless discharge. Eckert's work represents an important advancement in understanding the basic processes active in the inductive discharge, although the range of field conditions for which he has presented specific results does not include the conditions existing in our experimental work.

4.3 Space Charge Effects

Space charge forces will tend to bind the ion and electron components together, much as they did in the sheet beam situation analyzed in Chapter III. One can deduce this qualitatively by first hypothesizing that the electrons and ions do initially separate, leaving net charge densities and potentials as shown in Figs. 4.2(a) and 4.2(b). In this condition, the radial electric field due to charge separation acts inwardly on the ions and outwardly on the electrons, thereby serving to counteract the separation tendency. If the radial electric force is not large enough to overcome the Lorentz force, of course, the ions and electrons will continue to separate. If, on the other hand, the electric effect is the greater of the two, then the forces are in a direction to cause the charges to adjust themselves until the two effects are balanced. We will now bring in the radial equation of motion in an attempt to discover conditions necessary to achieve such a balanced state.

The radial force equations for electrons and ions, including the space-charge electric field, are given below:

$$\text{ions:} \qquad m_i \ddot{r}_i - r_i m_i (\dot{\theta}_i)^2 = q_e b_z r_i \dot{\theta}_i + q_e e_r \quad , \qquad (4.16a)$$

$$\text{electrons:} \qquad m_e \ddot{r}_e - r_e m_e (\dot{\theta}_e)^2 = - q_e b_z r_e \dot{\theta}_e - q_e e_r \quad . \qquad (4.16b)$$

On solving for the radial accelerations and inserting the expression for $\dot{\theta}$ from Eq. 4.2, we find the following:

$$\ddot{r}_i = \eta_i \left[r_i \eta_i \left(\frac{\bar{b}}{2} \right) \left(\frac{\bar{b}}{2} - b_z \right) + e_r \right] \quad , \qquad (4.17)$$

and

$$\ddot{r}_e = \eta_e \left[r_e \eta_e \left(\frac{\bar{b}}{2} \right) \left(\frac{\bar{b}}{2} - b_z \right) + e_r \right] \quad , \qquad (4.18)$$

where

$$\bar{b} \triangleq \frac{\varphi}{\pi r^2} = \frac{2}{r^2} \int_0^r r b_z dr \quad , \qquad (4.19)$$

this being an average quantity.

The effect of space charge on particle motion appears as the e_r term in these equations. Let us consider for a moment how this space-charge force influences the action of the ions and electrons. For space-charge distributions of the type suggested by Figs. 4.2(a) and 4.2(b), the field e_r will everywhere within the ionized region be directed inwardly. The magnitude of this field at any given radius, as we shall later see from Gauss' Law, is determined by the total net charge within the radius. Thus, we can conclude that at sufficiently low particle densities, the electric field e_r and its effect will be negligible, and each particle will move independently of the others.

At higher particle densities, it becomes likely that charge separation of the sort suggested in Figs. 4.2(a) and 4.2(b) might lead to electric field strengths which would not be negligible compared with this magnetic force. Let us postulate that this is so and consider the consequences. We have noted that the field is inwardly directed. The electric

force on ions will therefore be inward, while this force will be outward on the electrons. Note that these forces are both in the direction to oppose separation of the electrons from the ions. It is in fact quite reasonable to expect that, if conditions are proper, the space-charge-generated electric field will in fact be strong enough to prevent further separation of charges. An understanding of this balanced condition might be aided by the following representation, in which Eqs. 4.17 and 4.18, each represented by a magnetic acceleration term and an electric acceleration term, are equated:

$$\begin{bmatrix}\text{ion magnetic}\\ \text{acceleration}\\ \text{(small, inward)}\end{bmatrix} + \begin{bmatrix}\text{ion electric}\\ \text{acceleration}\\ \text{(small, inward)}\end{bmatrix}$$

$$= \begin{bmatrix}\text{electron magnetic}\\ \text{acceleration}\\ \text{(large, inward)}\end{bmatrix} - \begin{bmatrix}\text{electron electric}\\ \text{acceleration}\\ \text{(large, outward)}\end{bmatrix}$$

We can be more specific in describing and defining this balance or equilibrium condition. This condition may essentially be described in terms of the net space-charge distribution throughout the ionized volume, since it is this charge which gives rise to the electric field. It must further be determined in relation to the strength of the magnetic field, since it is the force of this field which is being opposed, and certainly a stronger restoring electric force will be required to balance a stronger compressing magnetic field.

As a consequence of these arguments, it is reasonable to define this equilibrium state as the state in which, throughout the range $r_{eo} \leq r < 0$, electrons and ions at a given radius are moving inward at the same velocity. This definition raises several questions. Perhaps foremost of these is the apparent inconsistency arising from the fact that

we have in previous paragraphs been talking of a balance of forces (i.e., accelerations) whereas now we base our definition on velocities. Remembering, however, that the magnetic field rises from zero at a finite rate while compressing the gas rather than being switched on instantaneously at a high level, we realize that a continuous equality of accelerations implies equality of velocities. It is reasonable to assume that this equality of acceleration will exist if the field rises slowly enough so that the electrons, which are the more mobile of the charged species present, can continually maintain the equilibrium state.

Secondly, we must be concerned with the fact that the magnetic field does continually increase in magnitude. This necessitates that the electrons continually shift with respect to the ions to the degree necessary to maintain the proper balancing electric field. This requires some modification of the description of the equilibrium state. We must incorporate in the equilibrium model a provision that there will be a velocity of electrons at a particular radius, relative to the ions at that radius, as needed to maintain equilibrium, but that this will be small compared with the inward velocity of the ions and electrons at that radius. As a consequence of this requirement, we can say that while in equilibrium, distributions of ions and electrons will be approximately the same (that is, that n_e will be only slightly greater than n_i throughout the ionized volume) during compression. Sequences of equilibrium and nonequilibrium distributions suggested in Figs. 4.5(a) and 4.5(b) bring out this point more clearly.

For equilibrium conditions, ion and electron accelerations at a given radius r, expressed by Eqs. 4.17 and 4.18, can be equated to one another. Since these constitute a set of simultaneous, independent

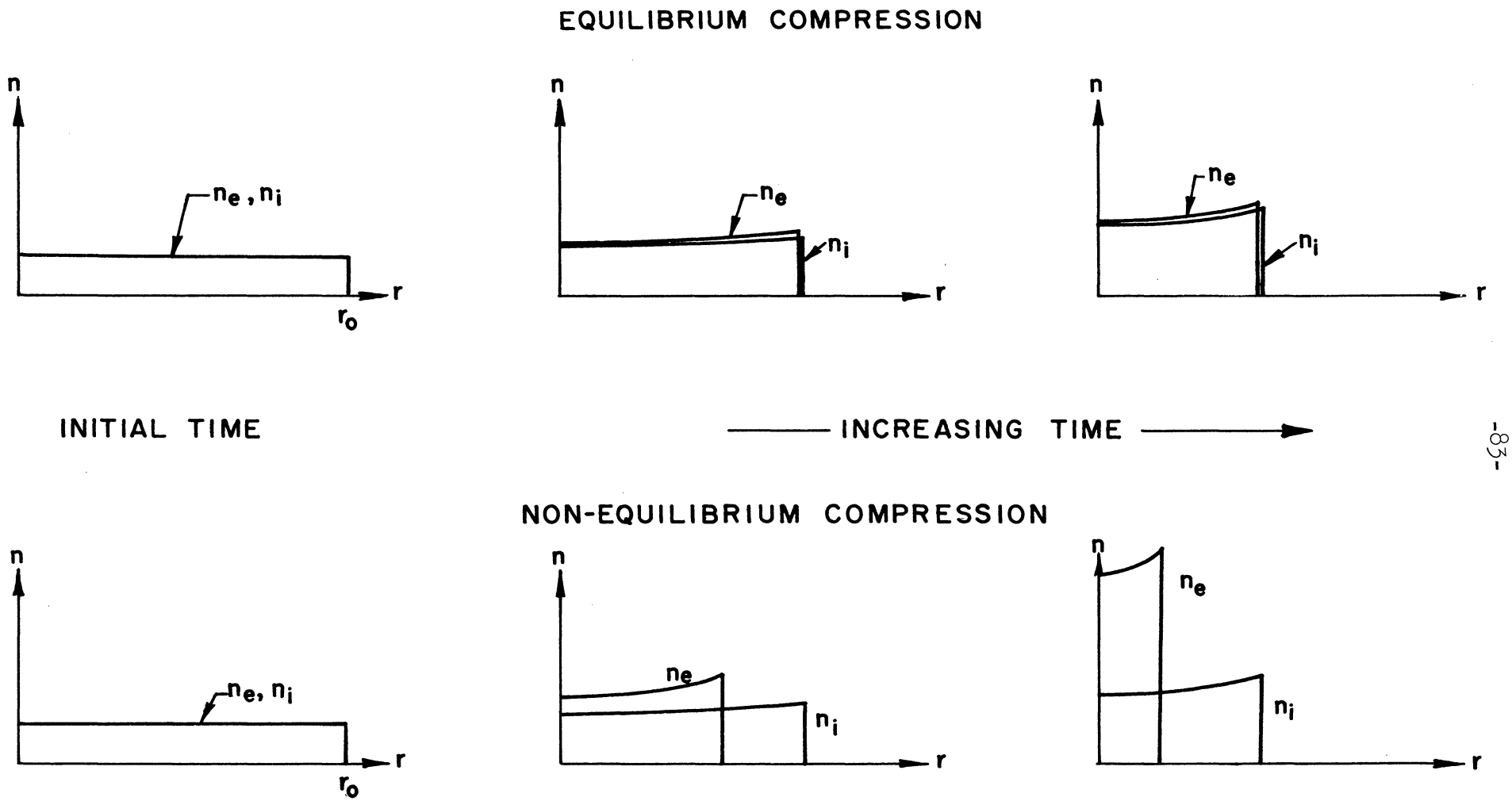

Fig. 4.5. Contrast Between Time Variations of Particle Density Distributions for Equilibrium and Non-equilibrium Compression.

differential equations, the electric field e_r may be eliminated between them, yielding:

$$\ddot{r} = \eta_e \eta_i r \left(\frac{\bar{b}}{2} \right) \left(b_z - \frac{\bar{b}}{2} \right) \quad . \tag{4.20}$$

Equations 4.17 and 4.18 are derived directly from the equations of motion after substituting for $\dot{\theta}$. If we were to follow the same procedure leading to Eq. 4.20 above, but retaining $\dot{\theta}$ explicitly, a better physical feeling of the acceleration may be gained from the resulting force equation, which is given below:

$$m_i \ddot{r} - m_e r(\dot{\theta}_e)^2 = - r b_z q_e \dot{\theta}_e \quad . \tag{4.21}$$

Note from this the following three items:

1. Inertial reaction is represented by the ions.
2. Centrifugal reaction is electron dominated.
3. The (Lorentz) force is transmitted from the field to the gas through the electrons.

As a consequence of the equilibrium condition representing equality of velocities as well as accelerations, we will later be able to integrate Eq. 4.20 and derive the position of a particular ion/electron group as a function of time. First, however, we wish to determine conditions under which an equilibrium situation will be likely and therefore under which such an integration will be valid.

Returning to Eqs. 4.17 and 4.18, we may solve for e_r rather than eliminate it, yielding:

$$e_r = + r \eta_e \left(\frac{\bar{b}}{2} \right) \left(b_z - \frac{\bar{b}}{2} \right) \quad . \tag{4.22}$$

The electric field e_r and the net space-charge density, $q_e(n_i - n_e)$, are related through Gauss' Law:

$$2\pi r\epsilon_o e_r = 2\pi q_e \int_o^r (n_i - n_e)rdr \quad ,$$

giving

$$e_r = \frac{q_e}{\epsilon_o r} \int_o^r (n_i - n_e)rdr \quad . \tag{4.23}$$

Combining Eqs. 4.22 and 4.23 yields the following integral equation for the particle distribution:

$$\int_o^r (n_i - n_e)rdr = -\frac{\epsilon_o}{m_e} r^2 \left(\frac{\bar{b}}{2}\right)\left(b_z - \frac{\bar{b}}{2}\right) \quad . \tag{4.24}$$

Differentiation of this gives an explicit expression for $(n_e - n_i)$:

$$(n_e - n_i) = \frac{\epsilon_o}{m_e}\left[\frac{1}{\rho}\frac{db_z}{d\rho}\int \rho b_z d\rho + b_z^2 + \frac{2}{\rho^4}\left(\int \rho b_z d\rho\right)^2 - \frac{2b_z}{\rho^2}\int \rho b_z d\rho\right] \quad . \tag{4.25}$$

Equation 4.25 may now be used to check the assumption that n_i and n_e are approximately the same. Specifically, if we start with n_o ions and n_o electrons, and if we find $(n_e - n_i)$ from Eq. 4.25 to be small compared with n_o, then the above derivation should be approximately correct.

Our initially uniform particle distribution yielded a Bessel Function dependence of b_z on ρ. For an interval of time before compression significantly distorts the particle distribution and before the magnetic field rises to a large enough value to separate the charges seriously, the particle densities will remain approximately independent of ρ, and the

field will be given by the Bessel Function. On using a Bessel Function for b_z in Eq. 4.25, the difference in densities $(n_e - n_i)$ becomes:

$$(n_e - n_i) = \frac{\epsilon_o b_o^2}{m_e} k_\alpha(\rho) \quad , \tag{4.26}$$

where

$$k_\alpha(\rho) \triangleq \frac{1}{J_o^2(j\alpha)} \left[J_o^2(j\alpha\rho) + \left(1 + \frac{2}{\alpha^2\rho^2}\right)\left(-jJ_1(j\alpha\rho)\right)^2 \right.$$

$$\left. - \frac{2}{\alpha\rho} J_o(j\alpha\rho)\left(-jJ_1(j\alpha\rho)\right) \right] \quad . \tag{4.27}$$

The function $k_\alpha(\rho)$ is a number whose maximum is at $\rho = 1$. The difference in charge densities $(n_e - n_i)$ will therefore be greatest at the inner edge of the ion sheath, and deviation from equilibrium will also be most pronounced at this position. If we now take as our criterion for equilibrium that the difference in densities $(n_e - n_i)$ at $\rho = 1$ be no more than 10 percent of the initial density n_o, then the following expression results for the maximum allowable external magnetic field:

$$b_o(\max) = \sqrt{\frac{0.1\, n_o m_e}{\epsilon_o k_\alpha(1)}} = 1.02 \times 10^{-10} \sqrt{\frac{n_o}{k_\alpha(1)}} \quad . \tag{4.28}$$

Table 4.1 indicates the field strengths $b_o(\max)$ for various initial particle densities.

Table 4.1. Maximum External Magnetic Field Consistent with Strong Ion-Electron Binding

n (particles/m^3)	10^{17}	10^{18}	10^{19}	10^{20}
b_o(max)(gauss)	448	1230	2880	7800

This value of maximum allowable magnetic field will be reasonable throughout the ionized volume for $n_o \leq 10^{17}/\text{meter}^3$, since $k_\alpha(\rho)$ is nearly a constant independent of ρ for these low densities. For higher densities (either because the initial density is higher or because the compression has raised the actual particle density above $10^{17}/m^3$), this maximum field will be conservative for locations inside r_{eo} due to the direct dependence of $k_\alpha(\rho)$ on ρ. For instance at $n_o = 10^{19}$, $k_\alpha(\rho)$ has fallen to about one-quarter of its peripheral value at $\rho \cong 0.5$, allowing the external field to be about two times as large as indicated in Table 4.1 before the equilibrium assumption at $\rho = 0.5$ is invalid.

4.4 Compression of the Ionized Column—General Survey of Phenomena to be Expected

From the discussion in the previous sections of this chapter, we can develop a qualitative picture of the compression process. In the model being studied, the ions and electrons will start at time zero in equal numbers uniformly distributed within a long coil, and these particles will begin to plunge inward as current is brought up in the coil. An ion sheath will immediately form, but its thickness will be quite small while the magnetic field is still low; current and field within the ionized region will have approximately Bessel Function dependence on radius. Knowing from earlier discussions the rapidity with which electrons move, we can assume during this early period at least that ions and electrons will continually stay in equilibrium with one another. As time progresses, however, two effects arise to disturb this situation:

1. If conditions are such that the total acceleration is linear with ρ, then the particle distribution will remain uniform as compression occurs. If, however, the force and therefore

acceleration are other than linear functions of radius, the initially uniform particle distribution will become a function of radius, thereby changing the current and magnetic field patterns.

2. As the magnetic field increases in strength beyond approximately the value shown in Table 4.1, the electrons will become increasingly separated from the ions, thereby intensifying the distortion of the particle, field, and current distributions.

The involvement of the complications outlined above makes integration of the radial equation of motion in general quite difficult. Two limiting cases can however be easily solved, bracketing the action of intermediate conditions. The first of these is at sufficiently low particle densities so that the magnetic field of the gas current is negligible and at sufficiently low values of external magnetic field so that equilibrium is maintained. The other is at sufficiently high particle densities so that the magnetic field is excluded entirely from the interior of the ionized column. These cases will now be considered.

4.5 Equilibrium Magnetic Compression Under Low-Particle Density Conditions

Consider the particle density to be so low that the magnetic field throughout the ionized region is equal to the external field b_o. Consider also b_o to be low enough so that the ion and electron components remain tightly bound together. Figure 4.3 indicates n must be 10^{17} or less, and, from Table 4.1, this limits us to b_o less than about 448 gauss. The radial acceleration expression, Eq. 4.20, in this case becomes

$$\ddot{r} - \frac{1}{4}\eta_e\eta_i r b_o^2 = 0 \quad . \tag{4.29}$$

The reader will note that this equation is identical with Eq. 3.24 for the case, $k_e = 0$; this is consistent with our assumption that the magnetic field is uniform and equal to b_o throughout the ionized region. Making the following assumption and definition,

$$1. \quad b_o = \mu i_o' \omega t \quad ,$$

where i_o' is the maximum value of the coil current, and

$$2. \quad \tau \triangleq \left[-\frac{1}{4} \eta_e \eta_i \mu_o^2 (i_o')^2 \omega^2 \right]^{\frac{1}{4}} t \quad ,$$

converts Eq. 4.29 to

$$\ddot{\rho} + \rho \tau^2 = 0 \quad . \tag{4.30}$$

Solution to Eq. 4.30 for zero initial velocity is presented in Fig. 4.6; the method of series solution was used to obtain this curve.

Two specific examples using the solution in Fig. 4.6 are worked out in Fig. 4.7. Note that the valid portions of these curves, indicated by solid lines, extend only out to about 1.1×10^{-7} seconds, beyond which time the field becomes strong enough to cause serious charge separation.

4.6 Magnetic Compression Under High Particle Density Conditions

4.6.1 Definition of Model. When the particle density is sufficiently high, the current carried by the gas particles flows as a thin sheet current on the surface of the gas, and the magnetic field does not penetrate beyond this skin. This has been demonstrated in Section 4.2, especially in Fig. 4.4(b); for the specific geometry and field conditions studied there (which are approximately the conditions under which the experiments discussed later in this report were carried out), the particle density necessary to achieve a true skin current is above approximately

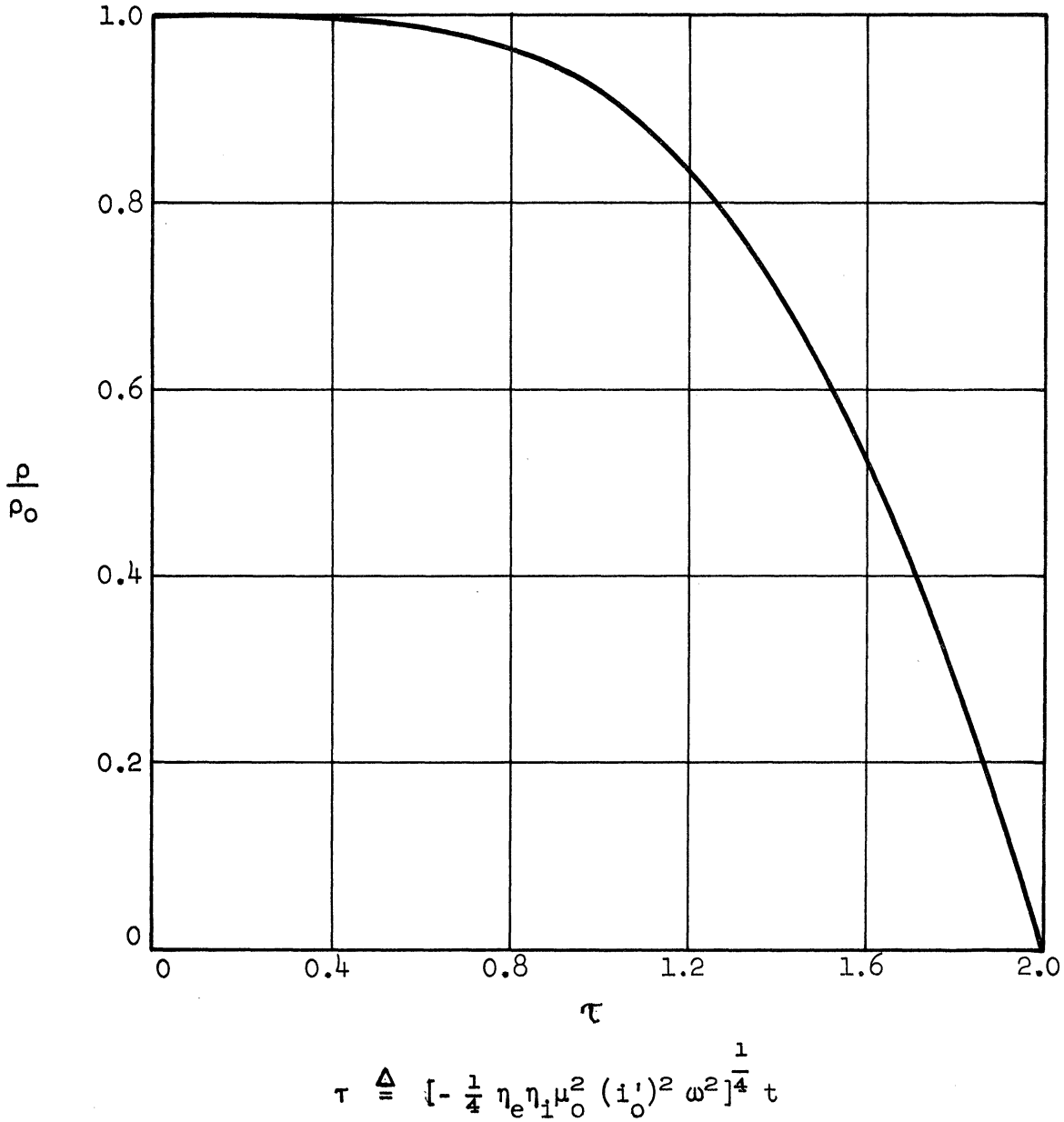

Fig. 4.6. Solution to Eq. 4.30, $d^2\rho/d\tau^2 + \rho\tau^2 = 0$ ($\rho = \rho_o$, $d\rho/d\tau = 0$ at $\tau = 0$).

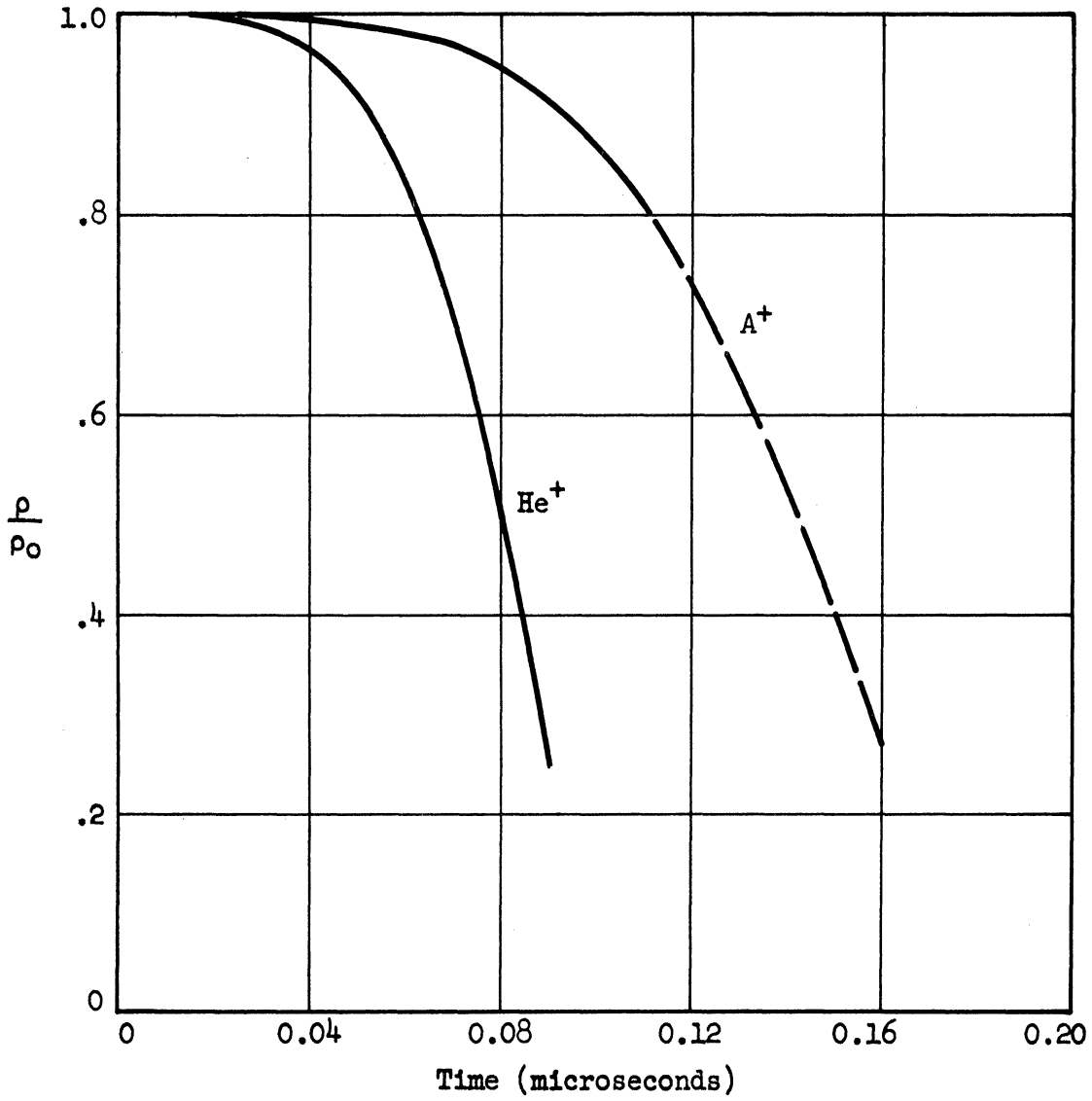

Fig. 4.7. Radial Position of Particle as a Function of Time; Singly Ionized Helium and Argon; Low Density Beam ($i'_o = 10^6$ amp/meter, $\omega = 3.14 \times 10^5$ radians/second, $n \cong 10^{17}$ ions/meter^3).

10^{20}/meter^3. Motion of these higher-density ionized gases is more easily studied by the "snowplow"[62,63] and "magnetic pressure"[64] concepts described below than by consideration of individual particle paths as heretofore employed.

Let us continue to study the long solenoid geometry shown in Fig. 4.1. The Lorentz force of the external magnetic field (b_z) acting on the surface gas current (i_θ) will cause an inwardly directed radial force on this current. If, as this current sheet moves inward, it sweeps up and carries along with it all the ionized particles it encounters, then the situation will be much like a snowplow carrying before it the snow it has gathered.

Such will be the case under the "beam" conditions defined in the introduction to this chapter; the gas is assumed to be fully ionized but initially to possess zero kinetic energy, and each overtaken particle will join the current sheet. It will also apply to a gas containing a small random velocity component (low but finite temperature) since ionized particles which attempt to escape through the current sheet are reflected back into the gas by the external magnetic field, much as they would be by a material piston compressing the gas[62]; further consideration will be given to temperature effects in the next section. It would also be reasonable to apply this "snowplow" model to a gas which internally is unionized or only weakly ionized, so long as the electrons comprising the current sheet ionize all the neutral gas particles which they encounter during the compression process.

It is interesting to note that this "snowplow" concept applied to our fully ionized model in effect brings us back to the sheet beam situation indicated in Fig. 3.3(c). This arises since, as the current sheet

sweeps inward, it gathers electrons as part of the current sheet and the ions swept up will be carried along in the positive ion sheath just outside this current layer.

The magnetic pressure concept arises from the knowledge that the energy density resident in a magnetic field B is given by $B^2/2\mu$. If now a gradient of this quantity exists across a surface of thickness Δr, a pressure p will be exerted normal to this surface, given by

$$p = \frac{\partial}{\partial r}\left(\frac{B^2}{2\mu}\right)\Delta r \quad .$$

A gradient in magnetic energy density in our case corresponds to the presence of a current flowing in the surface; this result can immediately be related back to the Lorentz force expression to give the pressure term.

The model which is to be analyzed can now be summarized as follows:

1. The electron current flows in a thin sheet on the surface of the gas; its strength i'_g (amperes/meter) will be identical with the coil current i'_c so there will be no net magnetic flux within the gas.
2. The radial force on the current sheet will be given by the difference of $B^2/2\mu$ across the current sheet; in light of statement 1 above, this becomes just $b_z^2/2\mu$, since internal to the current, there is no field.
3. As the current sheet moves, it gathers up all particles it encounters.

The procedure to be used in solving the problem presented by this model has been used extensively to study the linear pinch[62,63], in which a cylindrical plasma column carrying current parallel to its own axis is radially compressed by its own (azimuthal) magnetic field. The analysis

of our situation, in which a cylindrical plasma column is radially compressed by an externally applied magnetic field which is parallel with the plasma axis, has also been considered using a "snowplow" model[65]. In the latter reference, however, the problem was simplified by assuming (a) that the magnetic field is initiated instantaneously at some level and held there, and (b) that all the mass of the compressed gas is originally in the skin region rather than being swept up as this boundary compresses inward. In the analysis which follows, the time dependence of both the field and accelerated mass will be taken into account. In addition, the centrifugal effect of the rotating particles, an effect which has apparently been neglected heretofore, will be considered; it is shown, however, that this may indeed be neglected.

Comparison between the results obtained in this derivation and experimental measurements will be made in a later chapter.

4.6.2 Derivation and Solution of the Differential Equation. In order to derive the applicable radial equation of motion, we must return to the basic Newtonian formulation for force F, per unit length.

$$\vec{F} = \frac{d}{dt}\left(M_s \vec{v}_s\right) \quad ; \tag{4.31}$$

this vector equation will lead to both the inertial and the centrifugal terms in the radial component equation. Here M_s is the total mass per unit length being carried inward by the current sheet (a variable with time) and V_s is the velocity of this sheet. Insertion of the magnetic energy density expression for the force, and expansion of the right-hand side converts Eq. 4.31 to the following form:

$$-2\pi r \frac{b_z^2}{2\mu_o} = \frac{d}{dt}\left(m_i n'_s \frac{dr}{dt}\right) - m_e n'_s r \left(\frac{d\theta_e}{dt}\right)^2 \quad , \tag{4.32}$$

where n_s' ≡ number of particles (ions or electrons) per meter of axial length in the sheath. Note that as in Eq. 4.21, only the electron angular momentum is retained, since it is larger than the ion contribution by a ratio of m_i/m_e.

The magnetic field strength at the surface of the gas is given by

$$b_z = \mu_o i_c' \quad , \tag{4.33}$$

where i_c' ≡ coil current (amperes/meter). The number of accelerated particles n_s' may be calculated, thus

$$n_s' = n\pi(r_o^2 - r^2) \quad , \tag{4.34}$$

where n ≡ initial ion density, particles/m^3,

r ≡ outer radius of gas, meters,

r_o ≡ initial outer radius of gas, meters.

Finally, $d\theta_e/dt$ may be evaluated by knowing that the current carried by the electrons and by the coil must be identical, which gives

$$\frac{d\theta_e}{dt} = \frac{2\pi i_c'}{n_s' q_e} \quad . \tag{4.35}$$

Insertion of Eqs. 4.33 through 4.35 into Eq. 4.32 yields

$$-\pi\mu_o r(i_c')^2 = \frac{d}{dt}\left(m_i n\pi(r_o^2 - r^2)\frac{dr}{dt}\right) - \frac{4\pi^2 m_e}{n_s' q_e^2}(i_c')^2 r \quad . \tag{4.36}$$

We will assume that the compression of the gas takes place in a time short compared with the period of the coil current, so the following approximation is valid:

$$i_c' \cong i_o' \omega t \quad . \qquad \text{(amperes/meter)} \tag{4.37}$$

Equation 4.37 converts Eq. 4.36 to its final dimensional form:

$$\frac{(i_o')^2\omega^2\mu_o}{m_i n}\left(\frac{4m_e}{\mu_o n(r_o^2 - r^2)q_e^2} - 1\right) rt^2 = \frac{d}{dt}\left((r_o^2 - r^2)\frac{dr}{dt}\right) . \quad (4.38)$$

This may be put in dimensionless form by converting to the following dimensionless variables:

$$\rho \triangleq \frac{r}{r_o} , \quad (4.39)$$

$$\tau \triangleq \left(\frac{(i_o')^2\omega^2\mu_o}{m_i n r_o^2}\right)^{\frac{1}{4}} . \quad (4.40)$$

giving

$$\left(\frac{4m_e}{\mu_o n r_o^2 q_e^2(1-\rho^2)} - 1\right)\rho\tau^2 = \frac{d}{d\tau}\left((1 - \rho^2)\frac{d\rho}{d\tau}\right) . \quad (4.41)$$

If we use m.k.s. values for μ_o, m_e and q_e and let $r_o = 5 \times 10^{-2}$ meters, this reduces to

$$\left(\frac{4.52 \times 10^{16}}{n(1 - \rho^2)} - 1\right)\rho\tau^2 = \frac{d}{d\tau}\left((1 - \rho^2)\frac{d\rho}{d\tau}\right) . \quad (4.42)$$

Since n must be above approximately $10^{20}/\text{meters}^3$ in order to make the skin current assumption valid, we see that the centrifugal term (the first term in the left-side bracket) may be neglected. This gives the final equation which must be solved in order to predict the radial motion of the gas.

$$\frac{d}{d\tau}\left((1 - \rho^2)\frac{d\rho}{d\tau}\right) + \rho\tau^2 = 0 . \quad (4.43)$$

Equation 4.43 was numerically integrated (using the University of Michigan IBM 704 computer) for the initial conditions $\rho = 1.0$ and

$d\rho/d\tau = 0$ at $\tau = 0$. The results are presented in Fig. 4.8. In order to make the comparison with the low density situation (Figs. 4.6 and 4.7) more definite, the solutions to Eq. 4.43 are shown in Fig. 4.9 for He^+ and A^+ at $n = 10^{20}/meter^3$ and $10^{22}/meter^3$ with other parameters being identical to Fig. 4.7.

Equation 4.43 predicts that the radius ρ of the gas will go to zero at $\tau = 1.93$. Actually, competing processes will arise which will slow down the motion of the gas/field interface so that a finite minimum radius will result. Both kinetic pressure of the gas and pressure of any magnetic field which "leaked" into the gas during initial ionization will rise as the gas compresses. Eventually, a point will be reached at which the internal pressure exceeds the external pressure and oscillation of the gas column radius will result. This "bouncing" has been observed experimentally and attributed in the literature to both of the causes outlined above[65,66,67]. Further discussion of this aspect appears in the next section.

4.6.3 Slow, Adiabatic Compression—Temperature. Since the model proposed in Section 4.6.1 assumes no initial kinetic motion (zero initial temperature), particles interior to the imploding boundary sheet would remain at rest, and particles overtaken by this sheet would be swept up and bound to the sheet; these facts indicate that the "snowplow" approach is the proper one to use for this initially "cold", beam model. If, however, the ionized gas initially contains a finite, random velocity distribution, two items will possibly invalidate the simple analysis of Section 4.6.2.

1. The gas will initially exhibit a pressure, necessitating that the compressing field build up to a certain minimum level before the gas will begin to compress.

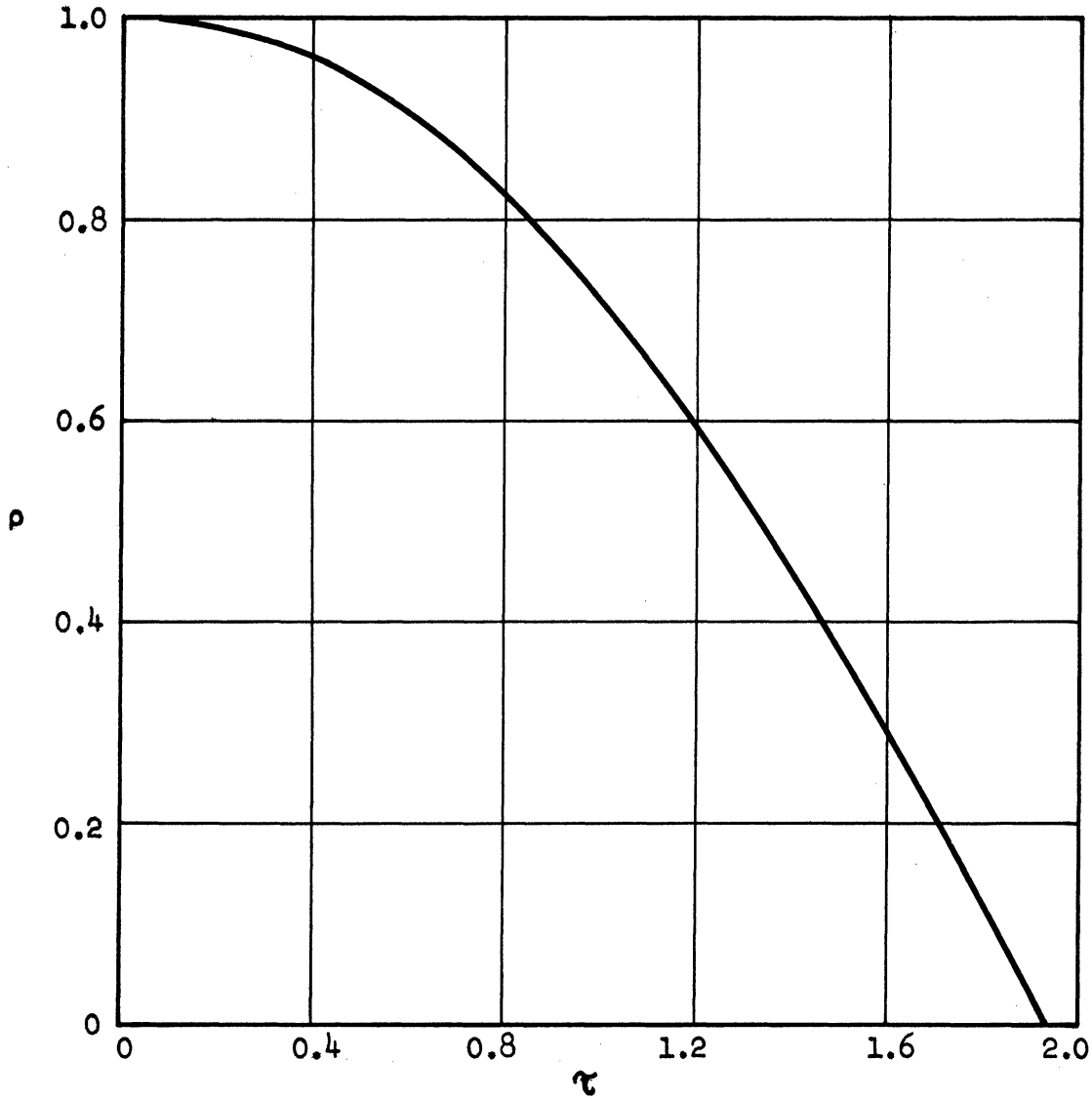

$$\tau \triangleq \left(\frac{(i_o')^2 \omega^2 \mu_o}{m_i n r_o^2} \right)^{\frac{1}{4}} t$$

Fig. 4.8. Solution to Eq. 4.43. $d/d\tau\,[(1 - \rho^2)\, d\rho/d\tau] + \rho\tau^2 = 0$ ($\rho = 1.0$, $d\rho/d\tau = 0$ at $\tau = 0$).

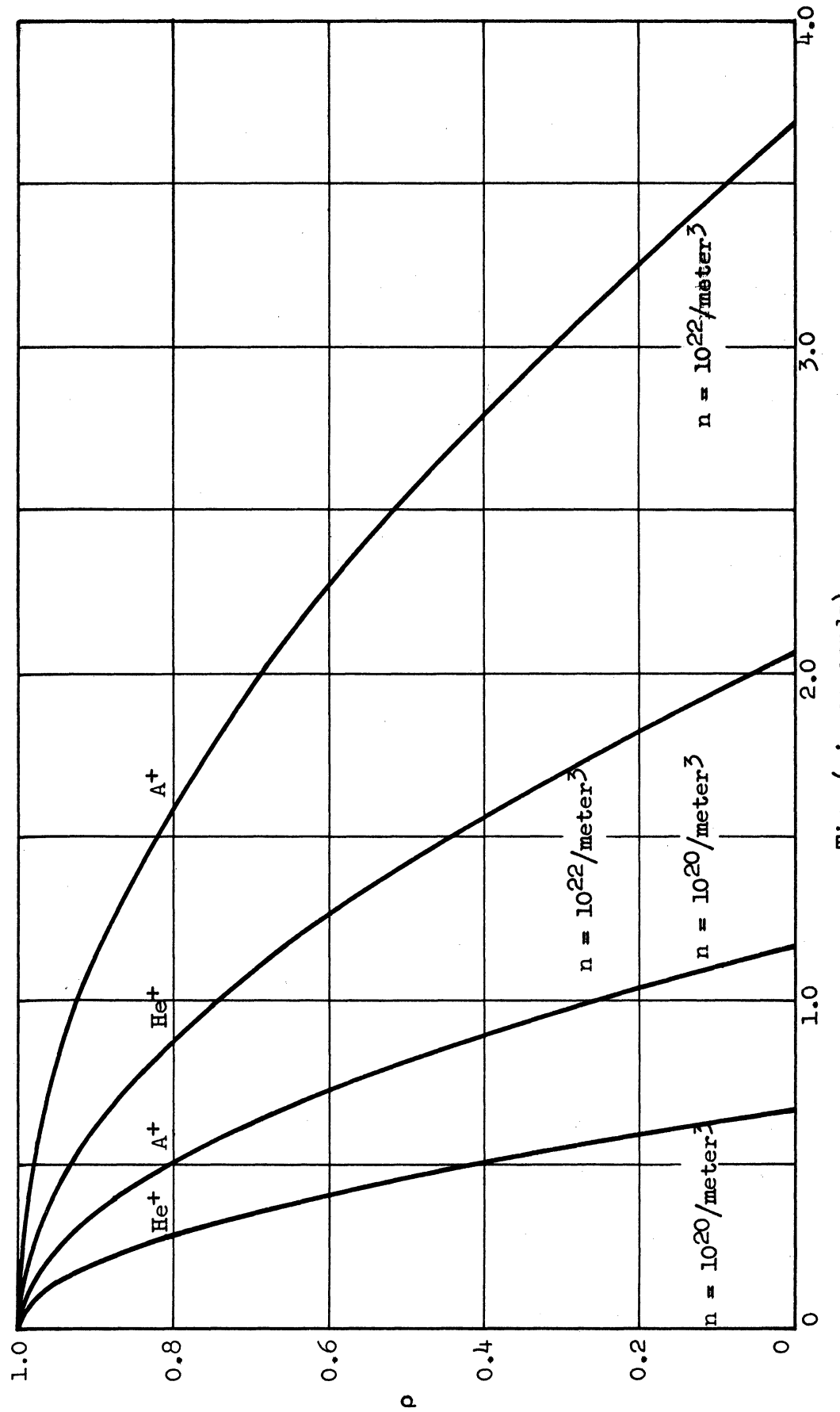

Fig. 4.9. Sheath Radial Position as a Function of Time—Skin Current Conditions ($i_o' = 10^6$ ampere/meter, $\omega = 3.14 \times 10^5$ radian/second).

2. The gas will support sound waves by which energy can be distributed throughout the interior of the plasma.

If the rate of compression is slow compared with the rate at which energy is distributed and randomized throughout the plasma column being compressed, but if it is sufficiently fast and the magnetic field acts as a good enough insulator so that there is no energy loss from the column, then the compression can be analyzed as a quasi-static, adiabatic process. Since this approach has been extensively applied by other authors to the inductive (b_z) compression process[63,68,69], the analysis need not be elaborated here. The basic derivation will, however, be given to confirm the validity of the results. These results will then later in this report be applied to the particular experiments performed during the course of this investigation.

(Note that the term "plasma" is now appropriate to describe the ionized gas, since the random energy content will be comparable with the directed energy.)

During a quasi-static, adiabatic process, the quantity pV^k remains a constant, where p, V, and k are respectively the gas pressure, temperature and ratio of specific heats. Our first relation is then,

$$pV^k = p_o V_o^k \quad , \tag{4.44}$$

where p_o and V_o are respectively the initial pressure and volume. Since in this slow process the external (magnetic) and internal (kinetic) pressures remain in balance, the pressure may be given as

$$p(t) = \frac{b_z(t)}{2\mu_o} \quad . \tag{4.45}$$

Combining Eqs. 4.44 and 4.45, we arrive at an expression for the radius at any instant in terms of the instantaneous field strength and initial parameters:

$$r(t) = r_o \left(\frac{2\mu_o p_o}{b_z^2(t)} \right)^{\frac{1}{2k}} . \qquad (4.46)$$

The internal pressure is known as a function of temperature T,

$$p = nk_b T , \qquad (4.47)$$

where k_b is the Boltzmann constant, and n is the particle density, so the temperature at each instant can also be written (for times greater than necessary to start compression) as a function of the instantaneous external field, thus

$$T = T_o \left(\frac{b_z^2}{2\mu_o} \right)^{\frac{k-1}{k}} . \qquad (4.48)$$

The minimum plasma radius and maximum temperature will be reached at the instant of maximum magnetic field.

Consider now the case where the compression is a little too rapid to allow equilibrium to be continuously maintained. The inertia of the particles will carry them beyond the equilibrium radius at maximum field leading to oscillation of the plasma boundary about the equilibrium point, as noted at the end of the previous section. (See also references 65, 66, and 67.)

Any magnetic field which, being left over from previous cycles or having diffused through the boundary current sheet, is internal to the plasma boundary must be taken into account in the above derivation. This

internal field will add to the kinetic pressure of the gas, resulting in a larger radius and lower temperature than given by Eqs. 4.46 and 4.48.

4.7 Summary

It will be helpful at this point to review the essential points brought out by Chapter IV as a guide to what might be expected from experiments described later in this report.

At low particle densities, on the order of 10^{17} per cubic meter, the magnetic field might be expected to penetrate readily throughout the ionized gas, very little gas current will be detectable, and compression of the column will be determined by the solution to Eq. 4.30 shown in Fig. 4.6. It will be difficult to achieve this condition experimentally due to the problem of ionizing such a low-density gas.

As particle density is increased, the gas current will increase and the magnetic field strength within the plasma will diminish; gas current and magnetic field will be Bessel Functions of the radius if the charge density is uniform and will deviate from this radial dependency in proportion to the nonuniformity of the charge distribution.

For sufficiently high particle densities, the gas current will take the form of a sheet current flowing on the surface of the plasma column, and the magnetic field will be kept out of the plasma. Depending on the relative values of compression rate and thermalization rate, the compression will follow some course intermediate between the "snowplow" and adiabatic processes discussed in Sections 4.6.2 and 4.6.3.

Charge separation will give rise to a radial electric field within the plasma. The intensity and geometric extent of this field will depend both on the charge density and on the strength of the external magnetic field.

CHAPTER V. AXIAL MOTION OF THE PLASMA—SHOCK WAVES

5.1 Introduction

Before entering upon a description of the experimental phases of this project, we must make an effort to remove the two-dimensional restriction of the past two chapters and say something about the axial motion to be expected from the pulsed crossed-field accelerator. A simplified model involving only the field components b_r and e_θ would not be at all realistic, since the b_z field necessary to balance out the centrifugal motion of the particles would be missing; furthermore, much energy is added to the gas by the radial (b_z) compression. A possible approach is to ascribe a specific configuration to the plasma, and carry out an energy analysis on the inductively coupled coil and plasma circuits. Such an analysis has been used in studying electromagnetic acceleration of solid conductors[70] and has also been applied to ionized gases[31], but the significance of the latter results is limited by the indefinite and constantly changing space characteristics of the plasma in a real accelerator.

In order, therefore, to get a meaningful description of the action of the ionized gas as it moves in the z-direction, we will again invoke the concept of magnetic pressure, introduced in Chapter IV, Section 4.4. A satisfactory description of the plasma motion will also necessitate investigation of shock waves traveling ahead of the ionized gas region.

5.2 Description of System

Let us adopt the following simplified picture of the acceleration process, explained with reference to Fig. 5.1.

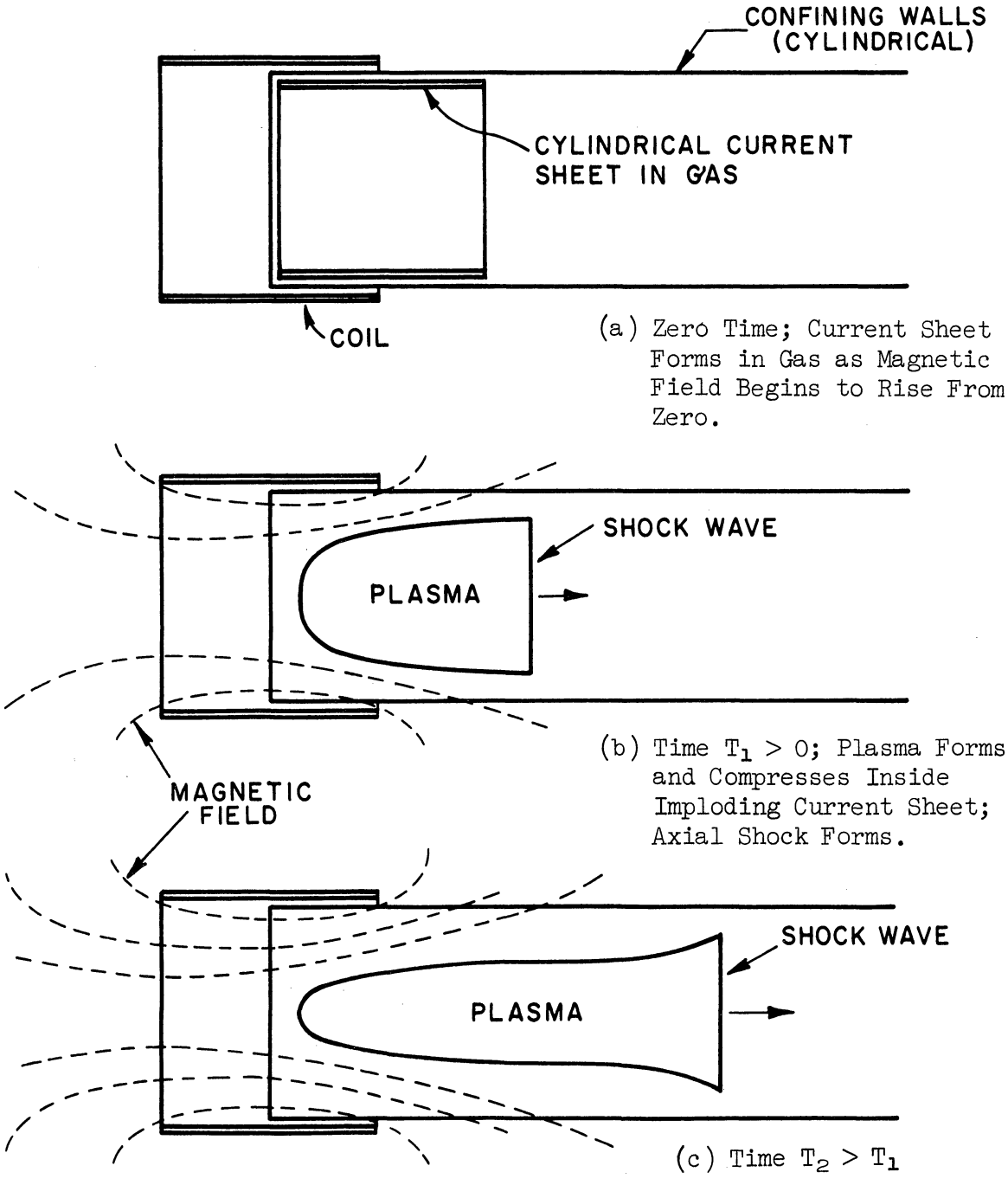

Fig. 5.1. Representation of Plasma Motion in the Induction Accelerator.

1. At time t = 0, when the induced electric field is maximum and the magnetic field is zero, a current begins to flow on the surface of the partially ionized gas, as shown in Fig. 5.1(a).
2. As the coil current rises, the current flowing on the surface of the gas will be forced radially inward due to the increasing strength of the external magnetic field; since the magnitude of this field decreases with axial distance away from the center of the coil, more rapid compression of the gas will occur at positions nearer the coil center, forming in effect a diverging "magnetic nozzle", as shown in Figs. 5.1(b) and 5.1(c). The gas will be heated by the radial magnetic compression process, as explained in Chapter IV.
3. This hot compressed gas will expand outward through the open end of the "magnetic nozzle". This flow of hot gas is impeded, however, by the cold, stationary gas "downstream" from the coil region, and the hot gas must therefore compress ahead of it the colder gas. If the velocity with which the interface between the two gas regions travels is above the velocity of sound in the cold gas, conditions are proper for the formation of an abrupt discontinuity, termed a shock wave[72]. The necessary conditions and characteristics of this shock will be briefly discussed in this chapter. This will be particularly for the purpose of developing background upon which interpretation can be made in a later chapter of experiments performed with an induction accelerator.
4. The fact that the gas is being compressed by a magnetic field having a <u>diverging</u> geometry should result in more energy being

transferred to the z-motion than would result merely from expansion through a stationary nozzle. That is, the radial component of magnetic field as well as the axial component will be working on the gas.

Many of the characteristics of the accelerating plasma "bunch", bounded behind and on its sides by the magnetic-field/current-sheet interface and ahead by the moving shock wave, may be inferred from observation of its boundary regions. From the radial motion and sharpness of the current sheet, we are able from Chapter IV to deduce information about charged particle density and heating of the gas (i.e., energy transferred to the gas by the radial compression). We will now turn to the characteristics of the forward-moving shock wave; observation of this will yield axial motion properties of the gas. This will complete the theoretical treatment of the inductive plasma accelerator, since we will be prepared to handle the complete, gross plasma motion (i.e., both the radial and axial motions) observed in the experimental device.

5.3 Necessary Conditions

In order that the processes described in Section 5.2 be valid, two conditions must be fulfilled:

1. The plasma charge density (or conductivity) must be sufficiently high so that skin currents form, i.e., so that the plasma does not diffuse through the driving magnetic field.
2. The thickness of the shock wave must be small in comparison with the dimensions of the system in order that the shock wave concept be meaningful.

The plasma conductivity requirement is identical with the conditions upon which Section 4.4 was based. We saw there that if the gas consists solely of electrons and singly ionized ions, the particle density needed to be above about 10^{20}/meter^3 for a true skin current to form. If instead we are considering a higher density gas in which the energy of the gas is in random or thermal form, and ionization is a function of temperature, then the skin current criterion would be determined by the density and temperature of the gas[71]. (In our experimental observations, the assumption that the magnetic field is rejected from the gas is good except at the lower density end of the operating range.)

We will now consider the shock wave criterion. A shock wave is a region in a flowing fluid through which the properties of the fluid change irreversibly (non-isentropically) and, in general, rather suddenly. The detailed mechanisms which occur in the transition region are difficult to analyze, but if this region can be taken as a pure discontinuity, then the properties on either side of the wave can be derived from consideration of the mass, momentum, and energy conservation equations. In order to apply these equations, however, it is first necessary to assure ourselves that the transition region or shock thickness is indeed small compared with the dimensions of the system.

In an un-ionized, compressible medium, the thickness of a shock wave will be on the order of the mean free path behind the shock[72]. In order to use the concept of a shock wave, this characteristic length must be small compared with the dimensions of the system (e.g., the diameter of the acceleration region in the pulsed, crossed field device). The mean free path ("Maxwell's mean free path") in cold, un-ionized gases is given by[84]:

$$\lambda_n = \frac{1}{4\sqrt{2}\,\pi n d^2} \quad \text{(meters)} \quad , \qquad (5.1)$$

where $n \equiv$ particle density, particles/m^3 ,

$d \equiv$ gas particle diameter, meters.

Since d is on the order of 10^{-10} meters, n must be above about 3×10^{21}/meter^3 in order that the mean free path be under a centimeter.

When the gas is ionized, as would be the plasma being accelerated behind the shock front in Fig. 5.1, phenomena occur which invalidate the use of Eq. 5.1. In the first place, the long range coulomb forces between the charged particles are much more effective in exchanging energy among particles than are close-approach collisions. One must then redefine the mean free path to describe the distance through which a typical particle will travel during the time necessary for the gas to "relax" to an equilibrium energy distribution from some nonequilibrium state. Using Spitzer's[73] expression for the mean relaxation time of a charged particle gas, and knowing that the root mean square particle velocity is given[74] by $(3kT/m)^{1/2}$, the mean free path in a gas made up of singly charged particles becomes

$$\lambda_1 = 1.80 \times 10^5 \frac{T^2}{n\,\ell n\,\Lambda} \quad \text{(cm)} \quad , \qquad (5.2)$$

where $T \equiv$ temperature, °K,

$n \equiv$ particle density, particles/cm^3 ,

$\ell n\,\Lambda \equiv$ function of n and T tabulated by Spitzer.

Note that Eq. 5.2 is independent of the mass and size of the particle. The electrons and ions will in general not reach the same equilibrium temperature[75,76], implying that each will have a different mean free

path. One must then be concerned with another quantity giving the mean length of particle travel during the time for equilibration of the ion and electron temperatures, given approximately by[77]

$$\lambda_2 = \sqrt{\frac{m_{ion}}{m_{elect}}} \quad \lambda_1(\bar{T}) \quad , \tag{5.3}$$

where $m \equiv$ particle mass (ion or electron) ,

$\lambda_1(\bar{T}) \equiv$ mean free path from Eq. 5.2 for temperature $\bar{T}$,

$\bar{T} \equiv$ ultimate temperature of the ion/electron mixture.

The mean free paths λ_1 and λ_2 are based on the existence of a Maxwellian (equilibrium) distribution, and they indicate the distance through which particles having the root mean square velocity travel during the time taken for a particle having the r.m.s. velocity to be deflected through 90°. These therefore best describe relaxation back to equilibrium from some near-equilibrium condition, and they will give only a very approximate measure of shock thickness, where the transition begins from a state (ahead of the shock) far from the final equilibrium condition. A further reason for caution in applying these expressions (λ_1 and λ_2) is given in the next paragraph.

As a shock wave propagates through an ionized gas in the presence of a transverse magnetic field, experiments indicate that the thickness of a shock wave may be much less than the mean free path[78,80]. Analysis of these shocks indicates that the transition region is determined by charge separation effects, and that its thickness will be on the order of the ion Larmor radius[76,78]. This will be about 0.5 cm for He at 1000 gauss and 3×10^4 °K; these figures are representative of conditions at the shock in the experimental accelerator.

5.4 Shock Wave Characteristics

We will assume that a true shock discontinuity is traveling down the acceleration chamber, as shown in Fig. 5.1; the validity of this assumption in any experimental situation may be checked by the theoretical considerations presented in Section 5.3. If the conditions ahead of the shock are known, then the properties behind the shock can be specified in terms of the shock velocity. For any given set of circumstances, the criterion for validity of the shock wave description may then be checked from Eq. 5.3.

Let us consider first a stationary shock wave, as shown in Fig. 5.2(a), with gas entering from the left at supersonic velocity V_x and leaving subsonically to the right. For an ideal, monatomic gas (ratio of specific heats k equal to 1.67), conservation equations yield the following results for this model[72].

$$\frac{p_y}{p_x} = 1.25\, M_x^2 - 0.251 \quad , \tag{5.4}$$

$$\frac{T_y}{T_x} = \frac{(1 + 0.34\, M_x^2)(4.99\, M_x^2 - 1)}{5.32\, M_x^2} \tag{5.5}$$

$$M_y^2 = \frac{M_x^2 + 2.99}{4.99\, M_x^2 - 1} \quad , \tag{5.6}$$

where $p,T \equiv$ pressure and temperature,

$M \equiv$ Mach number; $M \triangleq V/c$,

$c \equiv$ sonic velocity; $c = \sqrt{kRT/M.W.}$,

$R \equiv$ gas constant; 8.317 joule/°K-mole ,

$M.W. \equiv$ molecular weight; kg/mole.

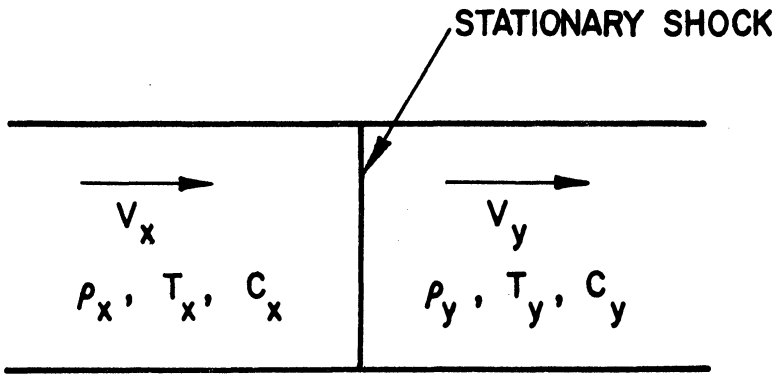

Fig. 5.2. Model for Shock Wave Analysis.

(a) Cold, Supersonic Gas Passes From the Left Through a Stationary Shock and Becomes Hotter and Subsonic.

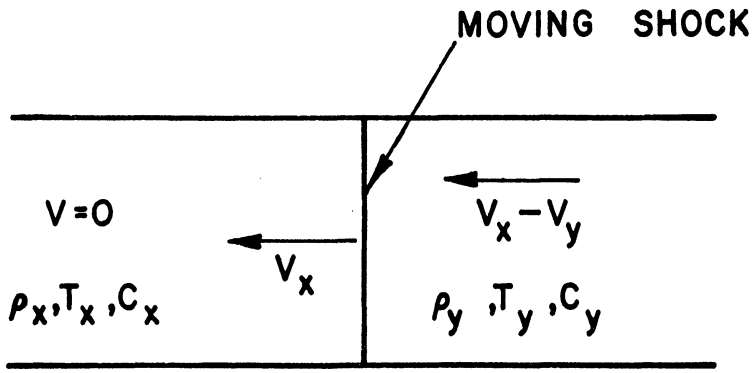

(b) Hot Gas, Flowing From Right to Left Drives Ahead of It Moving Shock Which Travels Into Cold, Stationary Gas.

Experimentally, we will observe a moving shock. Equations 5.4, 5.5, and 5.6 can be applied to the moving shock model shown in Fig. 5.2(b) by letting the shock velocity be V_x. The upstream flow velocity will then be $V_x - V_y$, while the velocity ahead of the shock will be zero. Mach number of the moving shock will be calculated using the speed of sound of the (cold) gas ahead of the shock. In the case of a strong moving shock, $M_x \gg 1$, we find from Eqs. 5.4, 5.5, and 5.6 the following results:

$$p_y = 1.25\, M_x^2\, p_x \quad , \tag{5.7}$$

$$T_y = 0.319\, M_x^2\, T_x \quad , \tag{5.8}$$

$$M_y = 0.447 \quad , \tag{5.9}$$

$$\text{gas flow velocity } V_x - V_y = 0.748\, V_x \quad . \tag{5.10}$$

If the kinetic energy per particle in directed motion behind the moving shock and the mean kinetic energy per particle in random (thermal) motion behind the moving shock are calculated using Eqs. 5.8 and 5.10, then one finds that behind the shock the energies in directed and thermal motion are divided equally. Using the relation between pressure and temperature, $p = nk_b T$, allows us further to say that the particle density behind a strong shock will be one-quarter of its value ahead of the shock.

The expressions which have been presented in this and the previous section will be used for evaluation of the experimental data discussed in Chapter VII. The reader is referred specifically to Table 7.2 for these empirical results. In addition, Chapter V has given a qualitative

description of the action in the induction accelerator, based on the earlier theoretical treatment and the experimental evidence to be presented in Chapter VII.

CHAPTER VI. EXPERIMENTAL APPARATUS

6.1 Introduction

An inductive, crossed-field accelerator of the type shown in Fig. 1.2 has been studied experimentally. The experimental apparatus will be discussed in this chapter and results of the experiments performed will be presented in Chapter VII.

As has been pointed out in Section 1.3, the present study has been oriented around the specific geometry shown in Fig. 1.2. With the cylindrical coil design (single turn, 10 cm long by 10 cm diameter) as a starting point, we will now first describe the electrical system used to supply the desired current to the coil and then discuss the vacuum system in which ionization and acceleration of the gas takes place. Design of instrumentation required to carry out the various measurements will be deferred until Chapter VII; in designing the basic apparatus, however, it is necessary to arrange for accommodation of the desired instrumentation.

Photographic views of the apparatus are shown in Fig. 6.6 at the end of this chapter.

6.2 Electrical System

The electrical circuitry is shown in block form in Fig. 6.1. The main circuit consists of the coil, which establishes the electromagnetic field, a switch to control the admission of current to the coil, energy storage capacitors, and a d-c power supply to deliver the energy to the capacitors at the desired voltage.

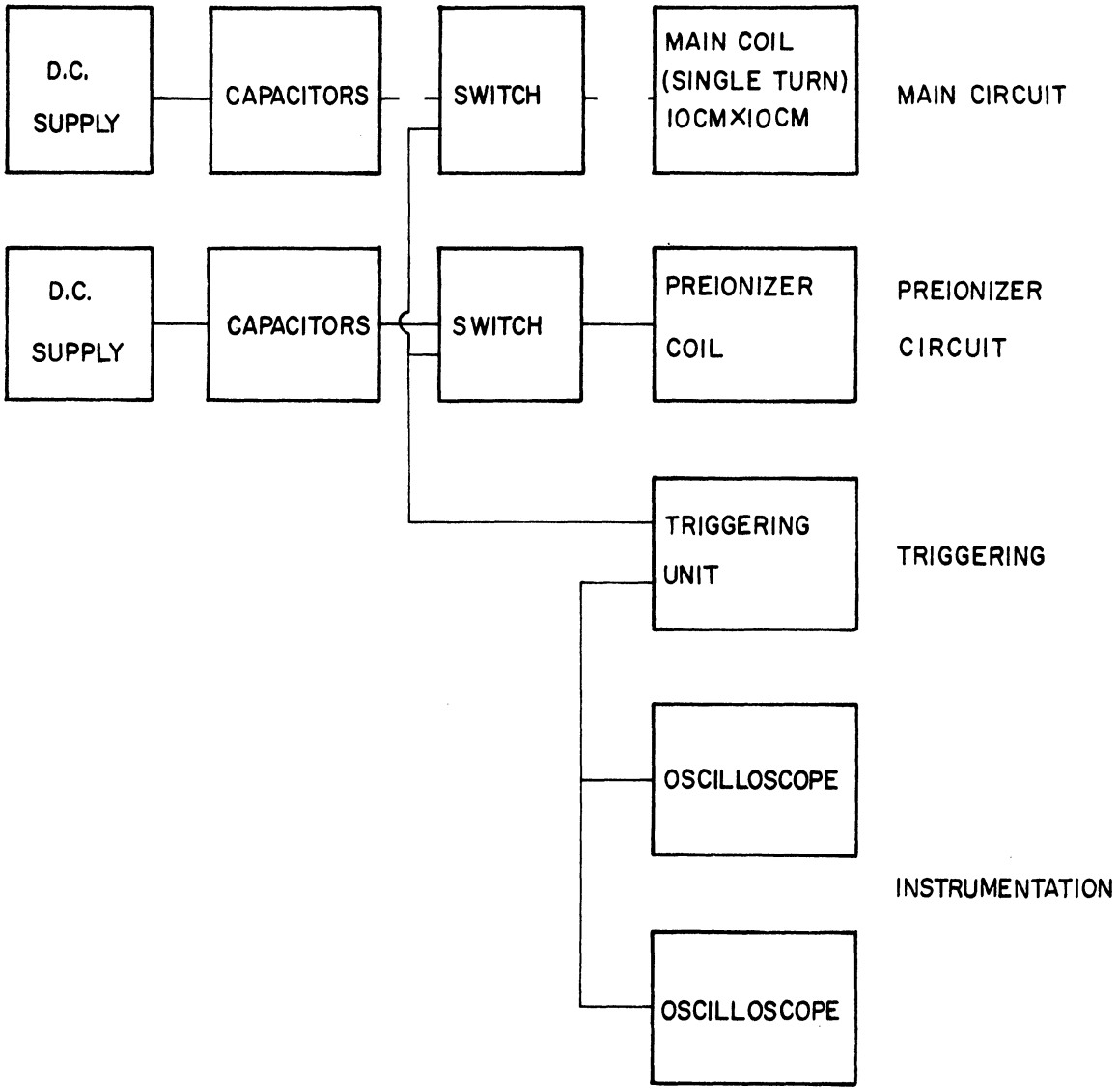

Fig. 6.1. Block Diagram of Electrical System Used in Experimental Program.

The coil consists of four coaxial sections, each 10 cm diameter and 2.5 cm long made of 0.022 inch copper sheet. These sections are mounted immediately adjacent to one another, thereby forming the 10 cm long coil. The segmented nature of the coil allows flexibility in changing coil geometry, and it also permits the processes inside the coil to be viewed by allowing narrow slits between sections. The calculated inductance of this coil is 0.0696 μhenries.

The switch is a three-element, triggered spark gap similar in design to types frequently described in the literature[79,80,81]; the design of the particular switch employed in these experiments is shown in Fig. 6.2. A thyratron triggering circuit to be described later causes a spark to occur between the trigger and ground electrodes. This spark then initiates a breakdown between the high voltage and ground electrodes, thereby switching the main capacitor bank to the coil. The time for this switching to take place is a rather critical function of the distance d between the two main electrodes. When this is properly adjusted, firing time of less than 0.2 μsec is obtainable; during the observations to be described in the next chapter, this was continually checked, since synchronization of this and other circuits was often required.

The capacitors used throughout these experiments were General Electric Company Catalog No. 14F609 units rated at 7.5 μfd, 20,000 vdc. Since these were not designed for high-current, oscillatory duty, they had to be considerably derated for our purposes. Operation for several months at 10-11 kv caused failure in two out of five units. At 9 kv, however, five such capacitors in parallel have been pulsed many hundreds of times without failure, and it was with this 5-unit, 37.5 μfd bank,

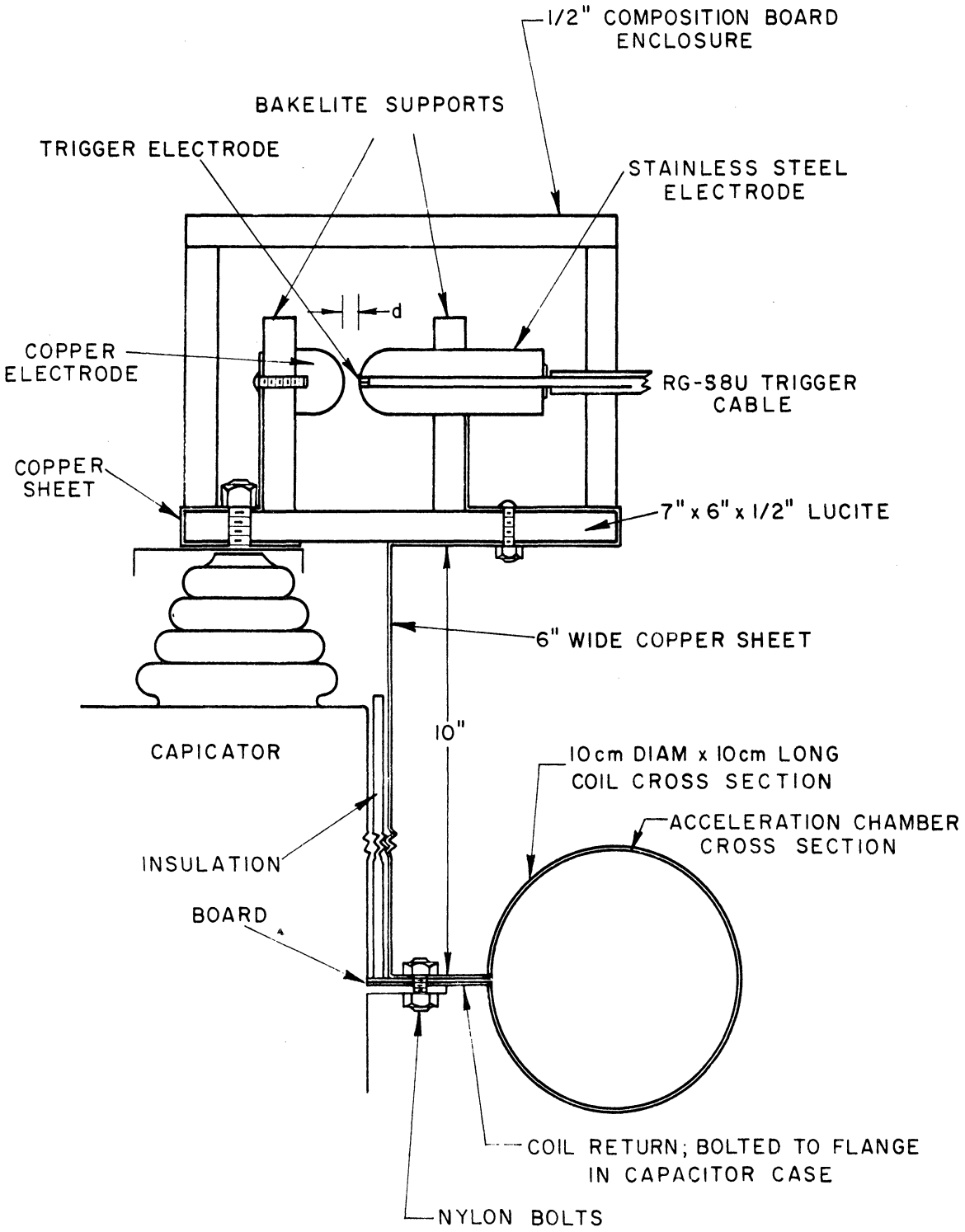

Fig. 6.2. Cross Section View of Main Circuit.

operating at 9 kv, that the experimental data to be described was obtained. The rated capacitance of this 5-unit bank, 37.5 μfd, was experimentally checked to an accuracy of about ± 1 μfd; both a charge rate test and a resonant bridge measurement were employed to arrive at this value. A Beta Electric Corporation Model No. 206 High Voltage d-c Power Supply, feeding through a 1.2 megohm high voltage resistor, was used to charge this bank before each firing; a 0-25 microammeter in series with 500 megohms across the capacitors was calibrated against a Rawson Electrostatic Voltmeter, Type 518C, and was then used to measure the capacitor voltage.

A signal proportional to the capacitor voltage during a pulsing of the main circuit is shown in Fig. 7.1(a). The following circuit characteristics may be determined from this decay curve.

Frequency f: 55.5 kc/sec.

Total circuit inductance L (knowing C = 37.5 μfd): 0.218 μhenries.

Voltage ratio, equal to the ratio of coil to total circuit inductance, $\frac{L_{coil}}{L_{total}} = 0.32$.

Maximum current at 9 kv charging voltage, $I_o = 1.18 \times 10^5$ amperes.

Maximum linear current density at 9 kv charging voltage, $i'_o = 1.18 \times 10^6$ amperes/meter.

Maximum value of vacuum magnetic field at center of coil, 1.04 weber/m^2.

Circuit resistance: 0.0107Ω.

Circuit Q: 7.13.

The voltage signal shown in Fig. 7.1(a) was obtained by a single turn pickup coil. By calculating the mutual inductance between this and the main coil and by comparing the peak measured voltage with the charging

voltage, an independent measurement of the voltage ratio can be obtained. The ratio obtained in this way agrees with the value listed above to within about 5 percent.

The preionization system is quite similar to the main circuit in that it consists of a coil, a triggered spark-gap switch and energy storage capacitors. The coil in this case is a close-wound, three-turn, 10 cm diameter coil made from insulated #18 copper wire. This coil was located coaxially with and immediately adjacent to the main coil as shown in Fig. 6.5. The switch and capacitors are arranged in the Marx doubling circuit shown in Fig. 6.3 so the capacitors could be charged at 20 kv and discharged at 40 kv. The triggered spark gap is similar in basic design to the one employed in the main circuit although smaller in over-all size; care must be taken here as with the main circuit gap to ensure proper spacing so undesirable firing delay does not occur. The capacitors (Cornell-Dubilier Type BT-14, 0.012 μfd, 25,000 vdc) were again not built for high-current oscillatory duty, but at 20,000 volts they withstood perhaps several thousand firings before failure.

The "ringing" and decay of the preionization voltage is shown in Fig. 7.1(b). From this we note a frequency of 1.56 mc/sec and a total circuit inductance of 1.73 μh; calculation of the coil inductance indicates that most of this circuit inductance is contributed by the coil itself.

This preionizer circuit is able consistently to cause an electrical breakdown of the gas in the neighborhood of the coil down to about 0.01 mmHg in helium and argon. Below this pressure, breakdown might occur but inconsistently. Although the brightness and appearance

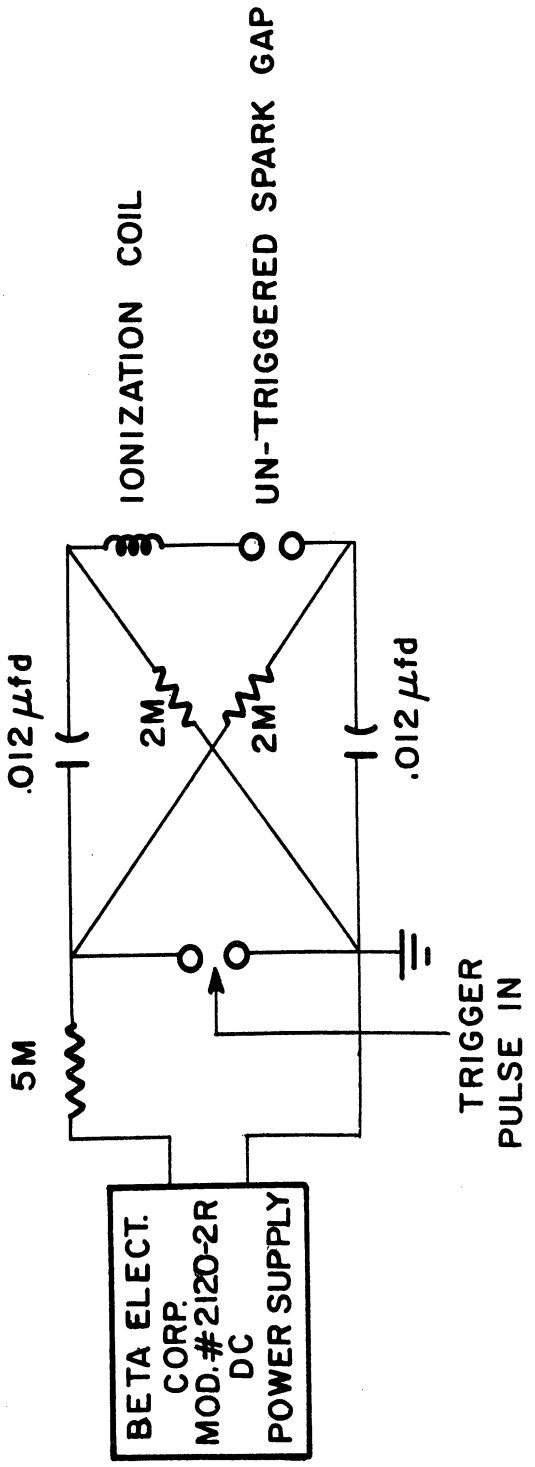

Fig. 6.3. Preionization Circuit.

of the preionization discharge depend on pressure to some extent (the discharge for instance becoming increasingly more diffuse and occupying a larger volume as pressure is decreased), the color is noticeably different for different gases, argon yielding a blue color, while the helium discharge is pink. (These color differences are also present in the main discharge although somewhat masked by the extreme brightness of this discharge.)

The preionizer serves two functions. At low pressures, where the field gradient of the main coil is not great enough to cause breakdown, the preionizer contributes sufficient electrons to allow the multiple ionization process by the main circuit to proceed. In addition, throughout the pressure range of interest, the preionizer considerably increases the shot-to-shot repeatability of the system. This is of utmost importance when a series of tests is being made throughout which one desires the discharge characteristics to remain uniform.

The final element of the electrical system, the triggering circuit, is shown along with the entire electrical system in Fig. 6.4. This triggering arrangement is a two-stage circuit. The 2D21 thyratron provides a pulse both to trigger the larger 5C22 thyratron and to trigger oscilloscopes. The 5C22 circuit then sends the high voltage impulse to trigger the main and preionizer spark-gap switches.

The high-voltage, high-frequency circuits, along with the vacuum system to be described in the next section, were housed in an expanded metal enclosure. This served two purposes. First, it shielded the externally located oscilloscopes from spurious signals generated by the spark gaps, etc. Secondly, the enclosure acted as a safety measure, since the door through which entrance was gained to the cage was interlocked.

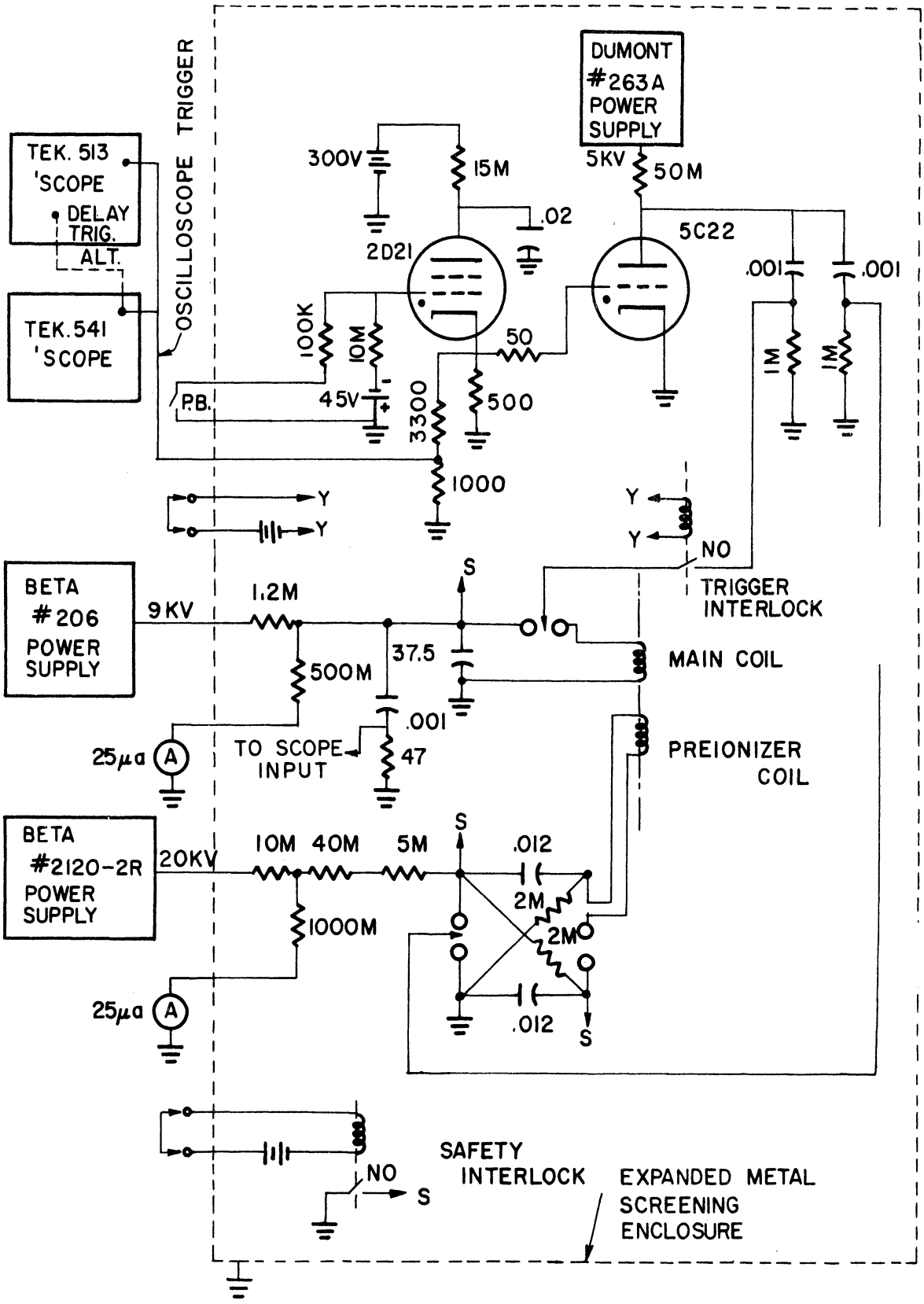

Fig. 6.4. Electrical System.

6.3 Vacuum System

The vacuum system includes the chamber in which the ionization and acceleration take place. For this purpose, it must provide five services, specifically:

1. The acceleration chamber itself,
2. Pumps to evacuate the chamber so gas of known composition can be introduced without dilution by residual impurity,
3. A gas handling system to introduce the desired gas at the desired pressure,
4. Gauges by which the gas (and vacuum) pressures can be measured, and
5. Entrance ports through which instrumentation can be inserted into the chamber.

This entire vacuum system is represented in the semi-schematic diagram shown in Fig. 6.5.

The acceleration chamber shown to scale with coils in place in Fig. 6.5 is constructed from 10 cm O.D. Pyrex tubing. Note that the end of the chamber is located approximately on the central cross section of the coil so gas will only be accelerated in one direction out of the coil.

The combination of mechanical and oil diffusion pumps enables the entire system (up to the intermediate gas storage section) to be evacuated down to about 5×10^{-5} mmHg; this vacuum is adequate in as much as the acceleration chamber is refilled to 0.010 mmHg or higher for each test. The ionization gauge serves the purpose of measuring this minimum pressure.

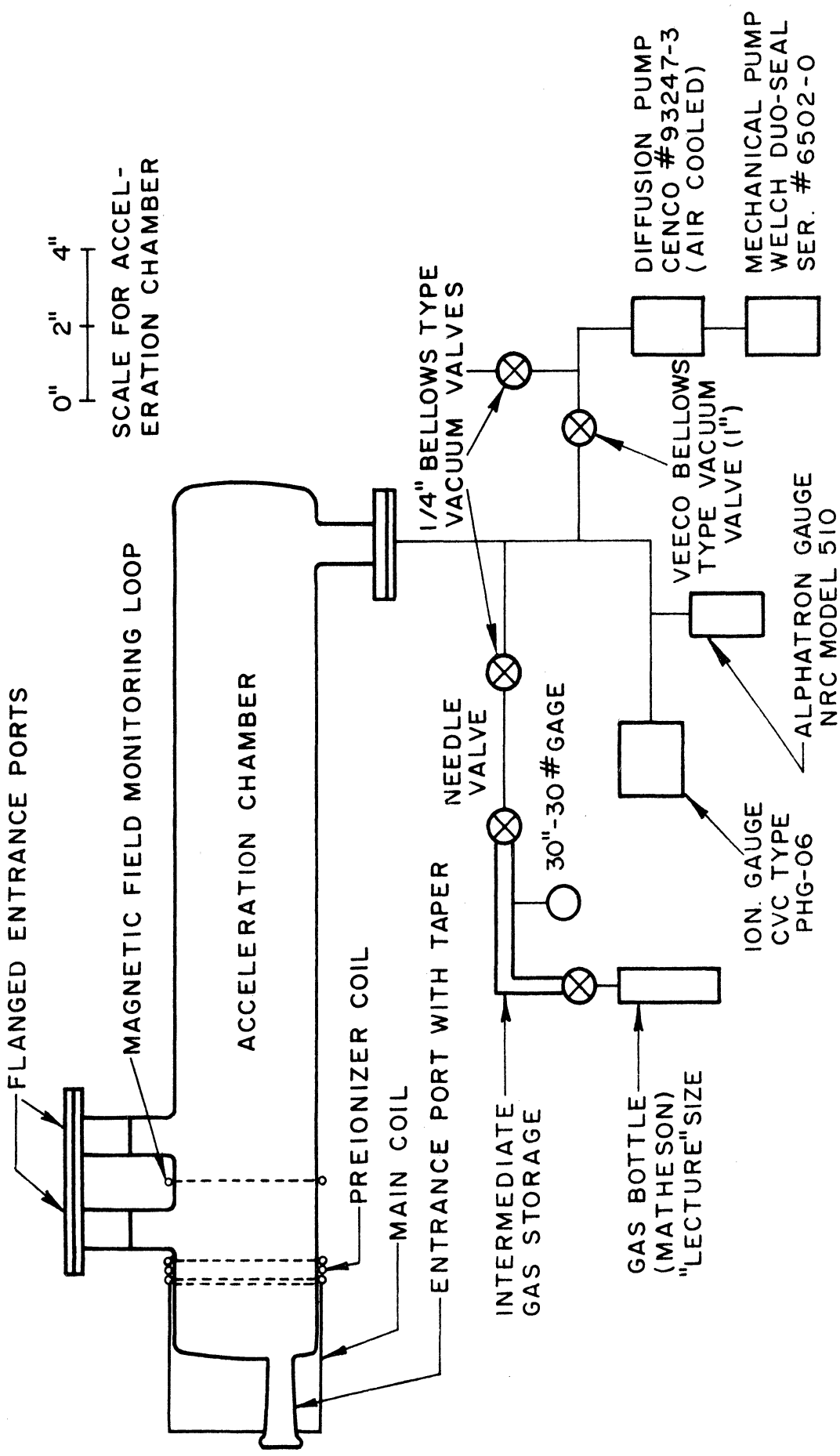

Fig. 6.5. Vacuum System.

The intermediate gas storage area, a piece of high vacuum rubber hose, is first pumped down to about $30^{\#}$ inch Hg vacuum and then filled from the gas bottle up to about 30 pounds with the desired gas. By proper manipulation of the two valves between this intermediate storage and the acceleration chamber, the chamber can be filled to any desired pressure (measured by the alphatron gauge). The procedure which was used before each firing was to pump the system (up to the intermediate gas storage) down as far as possible ($\sim 5 \times 10^{-5}$ mmHg), close off the system from the pump, and fill to the desired pressure. The system was sufficiently tight so that over perhaps a half-hour period any pressure change which occurred would be undetectably small. This is much longer than required to charge the capacitors and fire the electrical system.

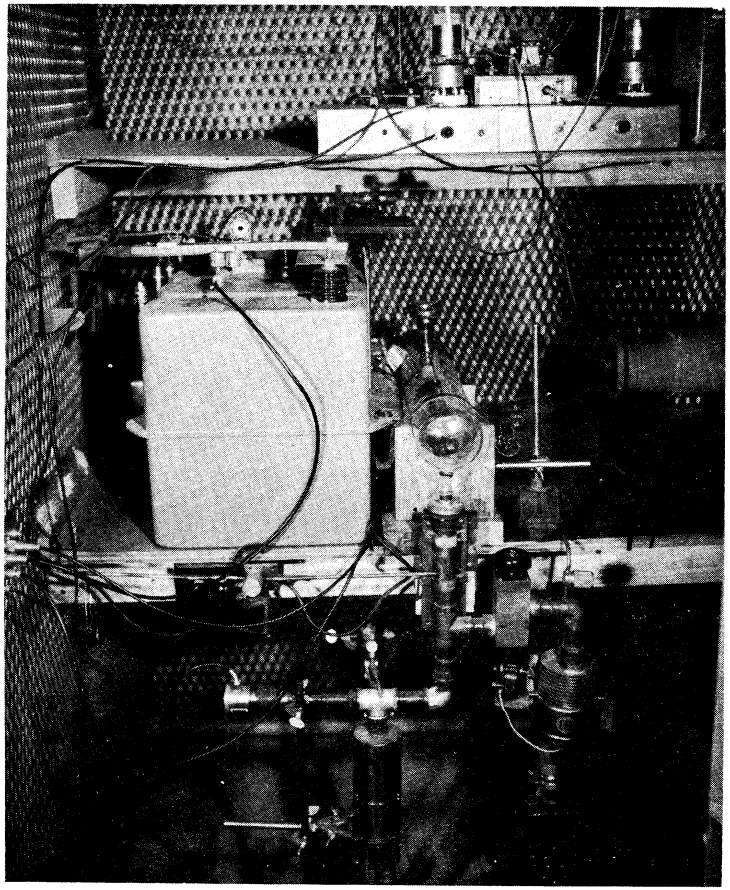

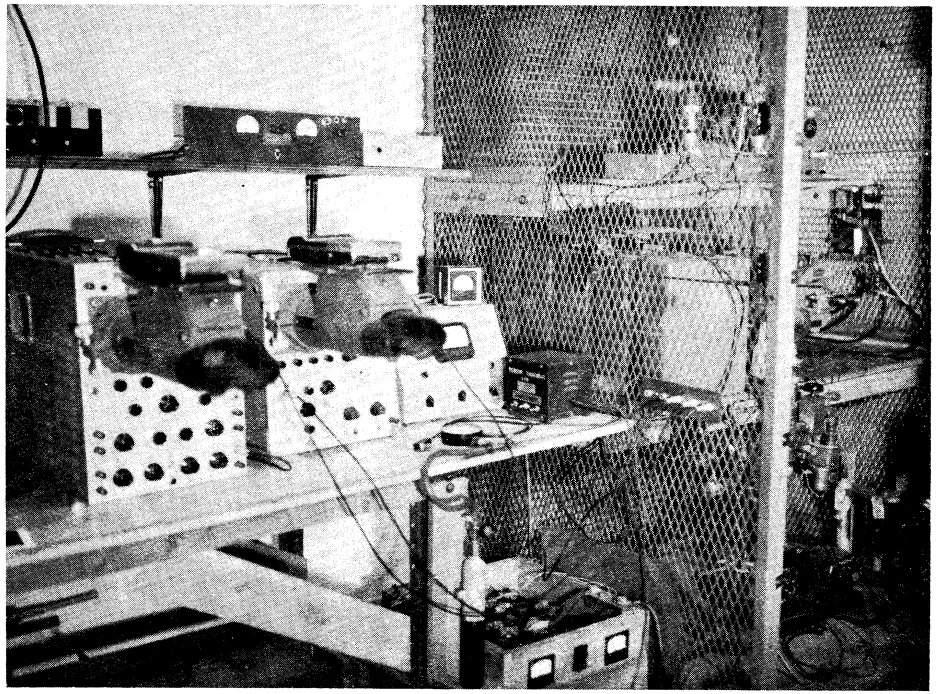

Fig. 6.6. Photographic Views of the Experimental Apparatus.

CHAPTER VII. EXPERIMENTAL RESULTS

7.1 Introduction

Chapter I has defined the objective of this effort, namely, an analytical and experimental study of the acceleration of ionized gases by inductively generated, time-changing magnetic fields. That chapter also went on to describe the particular geometry on which the investigation would concentrate. Chapters II through V dealt with analysis and theoretical prediction as to what sorts of activity we might expect from such an arrangement. Chapter VI then described the design and construction of apparatus on which experiments could be performed with the particular geometry of interest. It will be the task of the present chapter to describe the diagnostic techniques which have been applied to the experimentally observed phenomena, and to present and interpret the results of these experiments.

Two types of measurements are of interest. We are first of all interested in what might be called the kinetic characteristics of the device. These would be the parameters of immediate interest in the propulsion application, such as velocity, momentum, and energy of the ejected gas, and efficiency with which energy is delivered from the energy storage to directed motion of the gas. The second type of measurement deals with the internal mechanisms occurring during the ionization and acceleration of the gas; location of charge and current within the gas are of particular importance.

Wherever possible, the relation between the two types of information will be indicated, and correlations with the theoretical predictions will be pointed out.

The philosophy underlying the experimental effort has in general been to "look" at the operation from as many different diagnostic viewpoints as possible. It is felt that in carrying out this program sufficient independent measurements were made with sufficient accuracy to give a good over-all picture of the experiment. Occasionally, suggestions will be made as to ways in which the measurements might advantageously be continued.

The various types of instrumentation will be introduced one by one, discussing any pertinent theory, construction, and results of each in turn. It will be seen, however, that the individual techniques were not each applied independently, but rather, as often as possible several simultaneous measurements were made in order properly to monitor the operation of the device and to correlate among the various measurements.

Measurements were made in both helium and argon. These two gases were chosen because of their ready availability and because of their ten-to-one molecular mass difference. Voltage on the main capacitor bank was maintained for the most part at 9 kv, since, as explained in Chapter VI, this was deemed the maximum safe voltage at which they could be operated. Preionizer charging voltage was about 20 kv in all cases.

7.2 Magnetic Field Monitoring Loop

A No. 18, enameled copper wire, single-turn loop placed circumferentially around the outside of the discharge tube at z = 12 cm (midway between the two vertical entry ports as illustrated in Fig. 6.5) was used to monitor and measure the magnetic field. The two ends of this loop were connected through a coaxial cable and an attenuating probe to an oscilloscope. The probe was necessary, since the peak voltage induced around the loop during a pulse of the main circuit, in

the neighborhood of 200 volts, was too high to feed directly into the oscilloscope; the probe also raised to 10 megohms the input impedance seen by the loop, thereby insuring that the signal received would not be influenced by current in the loop.

The horizontal sweep of the oscilloscope was triggered at the instant the main and preionizer spark-gap triggers were initiated. Thus, a complete time picture of the magnetic field variation during a pulse was obtained, including any delays which might appear in the firing of the spark-gap switches.

The voltage induced in the loop consists of a component due to the current in the coils (main and preionizer) plus a component generated by the gas current. The latter quantity is also influenced by the motion of the gas. Much information can be obtained by observing this loop voltage as a function of time.

Using a very fast oscilloscope sweep, delays after time zero in firing of the main and preionizer switches can be ascertained; the operating characteristics of the system depend quite critically on relative times at which these circuits are initiated, so it is necessary to know that no random delays are present. With the pressure in the discharge tube low enough (or high enough*) so no electrical breakdown of the gas occurs, the natural period and damping of the main and preionizer circuits can also be measured from the monitoring loop signal, as shown in Figs. 7.1(a) and 7.1(b).

---

* Note that in the electrodeless discharge, as with discharges occurring between electrodes, a Paschen Law property exists, since, for a given capacitor voltage, no breakdown will occur if the pressure is above a certain maximum value, or below a critical minimum pressure; see Reference 29 for elaboration.

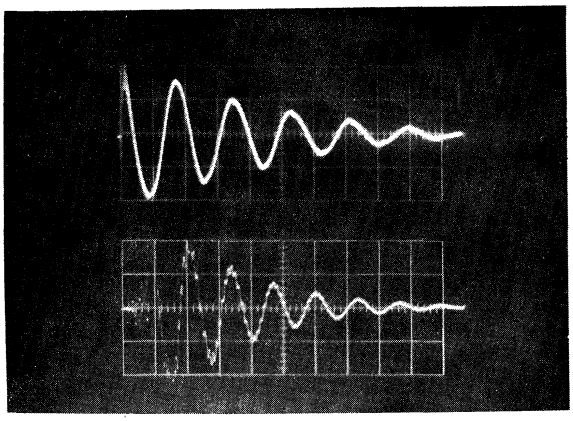

a) Main circuit only; 10 μsec. per major horizontal division; 100 volts per major vertical division.

b) Preionizer circuit only; 0.5 μsec. per major horizontal division; 200 volts per major vertical division.

Fig. 7.1 Monitoring loop signals without a discharge.

Fig. 7.2. Monitoring loop signals with an argon discharge present; 5 μsec. per major horizontal division; 100 volts per major vertical division; argon pressure given below.

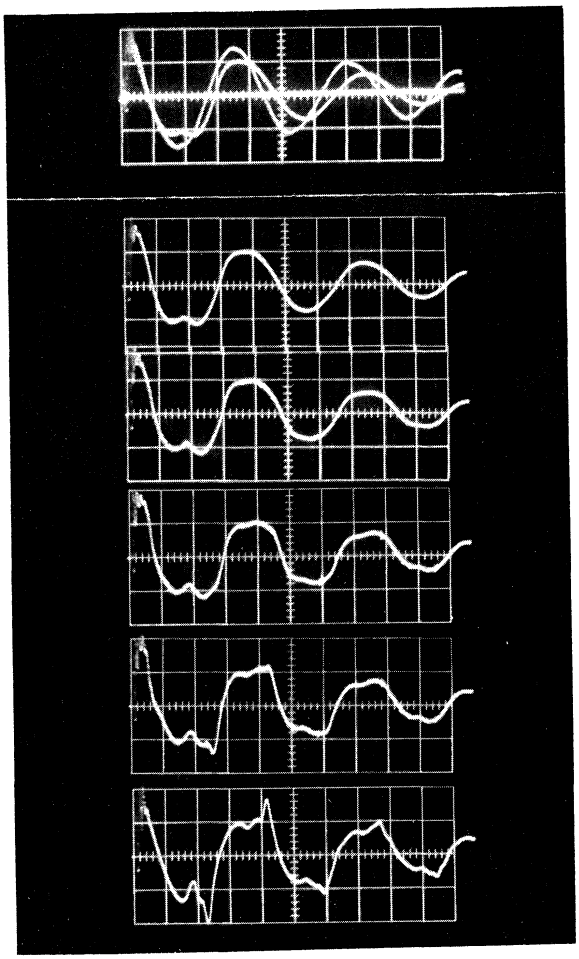

a) 0.80 mmHg; signal without discharge also shown.

b) 0.50 mmHg.

c) 0.30 mmHg.

d) 0.15 mmHg.

e) 0.075 mmHg.

f) 0.025 mmHg.

By close scrutiny of the monitoring loop signal under various gas conditions (type of gas and initial pressure) information can be deduced about the discharge. In this regard, the following items may be interpreted from the typical set of monitoring loop traces shown in Fig. 7.2.

1. Comparison of the signal with and without presence of a discharge reveals, at least on the second half cycle, a definite breakdown point.
2. Changing the pressure from 0.025 mmHg to 0.075 mmHg causes the voltage at breakdown to decrease, supporting the Paschen Law characteristic.
3. At low pressures, the discharge seems to be generated and extinguished each half cycle; in contrast, at higher pressures the gas current appears to flow continuously.
4. This gas current, being 90° out of phase with the coil current, causes a phase lag between the monitoring loop signals with and without a discharge, for instance as shown in Fig. 7.2(a).
5. The cusp in each half cycle, and the spike in the low pressure cases which rises above the no discharge signal are interesting phenomena which might bear further study at a later time. The motion of the gas might be a factor influencing these occurrences.

An extremely important function for which the field monitoring loop was continually used during the course of these investigations was to assure shot-to-shot repeatability of the discharge. If a series of tests had to be made under identical conditions, as for instance was the case in certain probe work to be described shortly, then the monitoring

loop traces were taken for each shot and compared. It turns out that the characteristics of the device, as revealed by this loop, are extremely repeatable, a fact which allows the taking of different data on consecutive shots rather than trying to gather all information simultaneously on a single pulse. The repeatability is exemplified by the series of consecutive traces shown in Fig. 7.3. This "signature" of the discharge will depend on type of gas and pressure but will always repeat under identical conditions.

Repeatability effectively limited the minimum density at which these experiments could be run. Breakdown of both helium and argon could be accomplished by the preionization circuit down to pressures in the 0.001 to 0.01 mm of Hg range, but operation was quite unpredictable. For pressures from 0.010 mmHg up to above 1 mmHg, however, dependable operation was achieved. These statements hold strictly only to the experimental conditions used in this investigation; characteristics of the electrodeless breakdown phenomenon depend in general on coil geometry, coil voltage, frequency and type of gas as well as on pressure[26,29,60]. Cooperative effects between the preionization and main circuits are also important in determining the ionization level obtained in such a device.

7.3 Voltage Divider

It is desirable to be able to measure the voltage (or current) at the main capacitor bank directly rather than inferring it from the monitoring loop described in the previous section. Such a measurement was made by use of the 1000 μμf/47Ω divider circuit shown across the main capacitor bank in Fig. 6.4. An attenuating probe similar to the one used with the field monitoring loop was used to convey the voltage across the

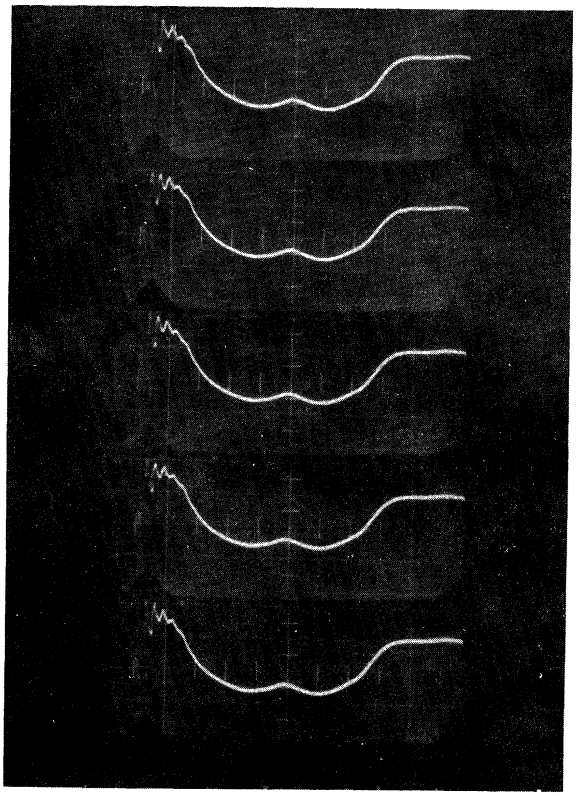

Fig. 7.3. Consecutive monitoring loop signals to show repeatability of discharge; 2 μsec. per major horizontal division; 100 volts per major vertical division; 0.20 mmHg of argon: ballistic pendulum measurement for each shot is also shown.

47Ω resistor to an oscilloscope. The frequency of the main circuit, as pointed out in Chapter VI, is 55.5 kc/sec. At this frequency, the impedance of the capacitor in this divider circuit is much higher than 47Ω, so the voltage measured across the 47Ω resistor by the oscilloscope will be proportional to the current flowing in the main circuit. One volt at the oscilloscope will be equivalent to approximately 50,000 amperes in the main circuit.

The important information which we desire from this voltage divider circuit is the effect of the plasma on the coil-current frequency and damping rate. Examples of these measurements are shown in Fig. 7.4. From these traces we deduce that there is no measurable frequency shift due to the presence of the plasma within the coil. The change in damping rate can, however, be detected; comparing the peak current in the coil at the 11th half cycle with and without plasma yields energies transferred to the plasma in the amounts shown in Fig. 7.5. Note the approximately linear dependence of energy on the logarithm of pressure.

At 9 kv capacitor charging voltage, the initial stored energy is 1520 joules. Since the ratio of coil to total circuit inductance is 0.32 (see Chapter VI), approximately 490 joules appears in the field of the coil at the first current maximum under vacuum conditions. Thus, we see from Fig. 7.5 that energy transferred to the plasma is on the order of 10 percent of the energy available to be transferred.

Calculation of energy from measurement of capacitor current damping in the manner employed to arrive at Fig. 7.5 is limited by the precision to which readings can be taken from oscilloscope traces such as shown in Fig. 7.4. The energies so measured have precisions varying

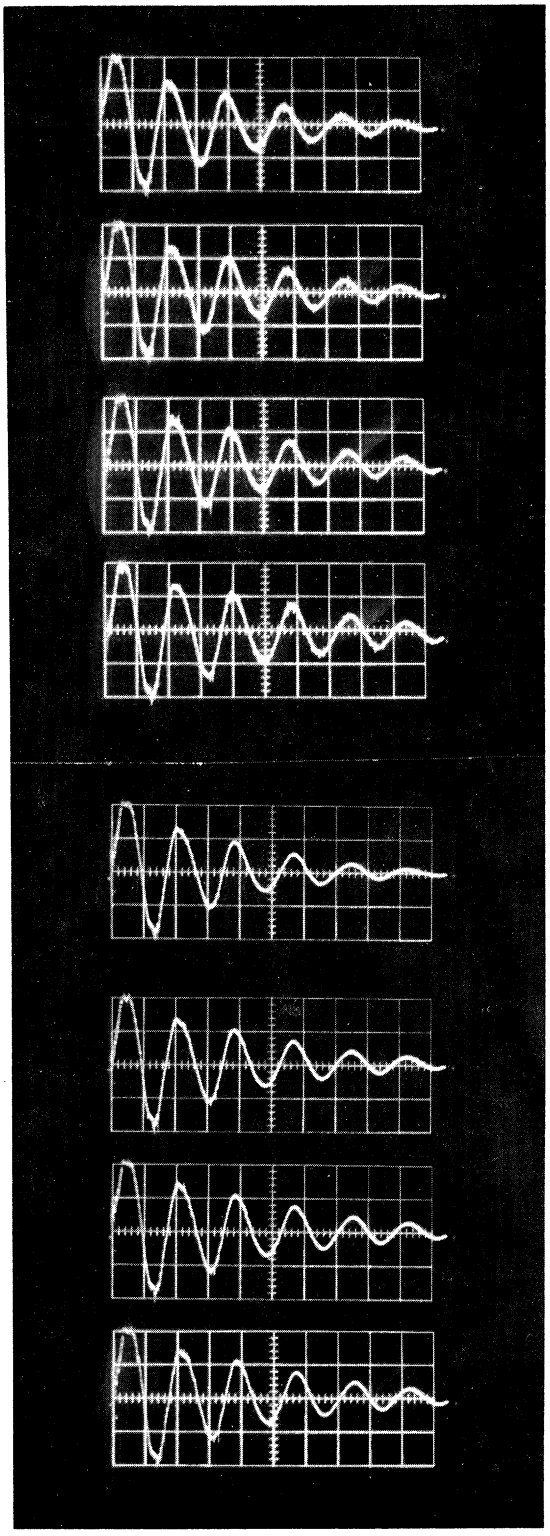

Fig. 7.4. Voltage divider signal; 10 μsec. per major horizontal division, 1 volt per major vertical division (proportional to capacitor current).

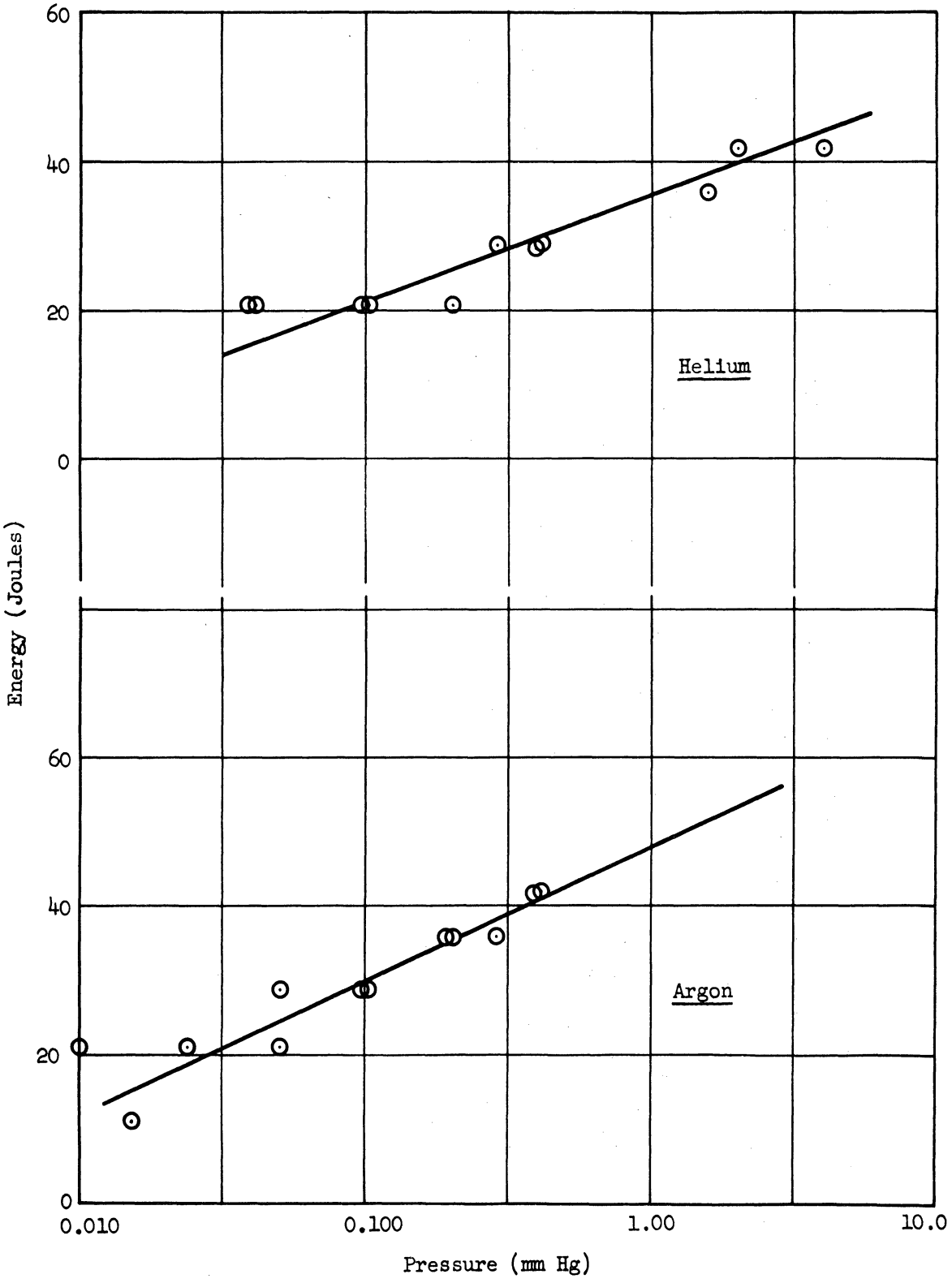

Fig. 7.5. Energy Transferred From the Circuit to the Plasma by the 11th Half Cycle.

from ± 5 joules at 11 joules to ± 2 joules at 47 joules. This is evidenced by the "quantized" nature of the experimental points recorded in Fig. 7.5. The precision of this measurement could be significantly increased by delaying the oscilloscope sweep for perhaps 50 microseconds and then using a higher gain in the vertical amplifier in order to spread the later cycles out over a wider range of vertical deflection.

7.4 Ballistic Pendulum

A ballistic pendulum was used to measure the momentum carried by the accelerated gas during a single pulsing of the apparatus. The pendulum used in these experiments consisted of a flat, rectangular glass piece approximately 7/8" on a side cemented to a 4-inch-long nylon rod; this structure was suspended in one of the vertical entry ports by a horizontal steel axle which was free to rotate about its own axis. When at rest, the glass piece was vertical with its normal parallel with the discharge tube axis. The angle through which the pendulum rotated was detected by reflecting a focused light beam off the glass collector plate onto a calibrated scale. The period of the pendulum being something more than a second, the maximum angle to which the pendulum deflected could be detected with sufficient accuracy visually.

The operation of this ballistic pendulum depends on the moving gas intercepted by the glass plate being brought to rest and transferring its entire momentum to the pendulum in a time duration which is short compared with the period of the pendulum. High speed photographs introduced in a later section indicate that the gas motion is over in at most a few milliseconds, a time which is short compared with the pendulum period. These photographs also show that gas is reflected from the pendulum, thereby necessitating that the pendulum carry off

more momentum than was initially carried by the intercepted gas. This reflection velocity is low, however, and may be neglected considering the accuracy which is desired of these measurements.

If one knows the total weight of the pendulum (collector plus arm) and position of the center of gravity, the momentum of the intercepted gas can be calculated from the maximum angle through which the pendulum rotates. With the glass collector centered in the discharge tube at z = 15 cm, momenta measured in the pulsed crossed-field accelerator are shown in Figs. 7.6(a) and 7.6(b) in terms of momentum per square centimeter of area normal to the flow.

Since the calibration of the scale from which pendulum deflection is read depends only on length and mass measurements, both the accuracy and precision of this calibration are quite good. The limiting factor in the pendulum measurement is then the precision with which an observer can read the deflection. Consideration of the size of the light beam and its moving nature leads to an estimate of about ± 0.2 gm-cm/sec-cm^2 for the precision of the measurements given in Figs. 7.6(a) and 7.6(b).

The momentum measurements presented in Figs. 7.6(a) and 7.6(b) all apply to the center of the stream at z = 15 cm. Variations of momentum with position along and across the stream are also of interest. First, consider variations across the stream. A pendulum with a short arm was suspended in the z = 15 cm port so that momentum parallel with the stream (i.e., parallel with the acceleration chamber and coil axes) would be measured half way between the center and the edge of the stream. Over the pressure ranges shown in Fig. 7.6, the resulting momentum was approximately half the momentum at the center of the flow.

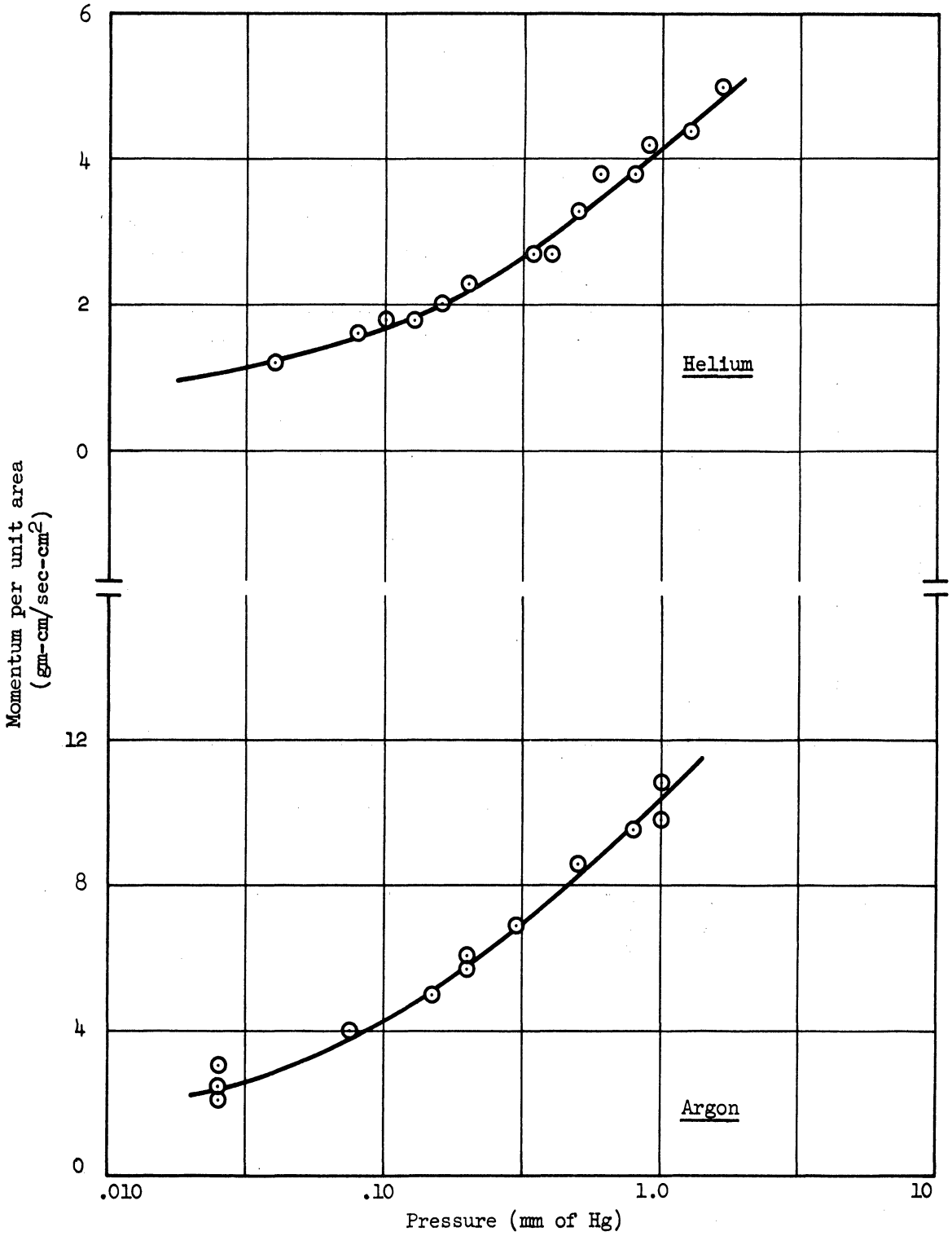

Fig. 7.6(a). Momentum Carried by Plasma at Center of Flow—as a Function of Pressure (C = 37.5 μfd, V = 9 kv).

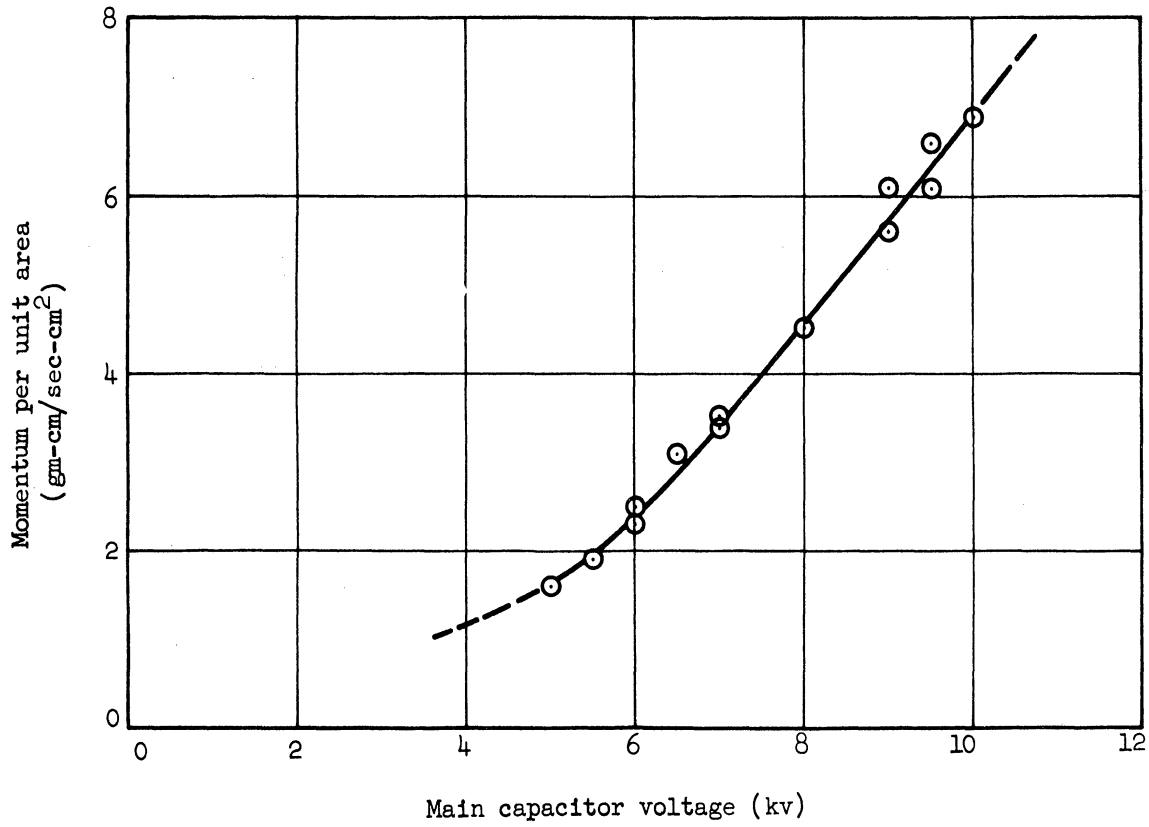

Fig. 7.6(b). Momentum Carried by Plasma at Center of Flow—as a Function of Main Capacitor Charging Voltage (C = 37.5 μfd, Argon, 0.200 mm of Hg).

With regard to variation of momentum along the stream, obstruction of the light beam due to the geometry of the apparatus prevented making a dependable pendulum measurement. Independent measurements of velocity and energy to be presented later show, however, that energy and velocity each decrease approximately by the same ratio between z = 15 cm and z = 8.5 cm, indicating that momentum remains nearly constant through this length of flow travel.

There was no detectable deflection of the pendulum when the capacitor circuits were energized with the discharge chamber at a pressure below that for which breakdown occurs. The deflection due to the preionizing circuit alone was less than 2 percent of the deflection when both main and preionizer circuits were employed.

Besides its use as an absolute measuring instrument, the ballistic pendulum was frequently used along with the field monitoring loop to indicate discharge repeatability during the taking of other data.

7.5 Calorimetric Collector

A procedure quite analogous to the ballistic pendulum measurement of momentum is a calorimetric method of measuring energy content of the accelerated gas. In fact, some experimenters have combined the two procedures into a single, multipurpose instrument[82,83]. In this energy measurement, the gas is collected, and the energy which is transferred to the collector is measured by measuring the temperature rise of the collector.

Flat pieces of 0.005" copper sheet were used as collectors. These were rigidly mounted in the gas stream by thermally-insulating, plastic supports. A thermocouple made from #30 iron and constantan wires was

fixed to the center of the back side of the collector and was connected externally to a Leeds and Northrup thermocouple bridge.

Temperature rises which were encountered during the experiments were generally in the range of 5 to 15°C. The approximately critically damped galvanometer of the bridge would indicate this temperature change in a few seconds. The rate at which the collector cooled was low, however, (typically a fifth to a tenth of a degree per second) so that the peak temperature as measured by the bridge gave a good indication of the actual temperature change experienced by the collector.

In Figs. 7.7 through 7.10 are shown energies measured calorimetrically in helium and argon for various pressures, positions and collector sizes. The following items can be interpreted from these curves.

1. Energies carried by argon and helium are approximately the same. The decay or loss of energy as the stream proceeds down the tube appears to be more rapid for argon than helium.
2. Collectors of two sizes were employed. As illustrated in the sketches accompanying Figs. 7.7 through 7.10, both were rectangular in shape, and both were oriented symmetrically with respect to the acceleration chamber axis during the taking of data for Figs. 7.7 through 7.10. Note that, while the larger collector samples nearly the whole stream radius, its rectangular shape prevents it from giving a true average measurement of conditions across the circular cross-section stream. Comparison of readings of the small and large calorimeters shows, however, that the average energy density across the stream is approximately 80 percent of that recorded by the large calorimeter.

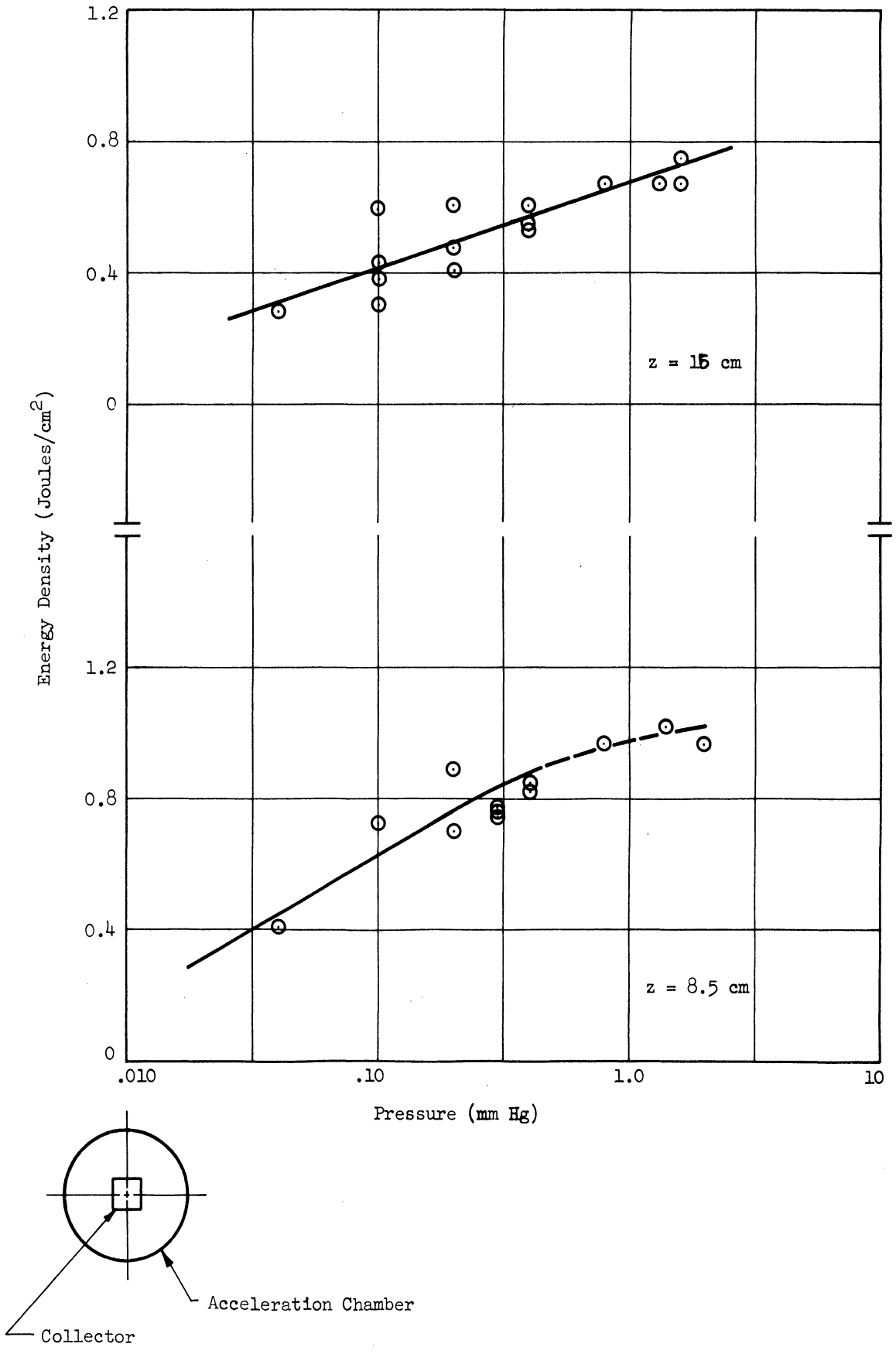

Fig. 7.7. Calorimetric Measurement of Energy Density in the Plasma, Helium; Small (27/32" x 7/8") Collector.

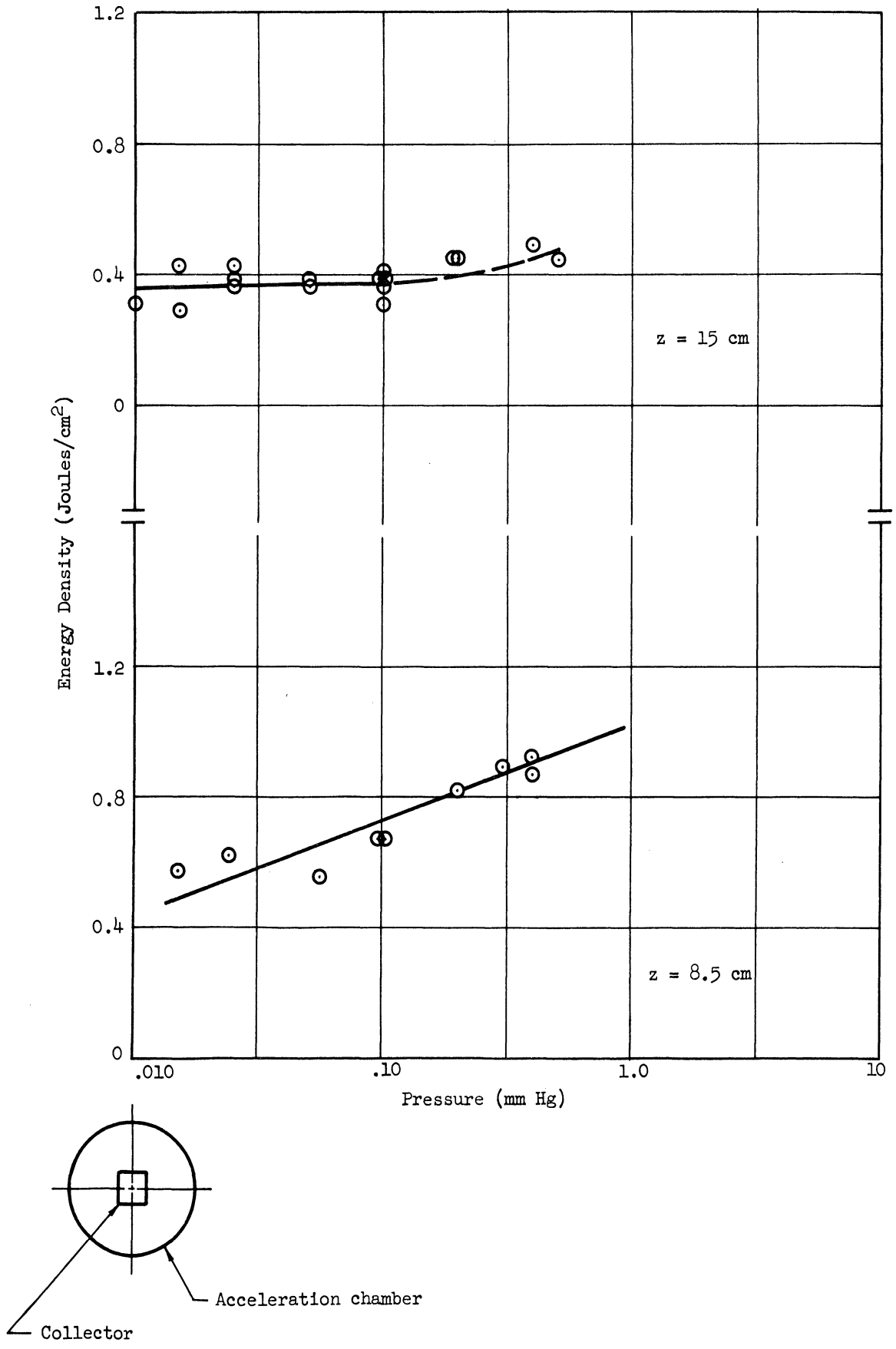

Fig. 7.8. Calorimetric Measurement of Energy Density in the Plasma, Argon; Small (27/32" x 7/8") Collector.

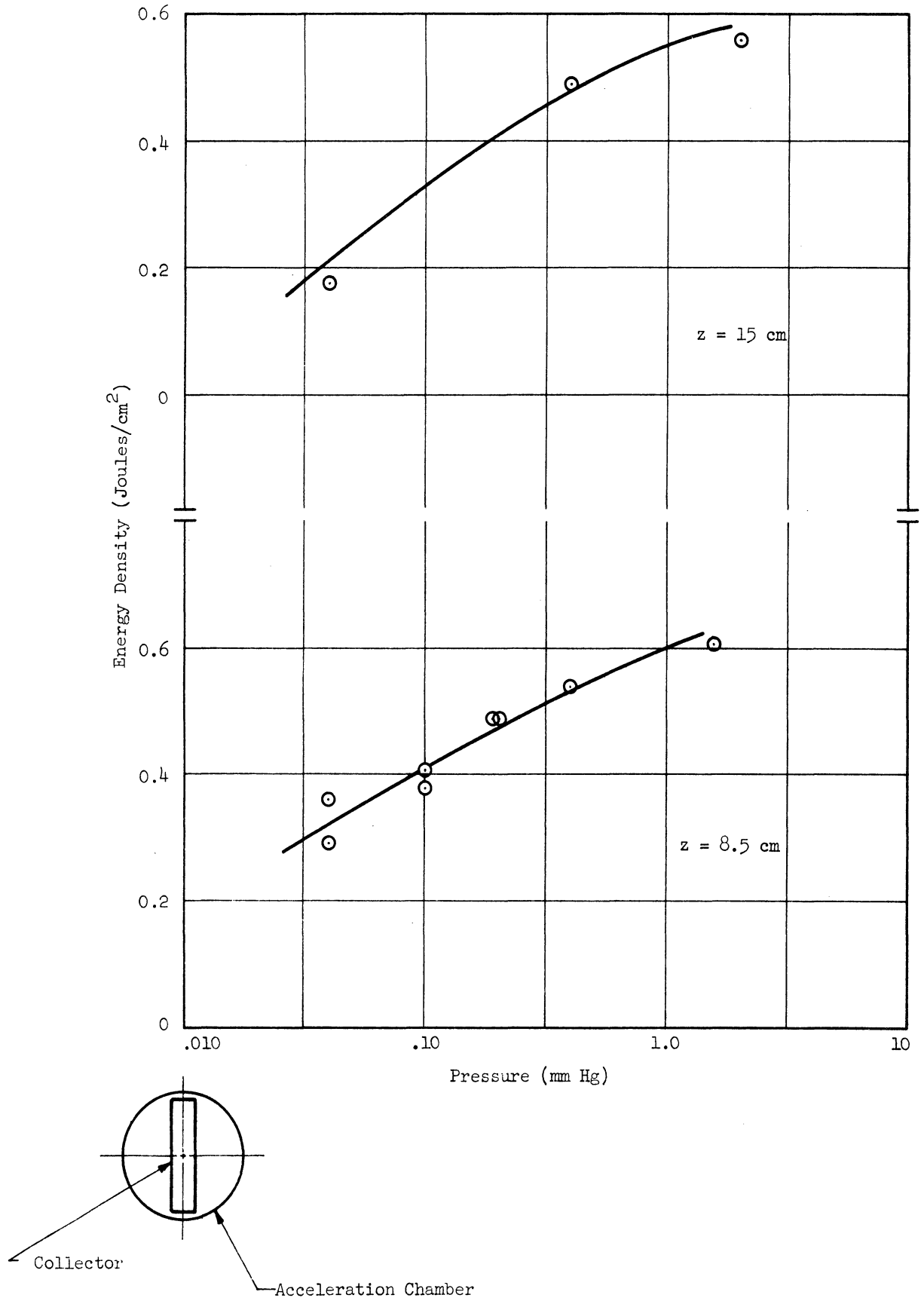

Fig. 7.9. Calorimetric Measurement of Energy Density in the Plasma, Helium; Large (3-1/2" x 13/16") Collector.

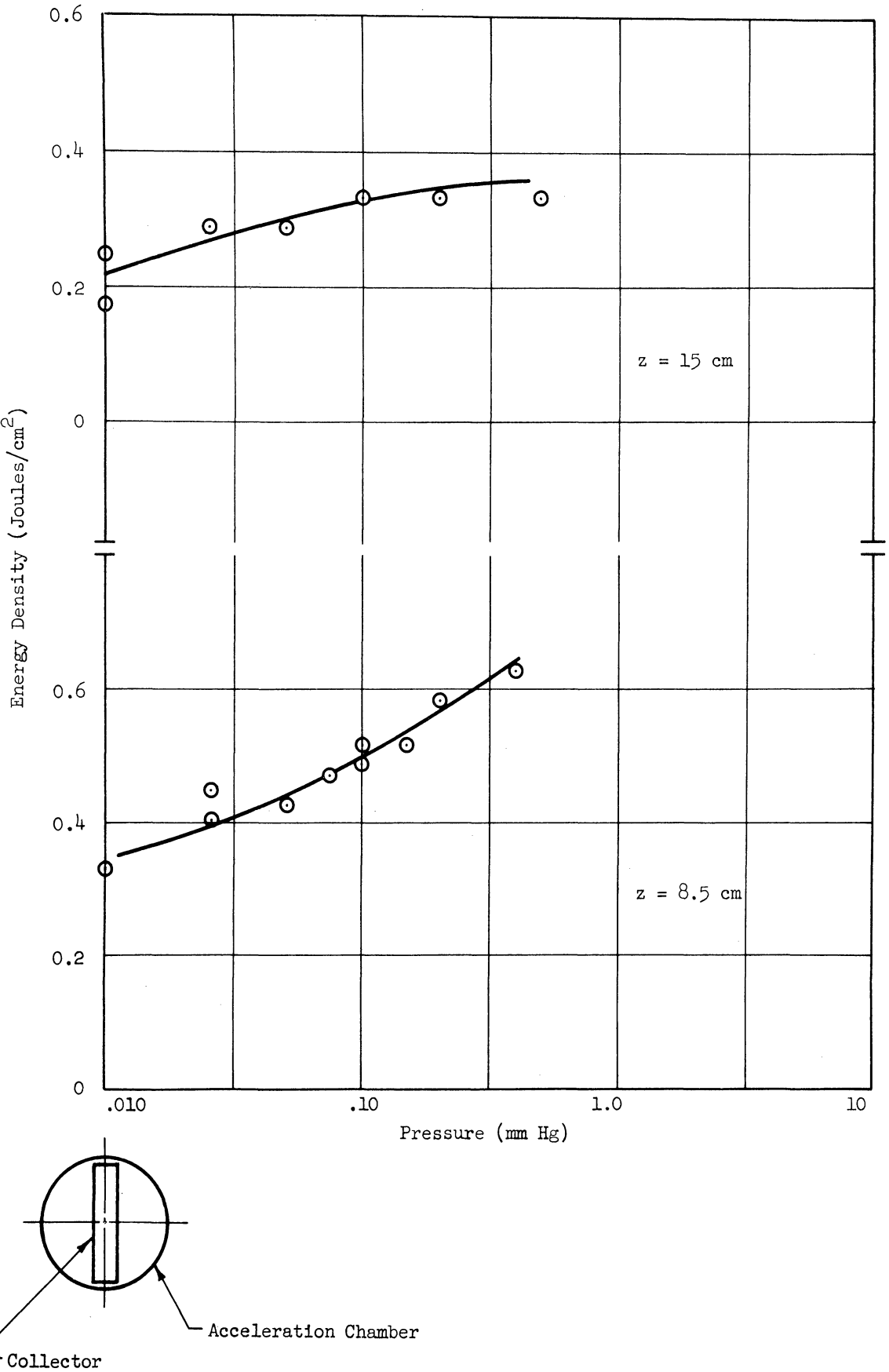

Fig. 7.10. Calorimetric Measurement of Energy Density in the Plasma, Argon; Large (3-1/2" x 13/16") Collector.

3. When the 80 percent factor pointed out in Item 2 above is taken into account, approximate agreement is obtained between the total energy in the plasma stream as measured by the large calorimeter close to the coil (z = 8.5 cm) and total energy transferred to the stream as determined by means of the voltage divider. The comparison is shown in Table 7.1.

Table 7.1. Comparison of Energy Measurements

Gas	Initial Pressure (mmHg)	Energy to Plasma (Voltage divider) (joules)	Energy in Stream at z = 8.5 cm (Calorimeter) (joules)
A	.010	12	22
	.030	21	26
	.10	30	31
	.20	36	35
	.40	41	40
	1.0	48	—
He	.030	14	19
	.10	21	26
	.20	25	30
	.40	30	34
	1.0	35	37

The fact that these two measurements yield much better than order of magnitude agreement tends to strengthen each measurement, giving us thereby reasonably good ideas of the level of plasma energy (i.e., roughly 10 to 50 joules) and the dependence of energy on pressure.

More careful consideration of Table 7.1 raises two questions.

a. Why is the energy measured in the stream often greater than the measured energy transferred from the circuit to the plasma?

b. Does radiation from the plasma, a form of energy which for the most part would not be detected by the calorimeter, actually represent as negligible a fraction of the total plasma energy as indicated by Table 7.1?

Let us consider each question separately.

The spread of the experimental points in Figs. 7.9 and 7.10 (from which Table 7.1 was constructed) coupled with the estimated precision of the voltage divider (see Section 7.3) can explain much of the absolute difference between the two measurements. The consistent lowness of the input energy in the case of helium is more likely attributable to a systematic error. (Note that the approximately 0.6 joules electromagnetically coupled from the coil to the large calorimeter at z = 8.5 cm even in the absence of plasma has been taken into account.) One systematic error which might be significant results from the calculation of energy to the plasma at the 11th half cycle, as explained in Section 7.3; thus, any energy transferred beyond the 11th half cycle would be neglected. Breakdowns from as many as 16 successive half cycles have been observed photographically, and it is possible that a joule or so of energy could be transferred over these latter, uncounted half cycles. The calculation of energy from the voltage divider signal depends on knowledge of the main circuit capacitance, inductance and voltage; errors of a few percent in these could also account for a systematic error in the energy measurement. The effect of the gas

reflected off the calorimeter is neglected, as in the case of the ballistic pendulum. This small systematic error would tend to increase the calorimeter reading.

Now, let us consider radiation. There are several possible sources of radiation within the plasma. Excitation radiation will first be taken up, others will then be mentioned, and finally an independent measurement of total radiation will be described.

Note that radiation resulting from recombination of ions and electrons within the volume of the gas is neglected, since in low density situations this is a very improbable occurrence[84]. Recombination of the ions will take place instead on surfaces such as the calorimeter and the acceleration walls. If the calorimeter is a microscopically flat surface, it is reasonable that at least half of the recombination radiation created there must be absorbed by the calorimeter. Since it is in fact microscopically "rough", much more than 50 percent should be received. Experiments cited in the literature tend to confirm this conclusion[85], although they do not indicate the exact percentage actually received.

a. Excitation Radiation: During the compression and acceleration of the plasma, excited states are continually being created by collisions and continually being lost, with the excitation energy being carried away as radiation. Plasma temperature measurements discussed in a later section are sufficiently high (roughly 20,000°K to 40,000°K for densities where equilibrium might be expected to exist) that nearly complete first ionization probably exists. Thus, very little excitation energy from ground states should be present. The first

excitation level of singly ionized helium is 40.9 ev above the ionization potential, however, so we might expect a low probability of such an energetic transition, and consequently not much total excitation radiation should be emitted from the helium plasma. In argon, unfortunately, this argument cannot be used as readily since the first ion excitation level is only 13.5 volts above the ionization level. Note that first excitation levels for both neutrals and ions of helium and argon are in the ultraviolet region and would not escape through the glass acceleration chamber walls*.

b. Other Radiation Sources: Bremsstrahlung, radiation resulting from deflection of electrons in the coulomb fields of the other charged particles, will result in ultraviolet or X-radiation emission from the plasma. Glasstone and Lovberg[86] present calculations for bremsstrahlung loss which indicate that, in the 20,000°K to 40,000°K range, power loss is on the order of a few watts per cm^3. The plasma in the induction accelerator occupies perhaps 1000 cm^3 and lasts for something on the order of 10^{-4} seconds, indicating that perhaps as much as a few tenths to one joule might be ascribable to bremsstrahlung loss.

So long as the magnetic field is prevented from penetrating the plasma region, cyclotron radiation, resulting from electrons spiraling about the lines of magnetic field, should be small.

Radio-frequency radiation is emitted from plasma. These arise from space-charge waves and similar wave phenomena within the plasma, but experimentally it has been observed that a

* Further consideration of thermal excitation and thermal ionization and an estimation of energy loss due to excitation radiation are given in Appendix B.

plasma is a very low efficiency source of r-f radiation[87]. An attempt was made to detect r-f energy (at 30 mc/sec and 1000 mc/sec) in the neighborhood of the accelerator, but no signals definitely ascribable to the plasma could be found; the background noise from the spark gaps was quite high during these tests.

X-rays might be generated when the electrons strike the glass walls or instruments placed in the plasma (in addition to bremsstrahlung in the X-ray range). Dental X-ray film kept near the accelerator tube during several hundred pulses showed a slight darkening, but one would estimate that very little energy was actually involved per shot.

c. Total Radiation Measurement: A piece of 0.001" thick copper sheet, 37.6 cm^2 in area, was placed against the outside wall of the accelerator tube in the region between the coil and the monitoring loop (see Fig. 6.5). The side of the sheet facing the plasma was blackened to enhance radiation absorption. A thermocouple (#30 iron-constantan) fixed to the center of the back side of the sheet registered temperature of the sheet. Considering thermal time constants of this arrangement, one would expect after a pulse that the copper temperature would immediately rise due to any radiation directly absorbed; some seconds later it should then come into equilibrium with the glass at some temperature dependent on the total energy which the glass and copper sheet had absorbed. This total energy measurement includes radiation absorbed and transmitted by the glass and also energy of ion-electron recombinations which occur on the glass surface.

The copper sheet itself had a sensitivity of 0.38 joule/°C. The combined sensitivity of the copper sheet and the 37.5 cm^2 glass area immediately adjacent to the copper was about 16 joules/°C. Note that, while the glass absorbing area was a section of the acceleration tube rather than a thermally isolated piece, we are assuming that the thermal conductivity of the glass was sufficiently low that this glass area retained the heat input for time durations which were long compared with the few seconds needed to make a temperature reading.

The reference junction in the thermocouple circuit was kept at 0°C in order to prevent detection of temperature changes due to randomness in the cold junction. A Leeds and Northrup Bridge (catalog #8667) was used to register the thermocouple potential. Changes of 0.02 millivolt could be resolved by this system; this temperature change corresponds to about 0.2 joule energy in the copper sheet and about 6 joules in the glass plus copper.

The acceleration circuits were pulsed with no gas in the acceleration chamber (i.e., no plasma), and with helium and argon at various pressures. With no plasma, temperature changes of about 1°C were recorded. Tests with plasma in the acceleration chamber yielded this same 1°C change (± about 1/2°C), except for one occasion which resulted in a temperature rise of about 2°C. All of these temperature changes occurred within a second or so, followed by a rapid fall back to the original equilibrium temperature; this indicates that the heat

energy causing the temperature change was in the copper collector rather than the glass.

The small amount of energy being absorbed instantaneously by the copper collector indicates that negligible energy is being radiated through the glass walls in the region between the coil and the z = 8.5 cm station. Since the glass heat capacity is relatively so high, the inability to detect any glass temperature rise indicates only that no gross error exists in the energy comparison in Table 7.1.

In these past few paragraphs, we have only attempted to add to the plausibility of the energy comparisons shown in Table 7.1. Thus, while several potential sources of error in the calorimeter measurement have been shown to exist, some evidence has been presented indicating that these will be small. It is the feeling of this author that the voltage divider technique on the other hand is inherently quite accurate, but, as pointed out in Section 7.3, its precision could be substantially increased.

Certain interesting transient phenomena detected by the calorimeter during these measurements should also be noted. For measurements taken with the larger collector at z = 8.5 cm (i.e., close to the driving coil), the temperature registered by the centrally located thermocouple would typically rise rapidly to an equilibrium point, pause there briefly, and then rise to a final equilibrium point (i.e., a point where the collector had reached a uniform temperature). When the same larger collector was used at z = 15 cm, however, the opposite effect was noted, namely, that the temperature would rise rapidly to a point, then drop slightly to the final equilibrium level.

These transient occurrences can be explained on the basis of time for heat to transfer throughout the collector by hypothesizing that the propelled gas leaves the coil as a converging ring of accelerated gas (see the Fig. 5.1 model). Close to the coil, the plasma maintains its ring shape, having maximum energy density at some off-axis radius and transferring its energy therefore near the ends of the calorimeter collector. The thermocouple, being centrally located on this collector, would first indicate a small temperature rise due to the (small) energy transferred from the plasma to the center of the collector; the thermocouple would then show a rise in temperature as the larger amount of heat energy transferred to the ends of the calorimeter flowed into the central region. Locating the calorimeter further out from the coil, where the plasma has been "focused" into a smaller diameter, causes the plasma to transfer its energy first to the center of the collector, causing an immediate, large rise in the thermocouple temperature. Subsequent flow of the heat from the center to the ends of the calorimeter results in the recorded fall of thermocouple temperature to an equilibrium level. The values for thermal conductivity (~ 1 cal/sec-cm^2-°C through 1 cm) and cross sectional area (.010 cm^2) of the copper collector are not inconsistent with these qualitative hypotheses.

For the curves in Figs. 7.7 through 7.10, the final equilibrium temperature was used.

7.6 Rotating Mirror Camera

A time-resolving, visual observation of the discharge in the pulsed, crossed-field accelerator is helpful in understanding the detailed structure of the discharge. For our purposes, a rotating mirror camera was employed to obtain this visual information. In this

camera, a mirror having six rectangular sides is rotated about its central axis by means of an attached air turbine. A narrow slit mounted in front of the discharge tube is focused onto the photographic film by means of a lens and the rotating hexagonal mirror as shown in Fig. 7.11; the rest of the discharge tube is blocked off so that light from the plasma can only reach the camera through the slit. Now, as the discharge progresses and the mirror rotates with time, the image of the discharge at different times will appear at different places on the film. An Avco type MC-300-2 camera was used in these experiments.

Two orientations of the camera have been used, allowing observation of a slit parallel with the discharge tube axis, as in Fig. 7.11, and of a slit normal to this axis. The former arrangement detects axial motion (in the form of shock waves—see Section 5.2) while the latter orientation provides observation of the radial compression process. For low density discharges, where the low luminosity level demands a high speed film, Kodak Royal Pan film was used, while at higher densities Contrast Process Ortho film was employed. Slit widths were generally 1/16" wide.

First, let us consider motion parallel with the (horizontal) discharge tube axis. The rotating mirror camera photos (or <u>streak photos</u>, as they are sometimes called) taken in this case are shown in Figs. 7.12 and 7.13. One can observe that at least one shock wave progresses out from the coil each half cycle; in some instances multiple shocks emerge, perhaps due to successive breakdowns occurring during a half cycle. The velocity of a shock wave may be calculated from the slope of the photographic image of the shock. The slowing down of the shock wave as it progresses outward from the coil is evidenced by the change of this slope.

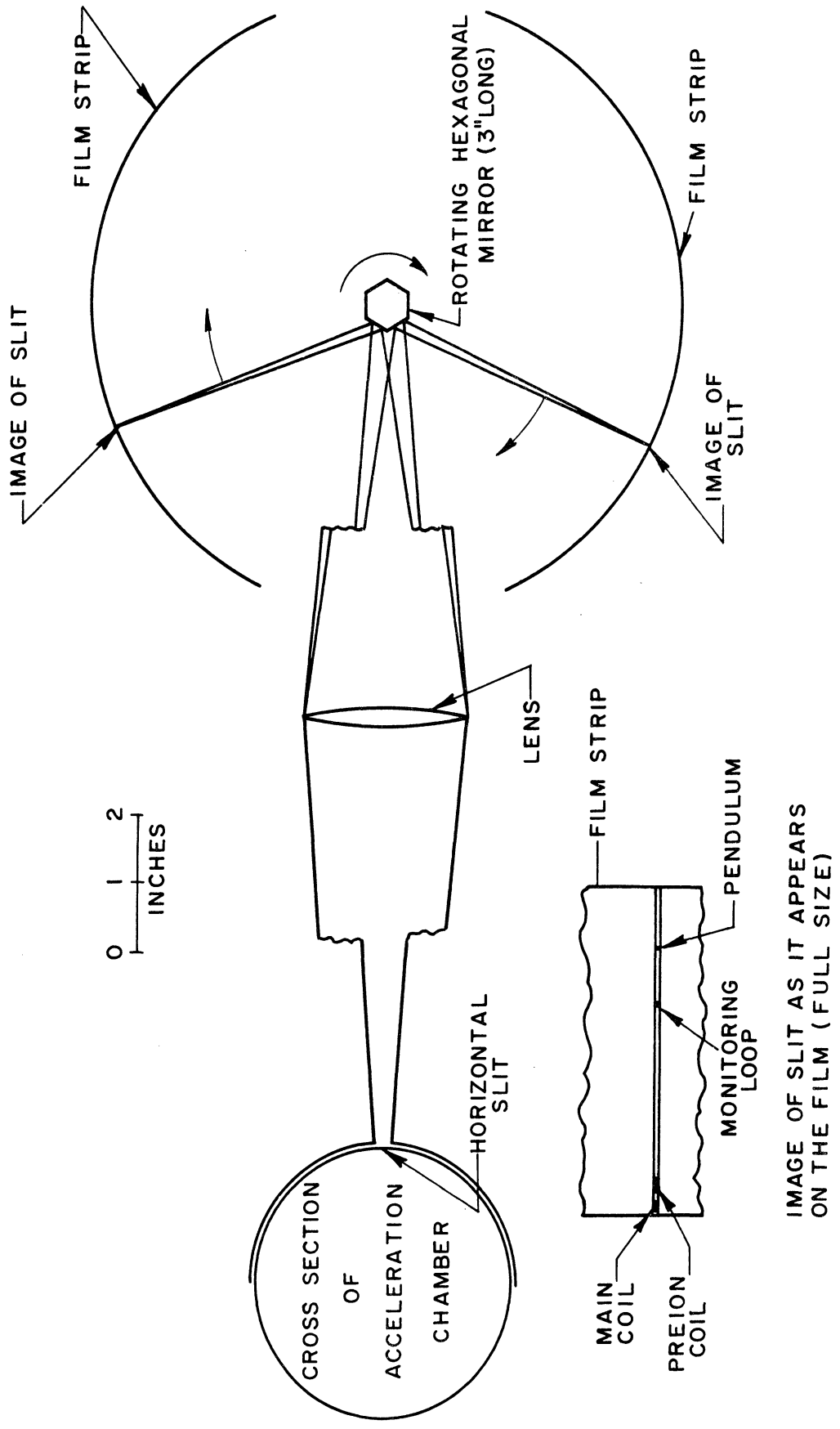

Fig. 7.11. Rotating Mirror Camera System for Taking Streak Photographs — Shown in Position to Study Motion Parallel with Acceleration Chamber Axis.

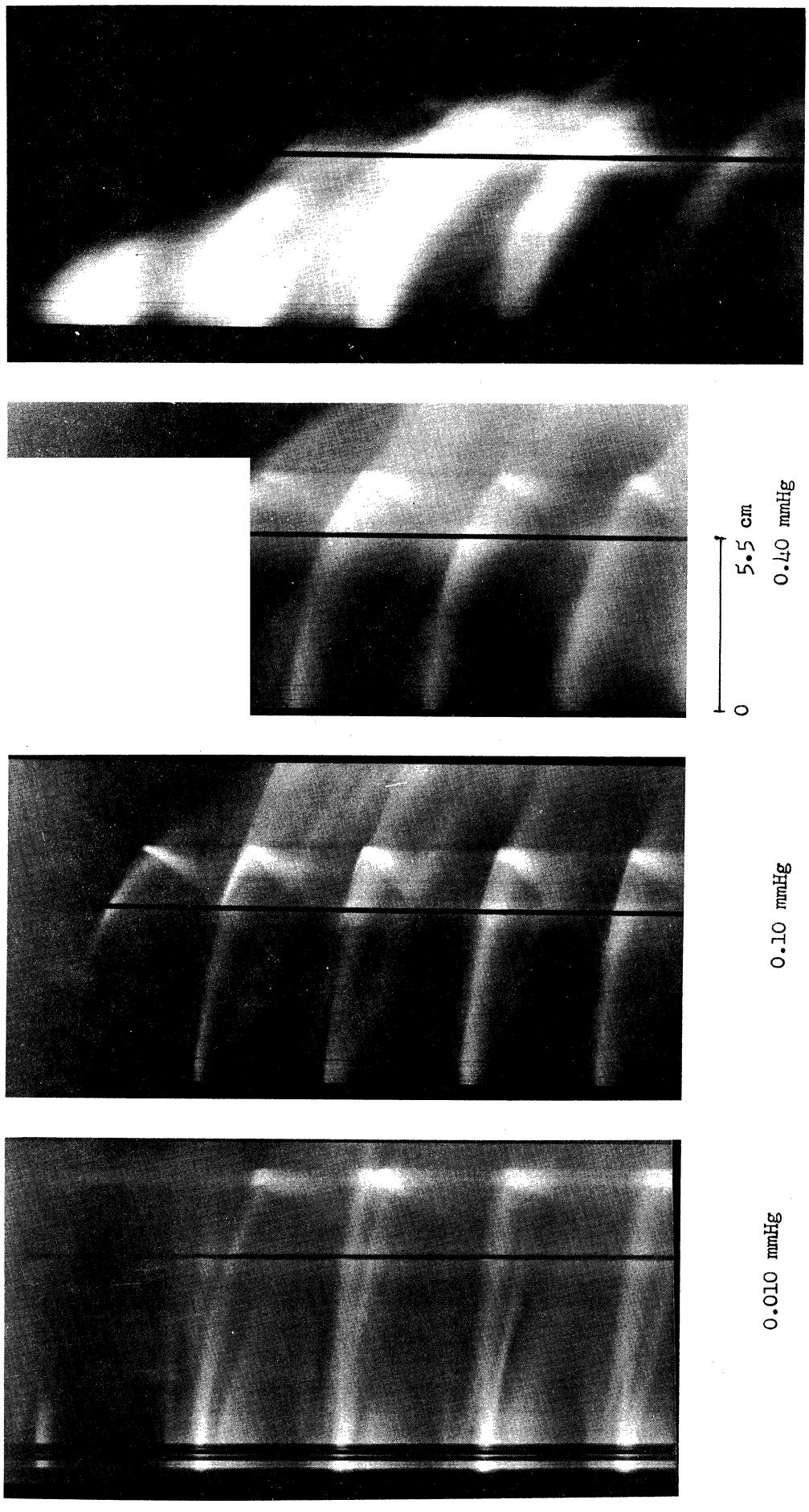

Fig. 7.12. Streak photographs showing axial motion along the tube axis in argon; the image repeats each half cycle, or once each 9 μsec.

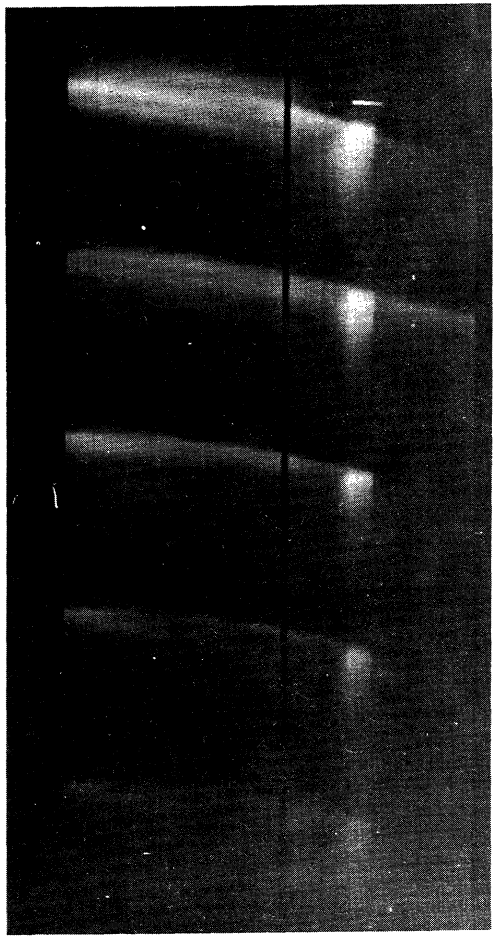

0.10 mmHg

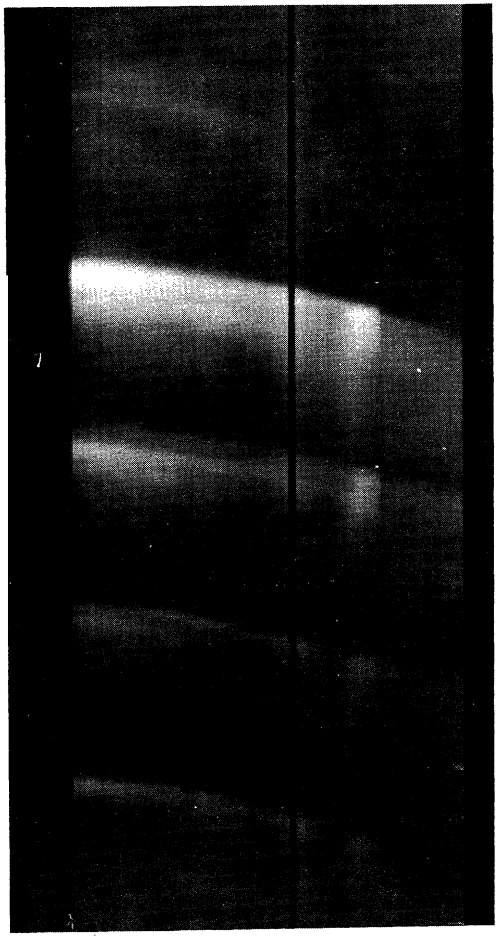

0.40 mmHg

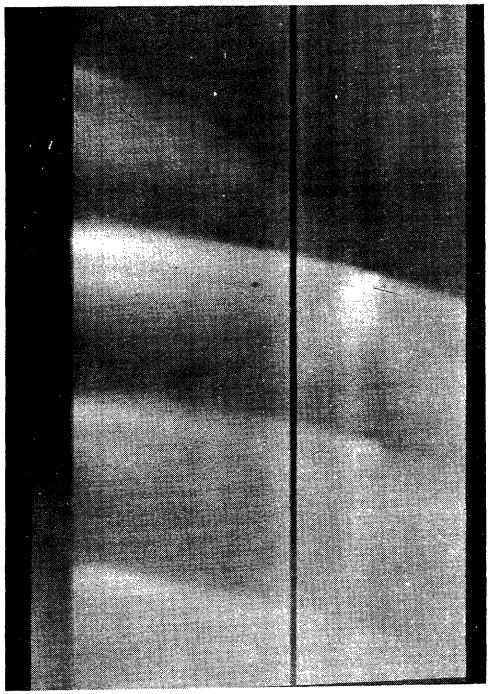

1.0 mmHg

Fig. 7.13. Streak photographs showing axial motion along the tube axis in helium; the image repeats itself each half cycle, or once each 9 μsec.

In Table 7.2 is tabulated information obtainable from these axial streak photos along with other measurements for comparison. The following items pertain to this table:

a. Shock velocity (column 3) is taken from the slopes of the shock images at the pendulum position. Due to the weakness (or complete absence) of the first half cycle shock in Figs. 7.12 and 7.13, the velocities used in Table 7.2 were taken in each case from the second half cycle image (second image appearing in each case).

b. Shock and gas velocities (columns 3 and 5) are seen from the streak photographs to be considerably higher as the plasma emerges from the coil than at pendulum position.

c. In relation to the temperatures (column 6) and mean free paths (columns 7 and 8), the following can be said: Space-charge forces tend to cause the ions and electrons to travel down the tube with a common axial velocity in a manner similar to the effect of space-charge forces on radial motion noted in Chapter III. Thus, the ions receive considerably more energy per particle than the electrons, and therefore have, after randomization of the energy, a much higher temperature than the electrons. Since at lower pressures the mean free path for equilibration of ion and electron temperatures is very long, we might then expect at these lower pressures to find the ions behind the shock to be at the temperature listed, but to find, for several centimeters of shock travel, that the electrons are at a substantially lower temperature than the ions.

Table 7.2. Axial Plasma Flow Characteristics in the Induction Accelerator

a. From measurement of streak photographs at z = 15 cm.
b. Using definition of Mach No., $M \triangleq v/c$, where c is the velocity of sound in the gas ahead of the shock, and v is the shock velocity.
c. Eq. 5.10.
d. Eq. 5.8; based on T_x = 293°K (temperature of gas ahead of the shock).
e. M.f.p. for each species, ions or electrons, to reach its equilibrium temperature.
f. M.f.p. for ions and electrons to equilibrate.
g. From Fig. 7.6.
h. Calculated by combining velocity and momentum measurements.
i. Using the results from the smaller calorimeter at z = 15 cm, Figs. 7.7 and 7.8, thereby measuring energy in the center of the stream at the pendulum position.

1	2	3	4	5	6	7	8	9	10	11	12
Gas	Initial Pressure (mmHg)	Shock Velocity[a] (cm/μsec)	Shock Mach Number[b]	Gas Velocity[c] Behind Shock (cm/μsec)	10^n Temperature Behind Shock[d] (°K)	Relaxation Mean Free Path Behind Shock (cm) λ_1^e	λ_2^f	Momentum Per Unit Area[g] gm-cm/sec-cm²	Energy Per Unit Area (joules/cm²) Directed from Streak Photo and Pendulum[h]	Total from Small Calorimeter[i]	Mass per Unit Area[h] (μgm/cm²)
A	.010	2.2	67	1.65	—	—	—	1.4	.12	.35	.85
	.10	1.2	36	.90	120,000	.37	100	4.4	.20	.37	4.9
	.20	.93	28	.70	73,000	.073	20	5.9	.21	.40	8.4
	.40	.79	24	.59	37,000	.009	2.5	7.8	.23	.45	13
	1.0	.61	18	.46	21,000	.0015	.37	10.3	.24	—	22
He	.10	2.0	20	1.5	37,000	.037	3.2	1.7	.13	.42	1
	.40	1.8	18	1.35	30,000	.0073	.61	3.0	.20	.58	2.2
	1.0	1.6	16	1.2	24,000	.0018	.12	4.4	.26	.68	3.7

d. Comparison of the energy calculations, columns 10 and 11, reveals an interesting fact. For argon, except at the lowest recorded pressure, the energy of directed motion is close to half the total energy. In helium, however, the energy in directed motion appears to be consistently less than half the total. Since the shock theory in Chapter V leads us to believe that thermal and directed energy behind the shock are equal, this suggests that in helium but not in argon there is a significant surplus of energy. As pointed out in the previous discussion of energy carried out in the calorimeter section (Section 7.5), the majority of this excess energy (in excess to energy in directed and random motion) is probably attributable to recombination of ions and electrons on the calorimeter surface.

e. A rough comparison can be made between the mass derived from experimental measurements (column 12) and the mass known (from knowledge of pressure) to be in the acceleration chamber before a pulse. The mass in any given initial volume V_o will be:

$$M_o = n_o m V_o \quad ,$$

where n_o is the initial particle density and m is the mass per particle. The mass per unit cross-sectional area will therefore be

$$\frac{M_o}{A} = n_o m \ell \quad ,$$

where ℓ is the length of volume V_o. Taking now the measured value for M_o/A from column 12 of Table 7.2 and using the values for $n_o m$ calculated for each pressure and type of gas, we can construct Table 7.3 below, indicating an equivalent length ℓ

from which the measured mass must have originated. When interpreting Table 7.3, one should remember that the measurement is taken 15 cm from the end of the acceleration chamber (see Fig. 6.5). A possible interpretation from Table 7.3 is that at lower pressures some gas flowed back each half cycle and so was accelerated more than once against the pendulum.

Table 7.3. Equivalent Length ℓ

$$\ell \triangleq \frac{M_o/A \text{ (measured)}}{n_o m \text{ (calculated)}}$$

gas \ P	0.10 mmHg	1.0 mmHg
He	50 cm	15 cm
A	21 cm	9 cm

Let us consider now the measurement of radial motion of the ionized gas; typical groups of streak photos of the radial motion are shown in Figs. 7.14, 7.15, and 7.16. Again we note the appearance of a new discharge each half cycle, and the compression of the gas is indicated by the triangular nature of the images. The significance of each of these photo groups will now be considered.

Figure 7.14, showing compression of argon at various pressures, will first be studied. The obvious conclusion from this series is that the rate at which compression takes place is inversely related to the ambient pressure, i.e., to the initial particle density; this is in accord with theory. Magnetic probe measurements, discussed later, taken under conditions identical with these photos show in the two higher

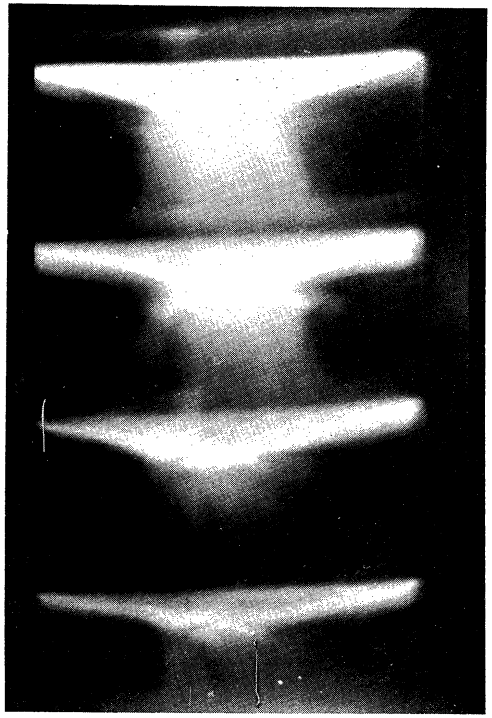

(a) 0.025 mmHg

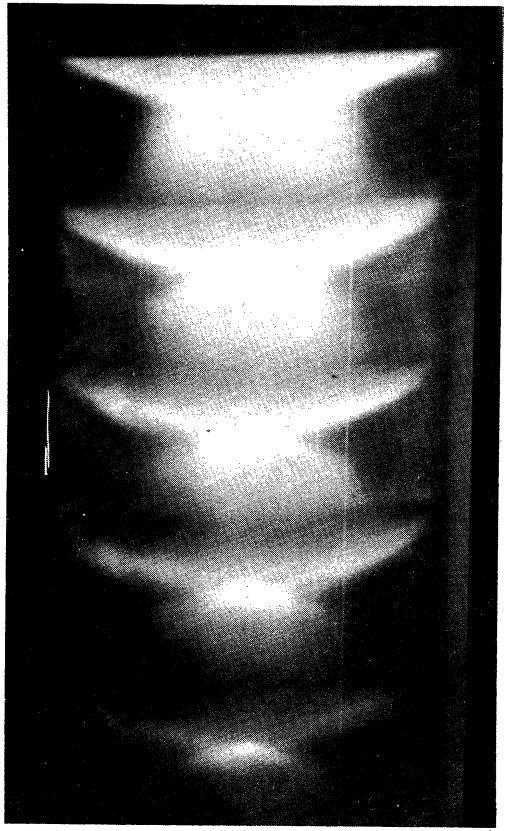

(b) 0.20 mmHg

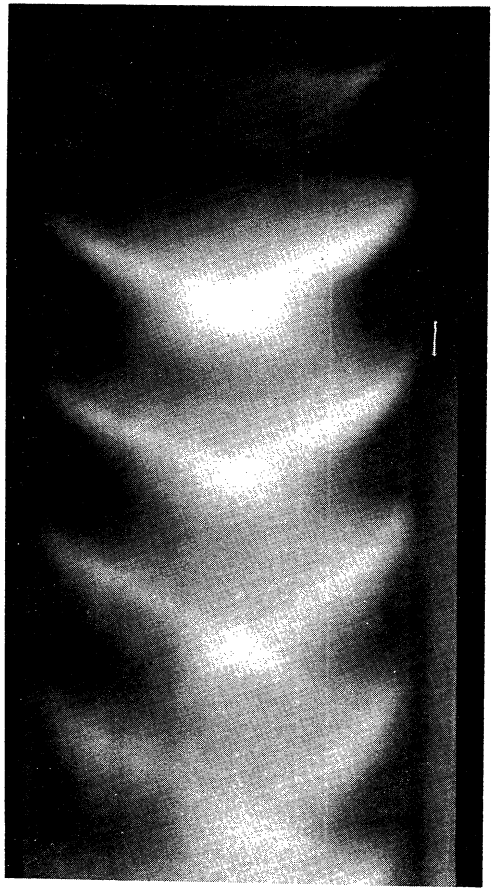

(c) 1.0 mmHg

Fig. 7.14. Streak photographs showing radial compression of argon; z = 2.5 cm; one image appears each half cycle, and half cycles are 9 μsec. apart.

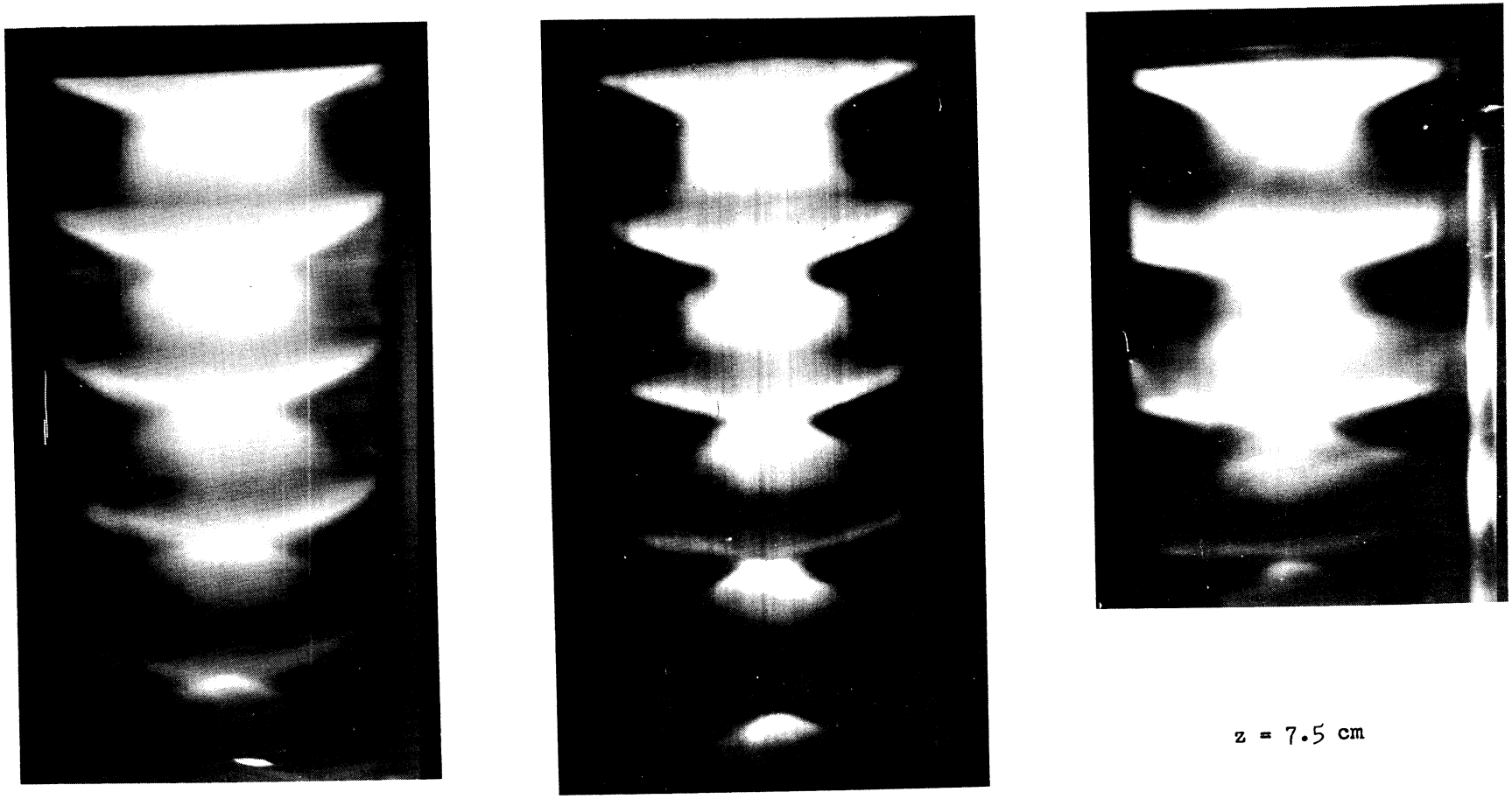

z = 2.5 cm

z = 5 cm

z = 7.5 cm

Fig. 7.15. Streak photographs showing radial compression of argon initially at .20 mmHg; one image appears each half cycle, and half cycles are 9 μsec. apart.

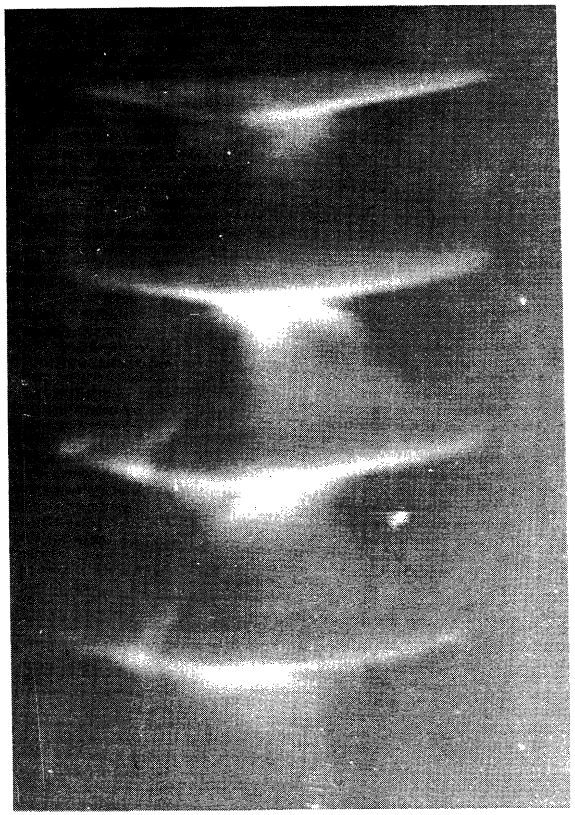

(a) 0.20 mmHg

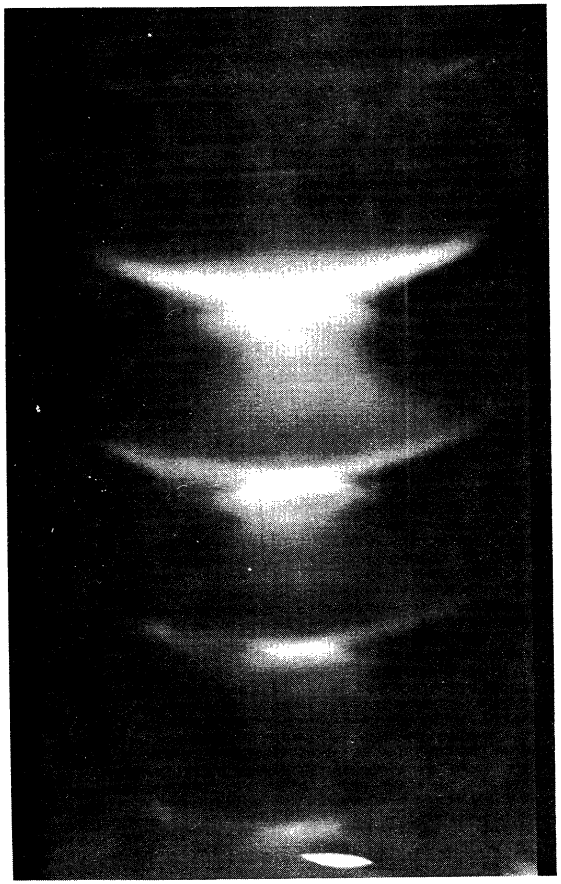

(b) 1.0 mmHg

Fig. 7.16. Streak photographs showing radial compression of helium; z = 2.5 cm; the image repeats itself each half cycle, or once each 9 μsec.

density situations (0.20 and 1.0 mmHg) existence of a current sheath whose radially inward progression corresponds reasonably well with the photographic record. The snowplow analysis should therefore be applicable. Comparing the time for compression in Fig. 7.14(b) with the theoretical curves in Fig. 4.9 indicates that the gas compresses much as a 10^{22} particle/m^3 gas would. Inasmuch as the gas originally contained about 6×10^{21} molecules/m^3, it would seem that not a great deal of gas is escaping through the sheath. The diffuse character of both the streak photo (Fig. 7.14(c)) and the measured current density distribution (Fig. 7.25) prevents making a similar comparison at 1.00 mmHg.

At 0.025 mmHg (Fig. 7.14(a)), the magnetic probe study does not reveal formation of a skin current sheath, but the experimental compression time does correspond roughly to the theoretical (snowplow) prediction for the particle density ($\sim 9 \times 10^{20}/m^3$) existing at that pressure.

The snowplow concept is not adequate to treat the "rebound" revealed each half cycle in the Fig. 7.14 photos. The minimum radius is better explained on the basis of an increasing internal pressure of the gas which eventually equals or surpasses the inward pressure of the external field. Thus, while the snowplow theory can be used to study the rate at which compression takes place and the approximate time taken for the gas to compress, the characteristics of the gas at maximum compression are better handled by the adiabatic theory in Section 4.6.3. For instance, under the assumption that initially in each half cycle the gas is at room temperature (293°K), Eq. 4.48 indicates on the second half cycle that argon initially at 0.20 mmHg approached about 60,000°K at maximum

compression. This should if anything be a high estimate, since some energy has gone into acceleration of the gas axially out of the coil; it is interesting to note, however, that this temperature and the temperature of the gas flowing axially down the tube behind the axial shock wave at this initial pressure are about the same (see Table 7.2).

We next turn to Fig. 7.15. Here gas and field conditions are identical in all three shots, and the radial motion of the gas is revealed at three different positions, within the main coil (z = 2.5 cm), at the edge of the coil (z = 5.0 cm), and beyond the coil (z = 7.5 cm). Close scrutiny of these pictures indicates that, for increasing z, the compression starts at increasingly later instants each half cycle. This phenomenon is corroborated by the magnetic probe information (see Figs. 7.21, 7.22, and 7.23). Such action should not be unexpected, since, with increasing z at any instant, the strength of the compressing field decreases whereas the pressure of the gas remains the same or may even increase due to the addition of gas being forced out of the interior of the coil. The fact that the gas appears to ionize at the beginning (e_θ peak) of each half cycle but (for instance at z = 7.5 cm) delays before imploding suggests that there is an internal pressure which must be overcome before radial motion can take place.

Finally, Fig. 7.16 will be considered. These streak photos should be compared with those in Fig. 7.14 with the difference being that helium rather than argon is now the working substance. Again, we note time for compression being directly proportional to particle density. At equal initial particle densities (pressures) we see that helium compresses in something like half the time required for argon; this is in approximate agreement with theory (see Fig. 4.9). Note also that in Fig. 7.16(b) oscillation of the plasma column radius is detectable.

7.7 Magnetic Probe

The voltage signal appearing across the terminals of a wire coil in a magnetic field is proportional to the time-rate-of-change of magnetic flux threading the coil; the time-integral of this signal divided by the area of the coil, for a small circular coil, then yields the strength at the coil position of the component of magnetic field parallel with the coil axis. A small search coil (magnetic probe) applied in this manner has been used to great advantage in detecting detailed characteristics of the discharge in the pulsed crossed-field accelerator. It is the purpose of this section to describe these measurements.

The theory of operation is completely encompassed by the simple statement of Faraday's Induction Law given in the previous paragraph. The technique has been applied quite often in connection with experiments concerned with controlled thermonuclear research[88-91]. The present aim is to apply these already developed techniques in order to gain a better understanding of the processes involved in our particular experiment.

The construction of the probe and the method in which it was used are shown in Fig. 7.17. The stainless steel support tube was free to rotate and slide in the rubber stopper, thereby enabling the probe coil to be positioned variously within the discharge. The vacuum seal in this arrangement was adequate to our needs, allowing the tube to be pumped down well into the 10^{-5} mmHg range and causing negligible leakage when the tube was filled with the test gas (see Section 6.3). Note that we have achieved satisfactory results by inserting the enameled wire directly into the plasma, whereas most other investigators separate their probes from the plasma by glass or quartz tubes.

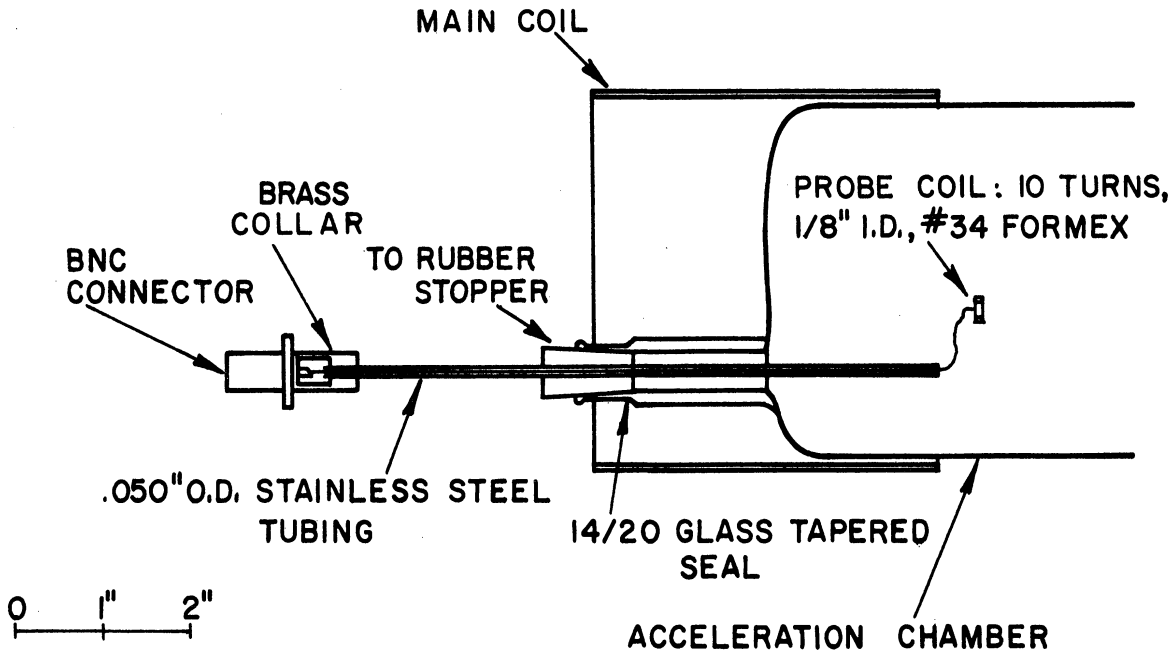

Fig. 7.17. Cross Section View of Magnetic Probe in Acceleration Chamber.

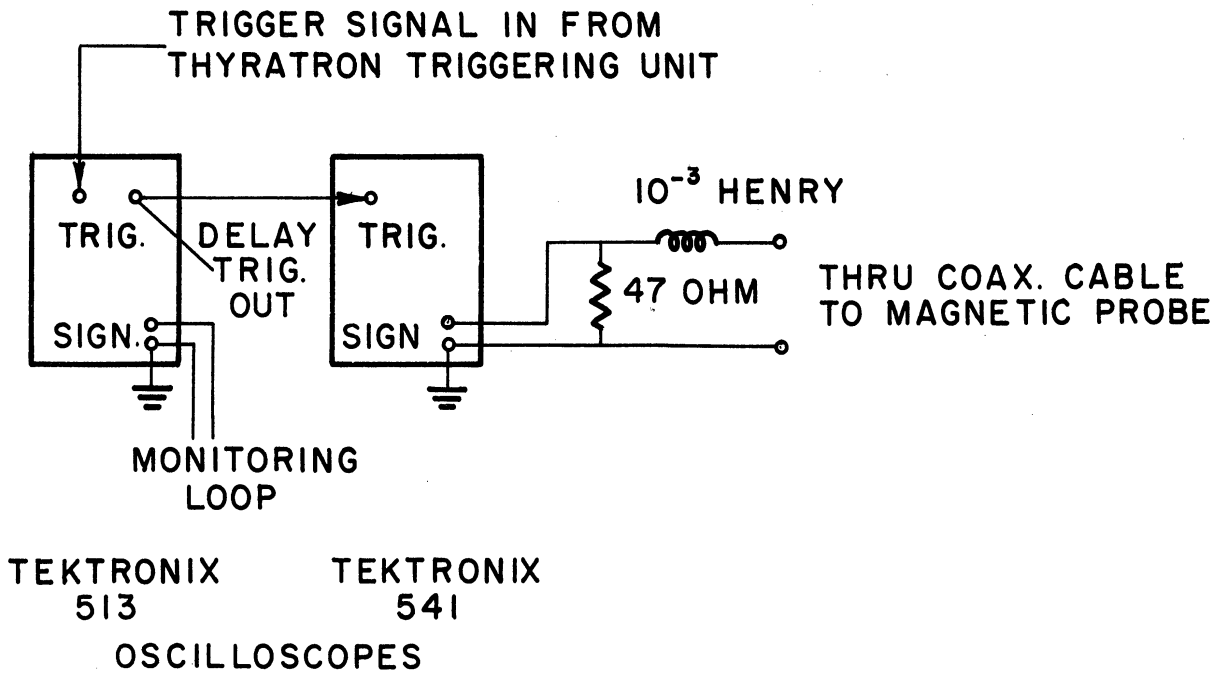

Fig. 7.18. Magnetic Probe Circuit.

The probe was connected through a coaxial cable to the integrating circuit shown in Fig. 7.18. This integrator then caused the signal displayed on the oscilloscope to be proportional to the magnetic field strength at the probe at any instant. An L-R circuit of the sort employed will give a true integration only of components whose radian frequencies are much greater than R/L. The values of R and L were therefore chosen to make this ratio much less than the lowest expected frequency, namely the natural frequency of the main circuit.

In Fig. 7.19 are shown typical integrated and unintegrated probe signals. The validity of the integrator may be observed in the Fig. 7.19 traces. Figure 7.19 and the early part of Fig. 7.20 illustrate the absence of the magnetic field in the interior of the plasma; this is discussed further later.

In order that data taken at various points within the discharge be significant, assurance must be obtained that the discharge characteristics remain constant from shot to shot. This is done by carefully regulating the gas pressure and capacitor voltages and by observing the monitoring loop signal and the ballistic pendulum at each shot. The results of this monitoring showed that at higher densities, the discharge repeated itself with excellent consistency; Fig. 7.3 shows the monitoring loop signal and ballistic pendulum measurement for five consecutive higher density pulses.

Data were generally taken on the second half-cycle of the capacitor current, since ionization and repeatability on the first half-cycle were generally not adequate in spite of preionization. Since a fast sweep speed was desired for sufficient time resolution, the Tektronix 541 oscilloscope used to detect the probe signal was triggered from the

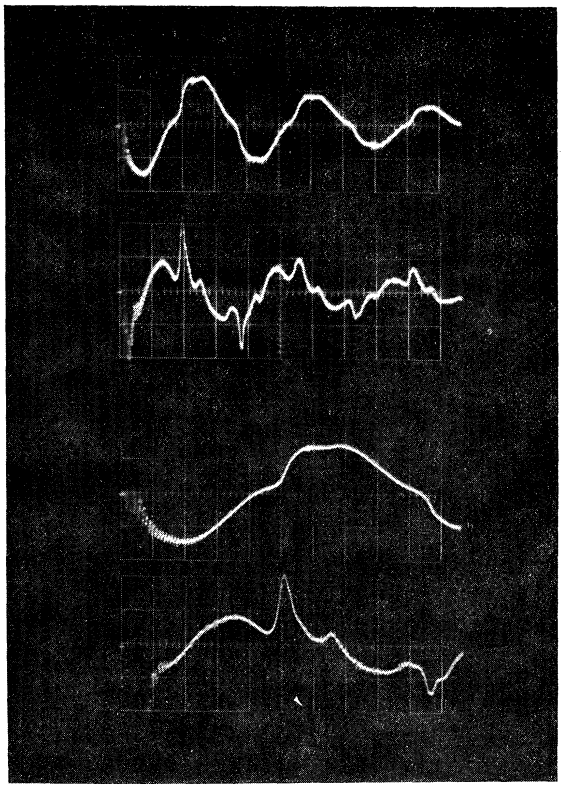

a) integrated; 5 μsec. per major horizontal division

b) unintegrated; 5 μsec. per major horizontal division

c) integrated; 2 μsec. per major horizontal division

d) unintegrated; 2 μsec. per major horizontal division

Fig. 7.19. Integrated and unintegrated magnetic probe signals; 20 volts per major vertical division for unintegrated traces and 2 volts per division for integrated traces (1 volt on the integrated traces is equivalent to .32 webers/m^2); argon at .20 mmHg; probe located at approximately z = 2.5 cm, r = 2.5 cm.

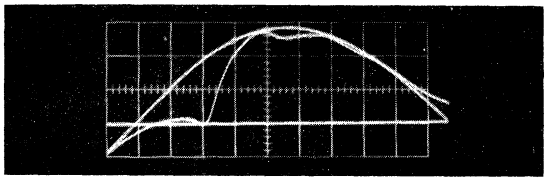

Fig. 7.20. Integrated magnetic probe signal; z = 2.5 cm, r ≅ 2cm; helium at 1.00 mmHg; 1 μsec. per major horizontal division; sweep delayed 8 μsec. so second half cycle is recorded; signal in the absence of a discharge is also shown.

delayed trigger circuit in the Tektronix 513 oscilloscope; this triggering arrangement is indicated in the circuits shown in Figs. 6.4 and 7.18.

Randomness in the timing of the spark gap switches and the 513 delay circuit could potentially cause error when correlating the several probe signals necessary in each run. (A "run" is a series of eight to ten consecutive shots each taken with the probe in the same z location but in a different radial position.) Repeated observation of these indicated that the randomness in the 513 delay circuit was under one tenth microsecond but that a total time variation of three or four tenths of a microsecond might appear due to the spark gaps. This being of the same order as the time resolution of the desired measurements, the following procedures were followed to reduce the effective time jitter. For each shot, the oscilloscope recording the monitoring loop signal was triggered at time zero and was operated with a fast sweep speed, so that variations in the times at which the spark gaps fired could be detected; variations of ± 0.2 microseconds about an average time were generally encountered. The oscilloscope observing the magnetic probe signal was then triggered after a time delay which would insure that the zero crossing of the signal just previous to the half cycle of interest would appear on the oscilloscope screen. A typical probe signal as used in these measurements is shown in Fig. 7.20 with and without plasma. Zero time for magnetic probe data interpretation was taken as the instant at which the probe signal without discharge crosses the horizontal axis on a pulsing which the simultaneous monitoring loop signal indicates has the average spark gap delay time, as discussed above. Each pulsing in a run was related to

this zero time by observing the time deviation from the average of the monitoring loop signal for that shot. In this way it is felt that data taken on consecutive pulses can be compared time-wise with a precision of about a tenth of a microsecond.

From traces such as shown in Fig. 7.20, taken with the arrangement indicated in Figs. 7.17 and 7.18, relative values of b_z, the axial component of magnetic field, are obtained at various times and places. An absolute scale must be attached to these measurements. This is done by comparing the peak probe signal at several probe positions in the absence of plasma with the calculated value of magnetic field for the peak coil current at those positions (given in the Appendix); the accuracy of this calibration depends on the accuracy with which the value of charging voltage, capacitance and frequency of the main circuit are known. Independently, this calibration may be checked by knowing the voltage of the integrated probe signal, the number of turns on the probe coil, and the area of the coil. As a result of these considerations, approximately a ± 10 percent accuracy may be attached to the absolute magnetic field calibration. However, relative accuracy appears to be substantially better than this.

Using the precautions and calibration procedure outlined above, the results which were obtained by the magnetic probe method are shown in Figs. 7.21 through 7.27 and are discussed below. In each of these figures, the value of b_z obtained directly from the probe signal is plotted as a function of radius for various times and axial positions. Zero time is taken as the beginning of the second half cycle while $z = 0$ is at the center of the coil, as usual.

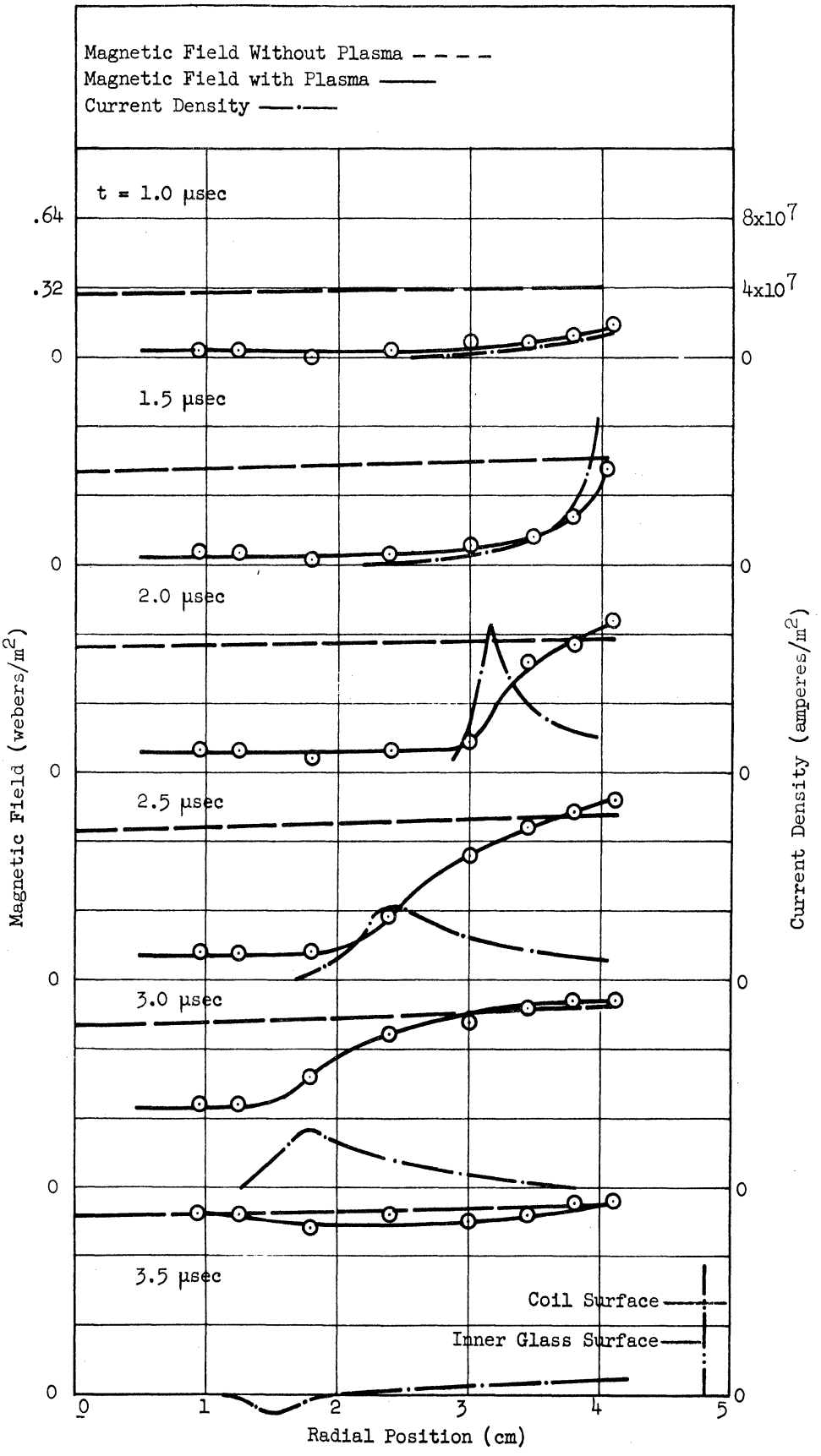

Fig. 7.21. Results of Magnetic Probe Measurements (Argon, 0.20 mm of Hg, z = 2.5 cm).

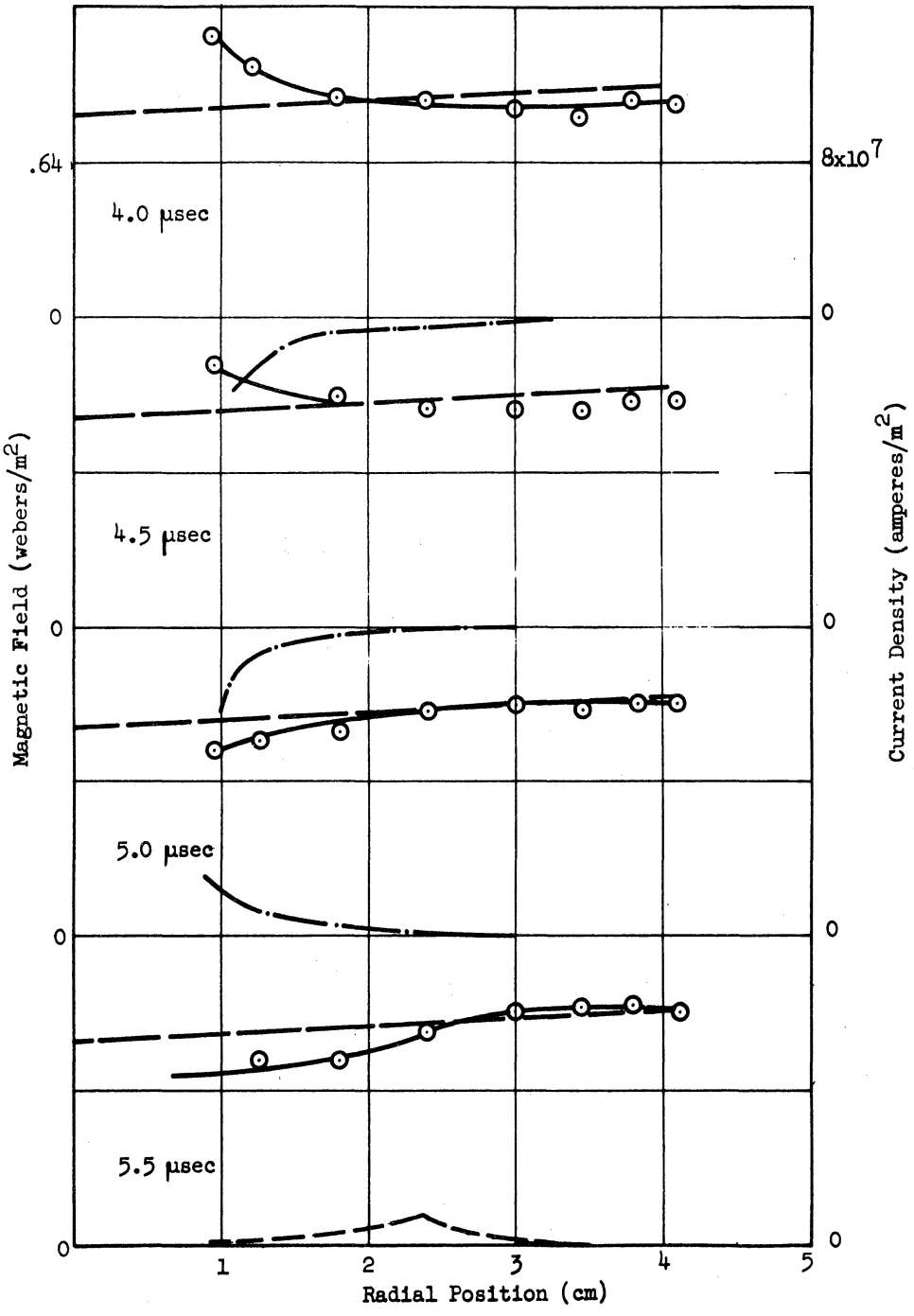

Fig. 7.21.(concluded).

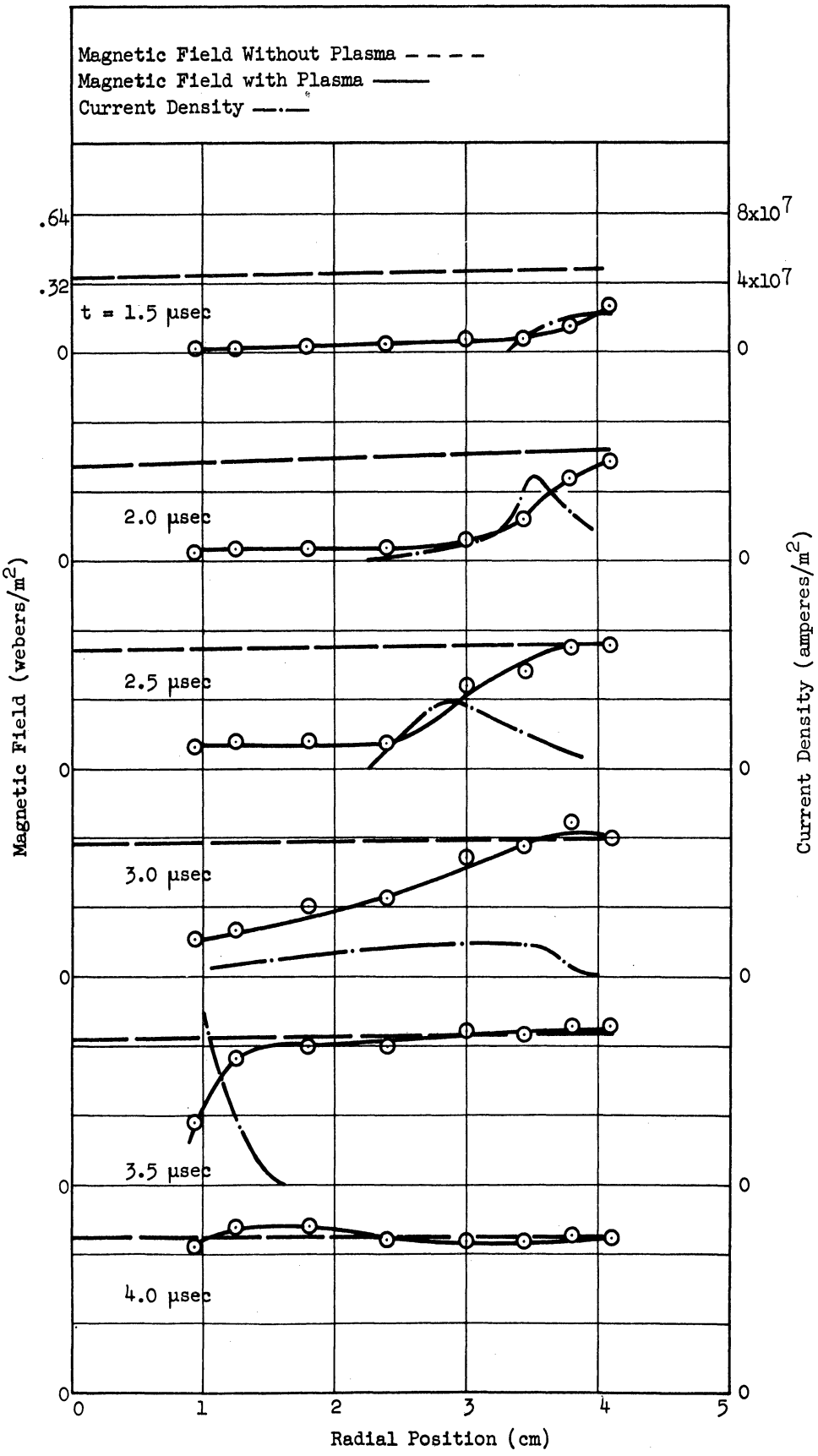

Fig. 7.22. Results of Magnetic Probe Measurements (Argon, 0.20 mm of Hg, z = 5.0 cm).

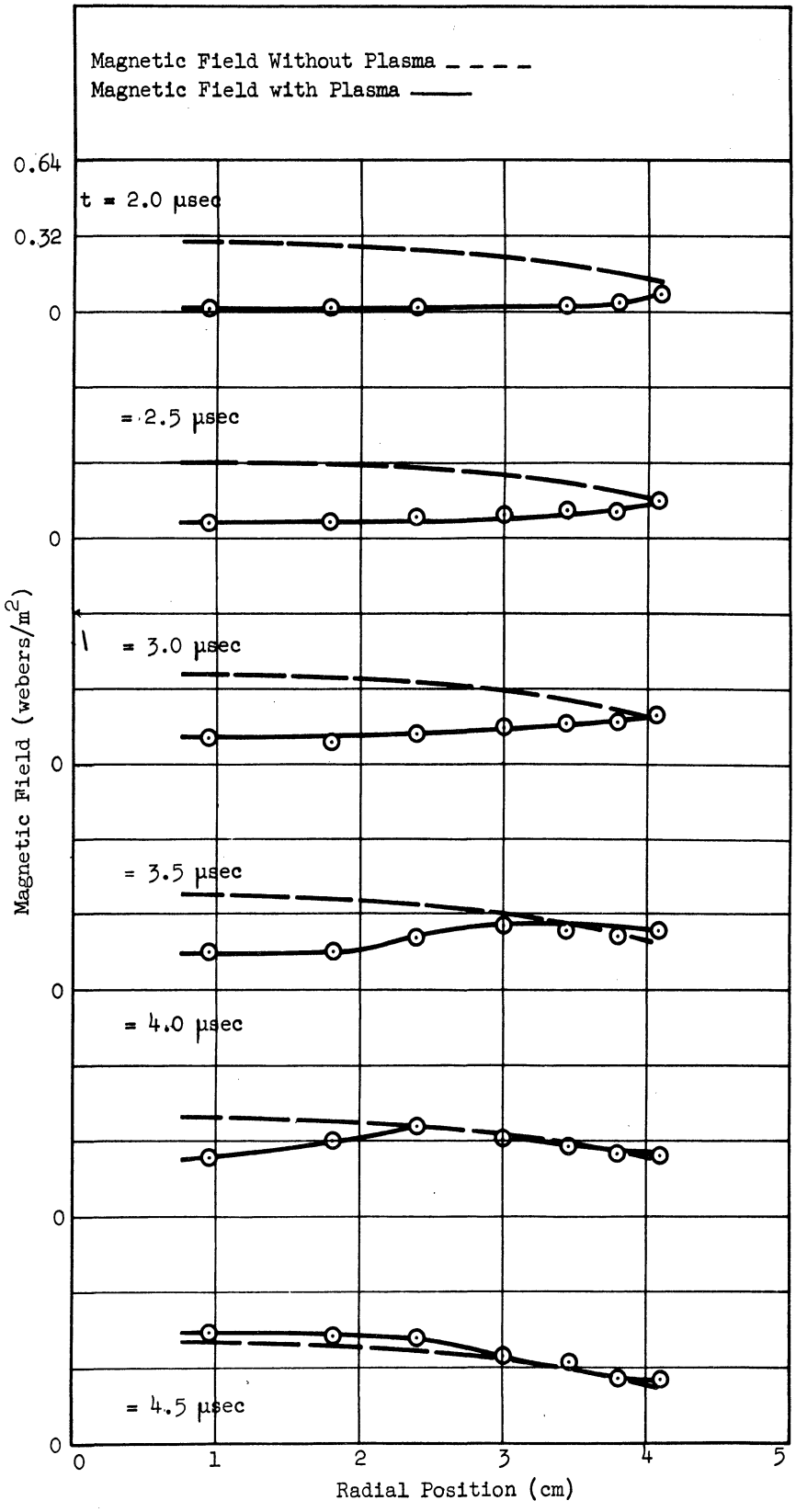

Fig. 7.23. Results of Magnetic Probe Measurements (Argon, 0.20 mm of Hg, z = 7.5 cm).

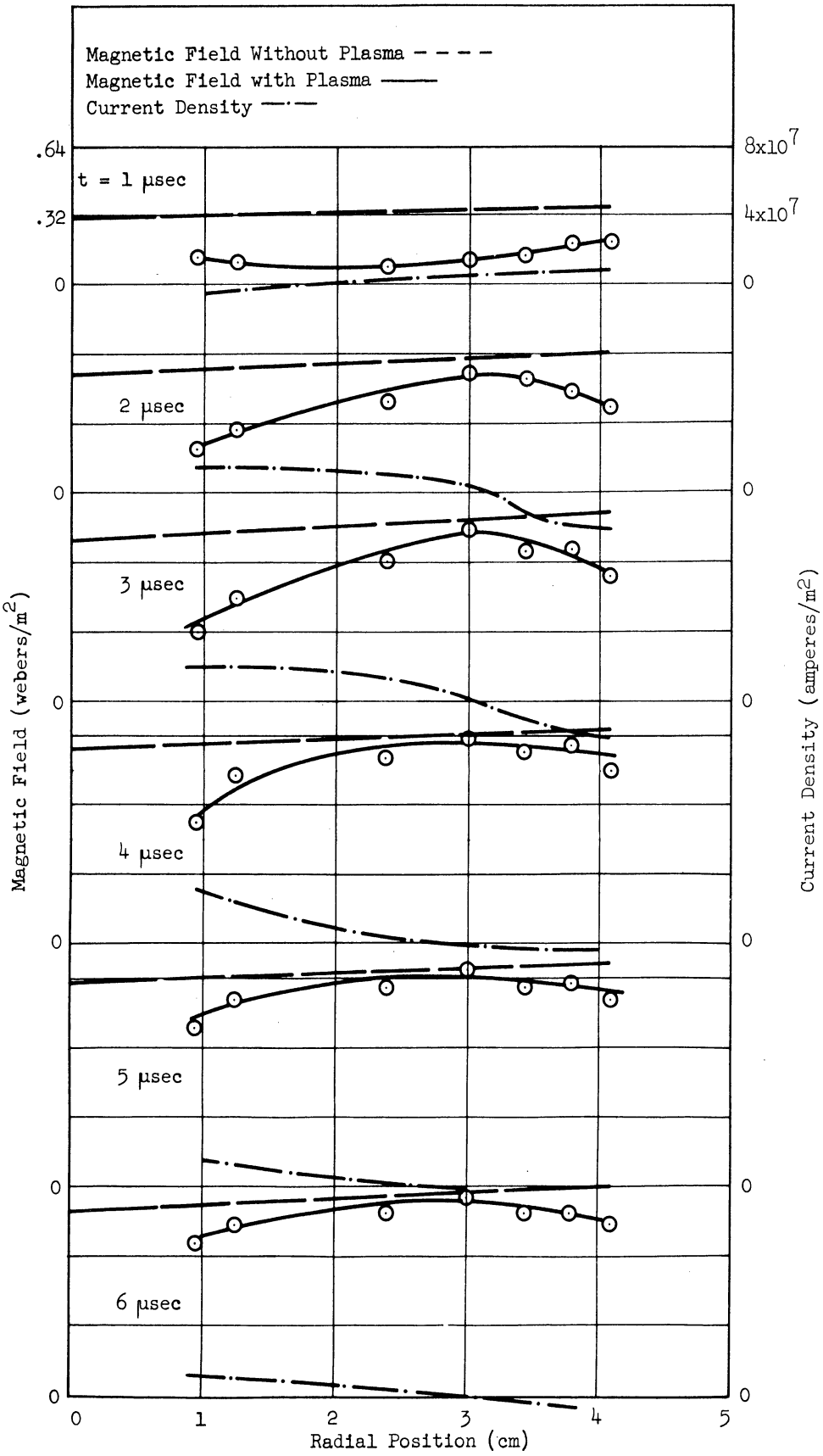

Fig. 7.24. Results of Magnetic Probe Measurements (Argon, 0.025 mm of I z = 2.5 cm).

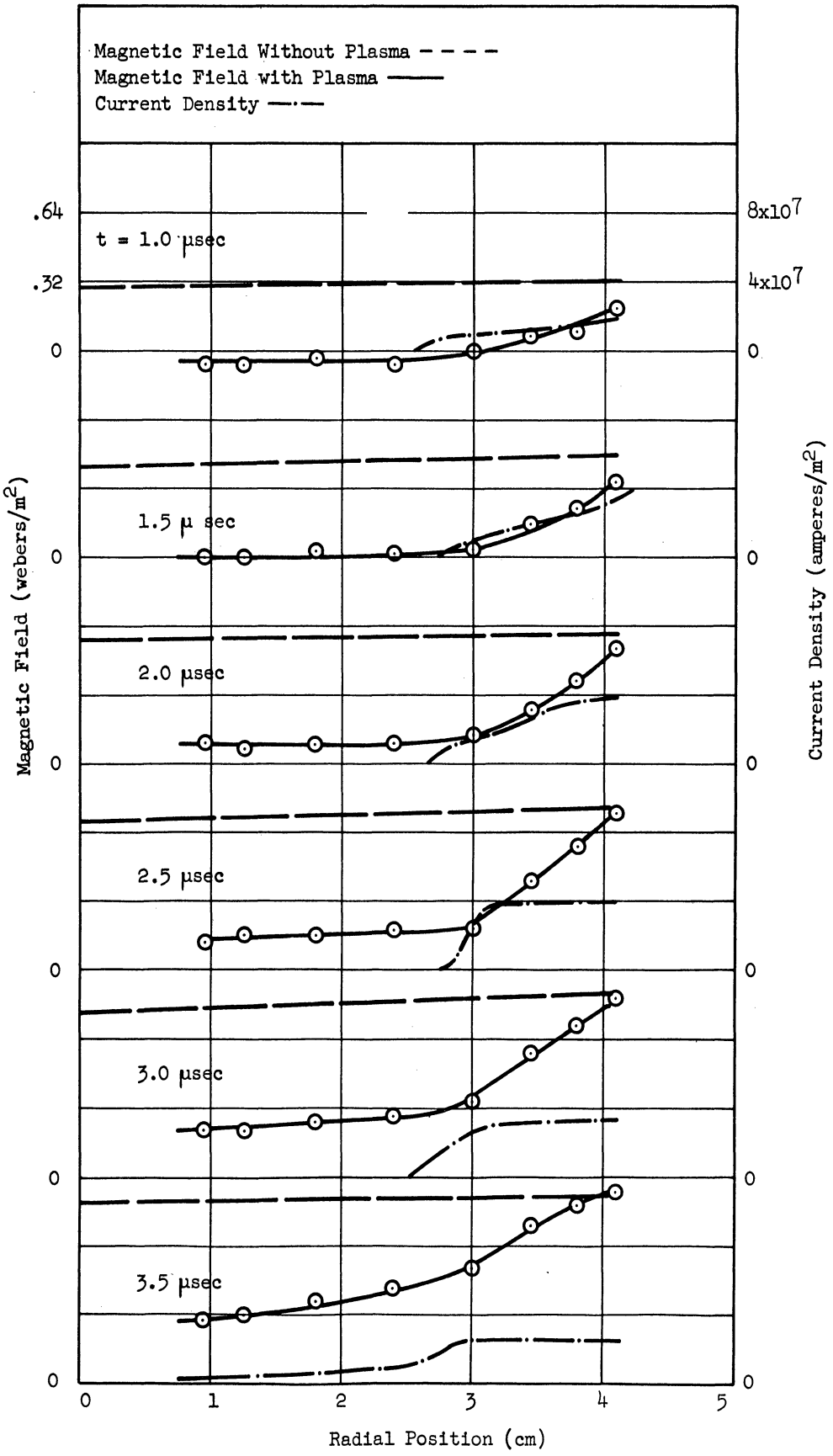

Fig. 7.25. Results of Magnetic Probe Measurements (Argon, 1.0 mm of Hg, z = 2.5 cm).

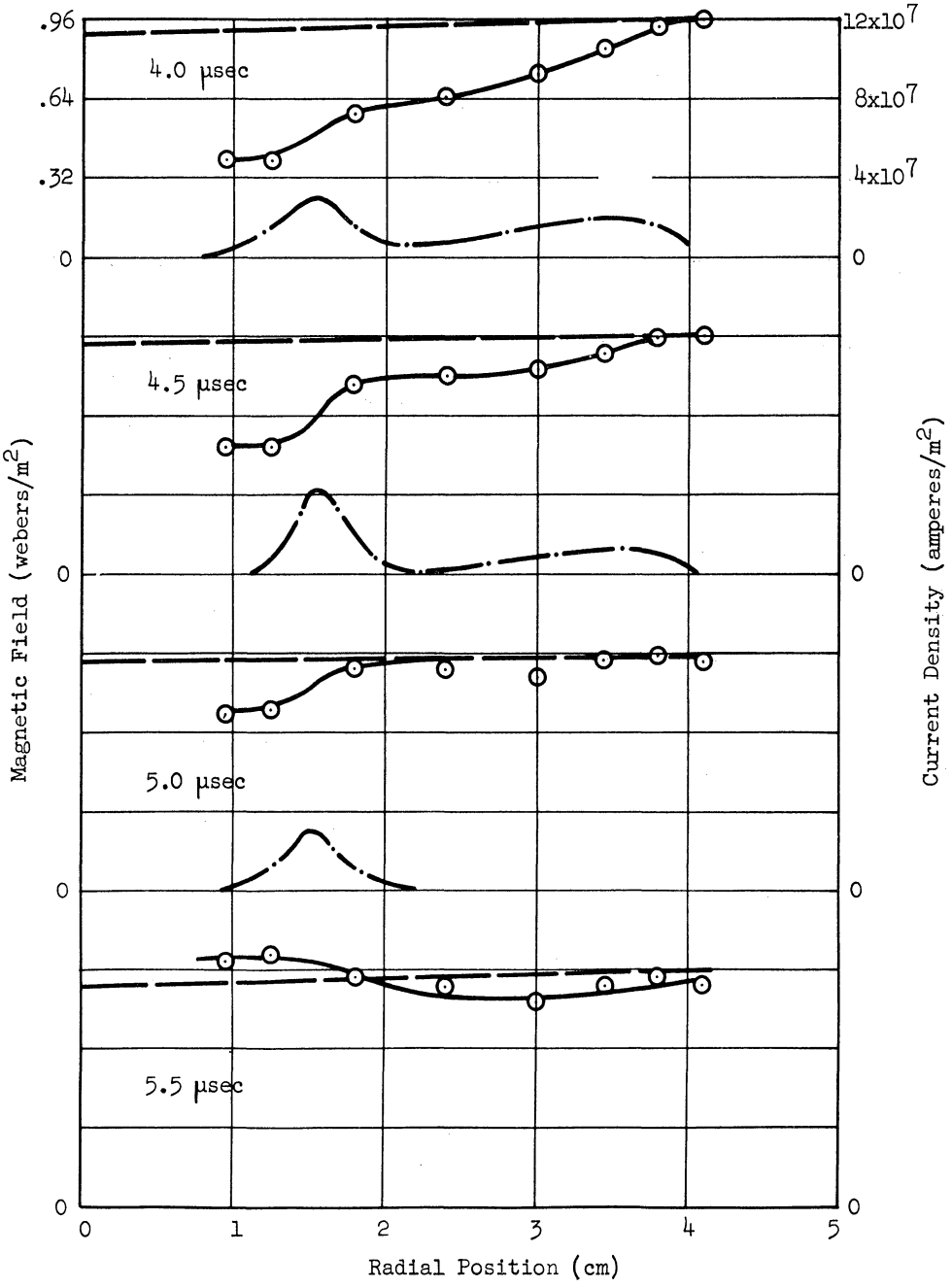

Fig. 7.25. (concluded).

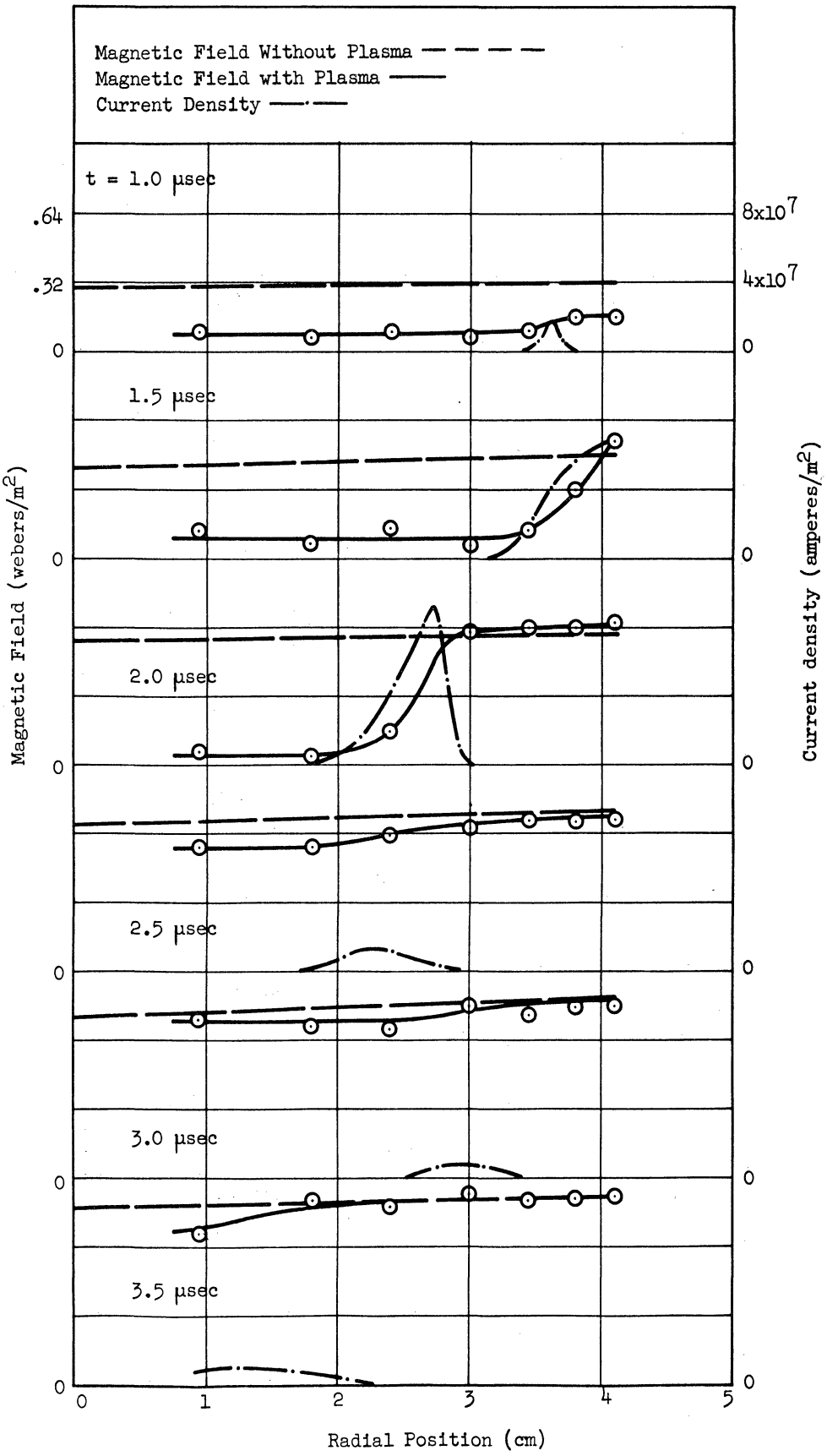

Fig. 7.26. Results of Magnetic Probe Measurements (Helium, 0.200 mm of Hg, z = 2.5 cm).

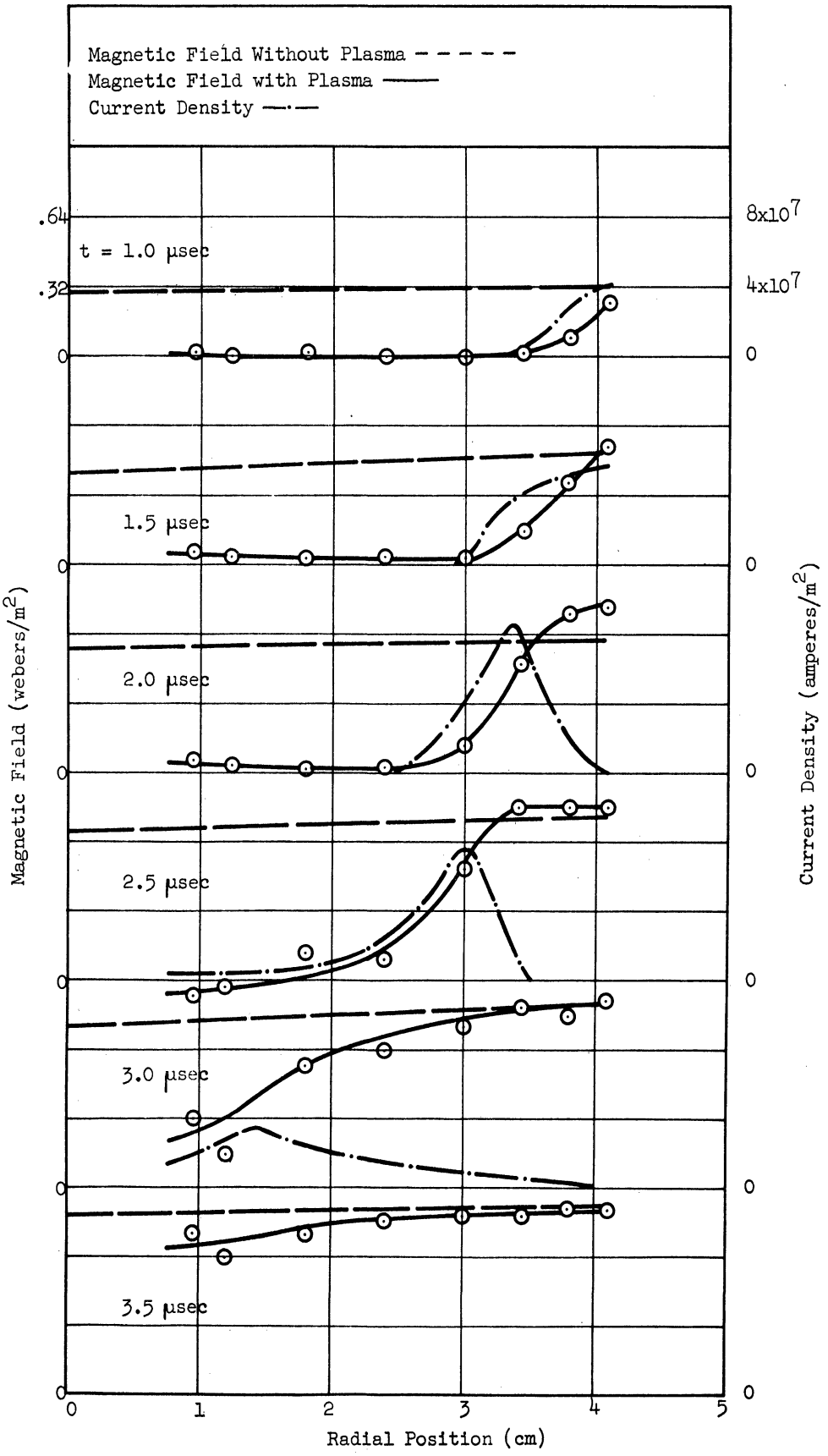

Fig. 7.27. Results of Magnetic Probe Measurements (Helium, 1.0 mm of Hg, z = 2.5 cm).

Current density in the plasma region is related to the magnetic field through the curl relation,

$$\text{curl } H = i \quad . \tag{7.1}$$

In our case, the current is tangentially directed, reducing Eq. 7.1 to the following:

$$\mu_o i_\theta = \frac{\partial b_r}{\partial z} - \frac{\partial b_z}{\partial r} \quad ,$$

where, as in Eq. 4.6, the induction and intensity fields have been related through the vacuum permeability μ_o. In Chapter IV, where action within a long solenoid was considered, b_r was assumed zero. In order to determine to what extent this assumption can be made in the experimental situation, a probe measuring the radial component of field was placed at various z-locations on the r = 1" surface. At no location on this surface out of z = 3" did the slope $\partial b_r/\partial z$ become comparable with the term $\partial b_z/\partial r$. Therefore using the simplified formula,

$$i_\theta = -\frac{1}{\mu_o}\frac{\partial b_z}{\partial r} \quad ,$$

the current density has been constructed on each of the probe data plots except Fig. 7.23 directly from the $b_z(r)$ curves. (The significance of the slope in Fig. 7.23 was deemed somewhat questionable, and no current plot was made.)

Some semi-quantitative conclusions can be drawn from the b_z and i_θ plots. First, we note that the radial compression and axial motion of the current sheet agrees fairly well with the motion revealed by rotating mirror photos of the discharge; the correlation between these photos and theoretical prediction has already been made in the previous

section. Secondly, we see that the magnitude of the current density is about what is predicted by the theory (compare Figs. 4.4(a) and 4.4(b)). The extent to which a "snowplow" effect has been established is revealed by the shapes of the b_z and i_θ curves. Looking at the z = 1", argon curves, we see that at 0.025 mmHg the magnetic field diffuses quite freely into the gas; at 0.20 mmHg, a definite sheet current forms but its width suggests that the electron density is not high enough to sustain a sharp field discontinuity; at 1.00 mmHg, the skin nature of the current has not sharpened up appreciably over the 0.20 mmHg appearance. This latter result indicates perhaps that ionization efficiency is better at 0.20 mmHg than at 1.00 mmHg; the increased pressure is shown by the slowness with which the current sheet implodes.

In order to increase accuracy and efficiency with which data is gathered using a magnetic probe, an improved probe geometry can be suggested. This design would be made of two pairs of search coils, each member of a pair wound in opposing directions and the two pairs connected in series so a difference signal results. The four coils would then be arranged in a three-dimensional, clover-leaf arrangement so that one pair monitors the b_z field, while the other couples only with the b_r component. If we assume the coils to be small and close together, the resulting signal would automatically register curl B, or, in other words, it would give i_θ directly. An attempt was made to use such a coil, but it was carried only far enough to indicate that considerable effort would need to be expended, particularly in calibrating the probe, before such an instrument could be applied usefully as a diagnostic tool.

7.8 Electric Probe

Probes consisting of electrodes can be used for two purposes in studying the internal mechanisms of a gaseous discharge. The electrodes can in one case be used as charge collectors, recording the ion and electron current to the collectors as a function of voltage externally impressed on the probe; this is known as a Langmuir probe[57]. A Langmuir probe may be used, for instance, to determine electron temperature and electron density. Exploring electrodes connected externally to a high impedance load (to prevent current flow) can also be used to detect electric fields within the discharge; in this case, the probe actually responds to potential differences within the plasma, from which the presence and strength of electric fields may be inferred. Both types of measurement have been made and are reported in this section.

Although several probe designs were tested during the course of this investigation, the configuration shown in Fig. 7.28 is adequate to demonstrate the types of experimental information obtainable with such probes. This probe is mounted in the acceleration chamber in the same

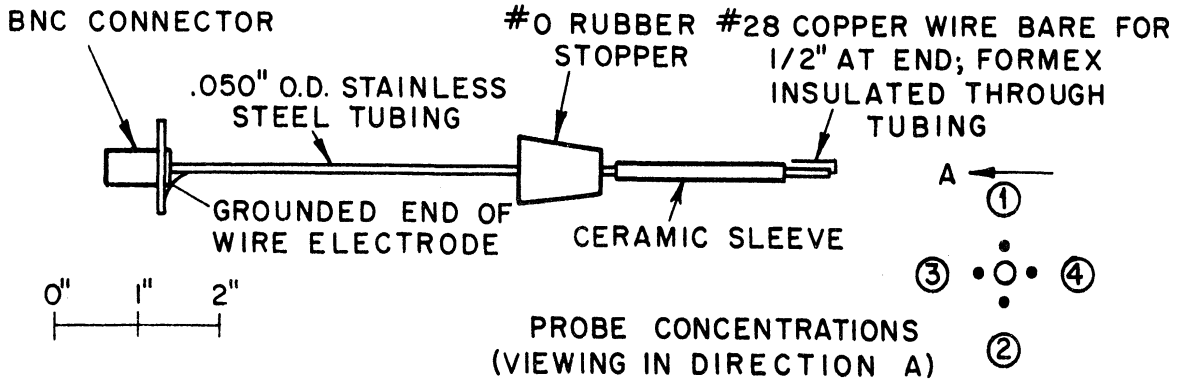

Fig. 7.28. Electric Probe Design.

way as demonstrated for the magnetic probe in Fig. 7.17. Note that this is a double electrode probe (as contrasted with the single electrode units such as employed by Langmuir and later experimenters studying low pressure discharges). Double (or bipolar) probes have been employed to study ionization in the upper atmosphere[92], temperature characteristics of decaying plasmas[93] and charge separation effects occurring in thermonuclear experiments[94]. Two characteristics of the bipolar probe make it admirably suited to studies of intense electrodeless discharges.

1. The probe circuit may electrically "float" and needs no reference electrode as does a single electrode probe.
2. The maximum current received by either electrode of the probe is the saturation ion current; this is considerably less than the saturation electron current so danger of probe burnout is reduced.

Let us first consider the bipolar probe as a detector of potential differences within the plasma. Two basic requirements must be satisfied before such a measurement can be made: a. The detecting instrument should have a sufficiently high impedance so that effects of current conduction through the plasma will not mask or distort the internal field character, and b. the potentials of the sheath on each electrode must not falsify the detection of the plasma field.

Connecting the probe directly across the input to a Tektronix 541 oscilloscope using a Type 53K/54K, wide band, vertical amplifier (1 megohm input impedance) yields signals such as displayed in Fig. 7.29. Shunting the oscilloscope input with resistances down to about 100 ohms did not affect the appearance of these voltages, so we can assume that the high impedance requirement is satisfied in the cases shown in Fig. 7.29.

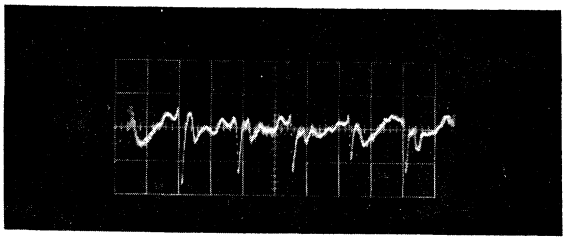

Fig. 7.29(a). Double electrode probe signal; 0.14 mmHg of argon; probe position (2) (see Fig. 7.28); 5 μsec. per major horizontal division; 10 volts per major vertical division; high impedance circuit.

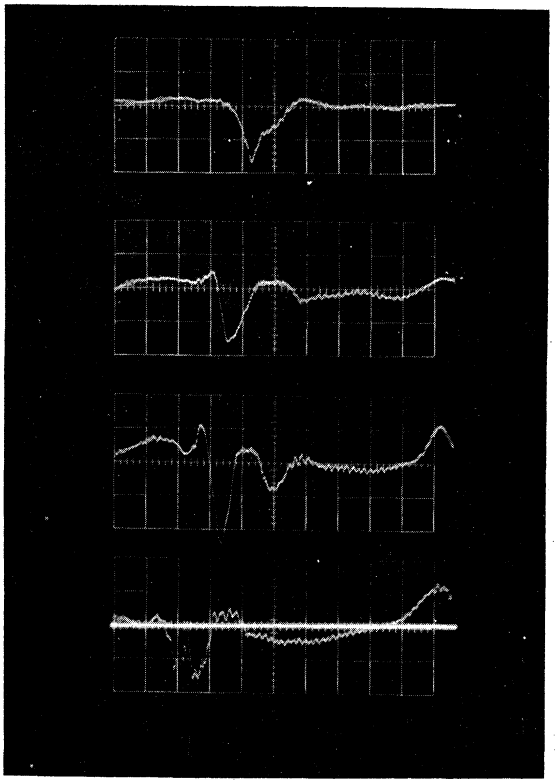

Fig. 7.29(b). Double electrode probe signal; various pressures in argon; probe position (2) (see Fig. 7.28); 1 μsec. per major horizontal division; 10 volts per major vertical division; 8 μsec. delay (so second half cycle is recorded); high impedance circuit.

Different patterns appear when the probe orientation is changed, as shown in Fig. 7.30. A consistent interpretation of these signals will now be made on the basis of an ion sheath existing on the surface of a conducting plasma column, as theoretically considered in Chapters 3 and 4. Note in Fig. 7.29(a) that a definite voltage spike occurs once each half cycle. Figure 7.29(b) indicates that the time position of this spike is increasingly delayed as the gas density increases, in accord with the radial compression theory and experiments. The radial direction of the field is independent of the relative orientations of the probe wires and is the same each half cycle, as shown by Figs. 7.30(a) and 7.30(c); the field in an ion sheath should of course show this independence of the probe. Finally, the azimuthally directed electric field indicated in Fig. 7.30(b) can be explained on the basis

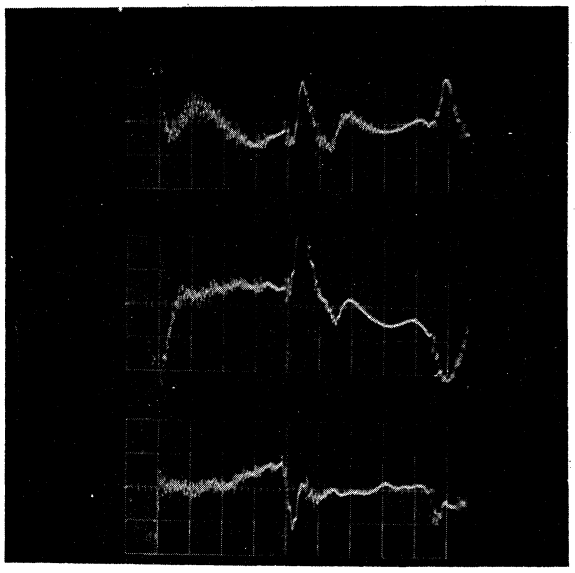

Fig. 7.30. Double Electrode Probe Signal; Various Probe Orientations as Shown (See Fig. 7.28), 0.20 mmHg of Argon; 2 μsec. Per Major Horizontal Division; 10 Volts Per Major Vertical Division.

of the conducting plasma passing radially through a z-directed magnetic field; notice that the direction of this induced field changes each half cycle as the magnetic field changes direction.

We might now consider the second of the requirements for electric field detection, concerning effects of sheaths, in light of these experiments. First of all, the sheath must respond rapidly to the changes occurring in these transient signals. Since sheath response is essentially a matter of rate of electron arrival at the probe surfaces, and since in general this arrival rate is very high, it is reasonable that the sheaths are responding sufficiently rapidly in the cases shown in Figs. 7.29 and 7.30. A more limiting sheath requirement, however, demands that the potentials across the two sheaths be the same so that the measurement is only of field effects within the plasma rather than that this measurement be a combination of plasma and sheath potential differences. No quantitative evaluation of this criterion can be made on the basis of the measurements reported here. Further effort along this avenue could take two forms; the theory which led to Fig. 4.2 could be extended so quantitative comparison between experiment and theory could be made, and more detailed experimental study of the temperature and density structure of the plasma could be made (since the sheath potential will depend on these two characteristics). It would seem, however, that the 10 to 20 volt signal being received would not be solely due to transient differences in sheath potentials.

Now, we will turn to detection of electron energy distribution, in which a variable external voltage is impressed across the probe electrodes, and the current through the probe circuit is measured. The appropriate circuit is shown in Fig. 7.31. Signals received at the

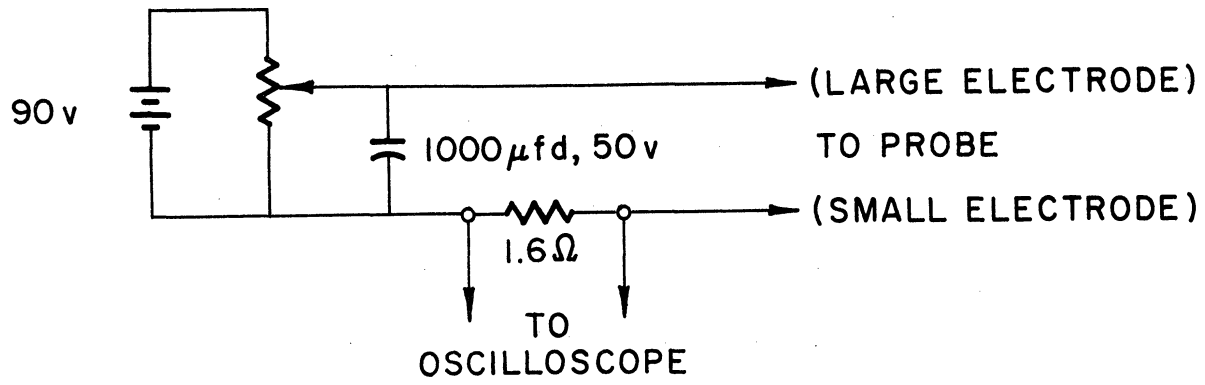

Fig. 7.31. Electric Probe Circuit—Low Impedance.

oscilloscope are exemplified by the series of oscilloscope traces shown in Fig. 7.32.

We will now pay specific attention to conditions existing at the instant of the peak of the second half cycle spike in each of the Fig. 7.32 traces. The circuit current I can be calculated from the measured voltage in each case, knowing that the measurement is across a 1.6 ohm shunt. The voltage V between the probe electrodes can also be obtained, since it is the sum of the externally applied voltage and the internal field voltage at the instant ofthe peak (known from Fig. 7.29 to be 15 volts) diminished by the measured voltage drop across the 1.6 ohm shunt. A plot of current I vs. voltage V is shown in Fig. 7.33(a).

The curve in Fig. 7.33(a) can be analyzed in light of the theory of single and double probes given in References 93 and 94. The following definitions will be required.

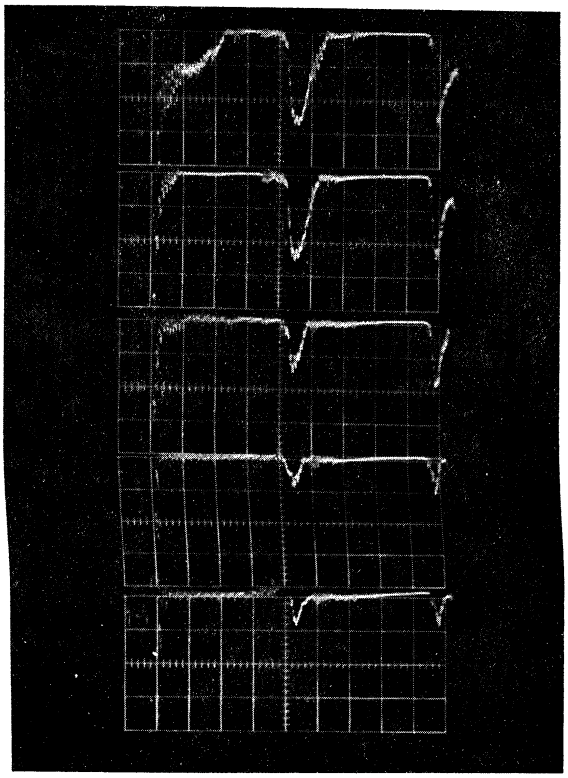

12 volts

9 volts

6 volts

3 volts

0 volts

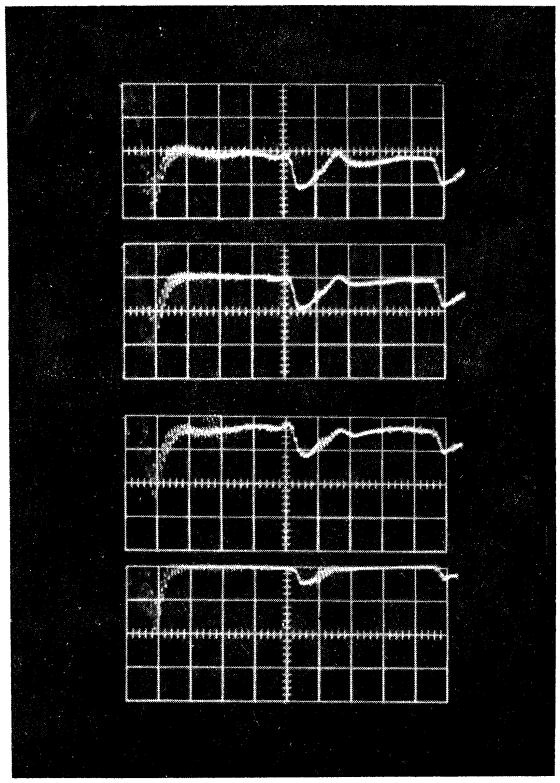

50 volts

30 volts

20 volts

10 volts

Fig. 7.32. Double electrode probe signals; low impedance circuit (see Fig. 7.31); probe position (2) ; 0.20 mmHg of argon; various voltages across the probe as shown; 2 μsec. per major horizontal division; 2 volts (top set) and 10 volts (bottom set) per major vertical division.

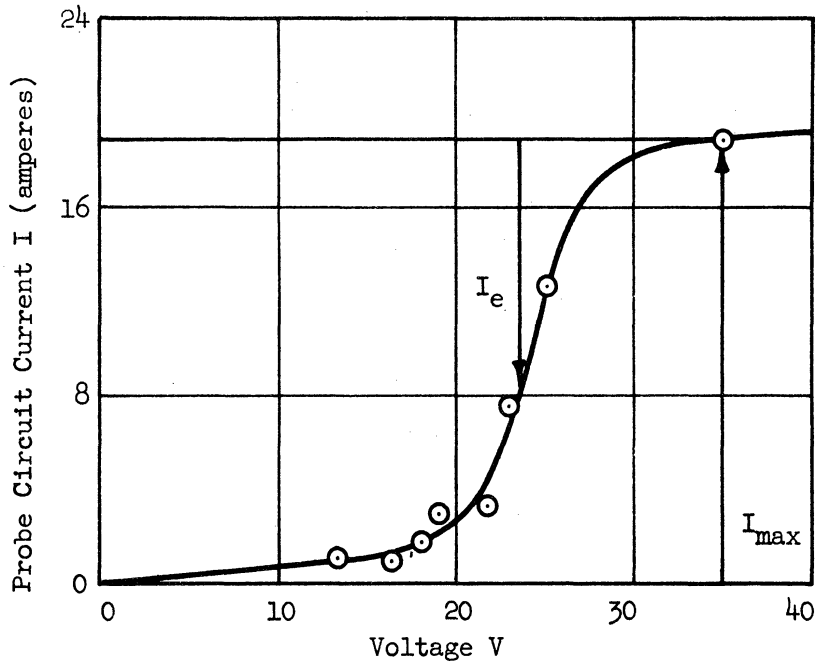

Fig. 7.33(a). Plasma Voltage-Current Characteristic as Measured by the Electric Probe.

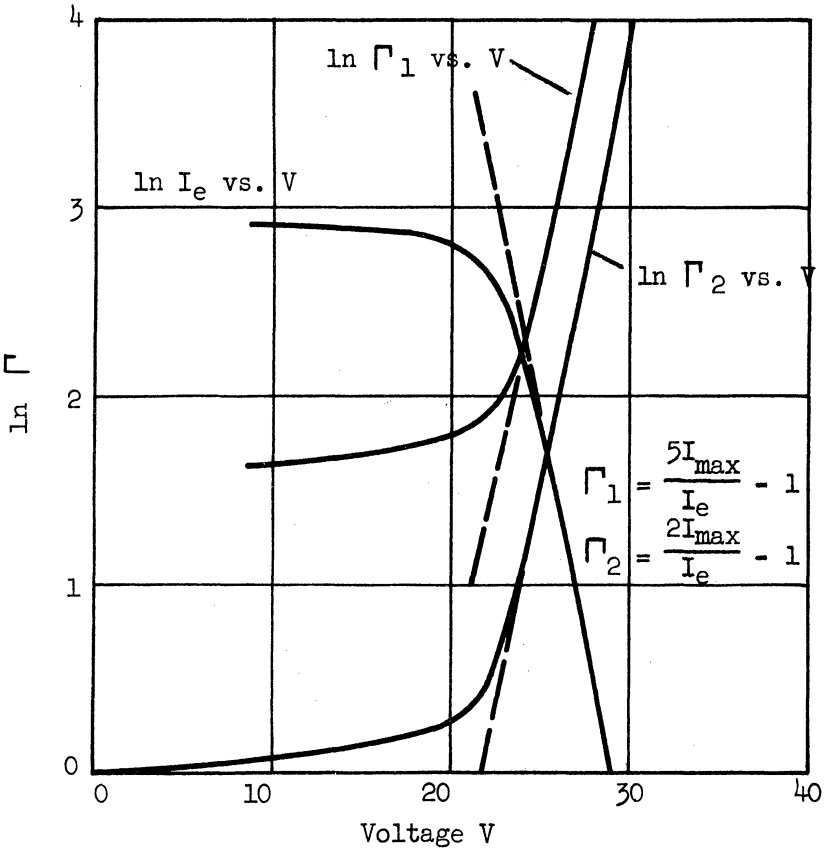

Fig. 7.33(b). Semilogarithmic Plot of Plasma Characteristic to Reveal Maxwellian Nature and Temperature of the Electron Distribution.

I_{max} ≡ saturation probe circuit current measured at high positive voltage on the larger of the two probe electrodes; this is equal to the positive ion current arriving at the smaller electrode, and in our case is taken as 18.8 amperes, as shown in Fig. 7.33(a).

I_{min} ≡ saturation probe circuit current measured at high positive voltage on the smaller of the two probe electrodes; the ratio of the absolute values of I_{max} and I_{min} will be given by the ratio of the collecting areas of the two electrodes[93].

I_e ≡ electron current flowing to the smaller probe; this is the difference between the probe current and I_{max}. Note that for this approximate calculation we have ignored the slope of the probe characteristic (Fig. 7.33(a)) at high voltages.

$\Gamma \triangleq \frac{I_{max} - I_{min}}{I_e} - 1$; as defined in Reference 93; since the smaller electrode radius is one-quarter of the larger, Γ in our case should approximately be given by:

$$\Gamma = \frac{5I_{max}}{I_e} - 1$$

If a plot is made of $\ell n\ \Gamma$ vs. V, the probe theory indicates[93] that, if the electrons are Maxwellian distributed off the smaller electrode, this curve will be a straight line, and its slope will yield the electron temperature. If the electron distribution has only a component which is Maxwellian, as for instance would occur with a beam whose electron energies are randomly distributed about a group velocity, then the logarithmic plot will be a straight line only over the random energy (voltage) range. Logarithmic plots from the Fig. 7.33(a) curve are drawn in Fig. 7.33(b); note that while the higher energy portions of

these curves are straight, the nonlinear behavior at lower voltages indicates a non-Maxwellian distribution (being in fact deficient). The electron temperature calculated from the linear portion of this curve is about 25,000°K. Note that while Γ has been defined from I_{max} in accordance with the known ratio of electrode radii, the slope is quite insensitive to the ratio actually used. In Fig. 7.33(b) are shown also the curve $\ell n\ \Gamma(V)$ for equal collection areas and the curve $I_e(V)$. Each yields about 25,000°K electron temperature.

It is interesting to note that the measured electron temperature is considerably less than the estimated ion temperature (compare Table 7.2). In this regard it might be fruitful for further studies to explore the rate at which the electrons take on a random distribution during the inward compression, and the rate at which the ions and electrons come into equilibrium behind the axially moving shock.

CHAPTER VIII. SUMMARY, CONCLUSIONS, AND RECOMMENDATIONS

The review of the presently developed state of electrical propulsion devices in Chapter I indicates that the simple inductive system for acceleration of charged particles and plasmas has not been studied sufficiently to arrive at any definite conclusion as to its engineering worthiness. The objective of this study has been to provide further information toward this end.

The inductive geometry may be used both as a particle accelerator (ion engine) and as a plasma device. A theoretical treatment of the particle device, based on an exact calculation of particle trajectories, has been included. Several important factors result from this analysis.

1. In as much as exact trajectories within the electromagnetic field of a cylindrical coil have not to our knowledge been reported in the literature, the specific path shapes and numerical values (e.g., time spent in accelerator, ultimate velocity and ejection angle) pertaining to a variety of particle masses, field strengths and field frequencies should in themselves be of interest. Some generalizations from these particular numerical results pointed out in the following paragraphs are also unique and highly significant.
2. The shapes of the various trajectories indicate that, whereas particles begin their motions with large radial velocity components, even well outside the coil, particles launched at certain critical positions may ultimately leave the accelerator on paths parallel with the coil axis (z-axis).

3. The shapes of the various trajectories, along with the numerical values for ultimate velocity, indicate also that particles which are launched from positions deep within the coil orbit for several revolutions around the coil axis before being ejected and therefore gain considerable energy from the azimuthally directed electric field. The action is somewhat similar to a betatron accelerator.
4. There is a marked difference in behavior when the field period is much less than and much more than the time taken for the particle to be ejected from the accelerator. This result is perhaps intuitive, but the particle analysis is additionally useful in supplying quantitative information on conditions which lead to one or the other type of behavior and on results which are obtained in each mode.

Further work on particle behavior might be devoted to launching conditions which will give higher eventual particle energies and to resonance phenomena which might occur in the transition range between fast and slow operation.

The theoretical treatment of the plasma induction accelerator has in this study been divided into calculations of radial and axial motion. Several unique items have resulted from the radial motion study. An extensive study (in Chapters 3 and 4) of the effect of self-fields on the radial motion has let to the analysis of the low density, or equilibrium, radial compression carried out in Section 4.5. At higher densities, a "snowplow" analysis, extensively applied to the linear pinch, has here been carried out for the inductive compression in a more complete manner than has hitherto come to our attention. In addition,

the radial variations of magnetic field and current density within the plasma have been plotted for various conditions; these may be used as criteria by which one can decide whether or not the snowplow model is applicable, and experimental results may also be judged by comparison with them.

In treating the axial motion of the plasma, we have been concerned with conditions under which a continuum analysis is applicable and with information which can experimentally be gained under such conditions.

Since an inductive accelerator of the type being considered here (Fig. 1.2) has heretofore not been experimentally studied, the experimental phase of this effort has attempted to present a "broad" view of the inductive plasma accelerator. A sufficient range of measurements has been taken to yield some corroboration of the theory presented earlier in this report andto allow a preliminary judgment to be made on the engineering feasibility of the system. Note that we are here concerned with a "fast" system, i.e., one in which the plasma moves out of the accelerator in less than a quarter cycle of the coil current. Drawing upon the results of the particle analysis, one would expect this to be a more energetic system than would be a "slow" system.

Energy is one item about which much was learned. It has been found that, in the apparatus used, on the order of 10 percent of the available energy (that is, energy which actually appears in the coil magnetic field) is transferred to the gas, the remainder appearing as resistive loss in the coil. A third to a half of this 10 percent appears in the z-directed plasma motion, the majority of the rest probably existing as thermal and ionization energies.

Energy is only one of several important considerations when dealing with the propulsion possibilities of the induction accelerator. Other characteristics, specifically velocity, momentum and mass, have been studied experimentally during this effort. Inasmuch as energy, velocity and momentum require only two parameters, independent measurement of each of these three can be compared with one another to substantiate the accuracy of each, and in this way a "package" of data, describing the over-all operating characteristics of the induction accelerator, has been presented. Thus, this form of electrical propulsion system has now been given the experimental scrutiny which heretofore has been lacking.

Specific measurements made on the 10 cm long by 10 cm diameter accelerator driven by 37.5 μtd at 9 kv give an idea of the general characteristics of the "fast" induction accelerator. Axial velocity of the gas as it emerged from the coil was typically 0.5 to 10 cm per microsecond. Energy in the amount of approximately 10 to 50 joules was transferred from the circuit to the gas. Momentum of the accelerated gas was in the approximate range, 75 to 400 gm-cm/second, averaged across the flow.

Continuation of these "kinetic measurements" might be fruitful particularly in more closely correlating (with each other and with theory) the experimental measurements of energy input to the plasma and of energy carried by the flowing stream. Further suggestions for a continued experimental program are outlined later.

Both magnetic and electric probes have been used to study the internal structure of the plasma. A suggestion for improving the magnetic method by using multiloop probes has been advanced in Chapter

VII. A useful future application of the electric probe might be to study the rate at which the ions and electrons come into equilibrium behind the axial shock wave, a subject which has been touched upon in Chapters V and VII.

Purity of the accelerated gas is an item which has not been quantitatively studied in this effort. It is obvious from comparison of the helium and argon results and from visual observation of the discharge that the behavior is largely determined by the test gas. It would require careful spectroscopic observation, however, to determine to what extent impurities (evolved from the glass walls and from the various instruments inserted into the plasma) contribute to the accelerated flow.

In addition to the several specific suggestions for future study made above, a broader development program, aimed at the engineering application of the induction system as a means of propulsion, can be suggested. One phase of such an undertaking would be to achieve maximum over-all system efficiency. Three steps could be taken toward this end.

1. The circuit resistance should be reduced in order to minimize the inherent I^2R loss.
2. The magnetic field should be properly shaped in order to optimize the coupling between the plasma and the coil. In the experiments described in this report, the plasma filled only half the coil length due to the symmetry of the field, as explained in connection with Fig. 6.5. If the coil were tapered or partly closed at one end, presumably the entire coil could initially be filled with plasma, approximately doubling the energy transfer.

3. The coil size, plasma density, main circuit current, and frequency should be adjusted for maximum energy transfer. Optimum conditions would ensure that a well developed skin current exist throughout the compression and that the total compression and expulsion process take place in approximately one quarter cycle. This would take maximum advantage of the field.

With these improvements incorporated into the induction accelerator design, it is conceivable that better than 25 percent of the field energy can be transferred to the plasma in a pulse.

Another phase of this development would be to achieve steady state rather than single pulse operation; that is, it would be desirable to drive the coil with a continuously running a-c power source. We might, on the basis of the experimental results herein reported, conjecture on possible gross features of such a steadily running device. For the plasma densities being considered, it appears that 50 kc/sec is a suitable driving frequency. If we then assume that energy in the amount of 5 joules is transferred to the plasma per cycle, and that half of this energy appears as directed motion of the gas, then a 125 kw exhaust stream results. If this stream leaves the accelerator with a velocity of 10^4 meters/second ($I_{sp} \cong 1000$ sec.), the resulting thrust will be 12.5 newtons, or 2.8 pounds.

APPENDIX A. THE MAGNETIC FIELD OF THE EXPERIMENTAL CYLINDRICAL COIL

In order to carry out the trajectory computations presented in Chapter II, it is necessary to know in detail the values of the radial and axial magnetic field components within and in the neighborhood of the coil. This information will also be helpful in understanding processes described in other sections of this report.

For our purposes the component strengths are needed at a sufficient number of points so interpolation (Laplacian interpolation, as described in Section 2.4.2) between them will not be greatly in error. We may either calculate the necessary data, using formulae available in the literature[52], or the field can be measured at the various required points using a coil of the desired geometry. Since the field values at over a hundred points are required, and since the theoretical formulae involve slowly converging series computations, it was decided that the empirical approach was the more advisable in this instance.

For purposes of this measurement, a coil of the required geometry, 10 cm diameter by 10 cm length, was constructed employing 74 turns of #16 enameled copper wire. This coil was excited by 35 amperes from a 12.3-volt battery supply which was continuously being charged. The field (radial and axial components separately) was measured by a Dyna-Empire, Inc., Model D-79 gaussmeter. The procedure for each reading (after allowing the gaussmeter to warm up for one-half hour) was to wait one minute to ensure full battery charge, switch on the current through the coil, allow a few seconds for steady state conditions to be achieved

and then read the field strength from the instrument. By this procedure, the current at each reading was constant within ± 2 percent. The instrument itself was calibrated against a known field, but, as we shall see, the more important consideration is relative uniformity among the various readings rather than absolute calibration; measurements taken on different occasions at the same location would fall within about ± 5 percent of one another. The measured values of magnetic field from this 74-turn, 35-ampere coil are presented in Table A.1.

The strength of the b_z component on the axis of the coil is given by a simple, well known expression,

$$b_z(\text{on axis}) = \frac{1}{2} \mu_o i_c' (\cos \beta_2 - \cos \beta_1) \quad , \qquad (A.1)$$

where i_c' is the coil current, amperes/meter, and the β's are the angles between the axis and the lines drawn from the field point (on axis) to the two ends of the coil. By now comparing the field strengths measured on the axis of the 74-turn coil with values calculated from Eq. A.1, a proportionality factor can be derived relating the measured field strength value to the absolute field strength per unit coil current at all points of interest. Thus, the absolute calibration of the measurements does not depend upon knowledge of the absolute value of the coil current and absolute calibration of the field measuring instrument but only requires that these be uniform from reading to reading. As an indication of the validity of these measurements and this calibration procedure, the comparison between measured values on the coil axis and values calculated from Eq. A.1 are shown in Table A.2. The resulting quantities, giving field strengths per unit coil current,

are of course the ψ_{b_z} and ψ_{b_r} functions introduced in Section 2.4.2. These quantities are tabulated in Table A.1 for all points of interest.

Several other quantities specified in Section 2.4.2 must be calculated from these ψ functions. The function ψ_{φ_o}, defined in Eq. 2.16 and repeated here,

$$\psi_{\varphi_o} \triangleq 2\pi \int_0^{\rho} \rho\psi_{b_z}\, d\rho \quad , \tag{A.2}$$

must be evaluated. This was accomplished by plotting the function $\rho\psi_{b_z}$ and carrying out the integration with a planimeter; a planimeter of Swiss manufacture, distributed by the Crosby Stream Gage and Valve Company of Boston, was employed (the loan of this instrument from the Mechanical Engineering Department is gratefully acknowledged). The values of ψ_{φ_o} are included in Table A.1.

Finally, we must calculate the quantities A_ρ and A_ξ, defined respectively in Eqs. 2.18 and 2.19. These are arithmetic functions of ψ_{b_z}, ψ_{b_r}, and ψ_{φ_o} and need no elaboration here other than to note that they, as the ψ functions, are properties of the coil geometry; by their use, the geometric properties of the magnetic field can be separated from the absolute strength of the field and its time dependence, as explained in connection with Eqs. 2.17a and 2.17b. The A functions are tabulated in Table A.1 and plotted in Figs. 2.2 and 2.3.

Table A.1. Measured Field Strength Values and Quantities Derived from These Measurements

z	ξ	r	ρ	b_z	b_r	ψ_{b_z}	ψ_{b_r}	$\frac{\psi_{\varphi_o}}{2\pi}$	A_ξ	A_ρ
in		in		gauss		x 10^6	x 10^6	x 10^6	x 10^{12}	x(-10^{12})
0	0	0	0	301	0		0		0	
		.25	.125	302						
		.5	.25	303		8.47		.27		4.46
		.75	.375	306		8.56		.62		6.85
		1.0	.5	308		8.63		1.09		9.3
		1.25	.625	312		8.74		1.72		11.85
		1.5	.75	315		8.82		2.46		14.54
		1.75	.875	320		8.96		3.36		17.52
.5	.25	0	0	299	0					
		.25	.125	300	3		.084	.066	.044	
		.5	.25	301	5		.140	.265	.148	
		.75	.375	303	9		.252	.604	.405	
		1.0	.5	305	12		.316	1.10	.694	
		1.25	.625	309	15		.420	1.67	1.13	
		1.5	.75	312	17		.476	2.42	1.54	
		1.75	.875	316	17.5		.519	3.31	1.96	
1	.5	0	0	296	0					
		.25	.125	297	6		.168	.065	.087	
		.5	.25	298	14	8.34	.392	.26	.408	4.35
		.75	.375	300	21	8.40	.588	.59	.926	6.63
		1.0	.5	303	32	8.48	.896	1.05	1.88	8.96
		1.25	.625	305	36	8.54	1.01	1.65	2.67	11.32
		1.5	.75	309	38	8.65	1.06	2.38	3.37	14.02
		1.75	.875	312	40	8.74	1.12	3.26	4.16	16.6
1.5	.75	0	0	253	0					
		.25	.125	255						
		.5	.25	255	19	7.14	.532	.222	.532	3.20
		.75	.375	257	32	7.20	.896	.509	.896	4.88
		1.0	.5	264	48	7.38	1.34	.915	1.34	6.82
		1.25	.625	275	60	7.70	1.68	1.43	1.68	8.8
		1.5	.75	290	73	8.12	2.04	2.21	2.04	12.3
		1.75	.875	305	87	8.54	2.44	2.93	2.44	15.8
1.87	.93	0	0	211	0					
		.5	.25	211	22	5.91	.616	.182	.449	2.18
		.75	.375	211	36	5.91	1.01	.415	1.12	3.28
		1.0	.5	211	53	5.91	1.48	.737	2.12	4.37
		1.25	.675	211	70	5.91	1.96	1.15	3.62	5.47
		1.5	.75	215	95	6.03	2.66	1.66	5.88	6.78

z	ξ	r	ρ	b_z	b_r	ψ_{b_z}	ψ_{b_r}	$\frac{\psi_{\varphi_o}}{2\pi}$	A_ξ	A_ρ
in		in		gauss		x 10^6	x 10^6	x 10^6	x 10^{12}	x(-10^{12})
		1.75	.875	225	125	6.30	3.50	2.30	9.21	8.70
		1.88	.94	240	150		4.20	2.66	11.9	
2	1	0	0	198	0					
		.25	.125	198	7	5.54	.196	.043	.068	
		.5	.25	198	22	5.54	.616	.173	.425	1.91
		.75	.375	198	36	5.54	1.01	.387	1.04	2.87
		1.0	.5	198	54	5.54	1.51	.690	2.08	3.84
		1.25	.625	198	70	5.54	1.96	1.08	3.39	4.81
		1.5	.75	197	95	5.52	2.66	1.56	5.54	5.71
		1.75	.875	188	125	5.26	3.50	2.09	8.37	6.06
2.25	1.13	0	0	173	0					
		.5	.25	172	20	4.82	.560	.150	.336	1.45
		.75	.375	170	35	4.76	.980	.340	.888	2.13
		1.0	.5	165	52	4.62	1.46	.597	1.74	2.65
		1.25	.625	160	67	4.48	1.88	.925	2.78	3.14
		1.5	.75	150	87	4.20	2.44	1.29	4.22	3.27
		1.75	.875	133	110	3.72	3.08	1.70	5.97	2.92
		2.0	1.0	83	125	2.32	3.50	2.07	7.20	.52
		2.25	1.13	20	125	.56	3.50	2.25	7.00	- 2.44
2.5	1.25	0	0	152	0					
		.25	.125	150						
		.5	.25	148	20	4.14	.560	.128	.286	1.07
		.75	.375	145	33	4.06	.925	.296	.730	1.54
		1.0	.5	140	48	3.92	1.34	.514	1.38	1.91
		1.25	.625	130	60	3.64	1.68	.775	2.08	2.06
		1.5	.75	117	74	3.28	2.07	1.07	2.95	1.95
		1.75	.875	100	90	2.80	2.52	1.39	3.99	1.55
		2.0	1.0	73	100	2.04	2.80	1.67	4.67	.63
		2.25	1.125	40	95	1.12	2.66	1.88	4.45	- .62
		2.5	1.25	20	75	.56	2.10	2.00	3.36	-1.16
3.0	1.5	0	0	106	0					
		.25	.125	105	5		.140		.026	
		.5	.25	105	15	2.94	.420	.0938	.158	.539
		.75	.375	103	24	2.88	.672	.201	.360	.774
		1.0	.5	101	33	2.83	.925	.362	.669	.995
		1.25	.625	95	42	2.66	1.18	.556	1.05	1.10
		1.5	.75	82	50	2.29	1.40	.770	1.44	.94
		1.75	.875	68	54	1.91	1.51	.980	1.69	.70
		2.0	1.0	54	58	1.51	1.62	1.18	1.92	.39
		2.25	1.125	40	58	1.12	1.62	1.36	1.95	.06
		2.5	1.25	28	52	.78	1.46	1.49	1.75	- .21

z	ξ	r	ρ	b_z	b_r	ψ_{b_z}	ψ_{b_r}	$\frac{\psi_{\varphi_o}}{2\pi}$	A_ξ	A_ρ
in		in		gauss		x 10^6	x 10^6	x 10^6	x 10^{12}	x(-10^{12})
3.5	1.75	0	0	76	0					
		.25	.125	74						
		.5	.25	73	10	2.04	.280	.063	.070	.26
		.75	.375	70	17	1.96	.476	.148	.188	.36
		1.0	.5	67	22	1.88	.616	.248	.304	.44
		1.25	.625	62	28	1.74	.734	.372	.436	.47
		1.5	.75	56	32	1.58	.896	.512	.610	.46
		1.75	.875	48	36	1.34	1.01	.658	.760	.36
		2.0	1.0	40	37	1.12	1.04	.802	.835	.25
		2.25	1.125	32	37	.90	1.04	.936	.865	.13
		2.5	1.25	23	36	.64	1.01	1.05	.852	- .03
4.0	2.0	0	0	55	0					
		.25	.125	54						
		.5	.25	53	7	1.48	.196	.046	.036	.137
		.75	.375	51	11	1.43	.308	.105	.086	.190
		1.0	.5	48	15	1.34	.420	.183	.154	.216
		1.25	.625	44	18	1.23	.504	.269	.217	.232
		1.5	.75	40	21	1.12	.538	.368	.264	.228
		1.75	.875	36	23	1.01	.644	.478	.348	.211
		2.0	1.0	32	26	.90	.728	.590	.430	.183
		2.25	1.125	28	26	.78	.728	.699	.452	.142
		2.5	1.25	23	26	.64	.728	.801	.467	.081
4.5	2.25	0	0	42	0					
		.25	.125	42						
		.5	.25	41	5	1.15	.140	.035	.020	.081
		.75	.375	39	7	1.09	.196	.080	.042	.111
		1.0	.5	38	9	1.06	.252	.140	.071	.140
		1.25	.625	35	12	.98	.336	.221	.119	.147
		1.5	.75	32	14	.90	.392	.291	.152	.147
		1.75	.875	29	16	.81	.448	.375	.193	.138
		2.0	1.0	25	17	.70	.476	.465	.221	.119
		2.25	1.125	22	18	.62	.504	.541	.243	.092
		2.5	1.25	19	18	.53	.504	.633	.255	.063
6.0	3.0	0	0	16	0					
		.25	.125	16						
		.5	.25	15	2	.42	.056	.013	.003	.011
		.75	.375	15	3	.42	.084	.029	.006	.016
		1.0	.5	15	4	.42	.112	.051	.012	.022
		1.25	.625	14	4	.39	.126	.081	.015	.024
		1.5	.75	14	5	.39	.154	.114	.023	.027
		1.75	.875	13	6	.36	.182	.151	.032	.028
		2.0	1.0	12	7	.34	.196	.194	.038	.028
		2.25	1.125	11	8	.31	.224	.232	.046	.026
		2.5	1.25	9	9	.25	.252	.276	.056	.016

Table A.2. Comparison of Measured and Calculated Magnetic Field Strengths on Axis for Calibration of Field Measurements

Normalization factor: $\frac{\cos \beta_2 - \cos \beta_1}{b_z(\text{measured})} = 0.455 \times 10^{-2}$

z (in)	Measured b_z on Axis (gauss)	$\cos \beta_z - \cos \beta_1$	Measured b_z on Axis Normalized to $\cos \beta_z - \cos \beta_1$ at z = 2"
0	301	1.41	1.36
1/2	299	1.38	1.36
1	296	1.28	1.34
$1^1/_2$	253	1.11	1.15
2	197.5	.896	.896
$2^1/_2$	152	.670	.692
3	106	.482	.482
$3^1/_2$	76	.339	.346
4	55	.243	.250
$4^1/_2$	42	.174	.192
6	16	.076	.073

APPENDIX B. FURTHER CONSIDERATION OF THERMAL IONIZATION AND THERMAL EXCITATION—ESTIMATE OF EXCITATION RADIATION LOSS

In order to make some quantitative estimate of the energy loss due to excitation radiation (briefly considered in Section 7.5), the population of excited states must be calculated. Multiplying this population by the mean life time of an excited state and by the excitation energy will then yield an approximate value for the radiation power loss.

When a gas is in equilibrium at temperature T(°K) and pressure p(mmHg), collisions occurring due to the random motion of the particles will cause a certain equilibrium degree of ionization x to exist, where x indicates the ratio n_1/n of the densities of singly ionized to original (cold gas) particles. The Saha Equation[95] may be used to calculate x; this relation follows:

$$\frac{x^2}{1-x^2}\, p \;=\; 2.4 \times 10^{-4}\, T^{2.5}\, e^{-\frac{q_e V_1}{k_b}} \quad , \qquad (B.2)$$

where V_1 is the first ionization potential of the species being considered. The pressure p must be the pressure existing at temperature T and must account for the partial pressures of the neutrals, ions and electrons, thus,

$$p \;=\; (n+n_e)\, k_b T \quad . \qquad (B.3)$$

In the ensuing calculations it will turn out that approximately complete single ionization is achieved. We will therefore be concerned with the population of excited states of the ions (HeII and AII).

The ratio of the density n_{11} of ions in the first excited state to the total density of ions n_1 is given by the Boltzmann relation.

$$\frac{n_{11}}{n_1} = \frac{g_{11}}{B_1} e^{-\frac{X_{11}}{k_b T}} , \tag{B.4}$$

where g_{11} is the statistical weight of the excitation level, B_1 is the partition function of the ion, and X_{11} is the excitation energy.

The statistical weight g is determined from the spectral term or degeneracy of the level[96,97]. The partition function B is given as a sum over the statistical weights[98].

$$B_1 = \sum_m g_{1m} e^{-\frac{X_{1m}}{k_b T}} . \tag{B.5}$$

This series is divergent, but the general procedure[98] is to terminate it at the level where the orbit radius becomes of the same size as the interparticle distance. For our purposes, however, it turns out that the exponential terms are numerically so small that the approximation

$$B_1 \cong g_{10} + g_{11} e^{-\frac{X_{11}}{k_b T}} \tag{B.6}$$

suffices. The procedure then reduces to calculation of n_1 from the Saha relation B.2 and n_{11} from the following simplified form of the Boltzmann relation.

$$n_{11} = n_1 \frac{g_{11} e^{-X_{11}/k_b T}}{g_{10} + g_{11} e^{-X_{11}/k_b T}} . \tag{B.7}$$

Calculations will be performed for helium initially at 0.1 and 1.0 mmHg and argon initially at 0.4 and 1.0 mmHg; the temperatures will be those presented in Table 7.2 for these gas and pressure conditions. Ionization and excitation energies as well as spectral term values (used in calculating statistical weights and partition functions) are taken from C. E. Moore's table[99].

The results of these calculations are presented in Table B.1. These results indicate that in general the radiation energy loss from the induction acceleration plasma (~ 0.001 m^3 in volume) should be quite small.

Table B.1. Excitation Radiation Calculations

a. Argon has a group of allowed levels in the 18.3 ev to 19.5 ev range. The excitation potential (18.9 ev) is an approximate average of these while the statistical weight (100) is the sum of the weights of the individual levels.

b. E_r is the excitation radiation loss from the plasma. The calculation of E_r assumes that the mean life time of the excited states is 10^{-8} seconds and that the plasma radiates for 10^{-4} seconds.

Gas	P_o (mmHg)	T (°K)	V_1 (ev)	V_{11} (ev)	g_{11}	B	x	n_1 $\frac{\text{particles}}{m^3}$	$\frac{n_{11}}{n_1}$	E_r[b] $\frac{\text{joules}}{m^3}$
He	0.1	3.7×10^4	24.6	40.6	6	2	1	3×10^{15}	1.4×10^{-5}	2.7×10^{-3}
	1.0	2.4×10^4	24.6	40.6	6	2	.8	2×10^{16}	1.5×10^{-8}	2.9×10^{-5}
A	0.4	3.7×10^4	15.8	18.9[a]	100[a]	12.3	1	1×10^{16}	2.4×10^{-2}	7.2
	1.0	2.1×10^4	15.8	18.9[a]	100[a]	12.01	.98	3×10^{16}	8.0×10^{-4}	7.2×10^{-2}

BIBLIOGRAPHY

1. Sutton, G. P., Rocket Propulsion Elements, J. Wiley, New York; p. 20; 1956.

2. Space Handbook: Astronautics and Its Applications, (Staff Report of Select Committee on Astronautics and Space Exploration) Gov. Printing Office, Washington; 1959.

3. Sutherland, G. S., "Recent Advances in Space Propulsion", ARS Journal, p. 698; October, 1959.

4. Oberth, H., Wege Zur Raumschiffahrt, R. Oldenbourg, München; 1929.

5. Spitzer, L., "Interplanetary Travel Between Satellite Orbits", J. Brit. Int. Soc., vol. 10, p. 249; 1951.

6. Stuhlinger, "Possibilities of Electrical Space Ship Propulsion", Bericht uber den V Int. Astron. Kong, Springer-Verlag, Wien; 1955.

7. Wiech, R. E., "Heavy Particle Propulsion Research", Thiokol Chem. Corp., Rpt. No. RMD-1155-52, AFOSR-TR60-48; 31 December 1959.

8. Kaufman, H. R. and Reader, P. D., "Experimental Performance of Ion Rockets Employing Electron-Bombardment Ion Sources", Amer. Roc. Soc. paper No. 1374-60; November, 1960.

9. Hayes, R., Seitz, R. N. and Stuhlinger, E., "The U.S. Ion Propulsion Program" Astronautics, p. 30; January, 1961.

10. Schultz, R. D. and Branson, L. K., "Changed Colloid Propulsion System", Aerojet-General Corp. Rpt. No. 1728; December, 1959.

11. Langmuir, D. B., "Electrical Propulsion", Astronautics, p. 33; November, 1960.

12. Harned, B. W., Borman, G. L., Sherman, A., "Electromagnetic Plasma Propulsion Studies", Third AFOSR Contractors' Meeting on Ion and Plasma Propulsion, New York; March, 1960.

13. Cunningham, D. E., Weirick, R. G., Block, R. B., "MHD Channel Flow", AIEE Symposium on the Engineering Aspects of Magnetohydrodynamics, Philadelphia; February, 1960.

14. "T-Tube" Electrode Accelerators: Fowler, R. D., Atkins, W. R., Compton, W. D., Lee, R. J., "Shock Waves in Low Pressure Spark Discharges", Phys. Rev., vol. 88, p. 137; 1952: Kolb, A. C., "Production of High Energy Plasma by Magnetically Driven Shock Waves", Phys. Rev. vol. 107, p. 345; 1957: Kash, S. W., Gauger, J., Starr, W., Vali, V., "Velocity Measurements in Magnetically Driven Shock Tubes", The Plasma in a Magnetic Field, R. K. M. Landshoff, Editor, Stanford University Press, Stanford; 1958: Gorowitz, B., Moses, K., Gloersen, P., "Experimental Investigations of Plasma Accelerators for Space

Vehicle Guidance and Propulsion", General Electric Co., Missile and Space Vehicle Department, Rpt. No. R59SD466; November, 1959.

15. "Rail" Electrode Accelerators: Walker, R. C. and Early, H. C., "Velocities of Magnetically Driven Arcs in Air and He up to 30 Atmospheres", AIEE Winter Meeting; February, 1955: Korneff, T., Bohn, J. L., "Experiments in Plasma Acceleration", Conference on Extremely High Temperatures, H. Fischer and L. C. Mansur, Editors, J. Wiley and Sons; March, 1958: Thourson, T. L. and Schroeder, R. G., "Pulsed Plasma Propulsion—An Advanced Reaction Space Propulsion System", WADD Tech. Rpt. 60-432; June, 1960.

16. "Coaxial" Electrode Accelerators: Marshall, J., "Performance of a Hydromagnetic Plasma Gun", Phys. Fluids, vol. 3, p. 134; 1960: Gloerson, P. and Gorowitz, B., "Optical Observations of Plasmas Accelerated into a Vacuum", Bull. Am. Phys. Soc., vol. 5, p. 351; 1960: Wetstone, D. M. and Lary, E. C., "Analysis of a Coaxial Plasmoid Source", Bull. Am. Phys. Soc., vol. 5, p. 351; 1960.

17. "Conical" Electrode Accelerators: Josephson, V., "Production of High Velocity Shocks", Jour. Appl. Phys., vol. 29, p. 30; 1958: Kash, S. W., Gauger, J., Starr, W., Vali, V., "Velocity Measurements in Magnetically Driven Shock Tubes", The Plasma in a Magnetic Field, R. K. M. Landshoff, Editor, Stanford University Press, Stanford; 1958.

18. Patrick, R. M., "A Description of a Propulsion Device which Employs a Magnetic Field as the Driving Force", Avco Research Rpt. No. 28; May, 1958.

19. Bostick, W. H., "Experimental Study of Plasmoids", Phys. Rev., vol. 106, p. 404; 1957.

20. Kunen, A. E., "The Electromagnetic Pinch Effect as a Space Propulsion System", Advances in Astronautical Sciences, vol. 2, Plenum Press, Inc. New York; 1958.

21. Camac, M., Kantrowitz, A., Petschek, H. E., "Plasma Propulsion Devices for Space Flight", Avco Research Rpt. No. 45; February, 1959.

22. Adams, M. C. and Camac, M., "The Arc Heated Plasma Thrust Chamber", Amer. Roc. Soc. paper No. 791-59; April, 1959.

23. Heller, G., "The Plasma Jet as an Electric Propulsion System for Space Application", Amer. Roc. Soc. paper No. 1040-59; November, 1959.

24. Pierce, J. R., Traveling Wave Tubes, D. Van Nostrand, New York; 1950.

25. Kerst, D. W., "The Acceleration of Electrons by Magnetic Induction", Phys. Rev., vol. 60, p. 47; 1941.

26. Tomson, J. J. and Thomson, G. P., Conduction of Electricity Through Gases, Cambridge University Press, vol. II, p. 431; 1933.

27. Thonemann, P. C., Moffatt, J., Roaf, D., Sandus, H. H., "The Performance of a New Radio-Frequency Ion Source", Proc. Phys. Soc. (London) vol. 61, p. 483; 1948.

28. Smith, C. G., "Studies of a Ring Discharge", Phys. Rev., vol. 59, p. 997; 1941.

29. Eckert, H. U., "Equations of the Electrodeless Ring Discharge and Their Solution for the Breakdown Criterion", Corvair Scientific Research Laboratory, Res. Rpt. No. 5; August, 1959.

30. Thonemann, P. C., Cowhig, W. T. and Davenport, P. A., "Interaction of Traveling Magnetic Fields with Ionized Gases", Nature, vol. 169, p. 34; 1952.

31. Morozov, A. I., "The Acceleration of a Plasma by a Magnetic Field", Sov. Phys. JETP, vol. 5, p. 215; 1957.

32. Petschek, H. E. and Janes, G. S., "Magnetically Driven Shock Waves; Experiments at Avco", Magnetohydrodynamics, R. K. M. Landshoff, Editor, Stanford University Press, Stanford; 1957.

33. Blackman, V. H. and Niblett, B., "Experiments Using a Hydromagnetic Shock Tube", The Plasma in a Magnetic Field, R. K. M. Landshoff, Editor, Stanford University Press, Stanford; 1958.

34. Marshall, J., "Acceleration of Plasma into Vacuum", Proceedings of the Second United Nations International Conference on the Peaceful Uses of Atomic Energy, Geneva, vol. 31, p. 341; 1958.

35. Bostick, W. H., Plasma Motors", The Propulsion of Plasma by Magnetic Means", IX Astron. Congress, Amsterdam; 1958.

36. Miller, D. B., "An Electromagnetic Accelerator and Its Applicability to Acceleration of an Electrical Discharge Plasma", ARDC Conference on Ion and Plasma Research, ASTIA Doc. 162274; October, 1958.

37. Boyer, K., Elmore, W. C., Little, E. M., Quinn, W. E., Tuck, J. L., "Studies of Plasma Heated in a Fast-Rising Axial Magnetic Field (Scylla)", Phys. Rev., vol. 119, p. 831; 1960: see also Elmore, W. C., Little, E. M., and Quinn, W. E., "Neutrons from Plasma Compressed by an Axial Magnetic Field (Scylla)", Proceedings of the Second International Conference on the Peaceful Uses of Atomic Energy, Geneva, vol. 32, p. 337; 1958.

38. Bodin, H. A. B., Green, T. S., Niblett, G. B. F., Peacock, N. J., "An Experimental Investigation of the Rapid Compression of a Plasma Using Aximuthal Currents (Thetatron)", Proc. IV Conference on Ionization Phenomena, Uppsala, vol. 2, p. 1061; 1959.

39. Klein, M. M., and Brueckner, K. A., "Plasma Propulsion by a Rapidly Varying Magnetic Field", Jour. Appl. Phys., vol. 3., p. 1437; 1960.

40. Fonda-Bonardi, G., "Litton Research on Plasma Acceleration" ARDC Conference on Ion and Plasma Research, ASTIA Doc. 162274; October,

1958: Penfold, A. S., "Injection into a Linear Plasma Accelerator", Third AFOSR Contractors' Meeting on Ion and Plasma Propulsion, New York; March, 1960.

41. Meyer, R. X., "Magnetic Plasma Propulsion by Means of a Traveling Sinusoidal Field", Space Technology Laboratories, Physical Research Lab. Rpt. No. STL/TR-60-0000-09114; April, 1960: Clauser, M. U., "The Magnetic Induction Plasma Engine", Space Technology Laboratories, Physical Research Lab., Rpt. No. STL/TR-60-0000-00263; August, 1960.

42. Janes, G. S., "Magnetohydrodynamic Propulsion", Avco Research Rpt. No. 90; August, 1960.

43. Miller, D. B., "Crossed Field Acceleration of Ions and Plasmas", Third AFOSR Contractors' Meeting on Ion and Plasma Research, New York; March, 1960.

44. Josephson, V., "Production of High Velocity Shocks", Jour. Appl. Phys., vol. 29, p. 30; 1958.

45. Dow, W. G., Fundamentals of Engineering Electronics, Second Edition, J. Wiley and Sons, New York, p. 48; 1952.

46. Spangenberg, K. R., Vacuum Tubes, McGraw-Hill Book Co., New York, p. 116; 1948.

47. Linhart, J. G., Plasma Physics, North Holland Publishing Co., Amsterdam; 1960.

48. Post, R. F., "Sixteen Lectures on Controlled Thermonuclear Reactions", AEC Rpt. UCRL-4231 (Del.); February, 1954.

49. Chandrasekhar, S., "Adiabatic Invariants in the Motions of Charged Particles", The Plasma in a Magnetic Field, R. K. M. Landshoff, Editor, Stanford University Press, Stanford; 1958.

50. Spitzer, L., Physics of Fully Ionized Gases, Interscience Publishers Inc., New York, p. 7; 1956.

51. Alfven, H., Cosmical Electrodynamics, Clarendon Press, Oxford, pp. 24-34; 1953.

52. Dwight, H. B., "Magnetic Field Strength Near a Cylindrical Coil", Trans. AIEE, vol. 61, p. 327; 1942.

53. Penfold, A. S., "Particle Motion in an Axially Symmetric Magnetic Field", Litton Industries, Space Research Laboratories, AFOSR TN-60-961; May, 1960: also see Reference 58.

54. Busch, H., "Berechnung der Bahn von Kathodenstrahlen im axial-symmetrischen elektromagnetischen Felde", Ann. Phys., vol. 81, p. 974; 1926.

55. Kleen, W. J., Electronics of Microwave Tubes, Academic Press, Inc., New York; 1958.

56. Spitzer, op cit., p. 17.

57. Langmuir, I., and Mott-Smith, H. M., "Studies of Electric Discharges in Gases at Low Pressures", Gen. Elec. Rev., vol. 27, pp. 449, 538, 616, 762; 1924.

58. Penfold, A. S., "Two-Fluid Model for the Motion of a Rarified Plasma Accelerated by Induction", Amer. Roc. Soc. paper 1533-60; December, 1960.

59. Jahnke, E., and Emde, F., Tables of Functions, Dover Publications, New York; 1945.

60. Thomson, J. J., "The Electrodeless Discharge Through Gases", Phil. Mag. (London) vol. 4, p. 1128; 1927.

61. Eckert, H. U., "Diffusion Theory of the Electrodeless Ring Discharge", Corvair Scientific Research Laboratory, Res. Rpt. No. 9; February, 1961.

62. Rosenbluth, M., "Infinite Conductivity Theory of the Pinch", AEC Rpt. LA-1850; September, 1954.

63. Anderson, O. A., Baker, W. R., Colgate, S. A., Ise, J., and Pyle, R. V., "Neutron Production in Linear Deuterium Pinches", Phys. Rev. vol. 110, p. 1375; 1958.

64. Post, R. F., "Controlled Fusion Research—An Application of the Physics of High Temperature Plasmas", Proc. IRE, vol. 45, p. 134; 1957.

65. Niblett, G. B. F., and Green, T. S., "Radial Hydromagnetic Oscillations", Proc. Phys. Soc. (London) vol. 74A, p. 737; 1959.

66. Bodin, H. A. B., Green, T. S., Niblett, G. B. F., and Peacock, N. J., "The Formation and Implosion of a Cylindrical Current Sheath in Thetatron", Proc. IV Conference on Ionization Phenomena, Uppsala, vol. 2, p. 1065; 1959.

67. Clauser, M. U., "The Magnetic Induction Plasma Engine", Space Technology Laboratories, Physical Research Lab. Rpt. STL/TR-60-0000-00263; August, 1960.

68. Kolb, A. C., "Magnetic Compression of Shock Preheated Deuterium", Proc. Second United Nations International Conference on the Peaceful Uses of Atomic Energy, Geneva, vol. 31, p. 328; 1958.

69. Loos, H. G., "Heating and Confinement of a Plasma by a Magnetic Field of External Origin and with Short Rise Time", Phys. Rev. Letters, vol. 2, p. 282; 1959.

70. Miller, D. B., Dow. W. G., and Haddad, G. I., "An Electromagnetic Accelerator Utilizing Sequential Switching", The University of Michigan Research Institute, Rpt. 2522-10-F, AFCRC TR-58-267; September, 1958.

71. Spitzer, op cit., pp. 52, 84.

72. Shapiro, A. H., The Dynamics and Thermodynamics of Compressible Fluid Flow, Ronald Press, New York, vol. 1, p. 132; 1953.

73. Spitzer, op cit., p. 78.

74. Cobine, J. D., Gaseous Conductors, Theory and Engineering Applications, McGraw-Hill Book Co., p. 14; 1941.

75. Kolb, A. C., "Recent Progress in Shock Wave Research", IV International Conference on Ionization Phenomena; Uppsala; 1959.

76. Colgate, S. A., "Collisionless Plasma Shock", Phys. Fluids, vol. 2, p. 485; 1959.

77. Kantrowitz, A. R., and Petschek, H. E., "An Introductory Discussion of Magnetohydrodynamics", Avco Research Rpt. 16; May, 1957.

78. Fishman, F. J., Kantrowitz, A. R., and Petschek, H. E., "Magnetohydrodynamic Shock Wave in a Collision-Free Plasma", Avco Research Rpt. 85; January, 1960.

79. Craggs, J. D., Haine, M. E., Meek, J. M., "The Development of Triggered Spark Gaps for High Power Modulators", Jour. IEE, Pt. IIIA, vol. 93, p. 963; 1946.

80. Tuck, J. L., "Review of Controlled Thermonuclear Research at Los Alamos for Mid 1958", Proc. Second United Nations International Conference on Peaceful Uses of Atomic Energy, Geneva, vol. 32, p. 18; 1958.

81. Richeson, W. E., "Apparatus for Producing and Measuring High-Energy Electrical Discharges", Rev. Sci. Inst., vol. 29, p. 99; 1958.

82. Bostick, W. H., Byfield, H., and Nankivell, J., "Measurements on the Efficiency and Velocity Profile of a Coaxial Crater Pulsed Plasma Motor", Bull. Amer. Phys. Soc., vol. 5, p. 366; 1960.

83. Gorowitz, B., Gloersen, P., and Palm W., "Experimental Performance of a Pulsed Gas Entry Coaxial Plasma Accelerator and Applications to Space Missions", ARS paper No. 1535-60; December, 1960.

84. Dow, W. G., Fundamentals of Engineering Electronics, Second Edition, J. Wiley and Sons, New York, Chap. 15; 1952.

85. Lord Rayleigh, Proc. Roy. Soc., vol. A176, p. 16; 1940: Lord Rayleigh, Proc. Roy. Soc., vol. A189, p. 296; 1947.

86. Glasstone, S. and Loveberg, R. H., Controlled Thermonuclear Reactions, D. Van Nostrand Co., Princeton, New Jersey, p. 35; 1960.

87. Armstrong, E. B. and Emeleus, K. G., "The Generation of High-Frequency Oscillations by Hot-Cathode Discharge Tubes Containing Gas at Low Pressure", Proc. IEE, vol. 96, p. 390; 1949.

88. Janes, G. S. and Patrick, R. M., "The Production of High Temperature Gas by Magnetic Acceleration", Avco Research Rpt. No. 27; March, 1958.

89. Butt, E. P., et. al., "The Design and Performance of ZETA", Proc. Second United Nations International Conference on the Peaceful Uses of Atomic Energy, Geneva, vol. 32, p. 42; 1958.

90. Lovberg, R. H., "The Use of Magnetic Probes in Plasma Diagnostics", Ann. of Phys., vol. 8, p. 311; 1959.

91. Forster, H., and Schulter, J., "Measurements of Conductivity on Linear Pinch Discharges by Means of Magnetic Probes.", Proc. IV International Conference on Ionization Phenomena in Gases, Uppsala; 1959: North Holland Publishing Co., Amsterdam; 1960.

92. Reifman, A. and Dow, W. G., "Dynamic Probe Measurements in the Ionosphere", Phys. Rev., vol. 75, p. 987; 1949: Hok, G., Spencer, N. W., Reifman, A., Dow, W. G., "Upper Air Research Program Rpt. No. 3, Dynamic Probe Measurements in the Ionosphere", The University of Michigan, Engineering Research Institute, Project M824.

93. Johnson, E. O., and Malter, L., "A Floating Double Probe Method for Measurements in Gas Discharges", Phys. Rev., vol. 80, p. 58; 1950.

94. Colgate, S. A., and Wright, R. E., "Collapse—The Shock Heating of Plasma", Proc. Second United Nations International Conference on the Peaceful Uses of Atomic Energy, Geneva, vol. 32, p. 145; 1958: Harding, G. N., et. al., "Diagnostic Techniques Used in Controlled Thermonuclear Research at Harwell", same proceedings, vol. 32, p. 365.

95. von Engel, A., Ionized Gases, Clarendon Press, Oxford, p. 69; 1955.

96. Herzberg, H., Atomic Spectra and Atomic Structure, Dover Publications, New York, pp. 118, 160; 1944.

97. ter Harr, D., Elements of Statistical Mechanics, Rinehart and Co., New York, p. 56; 1954.

98. Martin, E. A., "The Underwater Spark: An Example of Gaseous Conduction at about 10,000 Atmospheres", The University of Michigan, Engineering Research Institute, Ann Arbor; 1956.

99. Moore, C. E., "Term Designations for Excitation Potentials", Princeton University Observatory, Princeton, New Jersey; 1934.

LIST OF SYMBOLS

A_ξ	Axial geometric magnetic force function (Eq. 2.18).
A_ρ	Radial geometric magnetic force function (Eq. 2.19).
B	Magnetic flux density (webers/m^2).
b_r, b_θ, b_z	Radial, azimuthal and axial components of B.
b_o	Value of b_z external to plasma (Eq. 4.13).
$\bar{b}$	Average magnetic flux density linked by particle (Eq. 4.19).
B_1	Ion partition function.
c	Sonic velocity.
D	Electric displacement field (coulombs/m^2).
E	Electric intensity field (volts/meter).
e_r, e_θ, e_z	Radial, azimuthal and axial components of electric intensity field.
E_r	Excitation radiation energy loss (joules/m^3, Table B.1)
F	Force.
g	Acceleration due to gravity.
g_{11}	Statistical weight of ion first excitation level.
H	Magnetic intensity field (amperes/meter)
I	Current (amperes).
I_c	Coil current (amperes).
I_o	Maximum value of coil current (amperes).
i	Current density (amperes/m^3).
i_θ	Azimuthal component of current density (amperes/m^3).
I_{sp}	Specific impulse(seconds).
i'	Linear current density (amperes/meter)
i'_c	Linear coil current density (amperes/meter).
i'_e	Linear electron current density (amperes/meter).

i'_g Linear gas current density (amperes/meter).

i'_i Linear ion current density (amperes/meter).

i'_o Maximum value of linear coil current density (amperes/m).

j Complex operator.

k Ratio of specific heats.

k_b Boltzmann constant.

k_e Electron self-magnetic field factor (dimensionless, Eq. 3.13).

k_i Ion self-magnetic field factor (dimensionless, Eq. 3.14).

k_α Density parameter (Eq. 4.27).

M Mach number (Section 5.4).

m_e Electron mass (9.11×10^{-31} kg).

m_i Ion mass (A.W. x 1.67×10^{-27} kg).

M_s Linear mass density in current sheet (kg/meter).

M.W. Molecular weight.

n Particle density (particles/m^3).

n_e Electron density (particles/m^3).

n_i Ion density (particles/m^3).

n_1 Density of singly ionized particles (particles/m^3).

n_{11} Density of singly ionized particles in first excitation level (particles/m^3).

n' Linear particle density (particles/meter).

n'_s Linear particle density in current sheet (particles/m).

p Pressure.

q_e Electronic charge (1.60×10^{-19} coulombs).

R Gas constant.

r Radial coordinate (meters).

r_{eo} Radius of outermost electron (meters, Fig. 4.2).

r_{io} Radius of outermost ion (meters, Fig. 4.2).

r_o Initial outer radius of ionized gas (meters).

T Temperature (°K).

V Velocity (meters/second).

V_{ex} Exhaust velocity (meters/second).

V_s Velocity of current sheet (meters/second).

V_o Maximum voltage around coil (Table 2.2)

X_{11} Energy of ion first excitation level relative to ion ground state (joules).

z Axial coordinate (meters).

α Convection current parameter (dimensionless, Eq. 4.10).

γ Displacement current parameter (seconds^2, Eq. 4.10).

ϵ_o Free space permittivity (8.85×10^{-12} farad/meter).

η Charge-to-mass ratio (coulombs/kg).

η_e Electron charge-to-mass ratio.

η_i Ion charge-to-mass ratio.

θ Azimuthal coordinate (radians).

λ Mean free path (meters).

μ_o Free space permeability ($4\pi \times 10^{-7}$ henry/meter).

ξ Dimensionless axial coordinate (Eq. 2.9).

ρ Dimensionless radial coordinate (Eqs. 2.8, 4.4).

τ Dimensionless time coordinate (Eq. 4.40).

φ Magnetic flux (webers).

ψ Magnetic field strength per unit coil current (webers/m^2-ampere, Eqs. 2.12, 2.13, 2.14, 2.15, 2.16).

ω Angular frequency (radians/second).

ERRATA FOR

ACCELERATION OF PLASMAS

BY INDUCTIVELY GENERATED ELECTROMAGNETIC FIELDS

Final Report, Project 2836

by David B. Miller

p. viii — Line 11; A_{θ}, not A_{θ}^{*}.

p. 11 — Line 3; 1.1d, not 1.1c.

p. 14 — Line 25; should read "... and is thereby generating a magnetic field going into the page and ..."

p. 39 — Ordinate scale on Fig. 2.6 should be 4 centimeters per division, as on Fig. 2.5(a), p. 37.

p. 53 — Outer current shell, at r_c on Fig. 3.2, should be labeled i_c', not L_c'.

p. 133 — Ballistic pendulum measurements are on a relative scale.

p. 149 — Line 12; add "chamber" after acceleration.

p. 185 — Fig. 7.28; should read "prote orientations", not "probe concentrations".

p. 208 — Line 4; should read "... population by the ratio of plasma life time to mean life time of an excited state and ..."

p. 208 — Eq. B.2; should be

$$e^{-\frac{q_e V_i}{K_b T}} .$$